A thesis submitted in fulfillment of the requirements for the degree of Doctor of philosophy Sciences

Designing Azo-functionalized Peptoids based on Phenylazothiazole for Solar Thermal Energy Storage: a Journey toward Eternal Sunshine

Gwendal Henrard

Academic year 2025-2026

Supervisors:

Prof. Pascal Gerbaux (UMONS)

Porf. Jérôme Cornil (UMONS)

Members of the jury:

Prof. Stéphanos Konstantinidis (UMONS)	–	President of the jury
Dr. Dimitri Stanicki (UMONS)	–	Internal reviewer
Prof. Benjamin Elias (UCL)	–	External reviewer
Prof. Jean-Yves Salpin (Université Évry Paris-Saclay, France)	–	External reviewer

Abstract

Renewable energies are increasingly recognized as the most promising alternatives to fossil fuels, offering clean and sustainable power sources. Among them, solar energy stands out as the most abundant: in just six hours, the Sun delivers more energy to Earth than humanity consumes in an entire year. However, its intermittent nature necessitates efficient storage and controlled release systems to enable large-scale applications.

One strategy relies on molecular systems capable of light-induced isomerization into metastable states, thereby storing energy for later release. These are known as MOlecular Solar Thermal systems (MOST). When energy is needed, the photoisomer reverts to its stable form through catalytic or thermal activation, releasing the stored energy as heat.

Among various photoswitching systems, azobenzene (AB) derivatives, undergoing reversible E → Z photoisomerization, are among the most extensively studied. Efforts have focused on improving key properties such as storage enthalpy, Z-isomer half-life, and absorption characteristics. To address these limitations, two strategies were explored in this thesis: (i) substituting one phenyl group with a thiazolyl moiety to red-shift absorption into the visible region, and (ii) grafting AB residues onto specific positions of a peptoid backbone to enhance energy storage capacity and prolong Z-isomer lifetime through cooperative effects.

This work investigates the design, synthesis, and evaluation of phenylazothiazole (PAT) derivatives and their incorporation into peptoid backbones as novel MOST candidates. The first part focuses on the synthesis and structural characterization of various PAT derivatives, alongside evaluation of their MOST properties to assess substitution effects. The second part examines peptoid trimers incorporating PAT units, comparing their MOST performance with free PATs to determine the influence of the peptoid scaffold.

Spectroscopic studies showed that PAT derivatives, whether free or peptoid-grafted, exhibit similar absorption profiles in or near the visible region—well-suited for solar applications.

Notably, incorporation into peptoid backbones significantly enhances Z-isomer stability, with intermolecular interactions extending the half-life. Additional investigations into solvent effects and catalytic activation revealed a strong dependence of Z-isomer stability on solvent polarity and proticity.

Overall, this thesis highlights the potential of PAT-grafted peptoids as innovative MOST systems capable of visible-light absorption without compromising Z-isomer stability. Furthermore, their properties can be finely tuned through molecular substitution. The methodology developed herein provides a robust foundation for future studies on broader families of isomers, paving the way toward next-generation MOST materials.

Acknowledgments

Et voilà, clap de fin ! Ce manuscrit marque la conclusion de quatre années de thèse et plus largement, de neuf années d'études à l'université mais une thèse, c'est quoi finalement ? Pour ma part ça peut se résumer à 40 % de procrastination, 20 % de synthèses infructueuses contre 5 % de synthèses qui daignent enfin fonctionner, 5 % d'idées géniales sur le papier mais beaucoup moins en pratique, 5 % de crises existentielles et de remises en question constante, 5 % de temps passer à manipuler pour 15 % de temps à traiter des données, 5 % de café noir (souvent tiède et d'un goût douteux) et enfin 5 % de moments magiques qui font relativiser sur tout le reste. Alors oui, je sais, ça fait 105 % mais quand on aime on ne compte pas. Et quand je regarde derrière moi, je réalise que cette aventure a réuni, de près ou de loin, une multitude de personnes sans qui rien n'aurait été possible. Il m'est donc impossible de remercier tout le monde individuellement mais je vais tout de même tenter de relever le défi.

Dans un premier temps, je tiens à remercier le Professeur Stéphanos Konstantinidis, le Docteur Dimitri Stanicki, le Professeur Benjamin Elias et le Professeur Jean-Yves Salpin d'avoir accepté de lire et d'évaluer ce manuscrit. J'espère sincèrement que vous trouverez davantage de plaisir à le lire que j'en ai eu à l'écrire.

Enchainons ensuite avec deux personnes sans lesquelles je n'aurai pas eu l'opportunité de faire une thèse, mes deux promoteurs : le Professeur Pascal Gerbaux et le Professeur Jérôme Cornil.

Pascal, je tenais tout d'abord à te remercier d'avoir cru en moi et de m'avoir permis de réaliser dans un premier temps mon mémoire et ensuite ma thèse au sein du S^2MOs. Je dois dire que j'admire énormément ta passion pour la spectrométrie de masse et plus généralement tout ce qui a trait aux sciences, passion que tu fais transparaitre chaque jour, que ce soit à travers les cours que tu donnes ou lors des discussions autour des résultats (et parfois de nos galères). Toujours présent lors des moments sérieux à prodiguer de précieux conseils ou des

suggestions avisées, mais jamais le dernier pour faire une blague, souvent d'un goût douteux on ne va pas se mentir, tu es une personne exceptionnelle. Mais si je peux me permettre un conseil, lève un peu le pied de temps en temps et prends du temps pour toi, la santé c'est ce qu'il y a de plus important. Enfin voilà, c'est un chapitre qui se clos et j'espère avoir laissé une trace indélébile dans le laboratoire, à la fois au sens spirituel et au sens littéral, on ne va pas se mentir, c'est complique de travailler avec des colorants sans en mettre partout !

Jérôme, je voulais te remercier d'avoir lu jusqu'à la dernière ligne de cette thèse, merci aussi d'avoir toujours pris le temps pour des réunions productives sur les MOST, pour ton enthousiasme communicatif et ton humour toujours bien placé. Je me souviens encore de ton intervention à propos de l'effet tunnel lors d'une réunion, qu'on a tous prise pour une blague alors que c'était totalement sérieux. Désole, mais en tant que chimistes organiciens, faut avouer que l'effet tunnel est un peu notre running gag quand on ne sait pas expliquer quelque chose. Je reste aussi impressionné par ta capacité à pouvoir expliquer de manière simple des concepts extrêmement complexes avec une aisance déconcertante. Pour tout ça, un grand merci, ce fut un vrai plaisir de travailler avec toi.

Que serait ces remerciements sans évoquer le magnifique, l'illustre, le grand Docteur Julien De Winter, dit le GOAT, dit le plus chauve, dit Juju. Tant de surnoms pour une seule personne… mais quelle personne ! Alors oui, tu vas sûrement me dire encore une fois : « je ne suis pas chauve, je rase mes cheveux ». Très bien, mais je te laisse avec la définition officielle de chauve que j'ai trouvée sur internet: « Qui n'a plus ou **presque** de cheveux ». Bon, on ne va pas se mentir, ça colle quand même pas mal. Niveau capillaire, il y a pire, mais on y reviendra plus tard. Ah, que dire de Julien à part que c'est une personne géniale toujours prête à aider lorsque tu en fais la demande, non sans une pointe d'humour lorsque c'est nécessaire ou pas d'ailleurs. Je n'oublierai plus jamais de vérifier mes équivalents quand une réaction ne fonctionne pas avant de venir te voir, étant donné que tu me le rappelles encore aujourd'hui. Merci aussi d'avoir été là pour m'écouter et me remonter le moral pendant les moments de doute et on sait qu'il y en a eu beaucoup. Ça a été un vrai plaisir de partager ces cinq années

avec toi au sein du labo, mais aussi lors des conférences. Parce qu'une thèse, c'est aussi partager des moments privilégiés lors de conférence que ce soit à Maastricht ou Paris, c'était vraiment des moments inoubliables. Mais bon, on ne va pas s'étendre sur le sujet, parce que comme on l'a dit à plusieurs reprises, « tout ce qui se passe à Maastricht reste à Maastricht », et aussi « tout ce qui se passe à Paris reste à Paris », enfin bref tout ce qui se passe en conférence reste en conférence quoi. Pour tout ça, tous ces moments géniaux, ces fous rires, ces coups de main et ces discussions, je te remercie énormément. Ah j'allais oublier : salue Paul Ledef de ma part, j'ai tellement hâte de le revoir… on sait jamais quand il peut surgir.

En parlant des membres du personnel du labo, comment pourrais-je oublier Amandine ? Franchement, il faudrait être une mauvaise personne pour ne pas te mentionner dans ces remerciements. Bon voilà, c'est fait, passons à la suite.

Non je rigole ! Amandine, t'es vraiment une personne en or, toujours partante pour discuter et rigoler de tout (enfin presque tout, on ne fait pas de blague sur les enfants, bordel !). Tu sais même si je taquine souvent sur le fait que tu sois française, bah au fond c'est justifié : on a perdu en 2018, c'est donc un juste retour des choses. Plus sérieusement, je voulais te remercier d'avoir été là pendant plus de deux ans et d'avoir tout fait pour que la logistique du labo roule sans accroc. La recherche, c'est important, mais pouvoir la faire dans un environnement où quelqu'un comme toi veille à ce que tout se passe bien, ça l'est encore plus. Merci aussi pour ces longues discussions sur nos galères respectives (tant professionnelles que personnelles), que ce soit pour chercher une solution ou juste pouvoir se plaindre sans être jugé, c'était un plaisir. Bref, merci pour tout ce que tu fais, le labo sans toi, c'est un peu comme un spectromètre de masse sans vide, ça ne sert à rien. #blaguedemassiste

J'en ai parlé plus tôt, mais comment ne pas remercier Antoine, et ses expériences capillaires d'un goût… disons discutable ? Eh oui, laisser pousser les cheveux qu'il te reste ne fera pas revenir les autres. Fais-moi plaisir, fais quelque chose : soit t'assumes et tu choisis une coupe adaptée, soit tu prends un aller-retour pour la Turquie, je suis même prêt à te payer le billet si besoin ! Antoine, jamais le dernier pour faire une blague ou poser une question un peu mal

placée, on ne va pas se mentir. Tu restes avant tout une personne profondément gentille, toujours à l'écoute et prête à aider les autres, parfois même avant toi-même. Merci pour tes conseils avisés en synthèse organique, pour ta bonne humeur et pour toutes nos discussions qui vont franchement me manquer. Plus que tout, tu vas laisser un vide au labo, parce qu'une personne comme toi, ça ne se remplace pas facilement. Je te souhaite le meilleur pour la suite de ta carrière, que ce soit dans un labo ou dans une salle de classe. Le plus important, c'est que tu sois heureux dans ce que tu fais, alors choisis bien ton chemin et si possible choisis en un qui passe proche d'un coiffeur.

Je tenais aussi à remercier le service de Chimie Générale, Organique et Biomédicale de l'université de Mons pour m'avoir permis de réaliser les RMN de mes différents azobenzènes synthétisés.

Viens ensuite le temps de remercier les doctorants avec qui j'ai partagé de super moments durant ces quatre années de thèse. Commençons par ceux qui sont partis trop tôt dans cette aventure… du calme, ils ne sont pas morts, ils ont juste terminé leur thèse d'une main de maitre avant la mienne.

Commençons par le commencement : petite Perrin, on n'a partagé le même bureau qu'une seule année, mais quelle année ! Soyons honnêtes, l'ambiance était vraiment top… quoique parfois un peu trop top, je crois qu'avec Philippe, on a dû te rendre folle à force de faire du bruit et des conneries pendant que tu essayais d'écrire. Mais bon, ta fin de thèse n'aurait sûrement pas été aussi amusante sans nous, non ? Cette année s'est clôturée en beauté avec une conférence mémorable à Maastricht et une super défense de thèse de ta part. J'espère que tout se passe bien chez QA et qui sait, peut-être qu'un jour nous serons de nouveau collègues. PS : Jean-Patricia est en de très bonnes mains… juste pas les miennes.

Viens ensuite Philippe, ah là là, Phil, quel duo on formait quand même ! Je pense qu'on en a énervé plus d'un durant les années qu'on a passées ensemble au labo. Comme Perrin a pu le vivre et tout le monde l'a constaté, notre duo était comparable à un ouragan, le mur en face

du bureau 251 en garde d'ailleurs une trace indélébile… malgré moi, je dois dire. C'est peut-être d'ailleurs pour ça que, après le départ de Perrin, personne n'a osé s'installer dans ce bureau jusqu'à ce qu'Emma ait le courage ou l'inconscience de le faire ! On n'était jamais les derniers pour faire une connerie, une petite blagounette ou à partager les derniers ragots du labo. Et puis, le 28 septembre 2023, tu es parti, me laissant tout seul… j'ai donc enfin dû commencer à travailler sérieusement sur ma thèse après ce terrible drame. Je voulais te remercier pour tout ce que tu as pu faire pour moi, pendant et même après ta thèse. Nos discussions, souvent très peu philosophiques, nos débats intenses sur Dokkan ou nos conversations où on parlait de tout et surtout de rien, entre deux blagues d'un goût douteux, tout ça, c'était juste énorme. Merci aussi de m'avoir écouté et conseillé dans les moments de doute. En bref, t'es vraiment une personne incroyable et je suis super content d'avoir pu passer la moitié de ma thèse à tes côtés. J'espère que l'on continuera à partager plein de bons moments dans les jours, mois et années à venir. Et puis finalement sans contexte et gratuitement : soyons honnêtes avec ton talent, tu pourrais vendre de l'eau à un poisson, et ça, c'est fort, surtout quand on sait que les poissons n'ont pas d'argent.

Passons ensuite à Benjamin, tu es le pionnier de l'investigation des systèmes MOST au sein du S^2MOs, finalement, t'es un peu notre Jésus à nous, les longs cheveux en moins quoi. D'abord ton mémorant, puis ton collègue de thèse, sur ce magnifique sujet qu'est celui des MOST, notre relation a évolué au fil du temps et tu as clairement contribué à forger le scientifique que je suis devenu aujourd'hui. Tu es la personne vers qui je me tourne dès que j'ai un doute sur quelque chose à propos de notre sujet commun mais pas seulement. Tu sais donner des conseils précieux, sincères et toujours avisés. Durant ces cinq années, on a partagé de franches rigolades, des moments de confidences, que ce soit au labo ou en conférences et ce fut un véritable plaisir de vivre tout ça avec toi. Pour tout ça, je voulais te remercier sincèrement et te souhaiter le meilleur pour la suite, à toi, à Lia et au petit Roméo, qui devrait venir agrandir votre magnifique famille courant mars, le meilleur mois de l'année, si tu veux mon avis.

Ah voilà le tour de Louis, l'homme pour qui la pilosité faciale n'a aucun secret, sérieusement, c'est quoi ton secret ? L'homme capable de porter des bottes en cuir, une chemise à carreaux (attention à ne pas confondre avec la chemise de Caro, la meuf de la compta) et un chapeau de cowboy sans paraître ridicule. Un vrai cowboy, my man. Que dire de toi à part que t'es une personne super sympa, toujours bienveillante et jamais dans le jugement. Tu fais partie de ces gars hyper investis dans leur thèse, qui avancent coûte que coûte, sans jamais rien laisser paraître même quand c'est dur et pour ça, franchement, je t'admire beaucoup. Je pense que j'ai passé mes meilleures conférences en ta compagnie, que ce soit à Paris, avec cette magnifique taverne du Korrigans, à Cagliari, où un tapis a vécu des moments qu'il n'aurait jamais dû vivre, ou encore lors de cet extraordinaire voyage aux États-Unis. J'y ai eu quelques moments de stress mais tu as toujours su trouver les mots pour me rassurer et faire de ce voyage l'un des plus beaux souvenirs de ma thèse. Alors pour tout ça, Louis, merci d'être la personne géniale que tu es.

Thomas, le seul et l'unique. Mon premier et dernier mémorant, faut peut-être y voir un signe, non ? Thomas, c'est le gars qui part toujours en dernier du labo ou qui débarque même le week-end. Si ça, ce n'est pas de la passion, je ne sais pas ce que c'est. Mais sérieusement, tu fais quoi tout seul au labo ? Quand je vois comment tu bosses et tous les trucs hyper compliqués que t'arrives à démontrer, je me dis que si tu ne fais pas une carrière scientifique magistrale derrière tout ça, je ne comprendrai absolument pas. Dès que j'avais un souci dans mes données ou que je ne sais pas quoi en faire, nos discussions m'ont toujours aidé, même si, faut l'avouer, t'es parfois sacrément têtu sur certains points. Mais c'est aussi ça qui fait ton charme : t'es quelqu'un de vrai, tu ne te caches pas, tu restes toi-même et si ça ne plaît pas, tant pis. Et ça, franchement, c'est une grande qualité. Ton humour, entre l'autodérision et la provocation, souvent à la limite de la limite, voire même au-delà, me fait mourir de rire et je pèse mes mots. Enfin voilà t'es quelqu'un d'exceptionnel avec un humour mordant qui est voué a faire de grandes choses… tout comme celui dont on ne doit pas prononcer le nom a

fait de grandes choses, terribles certes, mais stupéfiantes. En bref, je te souhaite le meilleur, merci pour tous, Thomas.

Quentin, ta justesse scientifique m'étonnera toujours, tu es un vrai passionné, tout comme Pascal ou Julien, et tu le fais transparaitre chaque jour à travers ton implication au labo. Il est vrai que je ne partage pas forcément cette même optique, disons que j'ai une approche un peu plus… artistique de la science mais je la comprends tout à fait. D'ailleurs, la manière dont vous voyez tous le nouveau cyclique comme un petit jouet, c'est juste hilarant à observer ! J'aimerais aussi te remercier pour tous ces moments passés ensemble aux États-Unis, tant de fous rires, de découvertes et d'émotions concentrées en si peu de temps. C'était vraiment un voyage incroyable que je n'oublierai jamais. Pour tout ça, merci beaucoup, et bonne continuation à toi au sein du labo, pour je l'espère, encore longtemps.

Passons ensuite aux plus jeunes personnes du labo, ça fait bizarre de se dire que je suis maintenant un des plus vieux… le temps passe vite quand on s'amuse ou qu'on galère c'est pareil.

Stella, après ton échec au FRIA l'année passée, tu as retroussé tes manches, décroché un financement d'un an et retenté ta chance. À force de travail, de persévérance et de motivation, tu as réussi à tous nous impressionner au fil des répétitions. Et sans surprise, tu as atteint ton objectif haut la main ! C'était vraiment génial de pouvoir assister à tout ça, je suis super content pour toi. Je suis persuadé que tu vas réaliser une thèse en béton armé.

Pauline, au moment où j'écris ses lignes, j'espère que tu te remets bien de ton opération et que tu reviendras en pleine forme pour poursuivre ta thèse dans les meilleures conditions. Je voulais aussi te remercier d'avoir ramené le Wizard au labo, parce qu'on se tape des barres en jouant à ce jeu tous les midis et ces moments valent de l'or.

Charlotte, toujours motivée, toujours positive, toujours prête à apprendre et surtout toujours en train de gagner avec un 11 ou 12 au Wizard. Sérieusement, comment tu fais ? C'est

statistiquement impossible d'avoir autant de chance. Merci pour ta bonne humeur et ton énergie contagieuse, ça fait vraiment du bien dans le quotidien du labo.

Sixtine, aussi dite Sistine ou le S, t'es vraiment une personne géniale et j'aurai aimé passer plus de temps au labo pour mieux te connaitre même si, au bout de 4 ans, on n'aurait pas appris grand-chose tellement tu ne parles pas de toi. Enfin, ta nonchalance et ta "joie de vivre" sont vraiment communicatives et, pour tous ces moments mémorables et parfois gênants, on ne va pas se le cacher, merci beaucoup, c'était vraiment cool de pouvoir venir parler de tout et de rien pendant la rédaction de cette thèse. PS: Je suis sûr que tout se passera bien pour la suite, et que tu feras une thèse qui vaudra vraiment le coup d'être lue.

Ari, merci pour tout le boulot que tu fais pour la team MOST, même si elle réduit petit à petit. T'es vraiment un gars super et j'admire ta capacité à vulgariser des trucs ultras complexes avec une certaine facilité, surtout pour nous, pauvres petits chimistes organiciens qui ne comprennent rien à la chimie théorique.

Vient ensuite le tour d'une personne qui, à ce stade, doit sûrement être en train de maronner en se demandant quand son nom va enfin tomber. Ne t'inquiète pas Emma, ton moment de gloire est arrivé, comme on dit, on garde le meilleur pour la fin. Emma, tu es clairement la personne avec qui j'ai passé le plus de temps au labo et s'il y a une raison à ça, c'est qu'on se ressemble sur pas mal de points. Bon, je reste quand même un peu plus mesuré que toi dans mes réactions. Que ce soit dans notre façon d'aborder la thèse ou dans nos crises existentielles à cause d'elle, on a souvent été sur la même longueur d'onde (mdrrr, longueur d'onde #blaguesdechimiste). Mais rassure-toi, je suis la preuve vivante qu'on peut en sortir sans trop de séquelles… enfin, je crois. Ce qui me fait le plus rire, c'est que parfois on n'a même plus besoin de parler, un simple regard suffit et c'est fini, on explose de rire. Ces moments-là vont clairement me manquer. Je crois qu'une vraie amitié est née au fil de ces années passées ensemble au labo et j'espère sincèrement qu'elle continuera après tout ça. Merci aussi pour tous ces souvenirs en conférence, des moments incroyables, souvent autour d'un verre mais bon ce n'est pas de l'alcoolisme si c'est juste un verre par jour t'inquiète pas.

Bref, merci pour tout, pour ta présence, ton humour et ta folie communicative. Reste comme tu es, une personne exceptionnelle, entière et toujours vraie. Et avant de conclure, un dernier petit conseil pour le futur, quand tu écriras ta thèse, pense à enregistrer ton document à chaque paragraphe. Ça pourrait t'éviter de maudire ton ordinateur, ou toi-même, au cas où, disons tu fermerais ton fichier sans sauvegarder.

Durant mes études, j'ai eu la chance de rencontrer des personnes exceptionnelles, sans qui ces neuf années n'auraient jamais eu la même saveur. Ce sont des gens avec qui j'ai partagé d'innombrables bons moments et je voulais les remercier sincèrement pour tout ça. Merci à Maxence, Loris, Lévy, Quentin, Justine, David, Louis, Pierre, Sylvie, et à bien d'autres encore, sans qui ces années n'auraient pas été aussi incroyables.

Comment faire une section de remerciements sans évoquer une partie si importante de ma vie : les scouts. Toutes les magnifiques personnes que j'ai rencontrées au fil de ces années de scoutisme m'ont énormément apporté dans la construction de la personne que je suis aujourd'hui. Il m'est impossible de tous vous remercier individuellement, mais je suis certain que vous vous reconnaitrez, alors, du plus profond de cœur merci.

Et ce n'est pas tout, puisque cette grande aventure s'est conclue cette année avec une dernière étape mémorable : la Route. Un petit groupe de personnes formidable ; Marion, Laura, Fabian, Manon, Antoine D., Camille, Antoine Z. et Lucas, avec qui nous avons décidé de nous lancer dans cette aventure extraordinaire. En juillet, nous sommes parties pour un voyage en van à travers plusieurs pays, pour explorer, rencontrer et mener à bien un projet. Je voulais vous remercier pour ce voyage exceptionnel, qui est venu couper en deux ma rédaction de thèse et m'a offert une véritable bouffée d'air frais dans cette période intense. Ce fut une expérience inoubliable, riche en découvertes, en rires et en moments partagés, des souvenirs précieux qui m'ont aidé à trouver l'énergie et l'inspiration nécessaires pour achever ce manuscrit.

Un merci tout particulier à Brieuc et Laura, deux amis sincères et précieux, qui ont toujours su comprendre à quel point cette étape comptait pour moi. Merci pour votre bienveillance, votre écoute, et pour l'intérêt que vous avez toujours porté à mon travail, même quand mes explications tenaient plus du charabia scientifique que d'un vrai discours cohérent. J'espère que la prochaine fois que vous partirez en randonnée avec Marion, je pourrai enfin me joindre à vous, histoire de troquer mon clavier et mes corrections contre un peu d'air frais, cette fois !

Pour terminer ces remerciements, je voulais parler de ceux sans qui rien de tout cela n'aurait été possible : ma famille. Alors voilà, mille mercis à mes parents. Papa, Maman, je vous remercie infiniment pour tout ce que vous avez fait pour que j'en arrive là aujourd'hui. Merci de m'avoir toujours poussé à aller plus loin, de m'avoir encouragé à donner le meilleur de moi-même, et surtout de m'avoir élevé avec autant de gentillesse et de bienveillance. J'espère qu'au bout de ces neuf années d'étude, j'ai su vous rendre fiers, même si le chemin n'a pas toujours été droit, même s'il y a eu des doutes. Vous avez toujours été là, présents, patients et prêts à me remotiver. Pour tout ça et pour tout ce qui viendra encore, merci du fond du cœur.

Une pensée aussi pour mon frère et mon filleul, pour tous ces moments de franche rigolade, que ce soit autour d'une manette de PlayStation ou lors de moments conviviaux qui m'ont permis de souffler un peu au milieu de cette montagne de travail. Et enfin, comment ne pas penser à toi, Bérangère. En écrivant ces lignes, c'est avec une petite larme à l'œil que je me dis que, de là-haut, tu dois être fière de moi. Je sais à quel point tu auras aimé partager ce moment avec nous, et d'une certaine manière, je suis sûr que tu n'es pas très loin.

Comment ne pas citer aussi la famille de Marion : Didier, Gabrielle, Fabian, Justine et Géa. À votre manière, chacun de vous a contribué à rendre cette expérience, plus agréable, que ce soit à travers les moments de rire, de convivialité ou encore lorsque vous nous proposiez de venir partager de délicieux petits plats. Faut avouer que la nourriture, c'est quand même le meilleur des remèdes ! J'espère aussi que vous êtes fier de ce que j'ai pu accomplir et je vous remercie énormément pour tout ce que vous avez fait pour moi.

Et finalement, comment conclure ces remerciements de la meilleure des manières qu'en remerciant la femme avec qui je partage ma vie depuis plus de onze ans maintenant. Marion, Mi Amore, toi qui es à mes côtés et me supportes depuis tant d'années, si tout ceci a été possible, si j'ai réussi à terminer la rédaction de cette thèse, c'est en grande partie grâce à toi.

Toi qui viens me faire des petits concerts improvisés autour de moi lorsque j'écris, juste pour me remonter le moral.

Toi qui me pousses à être la meilleure version de moi-même à chaque instant.

Toi qui regardes des séries de téléréalité complètement débiles pendant que je travaille et qui regardes encore "La Bataille" au moment où j'écris ces lignes, histoire de me motiver en me rappelant le genre de personne que j'ai bien fait d'éviter de devenir en poursuivant mes études.

Toi qui as fait, il faut le dire, souvent (pour ne pas dire tout le temps) à manger à la maison pendant mes dernières semaines de rédaction et qui as géré bien plus que les repas finalement.

Toi qui sais me faire mourir de rire avec une facilité déconcertante et qui m'as permis de tenir durant les périodes les plus difficiles.

Toi qui es une personne extraordinaire, magnifique, rayonnante, avec ses yeux d'un bleu éclatant et ce sourire capable d'illuminer mes journées, tu es ma plus grande source d'inspiration.

Je te suis infiniment reconnaissant pour tout cela, et je te promets que désormais, les rôles vont s'inverser, à ton tour de pouvoir te reposer sur moi, comme moi j'ai pu me reposer sur toi.

Et comment ne pas terminer sans remercier Rosco, Snow et Basile, nos magnifiques compagnons, qui, à leur manière, par des papouilles, des ronronnements ou des câlins, ont eux aussi apporté leur petite pierre à l'édifice. Voilà, cette fois-ci, ce sont vraiment les dernières lignes que j'écris. Je réfléchis à la suite, et même si je ne sais pas encore ce que l'avenir nous réserve, je sais une chose : je veux l'affronter avec toi, parce que tu es l'amour de ma vie,

parce que je t'aime et parce que je n'ai besoin de rien d'autre que ta présence à mes côtés. Lorsqu'il faut parler d'amour et des sentiments que j'ai pour toi, les mots me manquent souvent, mais j'espère réussi à les exprimer cette fois-ci.

Je t'aime ❤️ !

Je vous laisse avec trois citations qui me tiennent à cœur,

à vous tous, du fond de mon cœur, **merci** !

Gwendal

“Les gens les plus forts de cette planète ce sont les gens qui sont capables de se modérer. Un carré de chocolat, je ne savais même pas qu’il y avait des carrés. Pour moi il y avait un rectangle avec des décorations dessus, c’est quoi cette histoire de carré ?”

Roman Frayssinet, Ô dedans

“C’était difficile, alors j’ai essayé de rigoler, pour que personne ne s’ennuie. J’ai raté, mais je veux pas qu’on dise que j’ai rien foutu, parce que c’est pas vrai.”

Arthur Pendragon, Kaamelott, Livre V Le retour du roi

“Je suis le genre de mec qui peut passer d'un truc hyper profond à un truc complètement con en deux secondes.”

Alban Ivanov, Vedette 2.0

List of abbreviations

$\Delta G^{\ddagger}$	Gibbs free energy of activation
$\Delta H^{\ddagger}$	Enthalpy of activation
ΔH	Difference of energy between isomers/storage enthalpy
$\Delta S^{\ddagger}$	Entropy of activation
Φ	Quantum yield
δ	Chemical shift
λ_{max}	Maximum absorption wavelength
$\varepsilon_{\lambda max}$	Molar extinction coefficient at the λ_{max}
2D-NMR	Two-dimensional nuclear magnetic resonance
2-,4-,5-im	2-,3-,5-imidazole azobenzene
3-,4-,5-pz	3-,4-,5-pyrazole azobenzene
4-unit peptoid	PAT-based peptoid named N*spe*N2*tz*N*spe*N*spe*
AB(s)	Azobenzene(s)
Ac-Nter PAT 1	PAT-based peptoid named AcN2*tz*N*spe*N*spe*
Ac-PAT	Acetylated phenylazothiazole
Ac-PAT 1	(*E*)-N-(4-(thiazol-2-yldiazenyl)phenyl)acetamide
Ac-PAT 2	(*E*)-N-(4-((5-methylthiazol-2-yl)diazenyl)phenyl)acetamide
Ac-PAT 3	(*E*)-N-(4-((4-methylthiazol-2-yl)diazenyl)phenyl)acetamide
Ac-PAT 4	(*E*)-N-(3,5-difluoro-4-(thiazol-2-yldiazenyl)phenyl)acetamide
Ac-PAT 5	(*E*)-N-(4-(benzothiazol-2-yldiazenyl)phenyl)acetamide
ACN	Acetonitrile
Ac-ethyl	Ethyl acetate
Add/el	Addition/elimination
An-prot	Sodium (phenylamino)methanesulfonate
B30	Betaine 30/ Reichardt dye
$CDCl_3$	Deuterated chloroform
Center-AB	Pristine AB peptoid named N*spe*N*azb*N*spe*
Center-PAT 1	PAT-based peptoid named N*spe*N2*tz*N*spe*

Center-PAT 2	PAT-based peptoid named N*spe*N*5me*N*spe*
Center-PAT 3	PAT-based peptoid named N*spe*N*4me*N*spe*
Center-PAT 5	PAT-based peptoid named N*spe*N*benzo*N*spe*
Cter-AB	Pristine AB peptoid named N*spe*N*spe*N*azb*
Cter-PAT 1	PAT-based peptoid named N*spe*N*spe*N*2tz*
Cter-PAT 2	PAT-based peptoid named N*spe*N*spe*N*5me*
Cter-PAT 3	PAT-based peptoid named N*spe*N*spe*N*4me*
Cter-PAT 5	PAT-based peptoid named N*spe*N*spe*N*benzo*
CD	Circular Dichroism
CID	Collision-induced dissociation
Cter	C-terminus extremity of peptoid
CNT(s)	Carbon Nanotube(s)
D_2O	Deuterium oxide
DCM	Dichloromethane
DFT	Density functional theory
DHA	Dihydroazulene
DIC	Diisopropylcarbodiimide
DMSO	Dimethyl sulfoxide
DP	Degree of polymerization
$E_T(30)$	Dimroth–Reichardt parameter
$E_T^N(30)$	Normalized Dimroth–Reichardt parameter
E-isomer	Entgegen, *trans*-isomer
E_{col}	Collision energy
ED	Energy density
EDG(s)	Electron-donating group(s)
EI	electron ionization
EIC	Extracted Ion Current
EJ	Exajoules
ESI	ElectroSpray Ionization
EWG(s)	Electron-withdrawing group(s)
F-prot	Sodium ((3,5-difluorophenyl)amino)methanesulfonate

FT-IR	Fourier-transform infrared spectroscopy
$FvRu_2(CO)_4$	Fulvalene-teteracarbonyl-diruthenium
GC-MS	Gas chromatography coupled to mass spectrometry
GHG	Greenhouse gases
H-bond	Hydrogen bond
HCOOH	Formic acid
HPLC	High-performance liquid chromatography
HOMO	Highest occupied molecular orbital
HRMS	High-resolution mass spectrometry
H_2O	Water
IM-MS	Ion mobility coupled to mass spectrometry
IMS	ion mobility spectrometry
INC	Ion neutral complex
LC-MS	Liquid chromatography coupled to mass spectrometry
LUMO	Lowest unoccupied molecular orbital
m/z	Mass-to-charge ratio
m.p	Melting point
MCNT(s)	Multi-walled carbon nanotube(s)
MeOH	Methanol
MOST	MOlecular Solar Thermal system
MPM	Mobile proton model
MS	Mass spectrometry
MS/MS	Tandem mass spectrometry
M.W	Molecular weight
NBD	Norbornadiene
NH_2-PAT	Amino-phenylazothiazoles
NMP	N-methyl-2-pyrrolidone
NMR	Nuclear Magnetic Resonance
Nter	N-terminus extremity of peptoid
Nter-AB	Pristine AB peptoid named N*azb*N*spe*N*spe*
Nter-PAT 1	Pristine AB peptoid named N*2tz*N*spe*N*spe*
PA	Proton affinity
PAT	Phenylazothiazole

PAT 1	(*E*)-4-(thiazol-2-yldiazenyl)aniline
PAT 2	(*E*)-4-((5-methylthiazol-2-yl)diazenyl)aniline
PAT 3	(*E*)-4-((4-methylthiazol-2-yl)diazenyl)aniline
PAT 4	(*E*)-3,5-difluoro-4-(thiazol-2-yldiazenyl)aniline
PAT 5	(*E*)-4-(benzothiazol-2-yldiazenyl)aniline
PBD	Proton Bond Dimer
PCLT	Photochemical Crystal to Liquid Transition
PCMs	Phase change materials
PFTBA	Perfluorotributylamine
ppm	Parts per million
PSD	Photostationary state distribution
PSS	Photostationary state
QC	Quadricyclane
RGO	Reduced graphene oxide
Sar	Sarcosine
SCL	Side-chain loss
SCNT(s)	Single-walled carbon nanotube(s)
S_0	Ground state
S_{exited}	Excited electronic state
Spe	(*S*)-1-phenylethyl
$t_{1/2}$	Half-life time
tbu	Tertiobutyle
TFA	Trifluoroacetic acid
THF	Tetrahydrofuran
TLC	Thin Layer Chromatography
TMS	Tetramethylsilane
ToF	Time of Flight
VDW	Van der waals
VHF	Vinylheptafulvene
Z-isomer	Zusammen, *cis*-isomer

Table of contents

Part 1 – Introduction 28

1. Solar horizon: Dawn of energy transition 30

1.1 Fossil fuel for old plan 30

1.2 Solar storage: a new hope 31

2. MOlecular Solar Thermal systems : storing sunshine in bonds 33

2.1 Light to heat, heat to power 33

2.2 Back to the future of solar storage 38

2.3 Highway to MOST systems 39

2.3.1 Requiem for anthracene 41

2.3.2 Fifty shades of stilbene 41

2.3.3 The Fulvalene-tetracarbonyl-diruthenium team 42

2.3.4 When dihydroazulene met vinylheptafulvene 43

2.3.5 From norbornadiene to quadricyclane 44

3. Azobenzene: from coloring the past to powering the future 45

3.1 Azobenzene genesis 45

3.2 The chronicles of azobenzene substitution 51

3.2.1 Better call para substitution 53

3.2.2 Better call ortho substitution 59

3.3 Once upon a time… in heteroaryl azobenzene 68

3.3.1 The one with pyrrole 69

3.3.2 The one with pyrazole 71

3.3.3 The one with imidazole....74

3.3.4 The one with isoxazole....75

3.3.5 The one with thiophene....77

3.3.6 The one with thiazole....80

3.4 Templates: in the multiverse of grafting....84

3.4.1 The carbon nanotube rise....85

3.4.2 The lord of the templates: reduced graphene oxide....87

3.4.3 The polymer project....90

4. Who you gonna call? Peptoids!....94

5. A game of structure....95

5.1.1 Chain spotting....95

5.1.2 A fold odyssey....96

5.2 Legend of peptoid: a link to azobenzene....99

Part 2 - Objectives of the thesis....102

Part 3 – Experimental section....108

1. How I synthesized your phenylazothiazoles....111

1.1 Synthesis of sodium (phenylamino)methanesulfonate derivatives....111

1.1.1 Synthesis of sodium (phenylamino)methanesulfonate (An-prot)....111

1.1.2 Synthesis of sodium ((3,5-difluorophenyl)amino)methanesulfonate (F-prot) 112

1.2 Synthesis of amino-phenylazothiazole derivatives....112

1.2.1 Synthesis of (*E*)-4-(thiazol-2-yldiazenyl)aniline (PAT 1)....112

1.2.2 (*E*)-4-((5-methylthiazol-2-yl)diazenyl)aniline (PAT 2)....113

1.2.3 (*E*)-4-((4-methylthiazol-2-yl)diazenyl)aniline (PAT 3)....113

1.2.4 Synthesis of (*E*)-3,5-difluoro-4-(thiazol-2-yldiazenyl)aniline (PAT 4) 114

1.2.5 Synthesis of (*E*)-4-(benzothiazol-2-yldiazenyl)aniline (PAT 5) 115

1.3 Synthesis of acetamido-phenylazothiazole derivatives 115

1.3.1 Synthesis of (*E*)-N-(4-(thiazol-2-yldiazenyl)phenyl)acetamide (Ac-PAT 1) ...116

1.3.2 (*E*)-N-(4-((5-methylthiazol-2-yl)diazenyl)phenyl)acetamide (Ac-PAT 2) 116

1.3.3 (*E*)-N-(4-((4-methylthiazol-2-yl)diazenyl)phenyl)acetamide (Ac-PAT 3) 117

1.3.4 (*E*)-N-(3,5-difluoro-4-(thiazol-2-yldiazenyl)phenyl)acetamide (Ac-PAT 4) 117

1.3.5 (*E*)-N-(4-(benzothiazol-2-yldiazenyl)phenyl)acetamide (Ac-PAT 5).....117

2. the big synthesis theory of peptoids 117

2.1 General procedure for the solid-phase synthesis 119

2.1.1 Using DIC and bromoacetic acid 120

2.1.2 Using bromoacetyl bromide 120

2.2 Acetylation of the N-terminus amine 121

2.3 Resin cleavage 121

2.3.1 Test cleavage 121

2.3.2 Full cleavage 121

2.4 Peptoid purification 122

3. The fellowship of the structural characterization 122

3.1 Nuclear Magnetic Resonance spectroscopy 122

3.2 Mass spectrometry 122

3.3 Infrared spectroscopy 124

3.4 Melting point 124

4. MOST properties hunters 124

4.1 UV-vis spectroscopy 124

4.2 Irradiation sources 125

4.3 Photoisomerization experiments 126

4.4 Thermal back-isomerization 127

4.4.1 LC-MS analyses 127

4.4.2 UV-vis spectroscopy 129

4.4.3 Solvent effects 130

4.4.4 Catalytic activation 133

Part 4 – Results and discussion 134

1. The fifth phenylazothiazoles 136

1.1 Synthesis and structural characterization 136

1.2 Determination of MOST properties 138

1.2.1 NH_2-PAT derivatives 138

1.2.1.1 E-isomer spectroscopic properties 138

1.2.1.2 Photo- and back-isomerization processes 139

1.2.2 Ac-PAT derivatives 143

1.2.2.1 E-isomer spectroscopic properties 143

1.2.2.2 Photo- and back-isomerization processes 144

1.3 Intermediate conclusion 148

1.4 Appendices 150

2. The curious case of peptoids 165

2.1 Synthesis and structural characterization 165

2.2 Determination of MOST properties 174

2.2.1 E-isomer spectroscopic properties 175

2.2.2 Photoisomerization process 178

2.2.3 Thermal back-isomerization process 183

2.2.4 Acetylation of Nter-PAT 1 187

2.2.5 NspeN2tzNspeNspe derivative 190

2.2.6 N*spe*/N*sar* hybrid peptoids 192

2.3 Intermediate conclusion 195

2.4 Appendices 198

3. The silence of the solvents 204

3.1 Solvent polarity calibration 204

3.2 Thermal back-isomerization in different solvents 206

3.2.1 Ac-PAT derivatives 207

3.2.2 PAT 1 peptoids 209

3.3 Determination of kinetic parameters 211

3.4 Concordance between gas and liquid phases 214

3.5 Intermediate conclusion 215

3.6 Appendices 216

4. Too fast to relax, too furious to stay: catalytic activation 223

Part 5 – Conclusions and perspectives 230

1. A brief history of MOST 232

2. MOST reloaded 235

2.1 AB/PAT hybrids peptoids 236

2.2 Gas/liquid phase concordance 239

2.3 Catalytic investigation through triplet state 240

Part 6 – References....242

Part 7 - Accomplishments....262

1. Publications....264

2. Oral communications....264

3. Awards and grants....266

PART 1 – INTRODUCTION

Introduction

1. Solar horizon: Dawn of energy transition

1.1 Fossil fuel for old plan

Since the dawn of the Industrial Revolution, population never stops growing (**Figure 1a**) reaching 8.2 billion people on earth in 2024 and United Nations reported this year a projection toward 10.4 billion people in 2084.[1–3] This exponential population growth directly drives an increase in global energy consumption. In 2023, worldwide energy use reached 620 exajoules (EJ), representing a 3.3 % rise compared to 2022 and a 55 % increase since 2000.[4]

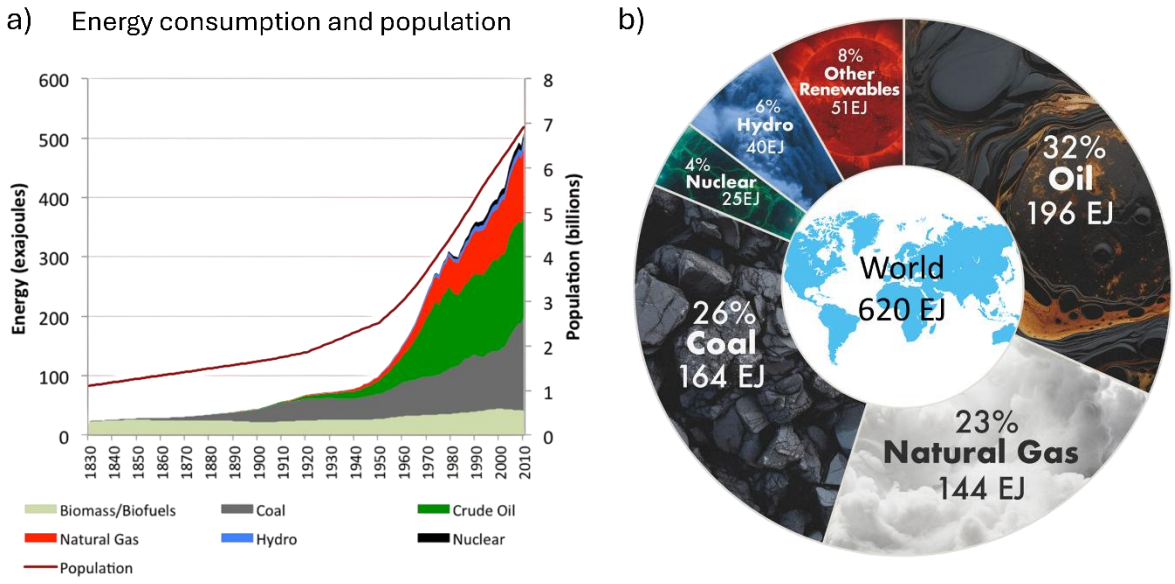

Figure 1. *a) Graphical representation of global population growth and energy consumption by different sources from 1830 to 2010. The left y-axis indicates energy consumption in exajoules (EJ), while the right y-axis shows population in billions.[2] b) Breakdown of the various energy sources powering the world in 2023 (percentages may not sum to exactly 100 due to rounding), reproduced from[4,5].*

To meet this energy demand, 81 % of the global energy supply in 2023 came from fossil fuels (oil (32 %), natural gas (23 %), and coal (26 %)), representing a marginal 1 % decrease compared to 2022 (**Figure 1b**).[4–7] Fossil fuels offer several advantages, most notably their high energy density. For example, gasoline has an energy density of approximately 44 to

46 $MJ \cdot kg^{-1}$, making it a highly efficient fuel for energy production and transportation[8]. However, this also comes with major drawbacks; typically they are non-renewable resources[9], their prices are heavily influenced by geopolitical factors as recently seen with the Russia-Ukraine conflict[10] and they have a significant environmental impact, contributing to issues such as ocean acidification[11], smog formation[12] and air pollution[13]. Indeed, the fossil fuel combustion releases various greenhouse gases (GHG) and pollutants, including CO_2, NO_x, CO and particulate matter, to name just a few.[14] Gasoline releases approximately 70 g of CO_2 per MJ of energy produced[8], contributing to the augmentation of anthropogenic CO_2 emission which increases each year, typically up to 0.8 % between 2023 and 2024.[15] This remains one of the most alarming issues contributing to global warming, with projections indicating a temperature increase of 1.5 to 2.5 °C by 2050.[16,17]

1.2 SOLAR STORAGE: A NEW HOPE

The United Nations has set the objective of reducing global GHG emission up to 45 % by 2030 in order to limit the rise in global temperatures to 1.5 °C. To achieve this, a major focus has been placed on increasing by up to 80 % the proportion of renewable energy in the global energy mix by 2030.[18] As a result, the growing demand for alternative energy solutions has shifted the global focus toward renewable sources such as solar, wind, geothermal, and hydro power. Among these, solar energy stands out as the most abundant energy source on Earth, as illustrated in **Figure 2a**. The annual solar energy reaching Earth amounts to a staggering 23,000 TW-years. In comparison, global world energy consumption is approximately 16 TW-years, and remaining reserves of fossil fuels are estimated around 1,655 TW-years. These figures highlight the immense potential of solar energy, since capturing just a small fraction of it could fully meet the world energy demands. Remarkably, if we could capture 100 % of the solar energy reaching Earth, just six hours of solar irradiation would provide enough energy to power the planet for an entire year.[9,19] In this context, the development of solar technologies is crucial.

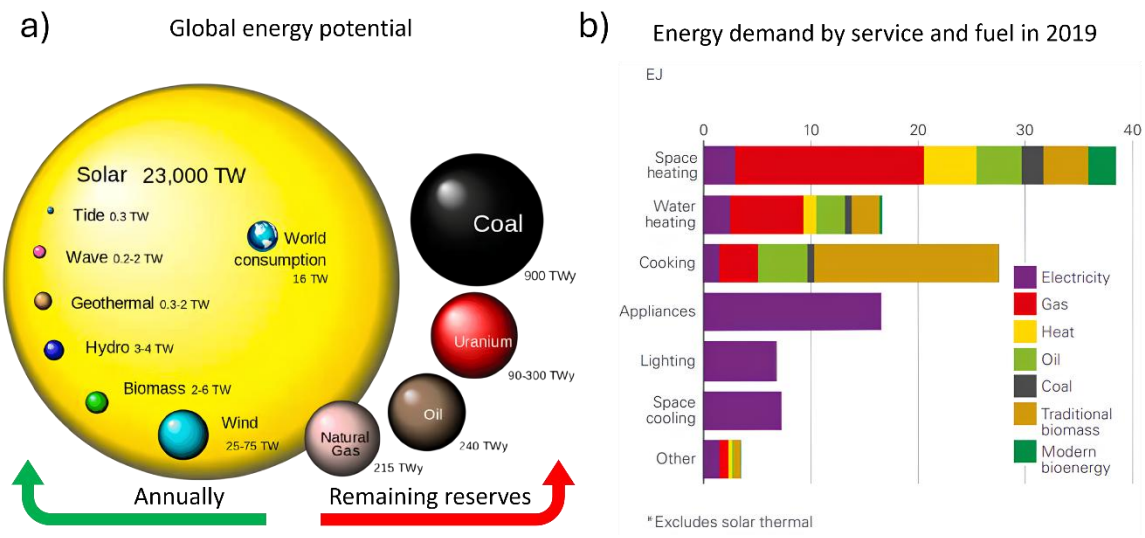

Figure 2. *Comparing finite and renewable planetary energy reserves (TW-years). Total recoverable reserves are shown for fossil fuels and yearly potential is shown for the renewable energy sources. adapted from[9]. b) Energy demand in building by service and fuel in 2019 (EJ).[20]*

In fact, solar power accounted for 42 % of renewable energy capacity in 2025[21]. Given its abundance, this share could be expected to be even higher. However, its intermittent nature and the challenge of converting it into usable energy remain major obstacles to wider deployment and prevents it to match supply with demand. For this reason, storing solar energy is essential to achieve the above mentioned environmental objectives.[22]

Collecting and converting solar energy into usable forms, such as electricity, chemical fuels, or heat, has been a major area of research for the last 20 years aiming at promoting efficient and sustainable energy production. Currently, three main approaches are employed; (i) photovoltaics, which converts solar energy into electricity; (ii) artificial photosynthesis, which transforms solar energy into chemical fuels; and (iii) solar thermal, which converts solar energy into heat.[23] Among these, photovoltaics and artificial photosynthesis have received significant research attention, particularly in the development of novel materials toward enhanced efficiency. Photovoltaic research explored a variety of materials, including inorganic, organic, and hybrid structures[24–26], while artificial photosynthesis has focused on wide-band metal oxides.[27] In contrast, solar thermal collection and storage has largely relied on traditional materials with high thermal capacity such as water, molten salts[28], and phase-change

materials[29] (PCMs) with limited innovation or material development in recent research. The use of these systems requires optimal thermal insulation, which can be challenging toward an effective implementation[30]. Given that heating represents approximately 50 % of the energy consumption in buildings today (**Figure 2b**) and that natural gas remains the primary fuel source, the development of new technologies on solar thermal materials is more critical than ever to reduce GHG emissions.[20,31]

A new class of closed-system solar fuels has emerged, offering the advantage of exchanging only energy with the environment, without generating any unwanted by-products. These systems store solar energy within chemical bonds and release it as heat, making them particularly attractive since they do not require special thermal insulation. Known as **Molecular Solar Thermal** (**MOST**) systems, they remain relatively underexplored compared to other energy storage materials, while representing a promising and complementary solution for solar energy storage.[30,32]

2. MOLECULAR SOLAR THERMAL SYSTEMS : STORING SUNSHINE IN BONDS

2.1 LIGHT TO HEAT, HEAT TO POWER

MOST are systems designed to store solar energy into chemical bonds through photochemical conversion process known as photochromism.[33] The working principle of these organic photochromic systems is illustrated in **Figure 3**.[32] Upon absorption of sunlight photons, the stable parent molecule in its ground state (S_0) is excited to a higher electronic state ($S_{excited}$). Upon relaxation, the molecule returns to the ground state via two possible pathways: either by reverting to the stable isomer or by undergoing photoisomerization into a high-energy (stereo)isomer known as the metastable isomer. The efficiency of this transformation is described by the photoisomerization quantum yield (Φ), which represents the probability of isomerization per absorbed photon. The energy stored (ΔH) within the systems corresponds to the difference of enthalpy between the metastable and stable isomers. The storage time is characterized by the half-life time ($t_{1/2}$) of the metastable isomer in given conditions, which

represents the time requires for 50 % of the metastable species to thermally revert to the stable form through back-isomerization. The half-life time of the metastable isomer is related to the height of the thermal back-isomerization energy barrier ($\Delta G^{\ddagger}$). When energy is needed, back-isomerization can be triggered by various methods, *i.e.* thermally, catalytically, photochemically and even electrochemically processes. The stable parent isomer is thus regenerated, and the stored energy is released as heat. This cycle can, in principle, be repeated indefinitely, enabling the continuous capture, storage, and release of energy from solar irradiation.[34–36]

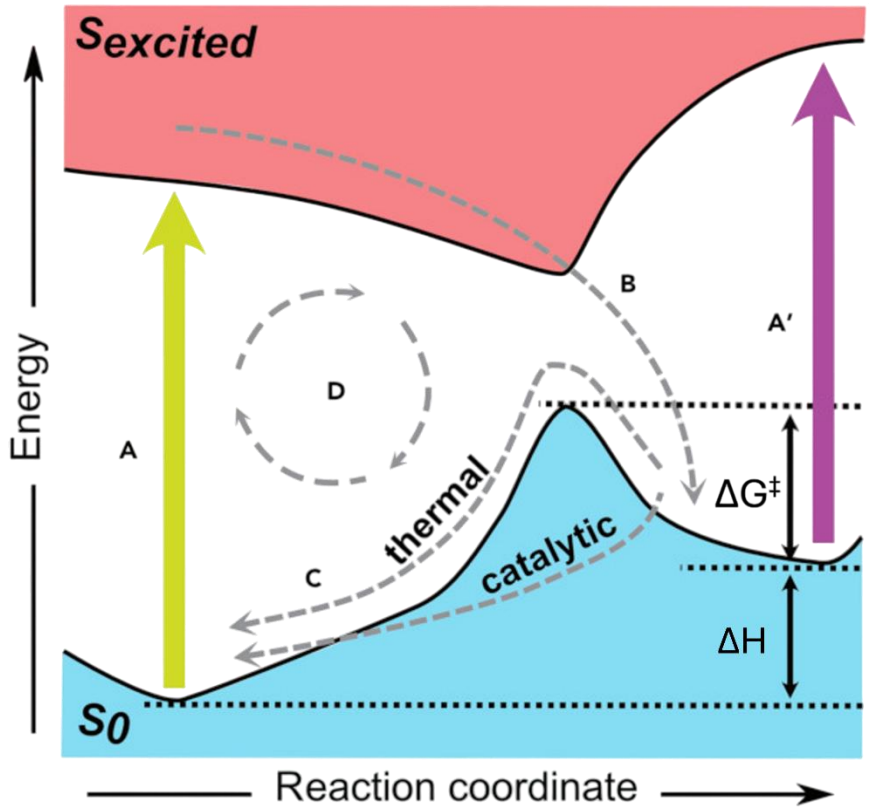

Figure 3. *Working principle of MOST system: (A) stable isomer absorbs sunlight and goes from ground state to excited state, (A') metastable isomer absorbs sunlight and goes from ground state to excited state, (B) deexcitation from the excited state to the metastable isomer ground state, (C) thermal or catalytic back-isomerization, (D) repeated cycle.*[32]

It is important to note that, amongst the MOST community, the stored energy is typically expressed as the isomerization enthalpy (ΔH) instead of free Gibbs energy (ΔG), since the parent compound and its metastable isomer generally have very similar molecular structures, making the entropic contribution minimal and often considered negligible[35] In contrast, the

entropic contribution to the thermal back-isomerization barrier ($\Delta G^{\ddagger}$) is no longer negligible, as notable entropy changes occur during the transition. This will be further addressed in the discussion of azobenzene (AB) back-isomerization.[37–39]

Based on **Figure 3** and various studies, the most important criteria to be fulfilled for an ideal MOST system are:

i. since the primary goal of MOST systems is to store solar energy, the amount of energy stored must be as high as possible, that is to say close to the energy of the absorbed/incident photons. In addition, the molecular weight (M.W.) of the compound should be minimized to maximize the gravimetric energy density (ED). In specific conditions, ED of 0.25 $MJ.kg^{-1}$ was achieved for AB placing it in a competitive range with other solar thermal storage systems such as salt hydrates.[35,40]

ii. the absorption spectrum of the stable parent compound should ideally be optimal within the visible wavelength range, since the solar emission spectrum has more than 50 % of energy reaching Earth between 400 to 800 nm. Matching the absorption profile of the parent compound with the solar emission will increase the probability of capturing solar photons effectively.[41] In contrast, the metastable isomer should not absorb in the same spectral region as the parent isomer and ideally outside visible region to prevent undesired back-isomerization triggered by photon absorption. When both isomers absorb in the same region, a competition of photons absorption occurs between the two isomers leading to a dynamic equilibrium, known as the photostationary state (PSS).[42]

iii. the quantum yield of photoisomerization ranges from 0 to 1, with 0 signifying that no isomerization occurs upon photon absorption, and 1 indicating that each absorbed photon results in isomerization. For MOST applications, the quantum yield should be close to 1 to ascertain that almost every absorbed photon effectively triggers photoisomerization.[43]

iv. the activation barrier associated to the back-isomerization process is a key factor in the design of MOST system. This barrier determines the thermal stability of the metastable isomer and is typically reflected in its half-life. To achieve efficient energy storage, the metastable isomer must be sufficiently thermally stable under ambient/storing conditions. The required storage time varies depending on the targeted applications. For example, a minimum half-life of 6 to 10 hours is often cited to align with the circadian cycle ($90\ kJ.mol^{-1} < \Delta G^{‡} < 100\ kJ.mol^{-1}$). Long-term applications such as seasonal energy storage require durations ranging from several months ($110\ kJ.mol^{-1} < \Delta G^{‡} < 120\ kJ.mol^{-1}$) to years ($\Delta G^{‡} > 130\ kJ.mol^{-1}$).[32,44,45]

v. for a MOST energy storage system to be practical, it is crucial to control when and how the energy stored is released, and the process must be quantitatively reliable to ensure consistent and efficient energy delivery. Several activation pathways have been explored, including thermal activation[45], optical activation[46], electrocatalytic[47], and catalytic triggers.[48]

vi. high cyclability is essential for an efficient MOST system. Both the parent and metastable isomers must exhibit excellent stability, allowing the system to undergo an “infinite” number of charge–discharge cycles without significant degradation.[49,50]

vii. for economic and sustainability considerations, MOST compounds should be synthetically accessible and cost-effective for large-scale industrial production. Additionally, the materials should be environmentally benign and non-toxic.[51]

MOST technology presents a promising strategy for solar energy storage, efficiently capturing and storing energy at the molecular level while remaining environmentally friendly. Their ability to store and release solar energy without thermal loss, using abundant materials and closed emission-free cycles, highlights their potential for future integration into clean energy technologies. In 2020, the European Union invested 4.3 million euros in a collaborative project involving research group from 6 different organizations in 5 different countries to investigate the creation of MOST prototypes.[52,53] This funding led in January 2024 to the development of

a special hybrid solar collector illustrated in **Figure 4**, this prototype was developed by the center for applied energy research (CAE) in collaboration with GREENNoneTec solarindustrie GmbH. The hybrid collector works with a fluid incorporating the MOST system that circulates through a closed-loop setup. A solar collector, positioned on the roof of a building, enables the generation of the metastable isomers via solar photon absorption. Following irradiation, the MOST-functionalized fluid can either be stored at ambient temperature in a dedicated tank or routed directly to a heat exchanger, where the stored chemical energy is released as heat to a secondary circuit for domestic heating purposes. The release of thermal energy is initiated through thermal or catalytic activation.[54]

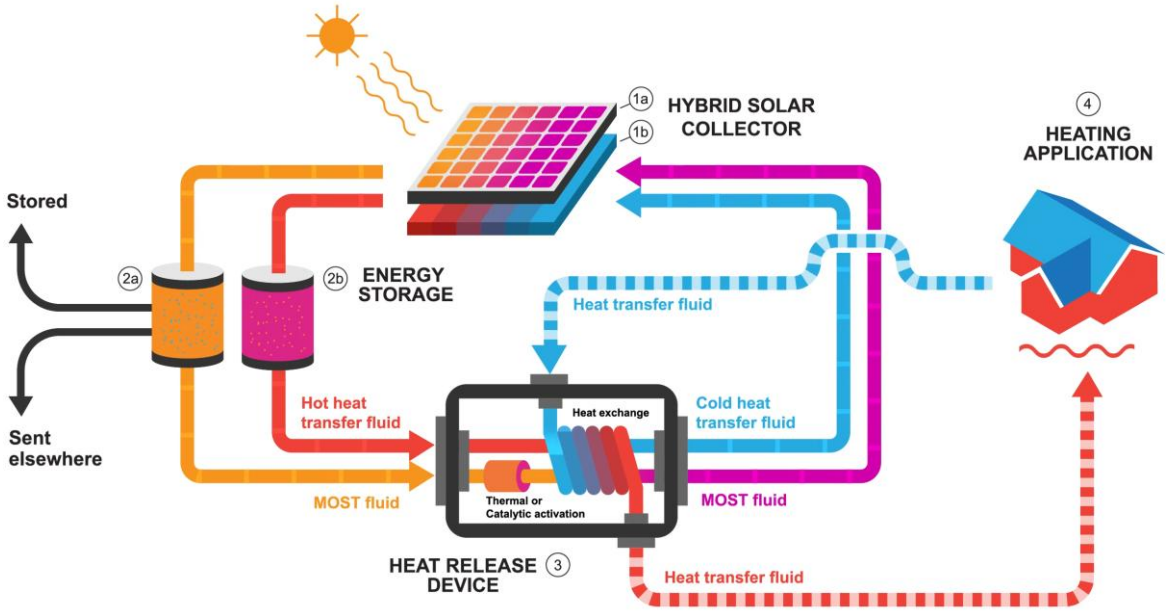

Figure 4. *Scheme of MOST prototype for household heating applications. The energy system works in a circular manner. First, the MOST fluid absorbs solar energy, in a solar thermal collector on the roof of a building. Then the fluid is either stored or sent to a heat exchanger where it transfers its chemical energy as heat to a secondary circuit. Illustration by Daniel Spacek/Neuron Collection.*[53,55]

However, despite technological advances and the prototypes currently under development, it remains difficult to produce a MOST system that has all the properties optimized to store efficiently solar energy which limits their large scale utilization. Thus, the MOST field represents a significant challenge in molecular design, aiming to create systems that meet as many of the

ideal criteria as possible. Some molecular candidates which will be discussed in the following section have demonstrated particularly promising properties and are currently the focus of intensive research efforts.

2.2 BACK TO THE FUTURE OF SOLAR STORAGE

It has been known since ancient times that sunlight is fundamental to life on Earth. As the planet most abundant energy source, Sun drives countless natural processes, with photosynthesis standing as one of the most efficient systems for converting solar energy into usable chemical energy.[36] The first study on the influence of light on chemical reaction was published by Scheele in 1770, when he discovered that light could reduce silver chloride into silver. He also demonstrated that UV light is more efficient than IR light to trigger such a reduction.[56] In 1819, Grotthuss observed that only the light of a certain color led to photochemical reaction and therefore established what is known now as the Grotthuss law of photochemical absorption; "*that only the absorbed light rays are active in the production of chemical changes".*[57]

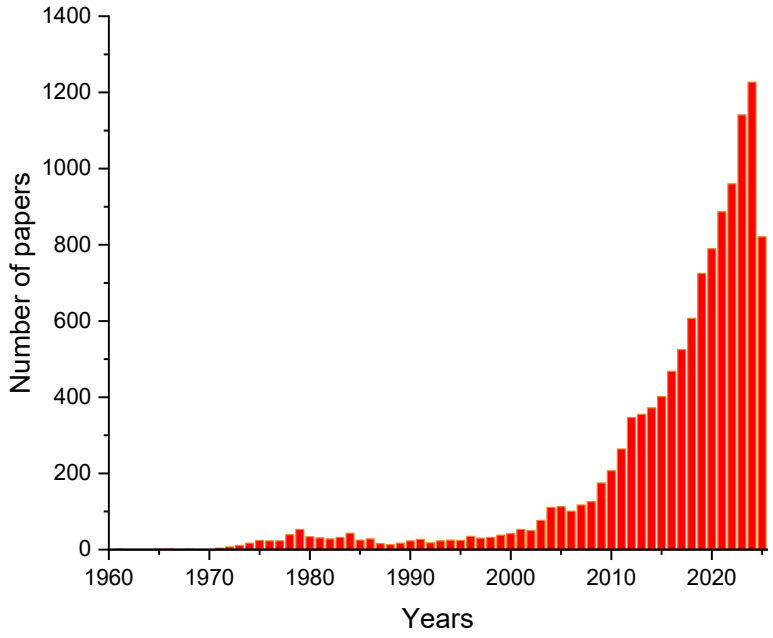

Figure 5. *Scientific Publications on Molecular Solar Thermal Systems by year.*[58]

In 1867, Fritzsche reported that irradiating a solution of anthracene led to the formation of crystals.[59] These crystals exhibited a higher melting point than anthracene itself and, upon melting, reverted back to anthracene. This process was further known as the reversible photodimerization of anthracene resulting in the formation of dianthracene (**Figure 6a**). This reaction was further explored by Luther and Weigert in the early 1900's.[60,61] They were the first to propose anthracene as a potential compound for solar energy storage. Weigert was the first to quantify the fraction of solar energy that could be stored chemically through anthracene photodimerization. He induced the formation of dianthracene from anthracene using sunlight and measured the heat release using calorimetry. His results led to the conclusion that about 5 % of the incident solar energy could be recovered as heat.[62,63] Since this pioneering work, interest in MOST systems has continued to grow steadily, with a rising number of publications exploring new molecules and storage strategies, as illustrated in **Figure 5**.[58]

The growing research activity in the MOST field has led to the development of various reversible photoswitches for solar energy storage. Among the most notable illustrated in **Figure 6**, we can mention stilbene and AB derivatives with C=C and N=N double bond *E*/*Z* isomerization, the dihydroazulene/vinylheptafulvene couple with its ring opening / closing isomerization, the norbornadiene/quadricyclane systems with its concerted transformation between C=C and C–C and the fulvalene-tetracarbonyl-diruthenium system with its organometallic photochromic complex. The following section will explore briefly each system with their advantages, limitations and advancements.[64,65]

2.3 HIGHWAY TO MOST SYSTEMS

The following section will provide a brief description of the principal MOST systems explored in the literature including anthracene, stilbene, the fulvalene-tetracarbonyl-diruthenium, the dihydroazulene/vinylheptafulvene couple and the norbornadiene/quadricyclane couple. The AB system, which constitutes the core subject of this PhD research, will be discussed in more details in a dedicated chapter.

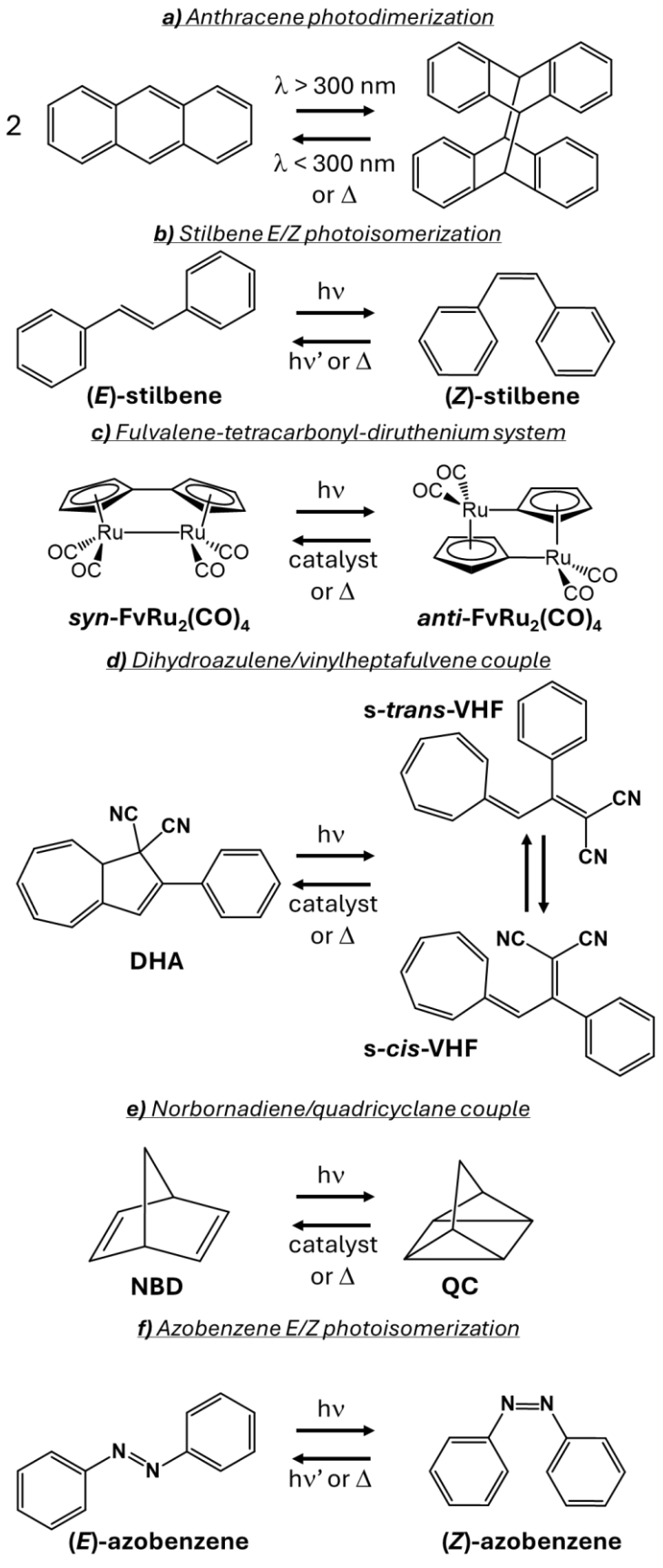

Figure 6. *Principal MOST systems explored in this research and described in the literature.*

2.3.1 Requiem for anthracene

Anthracene undergoes a [4+4] photochemical cycloaddition toward dimerization into dianthracene upon irradiation above 350 nm (**Figure 6a**). The stored energy can be released, during the retro-cycloaddition reaction, upon thermal activation or with deep UV wavelength under 300 nm. The storage energy that corresponds to the reaction enthalpy is about 65.2 $kJ.mol^{-1}$ and the half-life time of dianthracene ranges from several days to months depending on the solvent, temperature and substitution patterns.[66,67] The main limitations of these systems are the degradation of the anthracene monomer due to photooxidation and the concentration-dependent quantum yield of photodimerization, which reaches maximal value around 0.3 at high anthracene concentrations. One strategy to improve the systems involves solid-state cycloaddition using 9-cyanoanthracene with storing enthalpy up to 84 $kJ.mol^{-1}$. However, solid-state approach presents significant challenges for practical implantation as household applications.[67] Another interesting approach is the use of ortho-dianthrylbenzenes in which two anthracene units are bridged through an ortho-substituted aryl group. This kind of systems could lead to enormous half-life time depending on the substitution ranging from 9 to 37 years. However, these systems have poor cyclability with a decrease of 50 % of the absorbance after 8 cycles.[68] Despite its high energy storage density, anthracene has fallen out of the scope of MOST research. However, recent interest in crystal-to-crystal photoinduced phase transitions induces a revival attention toward this system.[67]

2.3.2 Fifty shades of stilbene

Stilbene derivatives constitute a class of organic molecules capable to undergo a trans to cis photoisomerization upon irradiation from 300 nm to 700 nm (**Figure 6b**). This range of photoactivity makes those molecules particularly suitable for solar energy storage since they efficiently absorb light within the visible region of the solar spectrum.[69–71] The major drawback of these systems is the low storage enthalpy that hardly reaches 5 $kJ.mol^{-1}$ for the unsubstituted stilbene. The storage enthalpy of stilbene derivatives can be maximize through molecular substitution.

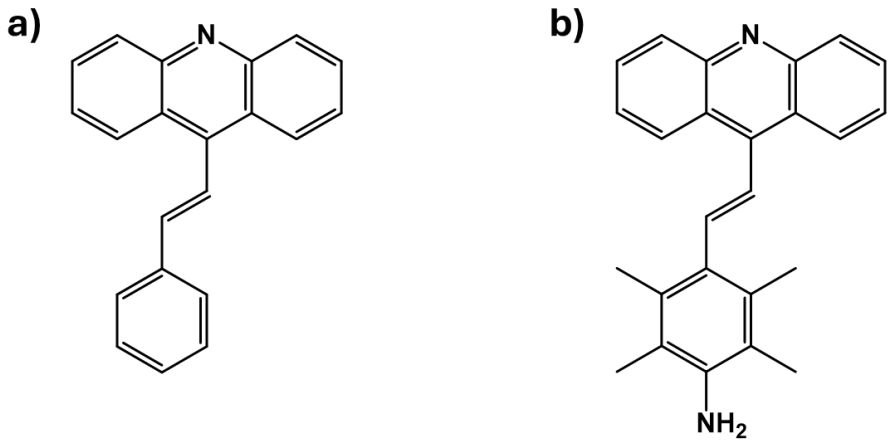

Figure 7. *representation of 9-styrylacridine derivatives synthesized by Bastianelli et al.* [69,72]*. A) unsubstituted 9-styrylacridine. B) 9-(4-amino-2,3,5,6-tetramethylstyryl)-acridine.*

For instance, Bastianelli *et al.* synthesized a series of substituted 9-styrylacridine (**Figure 7a**) and they achieved a storage enthalpy of 104 $kJ.mol^{-1}$. This was obtained by substituting the phenyl ring of 9-styrylacridine with 4 methyl groups at ortho and meta position and an amino group at para position, as illustrated in **Figure 7b**. This 20 fold increase can be attributed to the electronic delocalization that stabilizes the *E*-isomers combined with steric hindrance that destabilizes the *Z*-isomer.[44,69,72] However, the low quantum yield of photoisomerization ($\Phi \sim 0.03$) significantly limits the practical applicability of this system. A recent innovation within stilbene class is the development of stiff-stilbene, which incorporates a fused five-membered ring structure. These systems have demonstrated a greater stability compared to homologue stilbenes, with their application in solar anergy storage remaining in early stages and requiring further investigation.[73,74]

2.3.3 The Fulvalene-tetracarbonyl-diruthenium team

The Fulvalene-tetracarbonyl-diruthenium ($FvRu_2(CO)_4$) system represents a class of organometallic photochromic systems first reported by Vollhardt et al in 1983[75,76] (**Figure 6c**). The compound can be briefly handled in air, but prolonged exposure leads to gradual decomposition over time. Due to its poor solubility in usual polar organic solvents, the compound should be stored in non-polar solvents, such as THF or toluene.[75,77] In solution, $FvRu_2(CO)_4$ undergoes a reversible photoisomerization under visible irradiation ($\lambda \sim 470$ nm).

Interestingly, the metastable isomers do not absorb in the visible spectrum allowing almost quantitative photoisomerization.[36] The storage energy of the system is 83 $kJ.mol^{-1}$, corresponding to an energy density of approximately 0.2 $MJ.kg^{-1}$ limited by the high molecular weight of the complexes, which remains one of its main drawback.[78] The thermal back-isomerization barrier around 125 $kJ.mol^{-1}$ creates a good thermal stability for solar energy storage.[46,78] In order to reduce the synthetic cost of the complexes, it was proposed to replace the ruthenium by other transition metals, such as iron or osmium. Iron has been first explored as a low-cost and lightweight alternative. However no isolable photoisomer has been obtained since the intermediate singlet-syn-diradical relaxes too rapidly.[79] Osmium analogues were successfully synthesized, but the thermal back-isomerization of the photoisomer does not occur even at high temperatures, making these osmium complexes unsuitable for solar energy storage applications.[80]

2.3.4 When dihydroazulene met vinylheptafulvene

Vinylheptafulvene (VHF) was first discovered in the early 1960s[81], and the first evidence of ring closing thermal isomerization to dihydroazulene (DHA) was reported by Daub *et al.* in 1984.[82] Upon UV irradiation, DHA undergoes a ring opening reaction generating s-cis-VHF that further isomerizes into s-trans-VHF, the thermodynamically more stable isomer[83] (**Figure 6d**). The conversion from DHA to VHF is an example of one way photochromism where the forward reaction is photoinduced while the reverse reaction only occurs thermally leading to a complete photoisomerization of DHA into VHF.[84,85] The most significant advantage of this system is its relatively high quantum yield of isomerization compared to other MOST candidates. Note also that the yield is highly solvent depend, with nonpolar solvents more suitable due to a lower degradation rate.[86,87] Properties can also be optimized using substitution. For example, adding an electron-donor group (EDG) at C2 and an electron-withdrawing group (EWG) at C3 or C7 usually increases the half-life time.[88,89] One of the major drawbacks of these systems is the low energy storage density, typically around 0.11 $MJ.kg^{-1}$, even if certain specific derivatives exhibit storage density as high as 0.7 $MJ.kg^{-1}$, which is comparable to systems such NBD/QC

(see below).[42,83] Despite exhibiting some promising characteristics, DHA/VHF systems remain among the least studied MOST candidates in recent years, far behind systems such as NBD/QC or AB. Nevertheless, they found applications in other fields, such as photoelectrical switch[90] and photochromic materials.[91]

2.3.5 From norbornadiene to quadricyclane

Unsubstituted norbornadiene (NBD) was first synthesized in 1951[92] and its photoisomerization behavior was only observed in the early 1960's.[93] Upon irradiation below 250 nm, NBD undergoes an intramolecular [2+2] photocyclization, converting into quadricyclane (QC) as illustrated in **Figure 6e**.[94,95] One of the key advantages of this system is its high energy capacity. The conversion of NBD to QC stores approximately 87 $kJ.mol^{-1}$, that corresponds to an energy density of 0.97 $MJ.kg^{-1}$.[42,94,96] Such a high energy density is attributed to the high energy QC isomer induced by its strained structure. The thermal back-isomerization from QC to NBD goes through a high energy diradical-like transition state resulting in a large back-isomerization barrier of approximately 140 $kJ.mol^{-1}$, making the half-life time of the QC isomers really high.[97,98] The major limitation of this system is the poor spectral overlap between the absorbance spectrum of unsubstituted NBD and the solar spectrum, as well as its relatively low quantum yield of photoisomerization (Φ = 0.05).[99] These drawbacks could be balanced through substitution with EDG and EWG leading to efficient MOST systems.[100] However, this always comes with a decrease of the QC half-life time. To overcome this limitation, strategies based chemical sensitizers have been explored, notably using CuCl salt as sensitizer. In this approach, the Cu^{+} ions coordinate with the π-system of NBD, resulting in a redshift of the absorbance spectrum and a significant enhancement in the photoisomerization quantum yield.[101,102] Thanks to its advantageous properties, the NBD/QC couple has emerged as one the most studied and applied photoswitches for molecular solar thermal energy storage.

3. AZOBENZENE: FROM COLORING THE PAST TO POWERING THE FUTURE

3.1 AZOBENZENE GENESIS

The AB family of molecules is one of the most extensively studied systems in the field of solar energy storage. AB was first synthesized by Eihlard Mitscherkich in 1834.[103] Since their discovery, AB derivatives have been widely used as dyes and pH indicators.[104] It is estimated that approximately 70 % of commercial dyes contain AB-based structures.[105,106] In 1932, Prontosil (**Figure 8**) was synthesized by two Bayer chemists, namely Josel Klarer and Fritz Mietzsch, as a part of Gerhard Domagk's research program on antibacterial drugs. Prontosil was the first AB-based compound to be used as an effective drug against streptococcal infections. Nowadays, its use has significantly declined due to development of more effective medications.[107,108] Gerhard Domagk was awarded the Nobel Prize in medicine in 1939 for the development of Prontosil.[109]

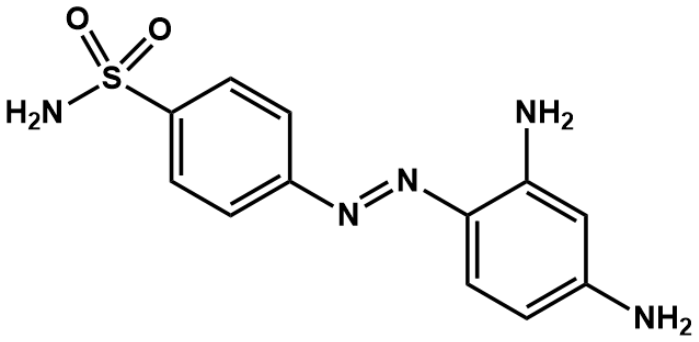

Figure 8. *Chemical structure of the sulfamidochrysoïdine, commonly known as Prontosil.*

It was only in 1937 that Hartley discovered the *E* to *Z* photoisomerization of AB through UV-vis spectroscopy (**Figure 6f**). He observed a significant difference in the AB absorption spectra before and after exposure to sunlight.[110] The second form was identified as the AB *Z*-isomer due to its larger polarity, resulting in a higher solubility in polar solvents and lower solubility in non-polar solvent.[111] The first trial to use AB to chemically store solar energy was attempted by Olmsted *et al.* in 1983. He concluded that, despite its spectroscopic properties and solubility in polar solvents, which could be improved, the AB system was not suitable for solar energy storage[112] However, in 1987, Toada *et al.* demonstrated that solar energy storage through AB

was indeed feasible under specific conditions, such as using a refrigerated tank to minimize thermal back-isomerization and employed a catalytic system to release the stored energy when needed.[113] Thanks to recent advances in organic chemistry, materials science, polymer chemistry, photochemistry, and computational modeling, several drawbacks can now be challenged. A few research groups, including ours, have resumed development of solar thermal fuels based on AB-containing materials. Newly synthesized AB derivatives show promise in overcoming the limitations of the AB compounds used in the 1980s.[114–117]

AB photoisomerization occurs under UV-visible light irradiation which photoconverts the stable planar *E*-isomer into the metastable non-planar *Z*-isomer. This results in the transformation of a planar E-AB with C_{2h} symmetry and low dipole moment (0.5 D) into a bent *Z*-AB configuration with C_2 symmetry and a significantly higher dipole moment (3.1 D).[118,119] The reverse back-isomerization can be triggered thermally[120], catalytically[121], photochemically[122] or even electrochemically.[123] The energy stored through this photoisomerization is approximately 49 $kJ.mol^{-1}$ and was measured for the first time by Adamson *et al.* in 1978 by photocalorimetry.[124] This value is, however, relatively weak compared to other systems such as NBD/QC or $FvRu_2(CO)_4$. The back-isomerization kinetics of the metastable isomer is highly solvent-dependent, with values that can double or triple when switching from non-polar to polar solvents. For instance, the measured $t_{1/2}$ at 20 °C are 4.2, 9.5 and 11.5 days in, respectively, heptane, toluene and MeOH.[37,111,112] Moreover, the AB systems have an excellent fatigue resistance, showing no degradation even after 10^6 cycles of photoisomerization and back-isomerization.[125] Finally, the photoisomerization quantum yield is relatively low in most common solvents, rarely exceeding 0.2 for the trans to cis photoconversion.[126,127] Furthermore, the quantum yield for the reverse cis to trans is always higher than the forward conversion with value from 0.4 to 0.5 depending on the solvent.[128,129] Another limitation is the relatively poor solubility of AB in polar solvents, due to the high nonpolar character of the *E*-isomer, restricting the range of solvents usable for practical applications.[130]

As part of the understanding and optimization of AB-based systems, it is essential to investigate the fundamental mechanism governing their photoisomerization behavior. The *E* → *Z* isomerization pathway of AB remains a subject of considerable scientific discussion, as several mechanisms can be involved depending on the nature of the AB substituents and the characteristics of the solvent employed. Currently, four main isomerization pathways have been proposed : (i) rotation, (ii) inversion, (iii) concerted inversion, and (iv) inversion assisted rotation. These mechanisms are represented on **Figure 9**.[70,128,131]

i) The rotation mechanism involves the cleavage of the N=N π-bond, allowing free rotation around the resulting N-N single bond. During this process, the N-N-C angle remains fixed at 120° while the C-N-N-C dihedral angle undergoes significant variations. This pathway can be facilitated by EDG or EWG, which modify the AB electronic structure and influence the relative energy states.[132,133]

ii) The inversion mechanism corresponds to an in-plane inversion of the N=N-C angle reaching 180° while maintaining a fixed C-N-N-C dihedral angle at 0°. This pathway processes through a dipolar transition state, in which one of the nitrogen atoms of the AB bond adopts an sp-hybridization. It is typically favored in sterically hindered AB derivatives, where rotation around the N=N bond is restricted or energetically inaccessible.[132,134]

iii) The concerted inversion mechanism involves the simultaneous linearization of both N=N-C angles to 180°, resulting in a fully linear transition state. This is the only pathway that does not involve a net dipole moment variation, thus producing a relatively non-polar transition state compared to the other isomerization mechanisms.[135]

iv) The inversion assisted rotation mechanism involves a substantial change in the C-N=N-C dihedral angle accompanied by a concomitant, though smaller, change in the N=N-C angle. These two structural changes occur simultaneously, resulting in a mixed pathway combining features of both rotation and inversion pathways.[136]

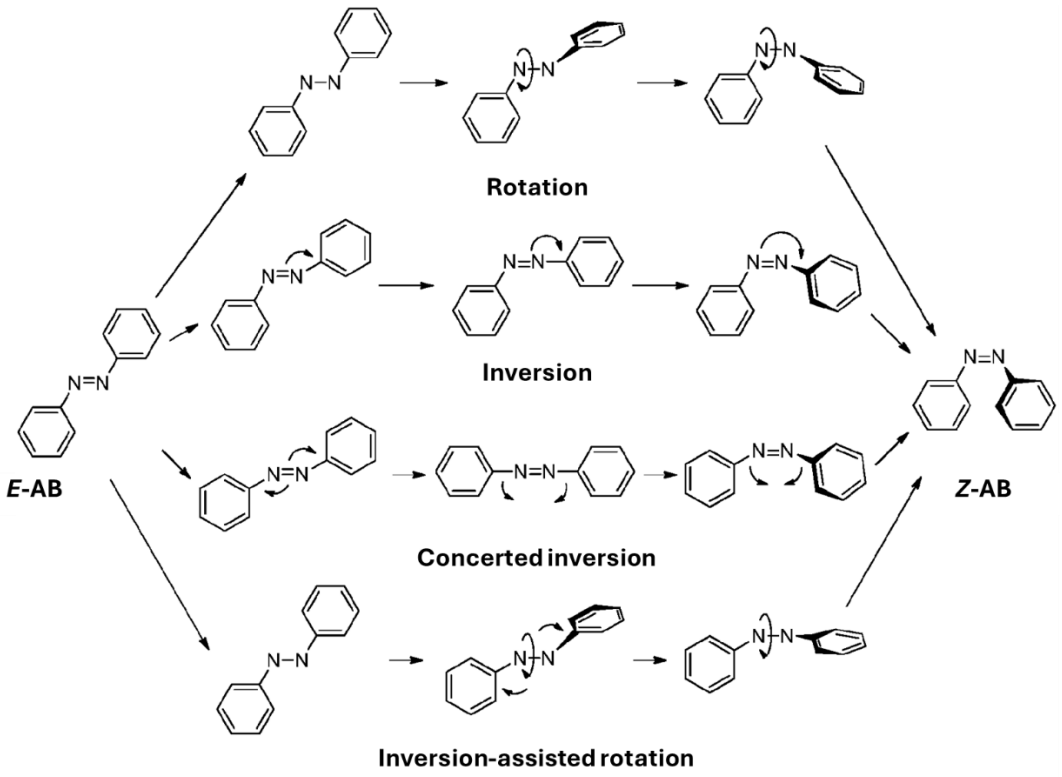

Figure 9. *Four known mechanisms for the azobenzene E → Z photoisomerization.*[128]

Relaxation from any of the four transition states can lead to the formation of either the cis or trans isomer. Consequently, whatever the mechanism, the formation of photostationary states resulting from a dynamic equilibrium between both isomers under irradiation seems inextricable.[70] The attribution to a given AB molecule of a unique photoisomerization mechanism is further complicated by the strong dependence on various parameters including temperature, pressure, substituents or excitation wavelength.[137,138]

The primary limitation in the use of pristine AB as an efficient MOST system remains its optical properties, as featured in the *E*/*Z* UV-vis absorption spectra**. Figures 10a, b** and **c** respectively represent the UV-vis spectra of both *E*- and *Z*-isomers, the corresponding energy levels of AB and a schematic representation of the photoisomerization process. The thermodynamically stable *E*-isomer (green curve in **Figure 10a**) exhibits two distinct absorption bands: an intense band in the UV region around 320 nm and a weak band in the visible region near 450 nm. The UV band is ascribed to the π-π* electronic transition corresponding to the $S_0 \rightarrow S_2$ excitation, this transition is symmetry-allowed and thus exhibits a high molar extinction coefficient

(~2.2 10^4 L.mol^{-1}.cm^{-1}). The weaker band in the visible range represents the n-π* electronic transition corresponding to the S_0 → S_1 excitation. This transition is symmetry-forbidden in the planar geometry, resulting in a low molar extinction coefficient (~400 L.mol^{-1}.cm^{-1}).[139–141] Since isomerization can occur from both S_1 or S_2 excited states (**Figure 10c**), each associated with a distinct quantum yield, the AB photoisomerization constitutes a violation of the Kasha's rule. This implies that the mechanism and efficiency of photoisomerization are strongly dependent on the excitation wavelength.[142–144]

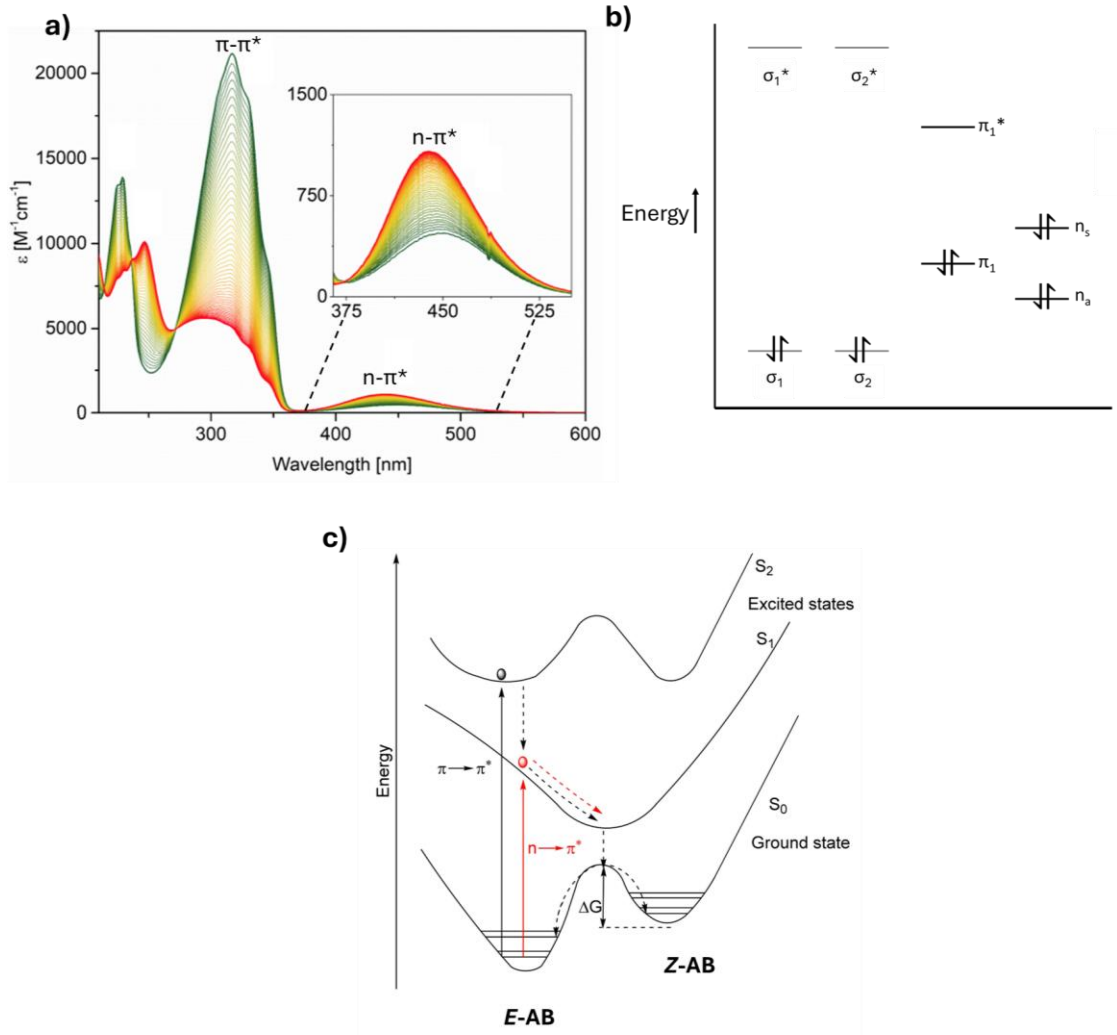

Figure 10. *a) UV-vis spectra of E (green line) and Z (red line) AB in cyclohexane. The intermediate lines from green to red correspond to the UV-vis spectra recording during the photoisomerization under a LED irradiation at 310 nm. Figure from reference*[142]*. b) Energy diagram representing the molecular orbitals of AB. Reproduced from reference*[145]*. c) Potential energy diagram of the trans-cis isomerization process after excitation of the π-π* and n-π* AB transitions in solution. Adapted from reference*[131,146]

.

As shown on **Figure 10a**, under irradiation the UV-vis spectrum undergoes major changes. The *Z*-isomer (red curve in **Figure 10a**) also exhibits both the π-π* and n-π* electronic transitions. Concerning the π-π* transition, the absorbance maximum undergoes an hypsochromic shift to 270 nm, accompanied by a significant decrease in intensity, resulting in a molar extinction coefficient of approximately 5000 $L.mol^{-1}.cm^{-1}$. On the other hand, even if the n-π* transition also undergoes a slight hypsochromic shift, unlike the π-π* transition, its intensity increases resulting in a higher molar extinction coefficient of about 1500 $L.mol^{-1}.cm^{-1}$. These significant changes can be attributed to the structural modifications upon photoisomerization, *i.e.* the loss of planarity in the molecule which leads to a reduction in electron delocalization, as well as changes in molecular size and polarity. For the sake of completion, the absorption bands observed below 250 nm are attributed to higher energy σ-σ* electronic transitions.[139,140,142,147]

From the absorption spectra of both *E*- and *Z*-isomers, it is apparent that they absorb within similar wavelength ranges, which constitutes a major limitation of the AB-based photoswitches. Indeed, if an *E*-isomer absorbs UV-vis light and undergoes photoisomerization into the *Z*-isomer, the reverse process is also possible, whereby the *Z*-isomer absorbs light and reverts back to the *E*-isomer. This leads to two major drawbacks. First, the photoconversion can never be quantitative (100%) and a PSS is inevitably established, resulting in a fixed distribution of both stereoisomers under a given irradiation wavelength. The second issue is that, once the PSS is reached under irradiation, the mixture of both isomers must be stored in the dark to prevent any unwanted photoconversion of the *Z*-isomer back to the E-isomer, thereby allowing only the thermal back-isomerization to occur.[51,128,131] Taoda et al. demonstrated that maximum E → Z conversion is achieved using irradiation at 340 nm, whereas visible-light irradiation results in PSS compositions with a lower proportion of the *Z*-isomer, due to its higher molar extinction coefficient at longer wavelengths (**Figure 10a**).[113] Consequently, this overlap leads to a relatively low solar conversion efficiency of approximately 25 %, which represents a

significant drawback for MOST applications. Nevertheless, the use of optical filters that selectively transmit UV light could improve isomerization efficiency for targeted applications. Notably, the existence of a PSS is consistent with all four proposed photoisomerization mechanisms discussed previously.[148]

Overall, AB exhibits several advantageous properties for the chemical storage of solar energy, including high photochemical cyclability, ease and low-cost synthesis and reasonable $t_{1/2}$. However, its practical application is limited by a relatively low storage enthalpy, poor solubility in polar solvent, predominant absorption in the UV region and formation of a PSS that reduces the conversion efficiency. Many of these limitations can be tuned through chromophore modifications. Two principal strategies have been reported in the literature, namely AB modification through substitution or the use of template-based method. These two approaches will be discussed in details in the following sections.[149,150]

3.2 THE CHRONICLES OF AZOBENZENE SUBSTITUTION

Substitutions on the AB benzene rings play a crucial role in tuning both thermodynamic stability and photochemical properties. Introducing substituents on benzene rings alters the AB electronic structure by modifying the energy gap between the HOMO and the LUMO, thereby influencing the positions and intensities of the π-π* and n-π* transitions. To enable AB absorption within the visible range, two main strategies have been employed. The first concerns the π-π* transition of the *E*-isomer by effectively redshifting its absorbance from the UV to visible range upon substitution, as shown on **Figure 11a**.[134,151,152] The second strategy rather focuses on the n-π* transition, which is already settled in the visible spectrum. Here, the objective is to minimize the spectral overlap between the n-π* of the *E*- and *Z*-isomers as shown on **Figure 11d**.[150,153,154] Achieving this spectral separation allows selective excitation of each isomer, enabling the control of the *E* → *Z* and the *Z* → *E* photoisomerization using monochromatic visible light.

Considering these two strategies, six major classes of substituted AB derivatives have been identified and their UV-vis spectra are shown on **Figure 11**. The first approach, aimed at redshifting the π-π* transition, includes AB type, amino-AB type and pseudo-stilbene type (push-pull AB), as shown on **Figure 11a**. The second approach, which intends to resolve the overlapping n-π* transitions of the *E*- and *Z*-isomers, includes bridge-AB, fluoro-AB and methoxy-AB, as shown on **Figure 11b**.

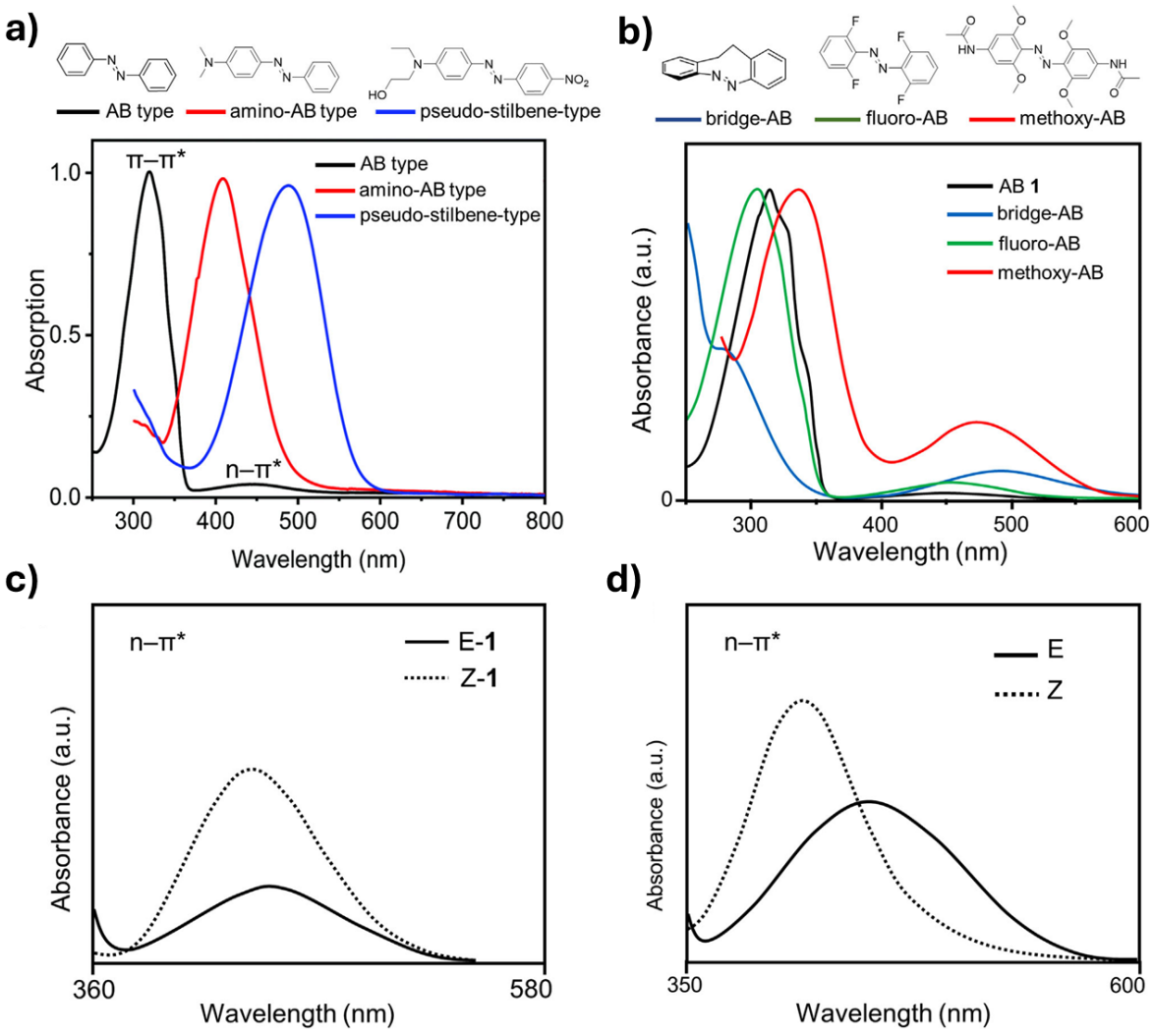

Figure 11. *a) Typical structures and UV-vis absorption spectra of different classes of AB with redshift of the π-π* transitions: AB type, amino-AB type and pseudo-stilbene type (push-pull AB). b) Typical structures and UV-vis absorption spectra of different classes of AB with separated n-π* transition between E- and Z-isomers: bridge-AB, fluoro-AB and methoxy-AB. c) Illustration of n-π* absorption band for pristine AB with both isomer spectra overlapping. d) Illustration of n-π* absorption band of ortho-substituted AB with separation of bands between E- and Z-isomers. Figure from*[115].

AB derivatives can be functionalized at three different positions (ortho, meta and para) of the benzene ring. It has been demonstrated that meta-substitution induces a significantly weaker resonance effect compared to substitution at the para or ortho positions. As a consequence, AB derivatives substituted at meta position with EDG or EWG exhibit photochemical and thermodynamic properties that remain largely similar to those of pristine AB.[138,155] Given the limited impact of meta-substitution, the following discussion will focus on the effect of para and ortho substitutions, which offer more substantial opportunities to tune AB behaviors.[128]

3.2.1 Better call para substitution

The para position is reflected as the terminal point of AB; thus, substitution at this position provides an effective means to modulate molecular length, dipole moment, and electronic distribution across the conjugated system, thereby modulating the conformational and spectroscopic properties of AB derivatives. Para substitution with EDG, EWG or π-conjugated group consistently results in a bathochromic shift of the absorbance as shown on **Figure 12**. The redshifting of the π–π* band reflects a reduction in the energy gap associated to the π–π* transition. However, these substitutions typically lead to a significant increase of the thermal back-isomerization kinetics of the metastable isomer.[156–158] Consequently, the para substitution strategy is generally unsuitable for solar energy storage applications due to the short half-life of the metastable isomer. However, it has found widespread application in fields that benefit from this rapid thermal relaxation, such as real-time information-transmitting systems[159], molecular transport process[160], and ion channel control[161].

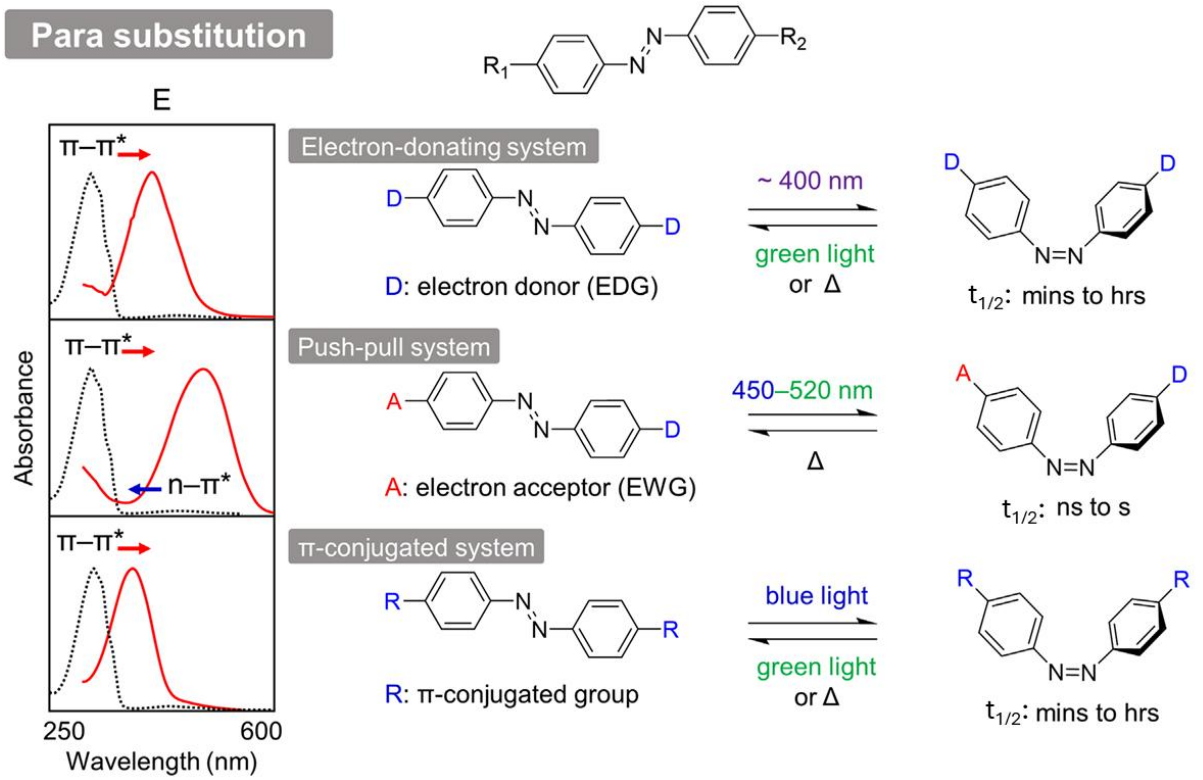

Figure 12. *Effect of para substitution with EDGs, push-pull system and extended π-conjugated group on the spectroscopic properties and thermal relaxation behavior of AB derivatives. The dotted black lines represent the UV-vis spectra of pristine AB while the solid red lines represent the substituted AB derivatives. Figure from*[115].

Substitution of AB with EDGs such as amino, alkoxy or hydroxy groups at the para position induces a redshift of the π-π* transition, while marginally affecting the n-π* transition. This results in a partial or even complete overlap of the π-π* and n-π* absorption bands, depending on the EDGs strength incorporated. In 1991, Mustroph synthesized a series of 4,4'-diamino-azobenzenes with various EDG groups as shown on **Figure 13**.[162] Their results demonstrated that increasing the donor strength lead to a larger redshift of the π-π* transition, accompanied by the emergence of a fine vibronic structure. Furthermore, such a substitution generally enhances the quantum yield of photoisomerization.[138] However, these modifications also significantly increase the rate of thermal back-isomerization. Whereas pristine AB exhibits $t_{1/2}$ of few days, EDGs para-substituted AB often show $t_{1/2}$ reduced to seconds or minutes.[163,164] The thermal stability of the *Z*-isomer is highly solvent-dependent. For instance, 4-amino-azobenzene exhibits $t_{1/2}$ of only 0.7 s at 17 °C in methanol, compared to 435 min in diethyl

ether, probably arising from differences in the dominant thermal back-isomerization mechanism depending on the solvent.[164]

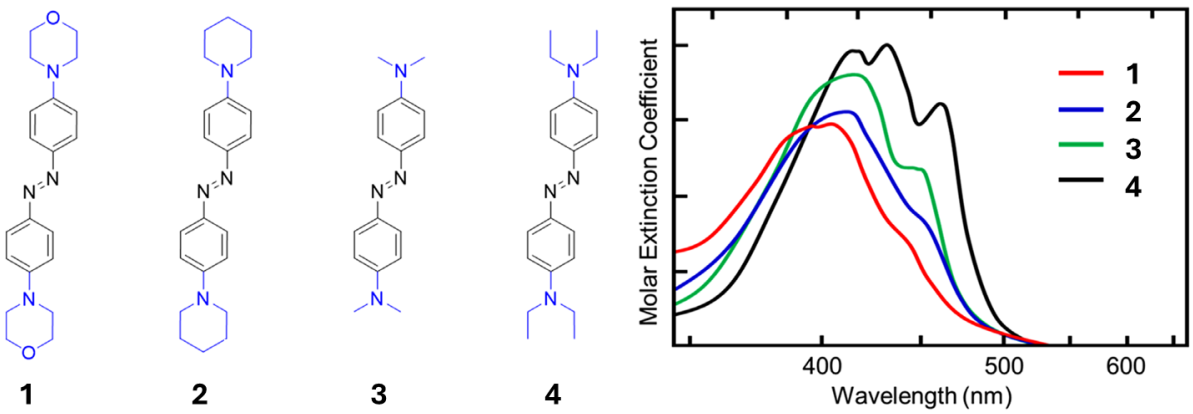

Figure 13. *Representation of the chemical structures of AB derivatives with EDGs (blue) substituted in para position and their corresponding UV-vis spectra in hexane. Spectral data adapted from*[162] *and figure adapted from*[115]*.*

Push-pull systems refer to AB derivatives bearing an EDG and an EWG in the para positions of both benzene rings, introducing a significant asymmetry into the electronic distribution of the π-conjugated system.[51] The absorption spectra of push–pull AB derivatives exhibit a more pronounced redshift of the π–π* band compared to systems containing only EDGs. This results in a larger overlap between the n-π*and π-π* bands of *E*-isomers. This shift is attributed to the simultaneous destabilization of the HOMO by the EDG and stabilization of the LUMO by the EWG which narrows the π-π* energy gap.[165] In 2011, Mourot *et al*. synthesized the series of push-pull AB derivatives shown on **Figure 14**, incorporating acylamino group (in red) as EWG and either dialkylamino or aryl alkylamino group (in blue) as EDG. These compounds were proposed as ion channel blockers, justifying the presence of a quaternary amine group at the molecular end.[161] Compared to symmetrical AB-1 derivatives bearing EWGs on both rings, the three push-pull variants display a redshifted π-π* absorption maxima, from 450 nm to 480 nm, making them particularly promising for MOST applications since nearly 50 % of the solar radiation that reaches the earth's surface lies within the visible spectrum. However, despite their improved spectroscopic properties, push-pull AB suffers from a critical limitation: the $t_{1/2}$ of the metastable isomers is extremely short, ranging from nanosecond to seconds.[166] This

instability is primarily due to the reduced electronic distribution around the AB double bond which facilitates the back-isomerization through rotation pathway. This hypothesis has been supported by several theoretical studies that consistently showed that the activation barrier for rotation-assisted thermal back-isomerization is significantly lower than for any other mechanisms.[165,167]

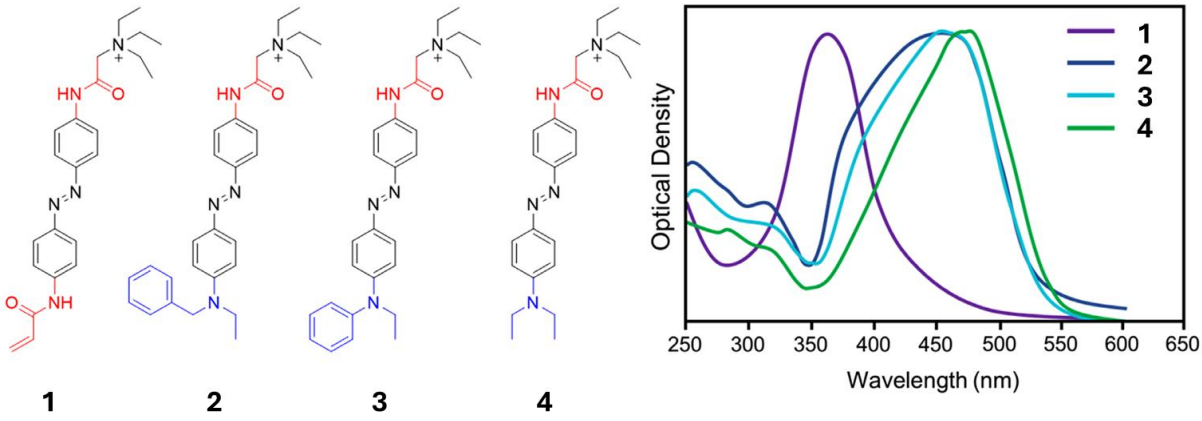

Figure 14. *Representation of the chemical structure of push-pull AB derivatives bearing EDGs (blue) and EWGs (red) in para position and their corresponding UV-vis spectra in phosphate-buffered saline solution at pH 7.4. Spectral data adapted from*[161] *and figure adapted from*[115]*.*

Extending the π-conjugated systems of AB has proven to be an effective strategy to improve the AB spectroscopic properties. The enhancement is primarily attributed to the decrease in the energy gap between the HOMO and LUMO orbitals as the π-conjugation increases. Larger delocalization leads to a more significant bathochromic shift of the π-π* transition, often resulting in an overlap with the n-π* transition, similar to what is observed in push-pull systems or EDW-substituted ABs.[168,169] In 2022, Dudek *et al.* synthesized the series of AB derivatives bearing extended π-conjugated systems shown on **Figure 15**. As expected, compounds 2 and 3 exhibit substantial redshifts of their π-π* transition with absorption maxima at 370 nm and 400 nm, respectively, compared to 320 nm for pristine AB. However, similarly with the two other substitution strategies discussed previously, the enhanced conjugation accelerates the thermal back-isomerization of the Z-isomer, thereby drastically reducing its $t_{1/2}$. They also measured the thermal back-isomerization kinetics of the compound 1, 2 and 3 in acetonitrile

at 25 °C using UV-vis spectroscopy and found $t_{1/2}$ values of 322 h, 9 h and 0.5 h, respectively. These results highlighted the trade-off between improving visible light responsiveness and maintaining thermal stability in π-extended AB systems.[115,170]

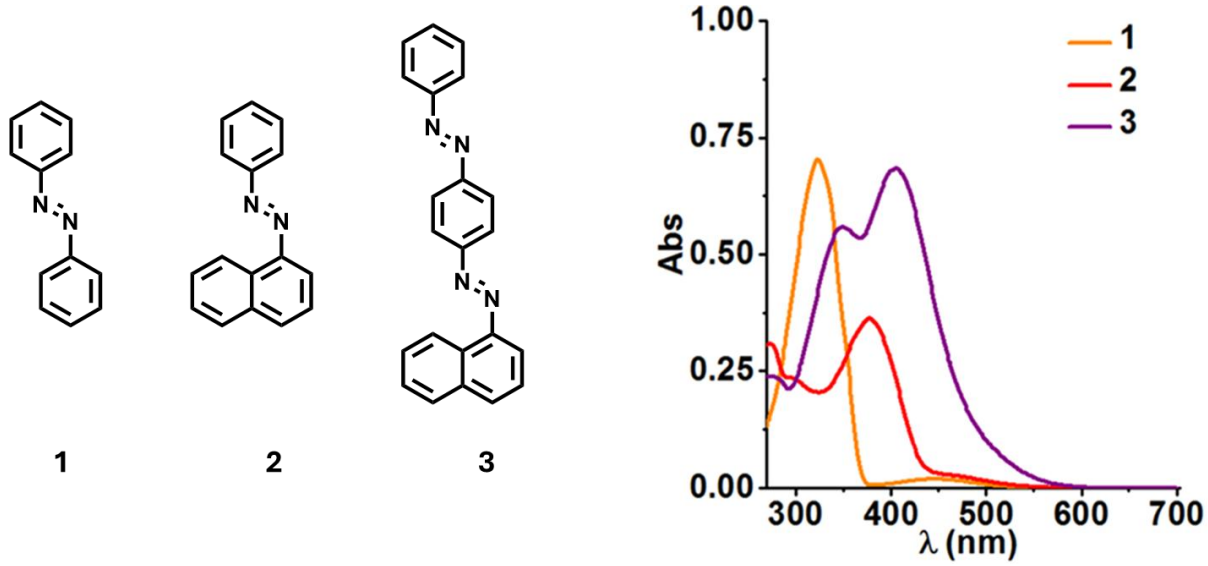

Figure 15. *Representation of the chemical structures of π-extended AB systems and their corresponding UV-vis spectra in phosphate-buffered saline solution at pH 7.4. Spectral data and figure adapted from*[170]*.*

Operating AB-based systems in the liquid phase typically requires the use of solvent capable to dissolve high concentration of active molecules. However, as already mentioned, the solubility of AB in common polar solvents is quite low, thus representing a major drawback toward practical applications. Solvent-free molecular strategies have been developed to avoid the use of solvents. The idea is to use a photochemical crystal-to-liquid transition (PCLT) which combines the latent heat of phase transitions and the AB storage enthalpy to enhance the solar energy storage of the systems. In this approach, at a given temperature, the stable isomer exists under a crystalline solid state, while the metastable isomer is in a liquid state, resulting in a phase-transition MOST materials.[32,67] In such systems, AB are chemically modified in para position through the introduction of an alkyl side chain which induces a phase change from crystal to liquid upon photoisomerization.[171] The major advantage of this method is that the

solar energy stored is enhanced without any major drawback on other properties of the systems. As depicted in **Figure 16**, the thermally and photochemically stable *E*-isomer, initially in the crystalline state, absorbs solar energy and is converted into the liquid *Z*-isomer, thereby storing both photon and thermal energy. Upon optically triggered back-conversion, the *E*-isomer recrystallizes, releasing both the stored isomerization energy (ΔH) and the latent heat from crystallization, thus enabling a more efficient energy storage and release process.[65,172,173] As for example, the compound shown on **Figure 16** exhibits an increase in the storage enthalpy from 50 kJ.mol^{-1} to around 80 kJ.mol^{-1}, with maximum absorbance wavelength at 350 nm and thermal $t_{1/2}$ of approximately 4 days comparable to the pristine AB in solvents such as toluene or hexane.[37,67,171,174] This approaches generally results in an increase in the energy storage capacity without introduction any significant drawbacks. This approach can be effectively combined with other substitution strategy to further enhanced additional properties such as spectroscopic properties with heteroaryl AB which will be discussed in more details later in this introduction or with ortho-substitution strategy as outlined in the following section.

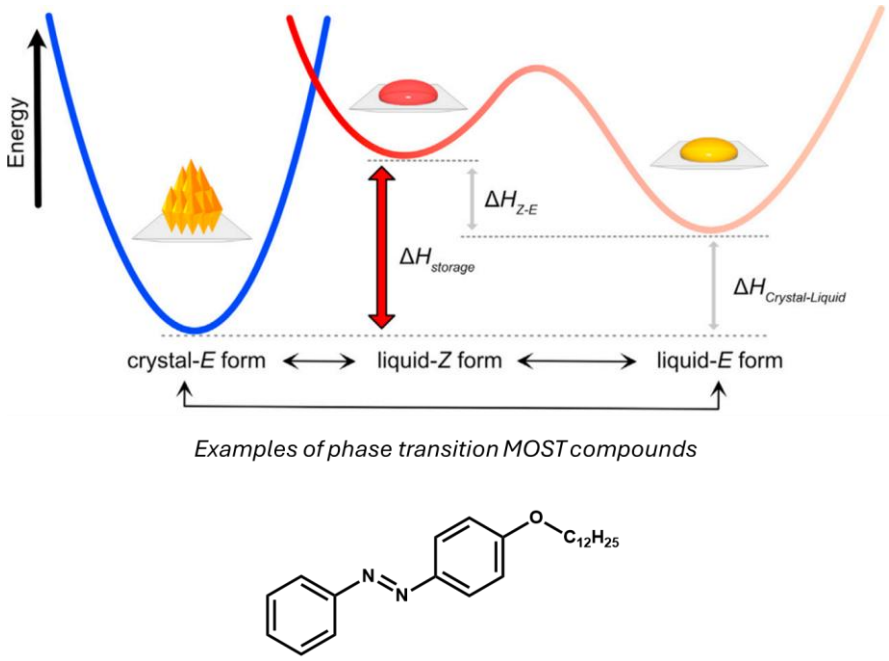

Figure 16. *Schematic representation of the phase transition principle combined with MOST systems, illustrated with AB derivatives. In this concept, the Z-isomer exists in a liquid form and stores both*

isomerization enthalpy and latent heat from crystallization. Upon back-isomerization, both energies are released as the system returns to the crystalline E-isomer. Figure adapted from reference[32].

3.2.2 Better call ortho substitution

Similarly to the para substitution strategy, introducing EDGs or EWGs at the AB ortho position also leads to a bathochromic shift of the π-π* transition, due to enhanced π-electron delocalization. In addition to its electronic influence, ortho substitution offers an unique advantage over para position: the spatial proximity of the substituents to the azo-bond enables direct electronic and steric interactions.[116] The nature of the ortho-substituent can significantly affects the energy levels of the non-bonding n-orbital in AB. For instance, methoxy or halogen substituents can introduce repulsive interactions between the lone pairs on the diazo bond and the ortho substituent, which destabilizes the n-orbital, thereby redshifting the n-π* transitions of the *E*-isomer.[175] Upon photoisomerization to the *Z*-isomer, this repulsion is reduced, leading to a pronounced separation between the n-π* absorption bands of the *E*- and *Z*-isomers as shown on **Figure 17**. This separation is beneficial, as it enables selective excitation and optimized photostationary state distribution. Moreover, excitation through n-π* transition is generally preferred, as it occurs at longer wavelengths and is often associated to higher quantum yields than the π-π* transitions. Furthermore, ortho substitution is also known to significantly retard the thermal back-isomerization, resulting in $t_{1/2}$ that are substantially longer than $t_{1/2}$ of pristine AB.[46] This increased thermal stability makes ortho-substituted AB derivatives particularly attractive for applications requiring long-term energy storage. In the following sections, we will examine in more details three major categories of ortho substitution strategies : bridge spacers, methoxy substituents and halogen substituents, each offering distinct effects on the photophysical and thermal properties of the AB derivatives.[115,155]

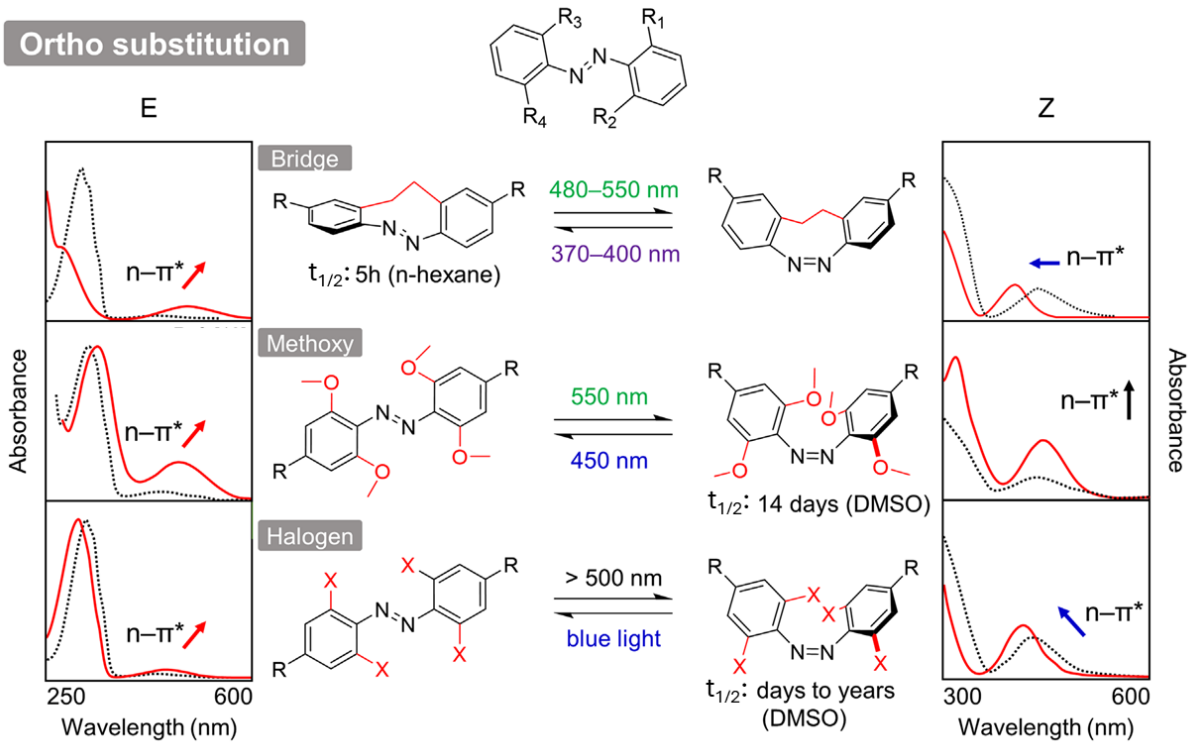

Figure 17. *Effect of ortho substitution with bridge linker, methoxy substituents and halogen substituents on the spectroscopic properties and thermal relaxation behavior of AB derivatives. The dotted black lines represent the UV-vis spectra of pristine AB, while the solid red line represents the substituted AB derivatives. Figure from*[115].

The use of bridge AB derivatives as MOST system represents a promising strategy, particularly due to their absorption in the visible range. One of the most studied compounds in this category is diazocine, an ortho ethylene bridged AB, illustrated on **Figure 18a**. The ethylene bridge connects the ortho position of the two phenyl rings, restricting rotation around the N=N double bond and significantly enhancing the molecular rigidity. In contrast to conventional AB derivatives, the stable isomer of diazocine is the *Z*-isomer which adopts a boat conformation. The *E*-isomer is the metastable isomer and can adopt two distinct conformations, a twist and a chair conformations.[176,177] These two *E*-conformers differ in energy, with the twist conformation being the more stable, with a relative energy difference of 7.6 kcal.mol^{-1} compared to the *Z*-isomer, whereas the chair conformation is higher in energy by 10.5 kcal.mol^{-1}.[178]

In 2009, Siewertsen *et al.* reported the spectroscopic properties of diazocine, highlighting its potential as a viable photoswitch system. As shown on **Figure 18c**, the UV-vis absorption spectrum of diazocine exhibits a distinct separation of the n-π* transitions of the *E*- and *Z*-isomers. Time-resolved UV-vis spectra recorded at intervals of 2, 4, 6, 10 and 15 hours, captured the thermal back isomerization of the metastable *E*-isomer into the stable *Z*-isomer in hexane at 28.5 °C. From this data, a $t_{1/2}$ of 4.5 h is determined, substantially shorter than the pristine AB in the same conditions.[112,177] Spectral analysis also revealed a blueshifted n-π* absorption band at 400 nm for the *Z*-isomer, while the *E*-isomer features a redshifted transition between 480 and 500 nm. This pronounced spectral separation allows for a highly selective photoisomerization, enabling near quantitative conversion between isomers under monochromatic irradiation. Specifically, *Z* → *E* photoisomerization can be induced using blue light (370-400 nm), while the reverse *E* → *Z* photoisomerization is efficiently triggered with green light (480-500 nm).[176] Regarding other MOST relevant properties, diazocine exhibits favorable quantum yield of photoisomerization, approximately 0.53 for the *Z* to *E* transition and 0.24 for the *E* to *Z* transition. In terms of cyclability, diazocine demonstrates excellent performances comparable to pristine AB, maintaining its switching efficiency even after a high number of photoisomerization cycles.[177]

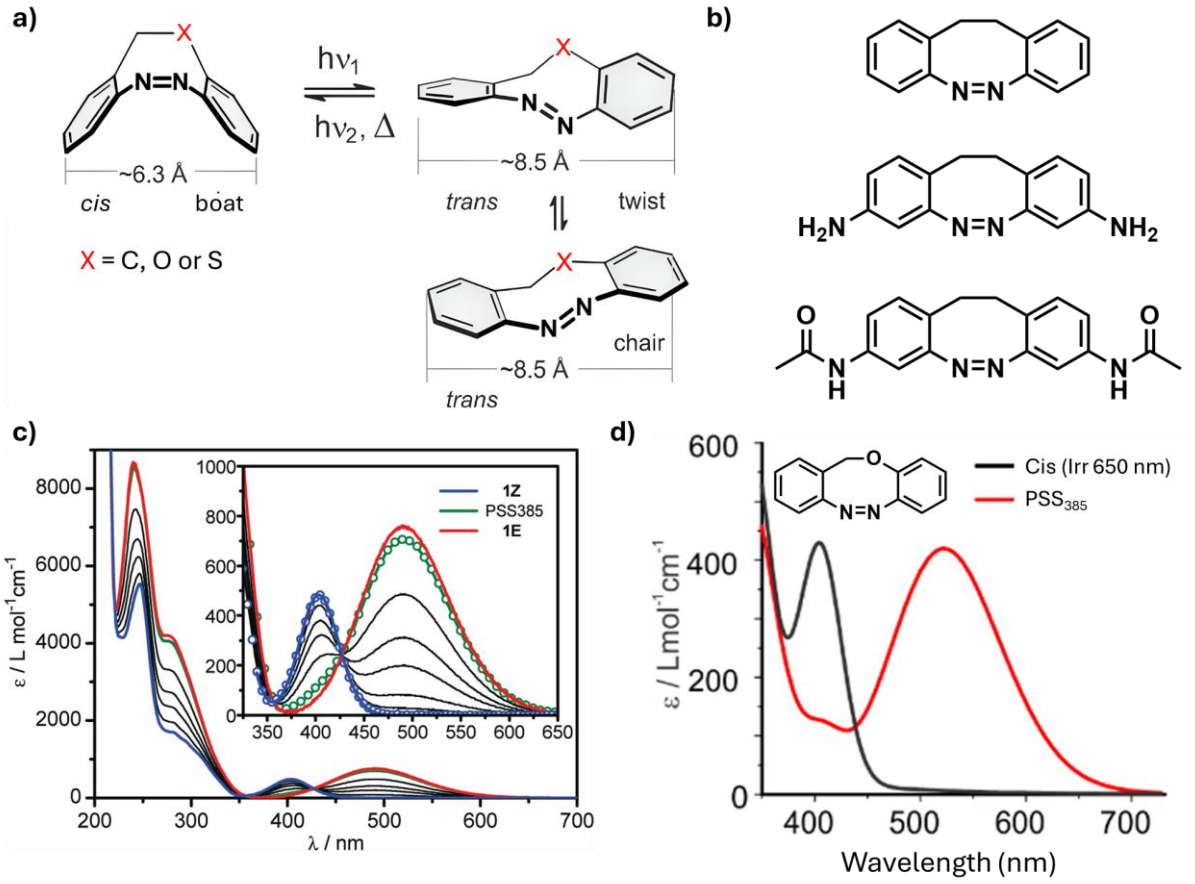

Figure 18. *a) Structure and photoisomerization of different diazocine derivatives. Figure adapted from*[176]*. b) Structures of different diazocines substituted with primary amine and amide groups. Figure reproduced from*[178]*. c) UV-vis absorption spectra of the Z-isomer (blue), E-isomer (red) and the photostationary state at 385 nm (green) in hexane. The thin black lines represent the spectral evolution during thermal back-isomerization from* PSS_{385} *at time intervals Δt : 2, 4, 6, 10 and 15 hours. Figure adapted from*[177] *d) UV-vis spectrum of the O-diazocine in acetonitrile. Figure adapted from*[176]*.*

In 2016, Hammerich *et al.* introduced structural modifications to the diazocine backbone in an effort to further optimize its properties. Specifically, they synthesized heteroatom-bridged diazocines in which a methylene group of the ethylene linker is replaced by an oxygen or a sulfur atom, as illustrated on **Figure 18a**. These modifications resulted in a notable change in spectroscopic and thermal properties. The n-π* transition of the *Z*-isomer remains unaffected by the substitution. However, the corresponding transition for the *E*-isomer exhibits a significant bathochromic shift, with a maximum detected at 525 nm, as shown on **Figure 18d**. Furthermore, the photoisomerization under 385 nm light irradiation is less efficient than diazocine, yielding a photostationary state distribution of 70 % for S-diazocine and 80 % for

O-diazocine. The thermal back-isomerization kinetics showed contrasting behaviors for both heteroatom substitutions. For O-diazocine, $t_{1/2}$ of the *E*-isomer decreases significantly to 89 s at 20 °C in acetone, whereas S-diazocine exhibits an extended $t_{1/2}$ of 3.5 days at 27 °C in acetone.[176] Despite these differences in the thermal stability and photo-switching efficiency, quantum yield and cyclability remain comparable to those of unmodified diazocine.

In 2013, Sell *et al.* synthesized a series of diazocine derivatives substituted with amino and acetamido groups, as shown on **Figure 18b**. The UV-vis absorption spectra of these derivatives are comparable to diazocine, exhibiting no significant shift in the absorbance bands. However, photoisomerization under 405 nm irradiation yield to a lower photostationary state distribution compared to diazocine, with 34 % and 54 % in *E*-isomer for amino and acetamido derivatives, respectively. Despite the reduced photoisomerization efficiency, the thermal stability of the *E*-isomer is significantly enhanced for both derivatives. The reported $t_{1/2}$ are 74 h for the amino derivative and 46 h for the acetamido derivative both in acetonitrile.[178] Overall, this strategy based on bridge AB and their unique *Z* → *E* photoisomerization behavior offers a promising technology for solar energy storage. The ability to achieve relatively long thermal half-lives while maintaining photo-switchability in the visible range highlights their potential and warrants further investigation in the context of MOST applications.

Incorporating methoxy groups at all ortho positions of the AB has proven to be a highly effective strategy for enhancing the AB properties. The UV-vis spectrum of tetramethoxy AB (**Figure 17**) differs notably from pristine AB. For the *E*-isomer, a blueshift of the π-π* transition to 305 nm is observed and is attributed to a reduction in π-conjugation. This reduction arises from steric hindrance introduced by the bulky methoxy groups, which induces a deviation from molecular planarity. In contrast, the n-π* transition of the *E*-isomer undergoes a redshift to approximately 480 nm due to the lone pairs of the ortho oxygen atoms of the methoxy groups and nitrogen atoms of the azo bond. This repulsion raises the energy of the nitrogen n-orbitals, thereby decreasing the n-π* energy gap and producing a bathochromic shift of the transition. For the *Z*-isomer, this destabilization is significantly reduced due to increased spatial separation

between the lone pairs, leaving its n-π* transition largely unaffected. As a result, the n-π* transition of the *E*- and *Z*-isomers are well separated, enabling wavelength selective photoisomerization: *Z*-isomers formation is favored under green light, while *E*-isomer regeneration is achieved with blue light irradiation.[150,179–181] Furthermore, the thermal stability of the *Z*-isomer is enhanced, with a $t_{1/2}$ exceeding 14 h at 37 °C in DMSO.[180] The substituted derivatives also maintain good quantum yield and demonstrate high cyclability, making them attractive candidates for MOST applications.

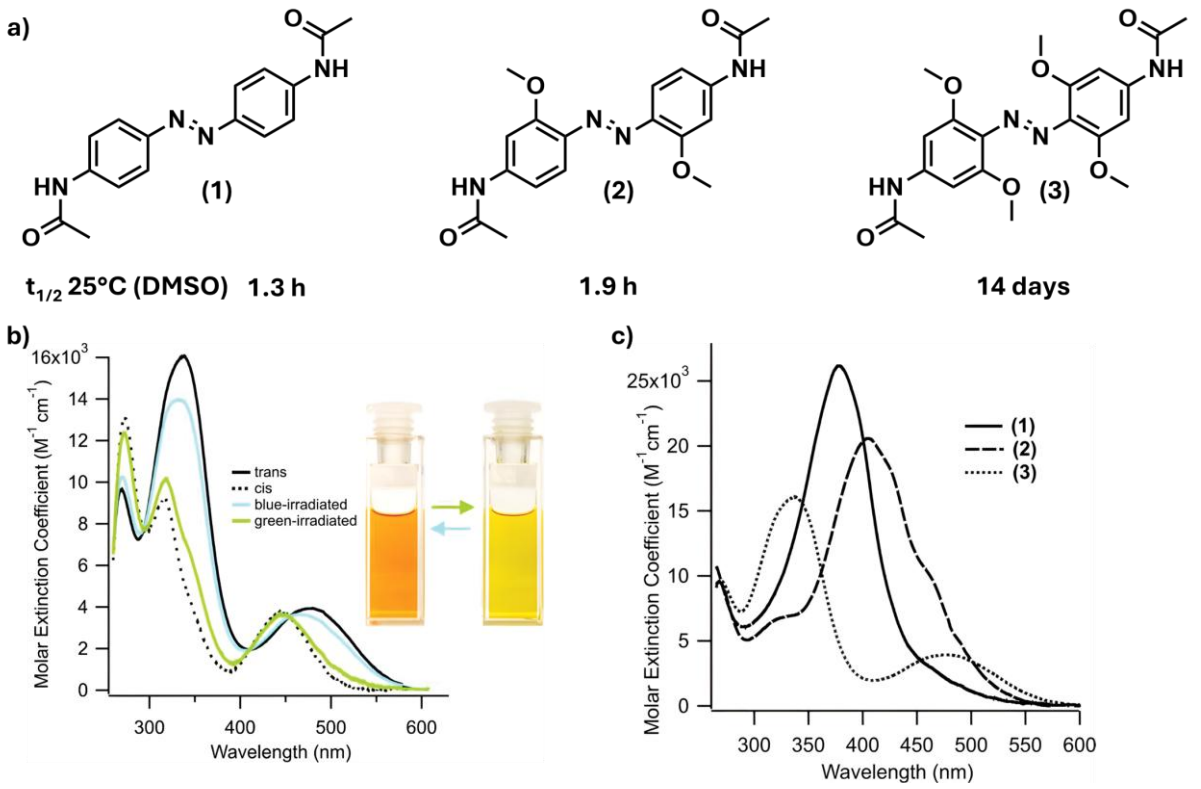

Figure 19. *a) Chemical structures of the 4,4'-diamidoazobenzene derivatives bearing zero, two and four methoxy groups at ortho positions, referred to compounds 1, 2 and 3. b) UV-vis absorption spectra in DMSO of the E-isomer (solid line), Z-isomer (dotted line), PSS under blue light (blue) and PSS under green light (green). c) UV-vis absorption spectra in DMSO of the E-isomers of compounds 1, 2 and 3. Figure adapted from*[150,153]*.*

In 2011, Beharry *et al.* synthesized 4,4'-diamidoazobenzene derivatives bearing zero, two and four methoxy groups at ortho positions, referred to compounds 1, 2 and 3, as illustrated on **Figure 19a**. The UV-vis absorption spectra (**Figure 19c**) reveal that compound 2, containing two ortho methoxy groups, exhibits a redshifted π-π* transition compared to compound 1. This

is attributed to the moderate electron-donating effect of the methoxy groups without introducing significant steric hindrance. In contrast, compound 3 which is tetra ortho-substituted, shows a blueshift of the π-π* transition. **Figure 19b** illustrates the separation of the n-π* transitions between the *E* and *Z*-isomers, a feature already observed in related systems lacking para substitutions. Regarding thermal stability, the incorporation of ortho methoxy groups significantly increases the $t_{1/2}$ of the *Z*-isomer, with values increasing progressively from 1.3 h (compound 1) to 1.9 h (compound 2) and up to 14 days (compound 3) at 25 °C in DMSO. These findings demonstrate that combining para substitution with strategic ortho substitution can simultaneously enhance both spectroscopic properties and thermal stability making such systems more viable for photoresponsive applications, including molecular solar thermal storage.[150,153,179]

Halogen substituents, due to their strong electron-withdrawing inductive effects, offer a promising strategy for enhancing the properties of AB system. Regarding their spectroscopic behavior, the UV-vis absorption spectra shown in **Figure 20b** reveal a progressive blueshift of the π-π* transition from 303 nm to 280 nm, depending on the degree of planarity of the AB derivatives. These variations in planarity are primarily attributed to steric hindrance induced by the halogen atoms, with larger halogens such as iodine inducing larger deviations from planarity and consequently a more pronounced blueshift of the π-π* transition.[182] For the n-π* transition, the effect differs between isomers. For the *E*-isomer, steric repulsion between the halogen and the N=N azo bond destabilizes the n-orbital, leading to a decreased n-π* energy gap and inducing a bathochromic shift of the transition. This effect intensifies with increased halogen size. In contrast, the *Z*-isomer that is less impacted by steric hindrance undergoes stabilization of the n-orbital due to the halogen inductive effect. This results in an increased n-π* energy gap and a hypsochromic shift of the transition, which is most pronounced for highly electronegative halogens such as fluorine. As a direct consequence, the n-π* transitions of the *E*- and *Z*-isomers become spectrally separated, a key feature that allows selective photoisomerization. However, this separation diminishes with increasing halogen size, leading

to larger overlap in the case of the bromine or iodine derivatives.[183] Consequently, the PSD under green light irradiation favors higher *Z*-isomer content for lighter halogens but is less efficient for bulkier halogens due to n-π* overlap. Quantum yields for photoisomerization are significantly enhanced in these derivatives, reaching values as high as 0.5 under optimal conditions.[154] Thermal stability of the *Z*-isomer also varies considerably with $t_{1/2}$ ranging from 5 min for ortho-iodine AB to 1.25 years for ortho-fluorine AB. This trend reflects the decreasing ability of larger halogens to stabilize the *Z*-isomer following a pattern consistent with electronegative substituents, relieving the N=N lone pair repulsion and stabilizing the overall energy of the *Z*-isomer.[183] A comparative overview of the key properties of ortho halogenated AB is provided in **Figure 20a**. Finally, their cyclability remains comparable to pristine AB with no significant degradation under a large amount of photoisomerization cycles.

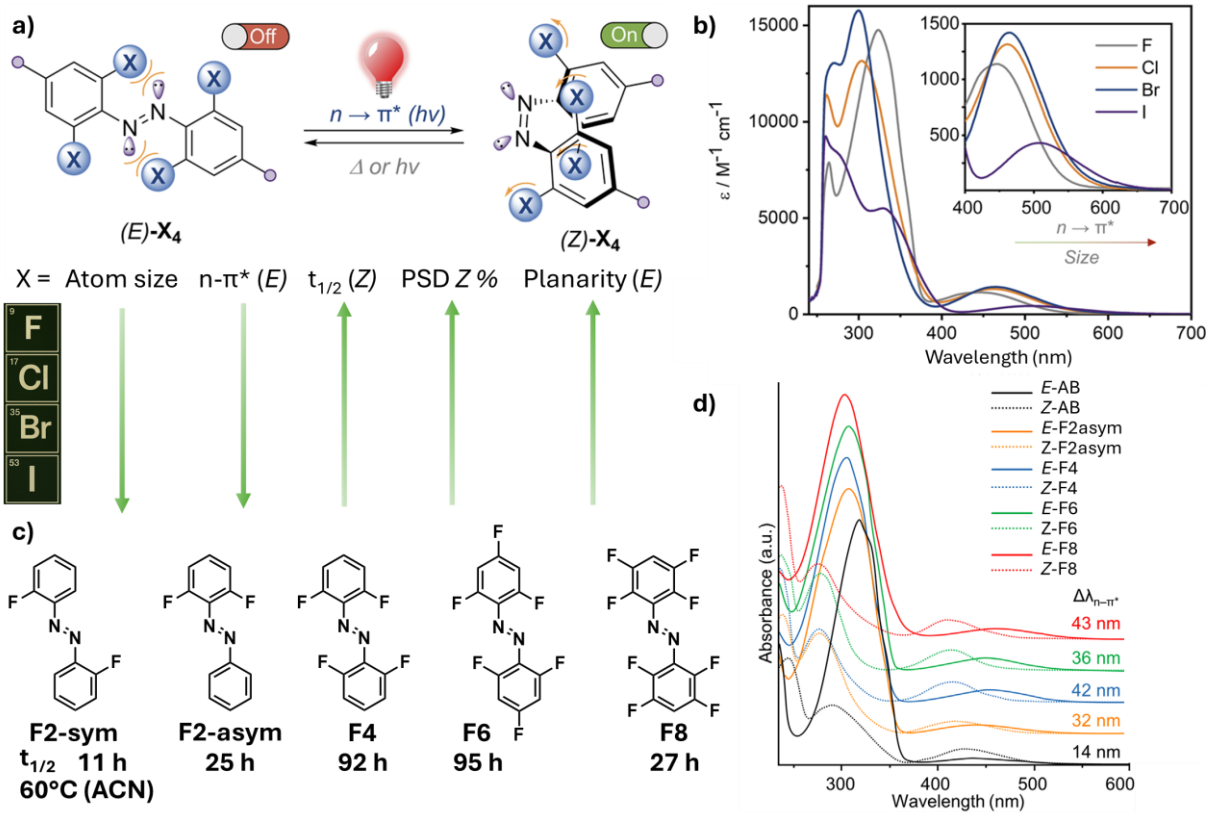

Figure 20. *a) Photoisomerization schematization of the tetra-ortho halogenated ABs with a general illustration of the trends exhibited by key (photo)chemical properties. Figure adapted from*[182,183]*. b) UV-vis absorption spectra of the tetra-ortho-halogenated ABs in DMSO. Adapted from*[182]*. c) Chemical structures of the various ortho-fluor AB derivatives with their* $t_{1/2}$ *in acetonitrile at 60 °C. Data from*[154] *d)*

UV-vis spectra in acetonitrile of the different ortho-fluor AB derivatives with $\Delta\lambda_{n-\pi^*}$, the difference between the maximum wavelengths of n–π bands of E- and Z-isomers. Data from*[154] *and Figure adapted from*[115].

In 2014, Knie *et al.* synthesized a series of ortho-fluorine AB (**Figure 20c**) to investigate the influence of fluorine atoms on the photophysical and thermal properties of AB derivatives. As discussed in the previous section, the UV-vis absorption spectra of these compounds (**Figure 20d**) show similar trends, with the notable exception of the F2-sym derivative. In this case, no significant bathochromic shift of the π-π* transition is observed which remains at 325 nm. Additionally, a 28 nm separation between the n-π* of the *E*- and *Z*-isomers is detected. For the other derivatives, a blueshift of the π-π* transition from 303 nm to 309 nm is observed, with the weakest value corresponding to compounds with larger steric hindrance. The n-π* bands of these derivatives appear between 450 nm and 455 nm, with the *E*- and *Z*-isomers displaying a spectral separation ranging from 32 nm to 43 nm. This separation allows for highly efficient, and in some cases nearly complete bidirectional photoisomerization under appropriate monochromatic light irradiation. Thermal back-isomerization studies reveal a clear trend: the $t_{1/2}$ increases from F2-sym to F2-asym derivatives, suggesting improved thermal stability when fluorine atoms are located on the same side of the molecule. A drastic enhancement in thermal stability is observed for the F4 derivative which exhibits a $t_{1/2}$ of 92 h in acetonitrile at 60 °C. However, for the F8 derivative, where additional fluorine atoms are also introduced in meta position, the $t_{1/2}$ decreases drastically to values comparable to the F2-asym derivative. This reduction in thermal stability has been rationalized by quantum chemical calculations, which indicate that the dipole moment of the transition state plays a critical role. The presence of strong EWGs at the meta position destabilizes the transition state and accelerates the back-isomerization. Therefore, meta-fluorine AB should be avoided when a long thermal stability of the *Z*-isomer is desired.[115,154,182,184]

Combining para EDG or EWG substitution with strategic ortho-fluorine substitution has proven to be an effective strategy for simultaneously improving both spectroscopic properties and thermal stability. Such modified systems are particularly promising for long-term solar energy storage, with $t_{1/2}$ extending from months to years.[185] To further advance the development of

molecules capable of long-term solar energy storage, attention has turned to more structurally modified AB systems. Notably, heteroaryl AB in which one or the two phenyl rings are replaced by heteroaromatic units offer significant potential. These structural modifications aim to fine tune electronic properties, enhance visible light absorption and substantially increase the thermal stability of the *Z*-isomer, thereby overcoming the limitations of unsubstituted AB for MOST applications.[142]

3.3 ONCE UPON A TIME… IN HETEROARYL AZOBENZENE

In order to improve AB systems for solar energy storage, replacing one or both phenyl rings with heteroaryl moieties has emerged as a promising strategy. This approach offers a wide range of structural and electronic tuning possibilities, as illustrated in **Figure 21**.

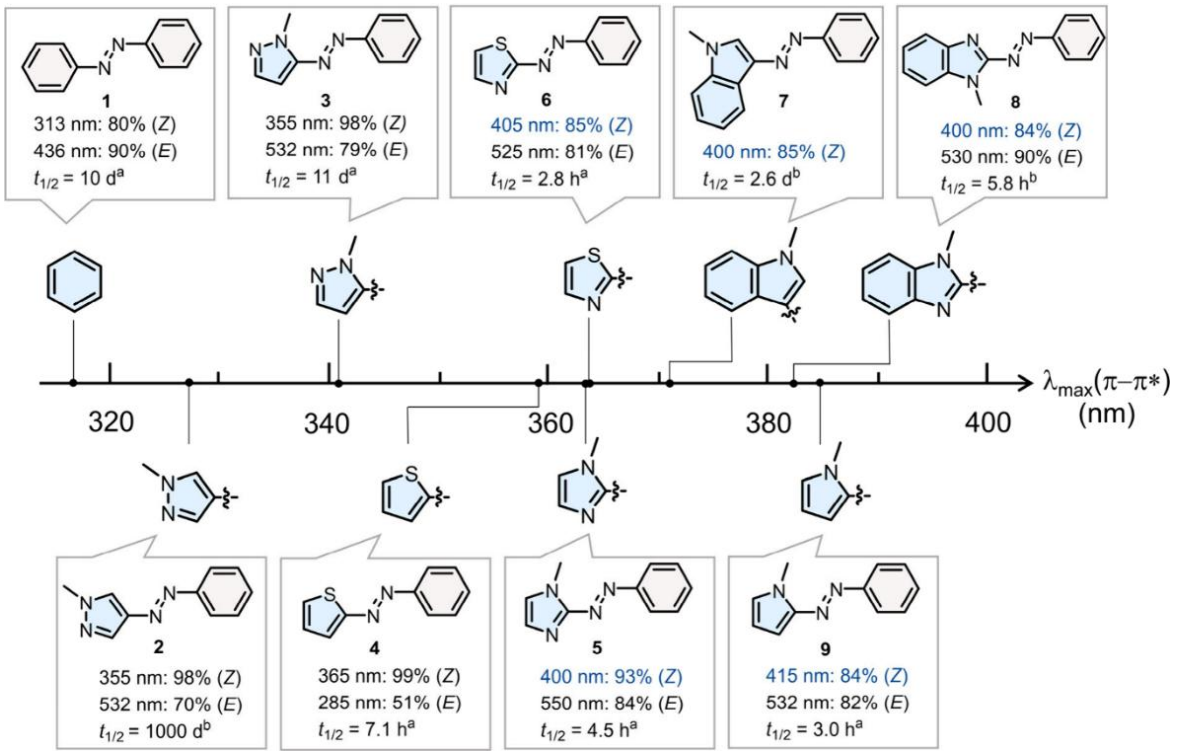

Figure 21. *Graphical representation of the maximum absorption of π-π* transition plotted along an ascending absorption scale. The figure compares the spectroscopic and thermal properties of various AB derivatives including pristine AB*[148,186] *and mono heteroaryl AB bearing rings such as 4-pyrazole*[187]*, 5-pyrazole*[188]*, 2-thiophene*[189]*, 2-imidazole*[190]*, 2-thiazole*[191]*, 3-indole*[192]*, benzimidazole*[193]*, and 2-pyrrole*[187]*. λ_{max} values were measured in ACN, except for compound 8, which was measured in DMSO. Thermal $t_{1/2}$ of Z-isomers were measured at 25 °C in [a] ACN and [b] DMSO. PSD were established under various irradiation wavelengths, with blue text indicating visible light excitation. Figure from*[194]*.*

The use of electron-rich heterocycles to replace one or both phenyl rings in AB derivatives offers an effective strategy for extending π-conjugation, thereby inducing a bathochromic shift of the π-π* transition. The extent of this redshift varies depending on the nature of the heteroaryl group. For instance, compounds 5 to 9 (**Figure 21**) exhibit efficient *E* → *Z* photoisomerization under visible light irradiation, although this is often accompanied by a decrease in thermal stability relative to pristine AB. In opposition, compounds 2 and 3 show enhanced thermal stability while maintaining π-π* transition close to pristine AB.[142,194] Notably, heteroaryl AB designed for solar energy storage typically involve five-membered rings attached to the N=N bond. This choice is driven by the reduced steric hindrance compared to six-membered rings, enabling the *Z*-isomer to adopt a stable T-shaped conformation, an arrangement that is sterically inaccessible to conventional six-membered analogs.[188] All these aspect will be discussed in greater details in the following sections.

3.3.1 The one with pyrrole

Pyrrole, one of the simplest heteroaryl group, consists of a five-membered ring containing a single nitrogen atom. The nitrogen lone pair contributes to the π-conjugated system, rendering the ring highly rich in electrons. In pyrrole-AB derivatives, the position of the N=N bond relative to the nitrogen, either at position 2 or 3, significantly influences the physicochemical properties (**Figure 22a**). Under the *Z*-isomer configuration, five-membered heteroaryl ABs such as pyrrole-AB can adopt a T-shape or a twisted conformation (**Figure 22b**). The T-shape conformation is generally more stable, due to the presence of stabilizing C-H···π interaction, which typically contributes by around 10 kJ.mol^{-1} to the molecular stability.[188,195,196] In contrast, the twisted conformation is less favorable due to steric hindrance. However, in specific compounds such as compounds 2 and 4 on **Figure 21a**, steric hindrance introduced by methyl substituents forces the AB into a twisted conformation, typically leading to a reduction in the thermal stability of the *Z*-isomer. The molecular design of the N-heteroaryl ring is critical in determining the thermal isomerization pathway. For instance, a notable difference exists between N-H azo and N-Me pyrrole-AB. N-H derivatives undergo rapid thermal isomerization

via a hydrazone tautomerism mechanism (**Figure 22c**), especially in protic or polar solvents, leading to ultrafast *Z* → *E* back-isomerization. To suppress this tautomerism and enhance the thermal stability of the *Z*-isomer, an essential requirement for solar energy storage applications, N-methylation of the heteroaryl ring is commonly employed.[192,197]

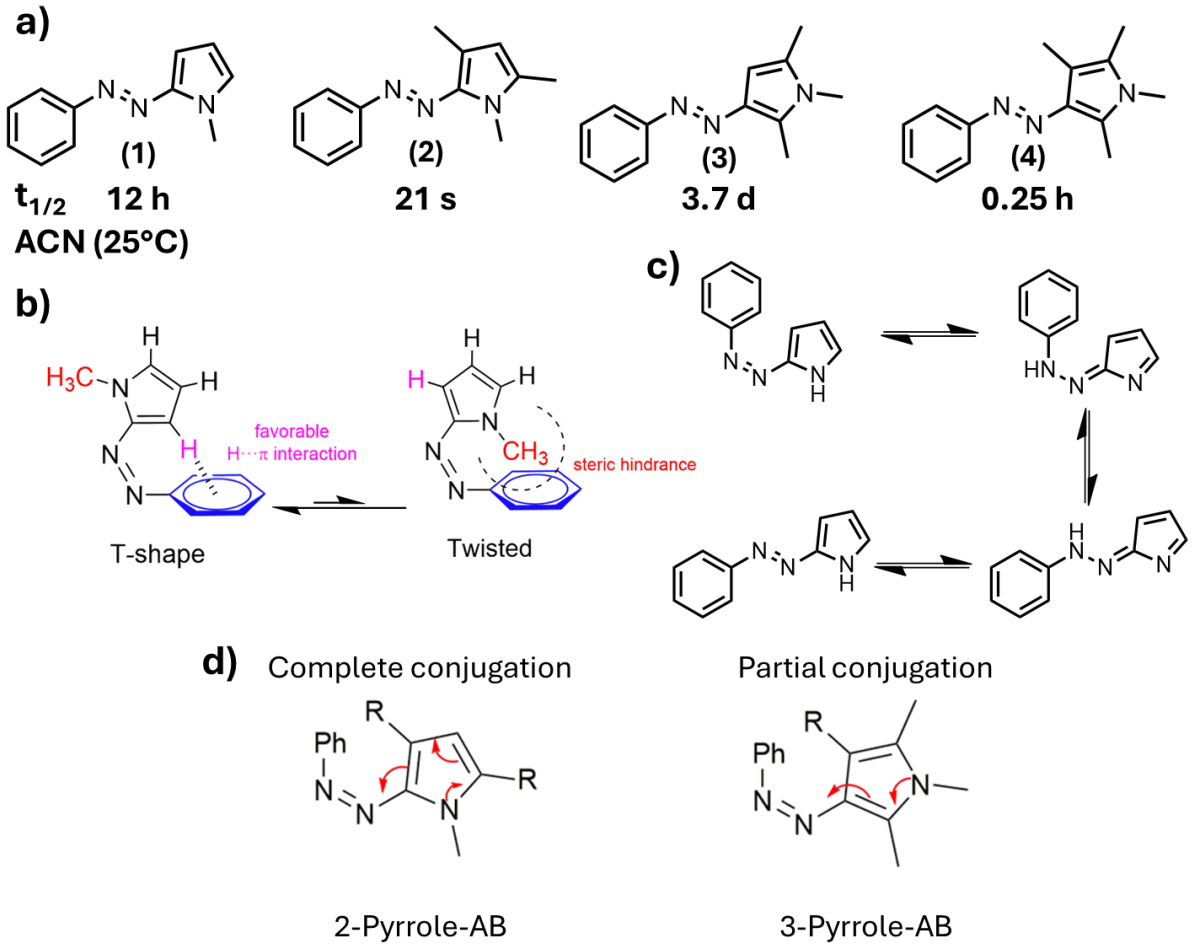

Figure 22. *a) Chemical structures of a series of N-methyl 2- and 3-pyrrole-AB derivatives with their corresponding $t_{1/2}$ measured in ACN at 25 °C. Data from[188]. b) Schematic representation of the two conformations accessible to the Z-isomer of pyrrole-AB derivative: the T-shape conformation, stabilized by C-H···π interaction, and the twisted conformation, typically induced by steric hindrance. Figure adapted form[188]. c) Azo-hydrazone tautomerism pathway that facilitates rapid Z → E thermal back-isomerization of non N-methylated pyrrole-AB. Adapted from[197]. d) schematization of a complete and partial conjugation in a pyrrole-AB. Figure adapted from[188].*

In 2017, Calbo *et al.* synthesized a series of N-methyl 2- and 3-pyrrole-AB derivatives with various methyl group substitutions to introduce different degrees of steric hindrance. The UV-vis absorption spectra reveal that the position of the π-π* transition maxima varies

depending on the pattern. Specifically, 2-pyrrole-AB derivatives exhibit absorption maxima at 385 nm and 394 nm for respectively compounds 1 and 2, while 3-pyrrole-AB derivatives absorb at 363 nm and 345 nm for respectively compounds 3 and 4. These variations are attributed to the differences in π-delocalization; compounds 1 and 2, with more delocalization involving the nitrogen lone pair, exhibit a more significant bathochromic shift compared to compounds 3 and 4, which display only a partial conjugation (**Figure 22d**).[188] Regarding the n-π* transitions, the ortho methyl group in compounds 2 and 4 induce steric hindrance that separates the n-π* transitions of the *E*- and *Z*-isomers, enabling more selective photoisomerization under specific irradiation wavelengths, as previously discussed. Thermal stability also varies across the series with compounds 2 and 4 adopting twisted conformations imposed by steric constraints, which leads to faster thermal back-isomerization. In contrast, compounds 1 and 3 adopt the more stable T-shape conformation, resulting in longer thermal $t_{1/2}$.[187,188]

Moving to extended conjugated systems, heteroaryl indole-AB can be viewed as π-extended analogs of pyrrole-AB. Given the increased conjugation, a bathochromic shift is anticipated. However, in a study by Simeth *et al.*, a series of indole-AB with strategic H or Me substitution demonstrated only a modest shift of the π-π* transition with λ_{max} at 380 nm in DMSO, and a thermal stability ranging from 2.5 h in MeOH to 2.6 days in DMSO. These findings suggest that, despite the π-extension, indole-AB exhibits photoswitching properties comparable to pyrrole-AB analogs, offering no substantial enhancement in MOST performance.[192]

3.3.2 The one with pyrazole

Pyrazole-AB represents one of the most studied and understood heteroaryl AB systems. The pyrazole ring is a five-membered aromatic heterocycle containing two adjacent nitrogen atoms, offering multiple sites for N=N AB attachment. Depending on the position of the azo linkage relative to the nitrogen atoms, three main regioisomers can be synthesized: 3-pyrazole-AB (3-pz), 4-pyrazole-AB (4-pz) and 5-pyrazole-AB (5-pz). In line with the previous section on pyrrole-AB, the incorporation of N-methylated pyrazole rings is often employed to suppress the hydrazone-type tautomerism, a pathway which leads to rapid thermal back-isomerization of

the *Z*-isomer. Furthermore, pyrazole-AB exhibits similar *Z*-isomer conformation as other five-membered heteroaryl AB, *e.g.* the T-shape and the twisted conformations. The equilibrium between both conformations is mostly driven by steric hindrance in ortho position of the N=N bond.

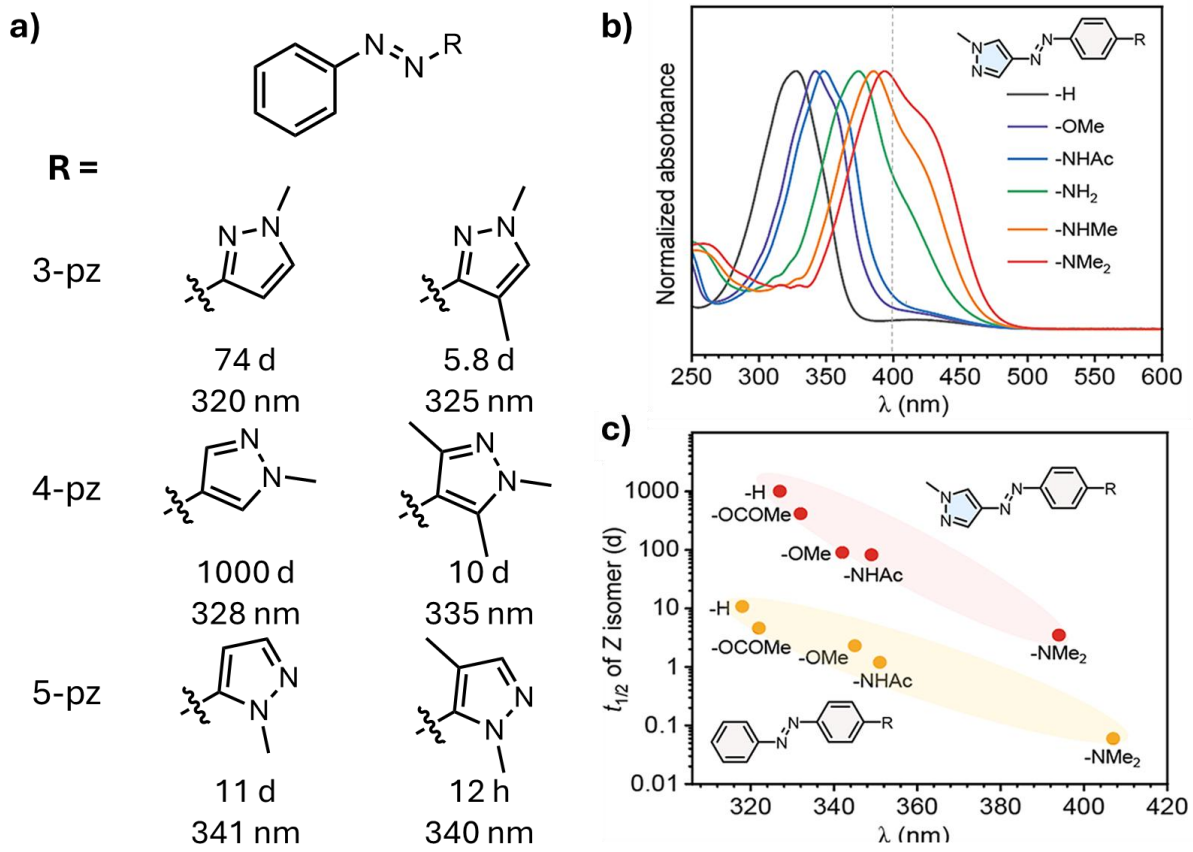

Figure 23.*a) Chemical structures of a series of N-methyl 3-, 4- and 5-pyrazole-AB derivatives with their corresponding $t_{1/2}$ and π-π* λ_{max} measured in ACN at 25 °C. Data from*[188]*. b) UV−Vis absorption spectra of pyrazole-AB derivatives bearing various para-EDGs measured in ACN. Data from*[198] *and figure form*[194]*. c) Correlation between the experimentally measured $t_{1/2}$ (25 °C) and the E-isomer π−π* λ_{max}. Data points are colored by molecular family: para-substituted pyrazole-AB (red) and para-substituted AB (orange). Data from*[148] *and figure form*[194]*.*

Calbo *et al.* synthesized a series of N-methyl 3-, 4- and 5-pyrazole-AB derivatives with methyl group substitutions in ortho of the N=N bond to introduce steric hindrance (**Figure 23a**). The UV-vis absorption spectra of the *E*-isomers reveal that the π-π* transition undergoes a slight redshift in the case of 5-pz, with maxima around 340 nm, whereas smaller shifts are observed for the 3-pz and 4-pz derivatives. This trend is attributed to the enhanced π-conjugation in 5-

pz derivatives due to effective delocalization of the N-methyl pyrazole nitrogen lone pair into the AB system, which increases in efficiency from the 3- to the 5-position. For the *Z*-isomers, the π-π* transitions are observed between 375-390 nm, depending on the specific substitution pattern. This spectral separation between *E*- and *Z*-isomers enables quantitative *E* → *Z* photoisomerization, under specific irradiation wavelength. In terms of thermal stability, most of the compounds exhibit longer $t_{1/2}$ compared to pristine AB with a notable exception for the 4-methyl-5-pz derivative which displays a relatively short $t_{1/2}$ of 12 h, likely due to the destabilizing effect of steric hindrance. More generally, ortho methyl substituted derivatives systematically present reduced thermal stability compared to their non-ortho substituted homologues. Among the series, the 3-pz and 4-pz derivatives demonstrate remarkable thermal stabilities, with values of 74 days and 1000 days, respectively. Notably, the 4-pz derivatives hold one of the longest $t_{1/2}$ reported to date for AB-based photoswitches, underlining the potential of such heteroaryl systems for long-term solar energy storage applications.[187,188,194,199]

To enhance the photoswitching properties of the heteroaryl-AB, such as pyrazole-AB, that are not sufficiently electron-rich to significantly redshift the absorption, their π system can be extended by introducing EDGs at the para position of the phenyl ring (**Figure 23b**)[194]. The magnitude of the resulting bathochromic shift depends directly on the electron-donating strength of the substituent, which correlates with their Hammett parameters.[200] Unsubstituted 4-pz exhibits a π-π* absorption maximum at 328 nm, confined to the UV region, resulting in a modest *Z*-isomer content of 55 % at the PSS upon irradiation at 395 nm. A series of para substituted derivatives bearing EDGs such as −OCOMe[201], −OMe[201], −NHAc[198], $-NH_2$[198], −NHMe[198], and $-NMe_2$[198] was investigated. As the donor strength of the substituent increases, the π−π* transitions are progressively redshifted, with the $-NMe_2$ showing a maximum at 395 nm, placing nearly half of the π−π* band in the visible region. This allows for nearly quantitative *E* → *Z* photoisomerization under 405 nm irradiation. However, this redshift comes at the cost of reduced thermal stability of the *Z*-isomer. Despite this, para-substituted 4-pyrazole-AB maintain significantly longer $t_{1/2}$ than their AB analogues bearing the same substituents

(**Figure 23c**). For instance, the para-NMe_2 AB exhibits a very short $t_{1/2}$ of 0.06 days, whereas its pyrazole analogue displays a much longer $t_{1/2}$ of 4.6 days.[198] This enhancement arises from the inherently long-lived *Z*-isomer of the parent 4-pz which has $t_{1/2}$ of 1000 days, compared to only 10 days for pristine AB. These findings clearly illustrate the advantages of heteroaryl AB derivatives like 4-pz for developing visible-light responsive candidates for solar energy storage application.[188,197,198]

3.3.3 The one with imidazole

Imidazole-AB are the second most extensively studied class of heteroaryl-AB, just following pyrazole derivatives. This interest is largely driven by their potential applications in biological systems and coordination chemistry, owing to imidazole strong ability to act as metal ion ligands.[202,203] Imidazole is a five-membered aromatic heterocycle and a structural isomer of pyrazole, differing by the relative position of its two nitrogen atoms, which are separated by a carbon atom. As with pyrazole-AB, N-methylation of the N-H imidazole ring is crucial when targeting solar energy storage applications. This prevents hydrazone tautomerism that otherwise leads to rapid thermal back-isomerization in N-H derivatives. Similar to other five-membered heterocycles, imidazole-AB *Z*-isomer can adopt T-shape and twisted conformations depending on the steric environment imposed by the substituents on the heterocycle.[190,204]

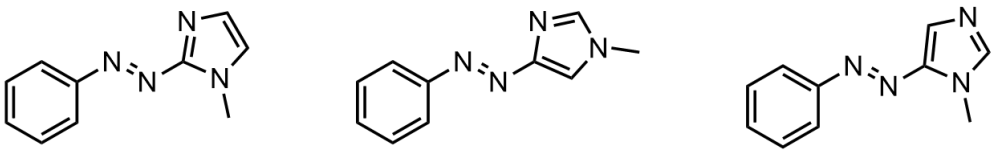

	2-im	**4-im**	**5-im**
$t_{1/2}$	9 h	2.4 d	6.5 d
π-π*	363 nm	336 nm	362 nm

Figure 24. *Chemical structures of a series of N-methyl 2-, 4- and 5-imidazole-AB derivatives with their corresponding $t_{1/2}$ and π-π* λ_{max} measured in ACN at 25 °C. Data from*[188,204]

Combining the work of Otsuki *et al*. and Calbo et al., three imidazole-AB derivatives (2-im, 4-im and 5-im) were investigated to assess the impact of the N=N bond position on the imidazole ring (**Figure 24**).[188,204] The π-π* absorption maxima of compounds 2-im and 5-im are located

around 360 nm enabling efficient E → Z photoisomerization under visible light irradiation. In contrast, the 4-im derivative exhibits a π-π* transition at 336 nm resulting in reduced absorption in the visible range. Nonetheless, even the least redshifted imidazole-AB exhibits higher π-π* transition than any pyrazole-AB counterpart, highlighting the better delocalization of the π-electron in imidazole-AB derivatives. The thermal stability studies revealed $t_{1/2}$ at 9 h, 2.4 d and 6.5 d at 25 °C in ACN for 2-im, 4-im and 5-im, respectively. These values are significantly lower than those of pyrazole-AB analogues, reflecting reduced thermal robustness. This trend correlates with the *Z*-isomer conformation. The T-shape conformation which promotes longer $t_{1/2}$ are observed for 4-im and 5-im, while 2-im adopts a twisted conformation due to steric repulsion between adjacent N=N bond and nitrogen atom, which destabilizes the *Z*-isomer and accelerates its thermal back-isomerization.[188,190,204,205] Further π-extension via benzimidazole-AB has been shown to induce bathochromic shift, with π-π* absorption band exceeding 400 nm. However this enhanced conjugation comes at the cost of drastically reduced thermal stability, with the *Z*-isomer $t_{1/2}$ ranging from few minutes to few hours.[193] In summary, imidazole-AB, while capable of absorbing visible light efficiently, generally exhibits low thermal stability compared to pristine AB. Therefore, their potential lies more in biological applications or coordination chemistry than in solar energy storage systems.

3.3.4 The one with isoxazole

Isoxazole-AB are among the least explored classes of heteroaryl-AB with no studies to date reporting their application in the storage of solar energy. Nevertheless, a few published works about phase transition materials[206] or anticancer drugs[207] provide preliminary insights into their potential as candidates as MOST. Isoxazole is a five-membered hetero aromatic cycle featuring adjacent nitrogen and oxygen atoms within the ring. Notably, isoxazole-AB as opposed to other nitrogen based-AB cannot undergo hydrazone tautomerism, owing to the absence of an N-H liaison in the heterocycle. This structural feature prevents rapid thermal back-isomerization, potentially resulting in enhanced thermal stability of the *Z*-isomer.[208]

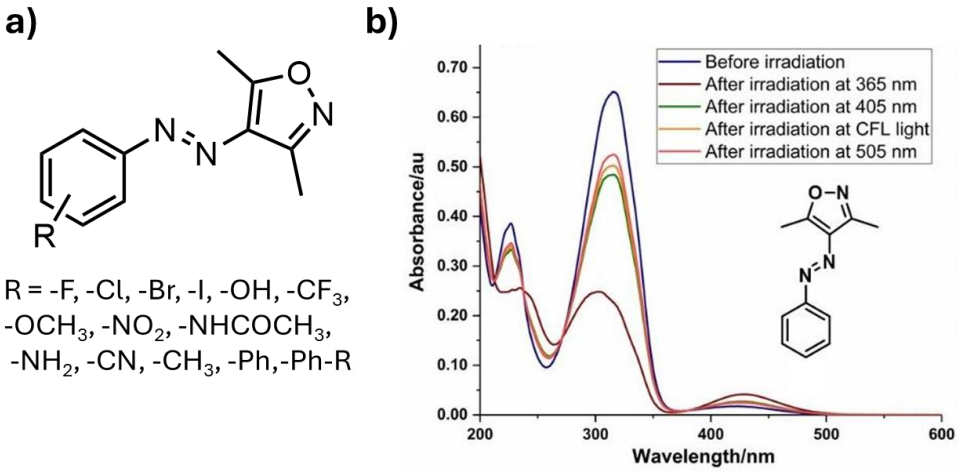

Figure 25. *Chemical structures of a series of substituted isoxazole-AB derivatives with R representing the substituent in ortho, para or meta position. UV-vis absorption monitoring of the photoisomerization reaction of phenylazo-3,5-dimethylisoxazole under different sources of irradiation. Data and figure from*[206].

In 2019, Kumar *et al*. synthesized a series of substituted isoxazole-AB derivatives (**Figure 25a**) in order to explore their potential as light-responsive phase transition materials. Notably, these isoxazole-AB exhibit photoinduced phase transitions without the need of long alkyl chains, unlike previously discussed systems. This behavior is particularly promising for enhancing energy storage capacity, as it enables the integration of both isomerization enthalpy and latent heat from phase transitions. Concerning the spectroscopic properties, most of the synthesized compounds exhibits π-π* absorption bands between 315 nm and 330 nm (**Figure 22b**) resulting in slight hypsochromic or bathochromic shifts relative to pristine AB, but still insufficient to shift absorption into the visible region. Exceptions were observed for derivatives bearing strong EDGs in para position, which exhibit absorption band around 340-350 nm, again still not sufficient to reach visible light absorption. In terms of thermal stability, the phenylazo-3,5-dimethylisoxazole (**Figure 25b**), one of the most simple isoxazole-AB synthesized, demonstrate a *Z*-isomer $t_{1/2}$ of approximately 45.5 days at 25 °C in DMSO. This value is particularly notable as it is nearly five times larger than pristine AB. Although the thermal back-isomerization kinetics of the other derivatives were not explored in details, the enhanced stability of the *Z*-isomer of isoxazole-AB is promising. However, the primary

limitation of the system remains its deep UV absorption, which restricts solar energy harvesting. Nonetheless, this issue could potentially be overcome through strategic molecular modifications, such as π-extended systems, making isoxazole-AB a compelling platform for further development in MOST technologies.[206]

3.3.5 The one with thiophene

Over the past decade, following the success generated by pyrazole-AB with exceptional thermal stability, researchers have expanded their investigations into other heteroaryl-AB systems. Among them, thiophene-AB have emerged as promising candidates for solar energy storage. Thiophene is a five-membered heteroaromatic ring, rich in electron due to the presence of a sulfur atom, which offers unique electronic and conformational properties. As with other heteroaryl-AB, thiophene-AB can adopt two distinct conformations in their *Z*-isomer: the T-shape conformation and the twisted conformation (**Figure 26a**). The T-shape conformation is an orthogonal structure, stabilized by a favorable lone pair···π interaction between the sulfur lone pair and the π-system of the adjacent phenyl ring.[209,210] In contrast, in the twisted conformation, the proximity between the sulfur atom lone pair and the azo nitrogen lone pair destabilizes the system, inducing a twist of the thiophen ring. This energetic difference favors the T-shape conformation by approximately 10 kJ.mol^{-1}, resulting in about 98 % of *Z*-isomers adopting the T-shape conformation at room temperature (R.T).[189,210]

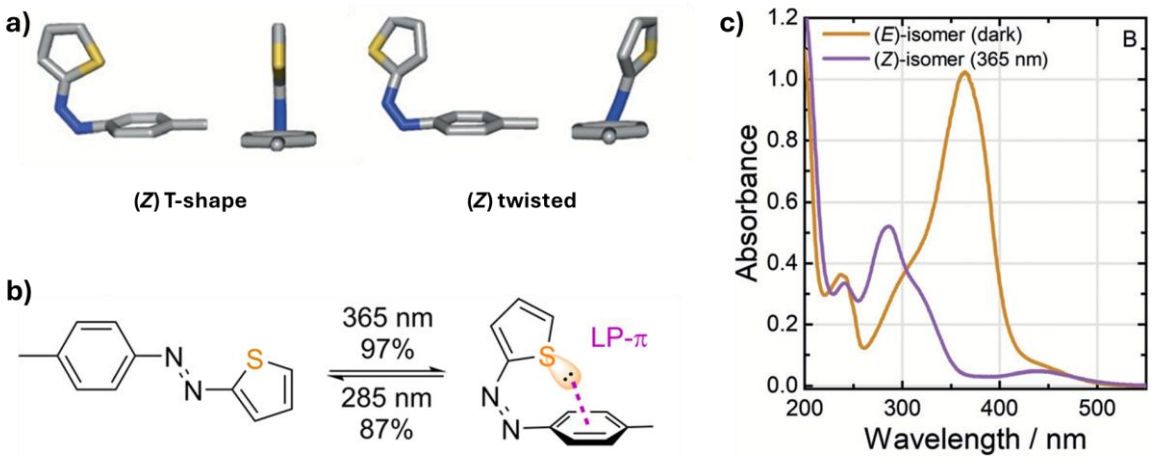

Figure 26. *a) Geometry-optimized conformations of the Z-isomer different conformations: T-shape and twisted. Figure adapted from*[210]*. b) Photoisomerization of the methyl substituted thiophene-AB where*

the Z-isomer is stabilized by lone pair···π interaction. Figure adapted from[189]*. c) UV-vis absorption spectra of the E- and Z-isomer of the methyl-substituted thiophene-AB. Figure adapted from*[210]*.*

In 2020, Slavov et al. synthesized a methyl substituted thiophene-AB (**Figure 26b**) incorporated at para position to assess its viability for solar energy storage applications. The UV-vis absorption spectrum of the *E*-isomer (**Figure 26c**) displays a dominant π-π* absorption band at 365 nm and a weaker n-π* around 450 nm. Upon irradiation at 365 nm, efficient *E* → *Z* photoisomerization is observed. The resulting *Z*-isomer exhibits a π-π* transition around 285 nm, notably weaker than that of the *E*-isomer, and a n-π* transition around 450 nm, that remains relatively unchanged. The clear spectral separation between the π-π* bands of the *E*- and *Z*-isomers allows for a selective photoconversion. Irradiation at 362 nm lead to a conversion of over 97 % to the *Z*-isomers, while reverse photoisomerization at 285 nm yielded at 87 % of *E*-isomers. The system also demonstrate a high quantum yield for E → Z photoisomerization (~0.44), which is significantly improved compared to pristine AB. Furthermore, the system exhibits a cyclability, with no notable degradation after more than 50 photoswitching cycles. However, a notable limitation lies in the thermal $t_{1/2}$ of the *Z*-isomer, which is relatively short at approximately 2 h at 20 °C in acetonitrile, comparable to certain pyrrole-AB. This drawback could potentially be relieved through strategic substitution to improve the thermal stability of the *Z*-isomer.[210]

Later in 2020, Heindl *et al.* expanded on this work by synthesizing a series of thiophene-AB bearing EDGs and EWGs. Their aim was to fine tune the system properties, as summarized in **Figure 27**, which categorizes the derivatives as para-phenyl AB (red), meta-phenyl ABs (green), thiophene-substituted ABs (blue) and push-pull thiophene-AB (purple). All the compounds exhibit absorption spectra similar to the reference thiophene-AB (**Figure 26c**), with bathochromic shift in the π-π* band relative to pristine AB, ranging from 365 nm to 414 nm. In the most redshifted systems, typically those belonging to the push-pull series, the π-π* absorption band is shifted sufficiently to overlap with the n-π* transitions, as previously described in the section on pristine AB substitution. Notably, all derivatives show excellent

cyclability, with over 10 photoisomerization cycles completed without any observable degradation. [189,210]

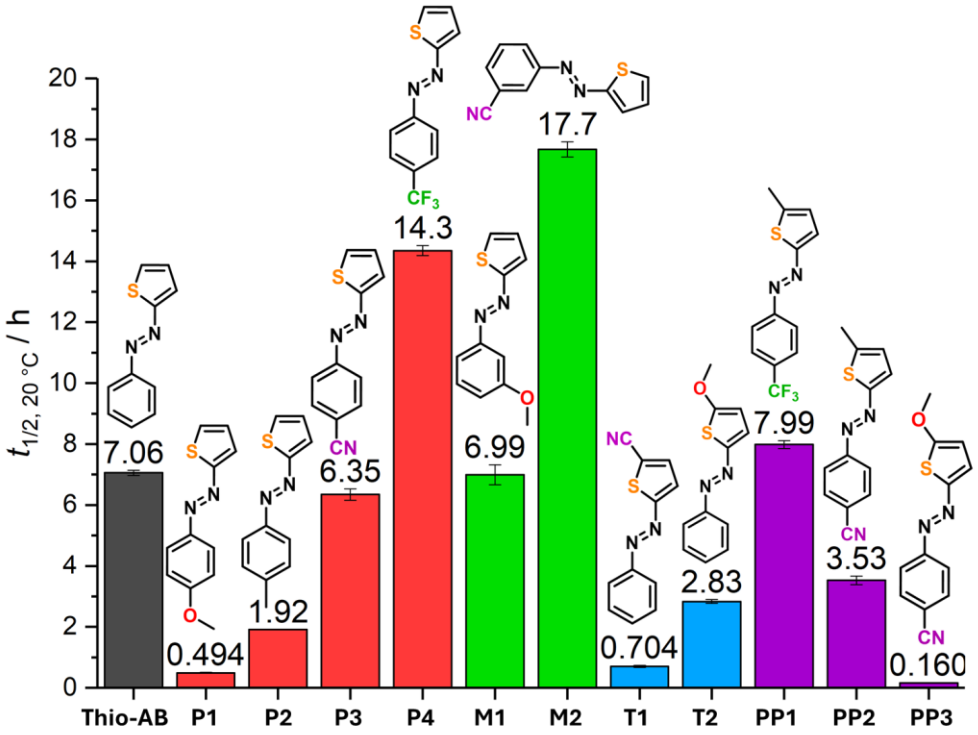

Figure 27. *Representation of the $t_{1/2}$ of various thiophene-AB derivatives in ACN at 20 °C. Red bars correspond to para-phenyl ABs, green bars correspond to meta-phenyl ABs, blue bars correspond to thiophene-substituted ABs and purple bars correspond to push-pull thiophene-AB. Figure adapted from*[189]

In terms of thermal stability, a variety of behaviors were recorded depending on the substitution pattern:

- For para-phenyl ABs (red on **Figure 27**), a clear trend is observed: compounds with mesomeric electron-donating groups have shorter $t_{1/2}$, while inductive electron-withdrawing groups lead to longer $t_{1/2}$ values. This trend is attributed to the electron-withdrawing groups which decrease the electron density of the phenyl ring, thereby strengthening the lone pair···π interactions that stabilize the *Z*-isomer.
- For meta-phenyl ABs (green on **Figure 27**), mesomeric effects of the substituent are suppressed due to the meta position, but inductive effects remain influential. Notably, compound M2 exhibits the longest $t_{1/2}$ of the series, reaching nearly 18 h.

- For thiophene-substituted ABs (blue on **Figure 27**), introduction of inductive withdrawing group adjacent to the sulfur atom likely destabilizes the lone pair···π interaction, resulting in lower thermal stabilities than the unsubstituted parent compound (grey on the **Figure 27**).
- Finally, push-pull thiophene-ABs (purple on **Figure 27**) exhibits the shortest $t_{1/2}$ values of the series, consistent with strong π-delocalization induced by the push-pull substitution previously discussed for classical ABs.

The results confirm that careful substitution enables fine-tuning of the optical properties and thermal stability of thiophene-AB, making them viable candidates for MOST application when appropriately engineered.[189,210]

3.3.6 The one with thiazole

Thiazole-AB represents one the most recently investigated heteroaryl-AB systems, with a comprehensive study conducted by Lin *et al.* in 2023.[191] Due to their promising photo- and thermochemical properties, thiazole-AB have rapidly attracted interest in the context of MOST. This class of compounds will form one of the core subject of this thesis, where various aspects of their design, behaviors and performance will be thoroughly examined. Before presenting the new investigations and results conducted in this work, it is important to first review the current state of research on thiazole-AB, summarizing the key findings and trends already established in the literature.

In 2023, Lin *et al.* synthesized a series of ortho- and para-substituted thiazole-AB derivatives (**Figure 28a**). Compound 1 represents pristine thiazole-AB without any substitution, while compounds 2 to 5 arise from ortho-substitution with halogen atoms. Compounds 6 to 8 feature ortho-substitution with amino, methylamino and dimethylamino groups and compounds 9 to 11 come from para-substitution with cyano, dimethylamino and methoxy groups. To analyze the conformational differences between isomers, single-crystal X-ray diffraction was performed on compounds 1 and 3 (**Figure 28b**). Both *E*-isomers exhibit coplanar phenyl and thiazole rings, similar to the geometry observed in pristine AB. In contrast, the *Z*-isomers adopt a T-shape

conformation. Compound 1 displays an almost perfect orthogonal arrangement between the phenyl and the thiazole rings, with dihedral angle of 89.7°. For compound 3, the T-shape conformation is slightly distorted, showing a dihedral angle of 98.4°, attributed to steric hindrance from the bulky chlorine substituent. Despite this deviation, the T-shape conformation is maintained and does not evolve into a twisted conformation. These T-shape geometries are stabilized by a lone-pair···π interaction, as also seen in thiophene-AB analogues. However, theoretical calculations revealed that compounds 10 and 11 preferentially adopt twisted conformations. This is likely due to weakened lone-pair···π interaction caused by strong EDG in the para position.[191] In 2025, Madappuram *et al*. synthesized a series of thiazole-, isothiazole- and thiadiazole-AB derivatives, demonstrating that both T-shape and twisted conformations can be observed depending on the electronic effects imposed by additional nitrogen atoms within the heterocycle.[211]

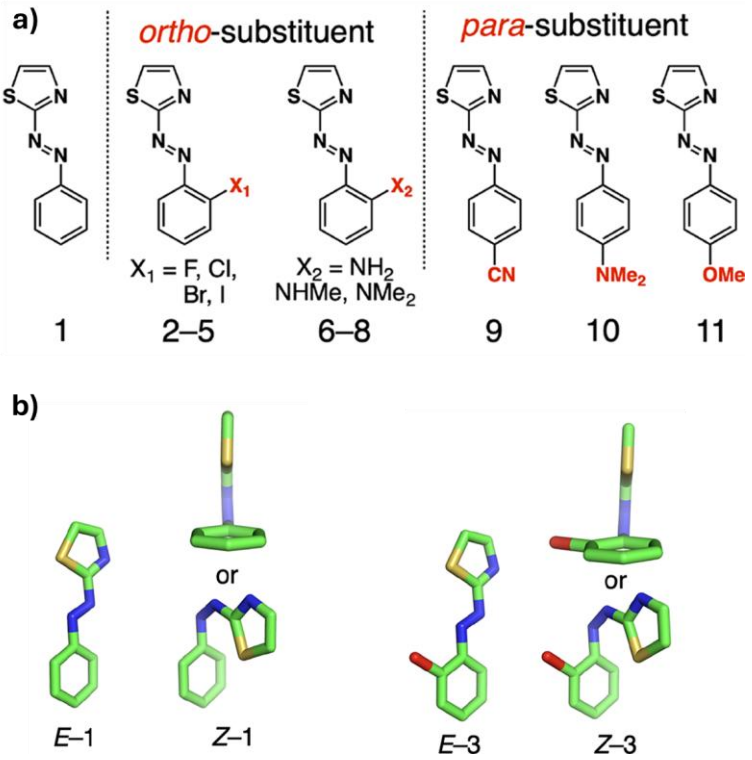

Figure 28. *a) Chemical structures of a series of ortho- and para-substituted thiazole-AB derivatives. b) Single-crystal X-ray structures of both E- and Z-isomers of compounds 1 and 3 (green = C; blue = N; gold = S; red = Cl). Figure adapted from* [191].

The UV-vis spectrum of compound 1 (**Figure 29a**) reveals two distinct transitions, *e.g.* the π-π* transition at 364 nm and the n-π* transition at 459 nm, representing a pronounced bathochromic shift compared to pristine AB. For the ortho-halogenated derivatives, the UV-vis spectrum of compound 5 is shown on **Figure 29b**, the transitions remain largely unmodified, with only a minor redshift (up to 10 nm) as the halogen atomic mass increases. In the case of ortho-amino substituted derivatives, the π-π* transition undergoes a hypsochromic shift due to steric hindrance, resulting in reduced planarity and thus less π-conjugation. The transitions occur at 351 nm and 353 nm for compounds 6 and 7, respectively, while compound 8 remains at 365 nm. In contrast, the n-π* transition shows a significant increase in intensity and is redshifted to 482 nm, 508 nm and 525 nm for compounds 6, 7 and 8, respectively. These effects can be attributed to the stronger EDG nature of the substituents, which destabilizes the n-orbital of the N=N bond and enhances the n- and π*-orbital overlap. The stronger are the EDGs group the more redshifted is the n-π* transition. For the para-substituted derivatives, the behavior aligns with basic push-pull AB, where strong electronic effects lead to substantial redshifts and total overlap of π-π* and n-π* transitions. The maximum absorptions are at 371 nm, 484 nm and 384 nm for compounds 9, 10 and 11, respectively. As expected, stronger EDG groups induce larger redshifts in the absorption maxima.[191]

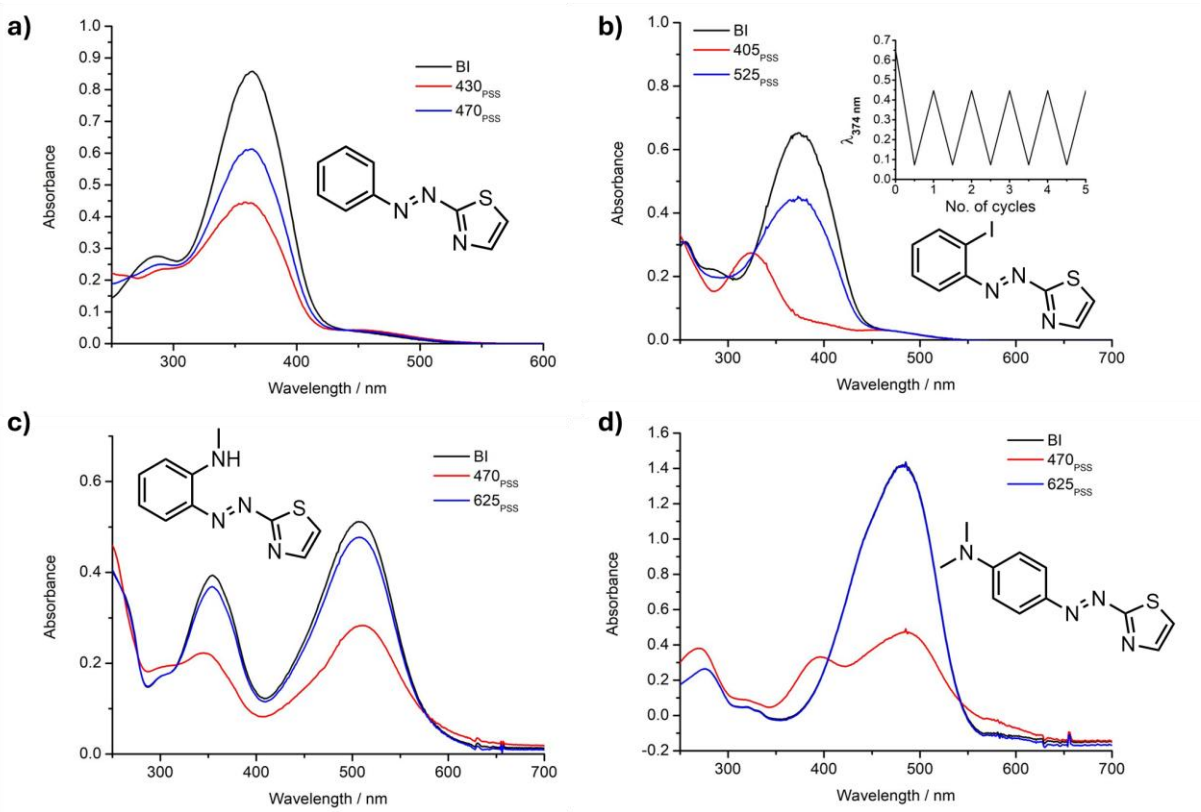

Figure 29. *(a-d) UV-vis spectra of the substituted thiazole-AB derivatives in ACN at 25 °C. Figure adapted from*[191]*.*

These characteristic UV-vis spectra observed for the different thiazole-AB derivatives enable efficient photoisomerization, resulting in *Z*-isomer populations exceeding 90 % under suitable irradiation wavelengths. The different thiazole-AB derivatives demonstrate excellent cyclability, showing no significant degradation after multiple photoisomerization cycles. However, their thermal stabilities vary greatly. The unsubstituted thiazole-AB exhibits a $t_{1/2}$ of 2.8 h at 25°C in ACN. For the ortho-halogenated derivatives, $t_{1/2}$ values are notably improved, ranging from 3.6 h to 7.2 h, with the bromine-substituted compounds displaying the highest thermal stabilities. In contrast, ortho-amino substituted derivatives suffer from very rapid thermal back-isomerization, with $t_{1/2}$ values between 6 s to 45 s, likely due to strong EDG effects and steric destabilization of the *Z*-isomer. Regarding, para-substituted thiazole-AB, thermal stability also varies with $t_{1/2}$ of 1.7 h, 2 s and 15 min for compounds 9, 10 and 11, respectively.[191,212,213]

From a spectroscopic perspective, thiazole-ABs are promising candidates for solar energy storage, as their π-π* transitions approach the visible light region. However, the relatively short

thermal $t_{1/2}$ remain a major limitation. While strategic substitution remains a conventional way to improve performance, a promising alternative involves the use of template architectures to enhance the key properties of the system. The following section introduces and expands on this template-based approach.

3.4 TEMPLATES: IN THE MULTIVERSE OF GRAFTING

In parallel with chromophore modification, a second strategy involves using a template to support AB derivatives. This approach enables a highly ordered, close-packed arrangement of AB units on the template surface. Such a special proximity organization promotes intermolecular interactions, along with steric hindrance, which might collectively influence and enhance both $\Delta H_{storage}$ and thermal $t_{1/2}$. When densely packed, attractive intermolecular forces stabilize the planar *E*-isomers, while steric repulsion destabilizes the twisted *Z*-isomers, leading to an increase in ΔH per AB unit. Moreover, the constrained environment restricts molecular motion, thereby slowing down the back-isomerization process and extending the storage time.[42,46,70]

Templates explored for this purpose include reduced graphene oxide (RGO), carbon nanotubes (CNTs) and various polymers. Although non exhaustive, this list of examples highlights the progress made in developing solid-state solar thermal fuels, which can exist in the form of films, suspended solids or powders. This solid-state form offers an advantage over liquid systems, which often require high concentration of photoswitches in solvent, a condition that can be challenging to achieve especially for ABs that are known to have poor solubility in usual polar solvents.[32,42,46,70] In grafted systems, the grafting density becomes a critical parameter. Excessively high densities may hinder photoisomerization due to spatial constraints, while insufficient densities reduce intermolecular interactions and lower the gravimetric energy density, as the inert template contributes to the mass system without participating in energy storage. These considerations underscore the molecular design challenges that must be addressed to optimize AB-templated MOST systems.[42]

In 2013, Grossman et al. used density functional theory to demonstrate that hybrid AB-template structure could reversibly store solar energy with energy densities comparable to those of Li-ion batteries. They further showed that the energy storage time, the temperature of the heat output, and the overall solar to thermal conversion efficiency could be optimized through the appropriate pairing of photoswitch molecules and template platforms.[214] However, achieving such high energy densities in practice remains challenging. A key limitation lies in the dependence of intermolecular interactions between chromophores depending on specific intermolecular distance and specific steric arrangements, which are difficult to control experimentally.[46]

3.4.1 The carbon nanotube rise

CNTs are tubular nanoscale graphite crystal consisting of seamless single- or multiple-layer graphene sheets rolled around a central axis with a specific helix angle. The carbon atoms in each layer are sp^2-hybridized, forming a cylindrical surface with hexagonal lattice. Owing to these unique structural features, CNTs are considered highly suitable templates for the preparation of hybrid AB materials.[149] The idea of using CNTs as templates to enhance the properties of AB derivatives emerged in 2011, when Grossman *et al*. proposed, based on DFT calculations, that anchoring AB molecules onto a single walled carbon nanotube (SCNTs) could improve their performance as MOST system. Their simulations show that, with an appropriate grafting density, the rigid CNT template could induce a highly ordered and compact arrangement of AB molecules. This structural organization, combined with specific chemical interactions, are predicted to enhance both $\Delta H_{storage}$ and $t_{1/2}$ of the system. For instance, at a grafting density of one AB unit every 4.24 Å, packing interactions are predicted to increase the ΔH per AB by up to 30 % compared to gas-phase AB, mainly due to the destabilization of the *Z*-isomers. However, this improvement comes at the expense of a reduced storage time. To achieve simultaneous enhancement of both ΔH and $t_{1/2}$, they evaluated the introduction of hydroxyl substituents on AB to modulate intermolecular H-bonds all along the template (**Figure 30a**). They showed that maximizing the number of H-bonds between the *E*-isomers,

while minimizing it between the *Z*-isomers, may significantly increase the ΔH and $t_{1/2}$, since both isomers would be stabilized through different ways. Their calculations indicate that, by adequately positioning the hydroxyl substituents on the AB, it would be possible to create six H-bonds between the *E*-isomers and only four between the *Z*-isomers. This AB-SCNTs system could lead to an increase of 260 % in ΔH and 20 % in ΔH* compared to AB in the gas-phase.[214,215]

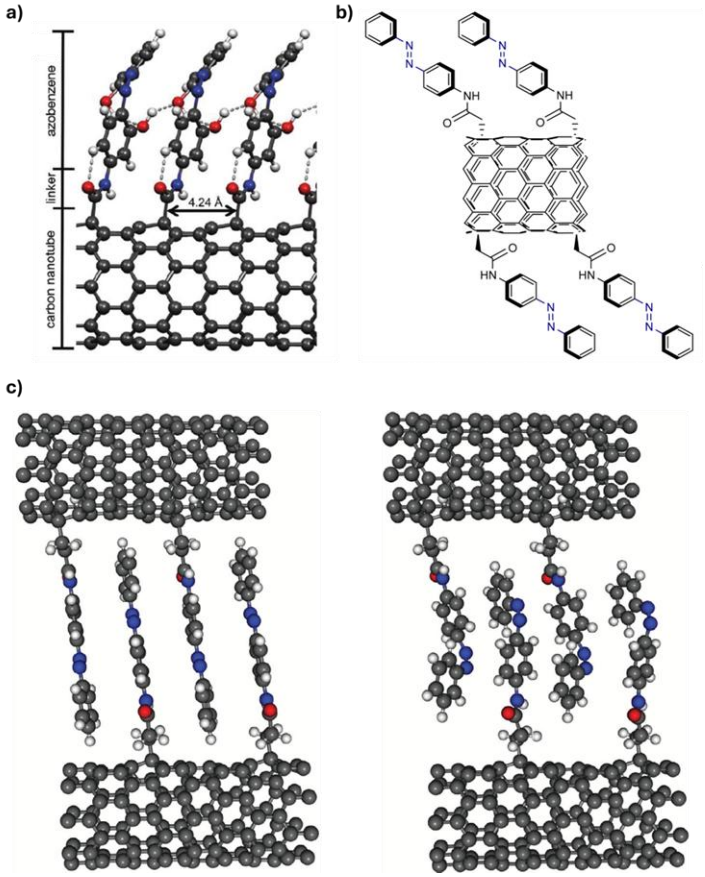

Figure 30. *a) DFT-calculated structure of 2,2-dihydroxyl-substituted AB grafted onto CNTs, illustrating proximity-induced interactions and H-bonds with a grafting density of one chromophore every 4.24 Å. Figure from*[215]*. b) AB covalently coupled to CNT via amide linker, synthesized by Grossman et al.*[216]*, Figure from*[131]*. c) Computed minimum energy of AB-SCNT structure of the E and Z configurations. Figure from*[216]*.*

In 2014, Grossman et al. experimentally synthesized a CNT-templated AB (**Figure 30b**), with no hydroxyl group incorporated. The grafting density achieved is 1/18 (one AB molecule grafted every 18 carbon atoms of the CNT), leading to an intermolecular spacing by far longer than the computed 4.24 Å require to induce strong packing interactions. As a consequence,

for dilute suspension, the expected improvements in storage energy are not observed. However, in the solid-state, packing effects and interaction between AB units on neighboring templates are envisaged, as shown in **Figure 30c**. In this arrangement, AB residues are separated by approximately 8 Å, leading to an increase in the stored energy from 58 $kJ.mol^{-1}$ (0.16 $MJ.kg^{-1}$) for the non-templated 4-acetamidoazobenzene derivative to 120 $kJ.mol^{-1}$ (0.2 $MJ.kg^{-1}$) for the CNT-templated system. This solid-state energy enhancement, combined with excellent stability and cyclability, highlights the potential of CNT-templated AB for further development.[149,172]

In 2017, Luo *et al.* reported a novel solar thermal storage material based on the AB-functionalized multi-walled carbon nanotubes (AB-MCNTs). They demonstrated that, for the same type of linkage, the spacing between AB molecules on MCNTs is smaller compared to SCNTs, resulting in stronger intermolecular interactions and, consequently, a higher energy density. The structural arrangement of MCNTs significantly improves the storage capacity, reaching 277.2 $kJ.kg^{-1}$, with a short-term lifetime approximately around 14 h and excellent cycling stability, over 30 cycles. This work presents a promising class of solar thermal storage materials with both high energy density and a suitable short lifetime for daily energy utilization. Nonetheless, a key limitation of CNT templates remains their modest gravimetric energy density (0.2 - 0.3 $MJ.kg^{-1}$), which is constrained by the high mass of the template, rising challenges for large-scale applications.[149,217]

3.4.2 The lord of the templates: reduced graphene oxide

Graphene, *i.e.* a two-dimensional sheet of sp^2-hybridized carbon atoms arranged in a hexagonal lattice, is an attractive template candidate owing to its exceptional mechanical, optical and electronic properties. Moreover, its growth process does not generate impurities, thereby eliminating the need for complex purification steps. Reduced graphene oxide (RGO) is frequently preferred over graphene because the incorporated surface functional groups (-COOH, -OH, epoxides) allow for the covalent grafting of AB derivatives onto the material.[46,70,218]

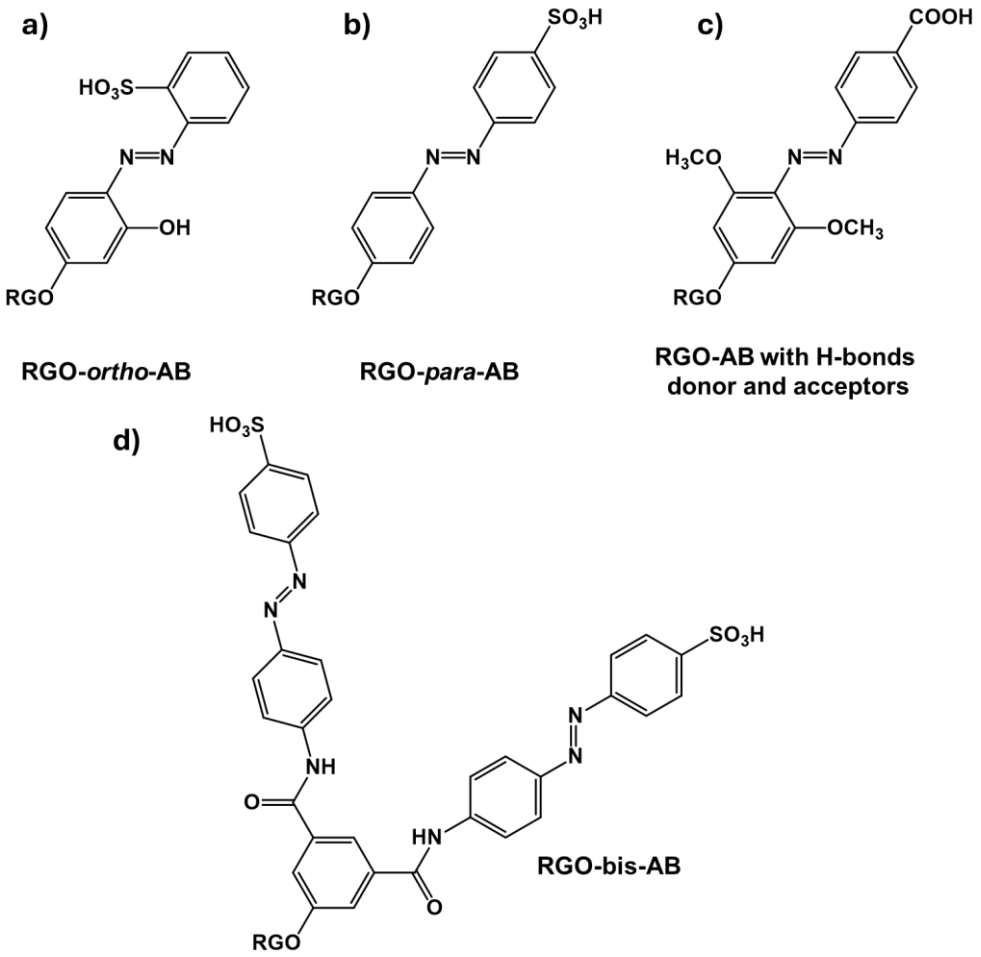

Figure 31. *Structures of AB derivatives covalently grafted on RGO surfaces. a) Ortho-substituted AB.*[219] *b) Para-substituted AB.*[219] *c) AB substituted with methoxy in ortho positions and carboxylic acid in para position to promote intermolecular H-bonds.*[220] *d) Bis-AB derivative linked by a 1,3-benzene dicarboxamide moiety.*[221]

Based on DFT calculations performed on CNT templates, Feng and coworkers decided to extend their investigation toward RGO template functionalization with different AB derivatives, aiming to tune intermolecular interactions and optimize the overall system properties. Their initial study focused on the effect of ortho and para substitutions in AB-RGO systems, as illustrated on **Figure 31a** and b. XPS characterization reveals a high grafting density of approximately 1/12, corresponding to one AB molecule grafted every 11-12 carbon atoms of the RGO sheet. In terms of thermal stability, the *Z*-isomers of the RGO-ortho-AB derivatives exhibit a significantly longer $t_{1/2}$ (225 days) compared to the *Z*-isomers of the RGO-para-AB (116 h), a behavior attributed to intramolecular H-bond stabilization in the ortho derivatives enabled by the proximal hydroxyl groups. However, the storage energy shows the opposite

trend: the para derivatives achieve 103 kJ.mol^{-1} (27 kJ.kg^{-1}), whereas the ortho derivatives reach only 60 kJ.mol^{-1} (15 kJ.kg^{-1}). This difference is explained by the H-bond pattern, since multiple intra- and intermolecular H-bonds in the ortho derivatives stabilize both the *E*- and *Z*-isomers, whereas the para derivatives can form only one H-bond, thus increasing the difference of energy between E- and Z-isomers.[46,131,219]

To further highlight the importance of optimizing the H-bond numbers in both isomers, Feng *et al.* designed AB derivatives bearing methoxy groups in ortho positions and a carboxylic acid in para position (**Figure 31c**). In this configuration, neighboring AB units form two intermolecular H-bonds in the *E*-isomer but only one in the *Z*-isomer, thereby increasing the storage energy while maintaining an acceptable $t_{1/2}$ for the *Z*-isomer. Notably, H-bonding occurs not only between AB on the same RGO sheet but also between two adjacent sheets, similar to what was previously observed for CNT templates. The grafting density reaches 1/16, resulting in a storage energy of 192 kJ.mol^{-1} (40 kJ.kg^{-1}) and a $t_{1/2}$ of 33 days. The nano-templated structure exhibits excellent stability, with no degradation observed even after 50 cycles under visible light irradiation, confirming the strong potential of template-mediated H-bond for enhancing MOST properties.[149,220,222]

A final example of RGO-templated AB system concerns the covalent attachment of closely packed bis-AB derivatives (**Figure 31d**). Feng and co-workers synthesized this material with a grafting density of 1/46. The intramolecular coupling of the bis-AB moieties is found to stabilizes the *Z*-isomer through increased steric hindrance, while simultaneously lowering the energy of the *E*-isomer. As a result, the material achieves an impressive storage energy of 572 kJ.mol^{-1} (47 kJ.kg^{-1}) with $t_{1/2}$ of 37 days, primarily, due to strong intermolecular interactions. Photothermal measurements on UV-irradiated films reveal a temperature rise of 15 °C, with 85 % of the stored heat released within 8 min. This remarkable photothermal effect, combined with excellent cyclability, underscores the potential of AB-template hybrids as efficient MOST systems for diverse applications. Nevertheless, despite these significant improvements in

energy density, graphene-based AB materials often require several hours of UV irradiation to fully isomerize, which leads to a low absorption capacity and low conversion rate.[46,221]

3.4.3 The polymer project

Template nanostructures such as CNTs or RGO thus present severe limitations, *e.g.* (i) competition between the absorption of the template material and the anchored AB resulting in slow and low photoisomerization and (ii) a high contribution to the global mass of the system resulting in a low energy density.[42,46] Researchers thus started working on polymers bearing photoswitches as a viable alternative for several reasons. Polymer backbones are more flexible, therefore reducing the steric constrain and enabling the photoisomerization to be facilitated compared to previous templates. Moreover, with non-conjugated backbones, polymers do not absorb in the same region as the AB photoswitches reducing the absorption competition. Three notable examples will be discussed in the present section.

The first example concerns a homopolymer, designed by Grossman et al, in which the aliphatic backbone possesses pendant AB side chains (**Figure 32a**). This architecture provides a larger conformational freedom to potentially maximize both energy density and thermal stability. The UV-vis spectrum of the polymer is measured similar to pristine AB, showing π-π* and n-π* transitions at respectively 325 nm and 450 nm. In a toluene solution, the pending AB chromophores undergo an efficient *E* → *Z* photoisomerization under 365 nm UV-irradiation. Nevertheless, the polymer exhibits a weaker energy density around 104 $kJ.kg^{-1}$ and a shorter storage time ($t_{1/2}$ = 55 h at R.T) compared to the monomer unit (ΔH = 151 $kJ.kg^{-1}$, $t_{1/2}$ = 92 h, R.T). This decrease could result from several factors, including reduced absorption efficiency, reduced quantum yield and excessive backbone flexibility.[223,224] Notably, both the polymer and the monomer display excellent cycling stability over more than one hundred cycles of photoisomerization and back-isomerization. Following the solution studies, a thin polymer film is prepared by spin coating to assess the solid-state behavior. After UV irradiation, a heating ramp is applied to trigger heat release. A temperature difference of 10 °C between charged

and uncharged film is achieved within ten seconds, highlighting the potential of such polymer films for rapid heat release applications.[224,225]

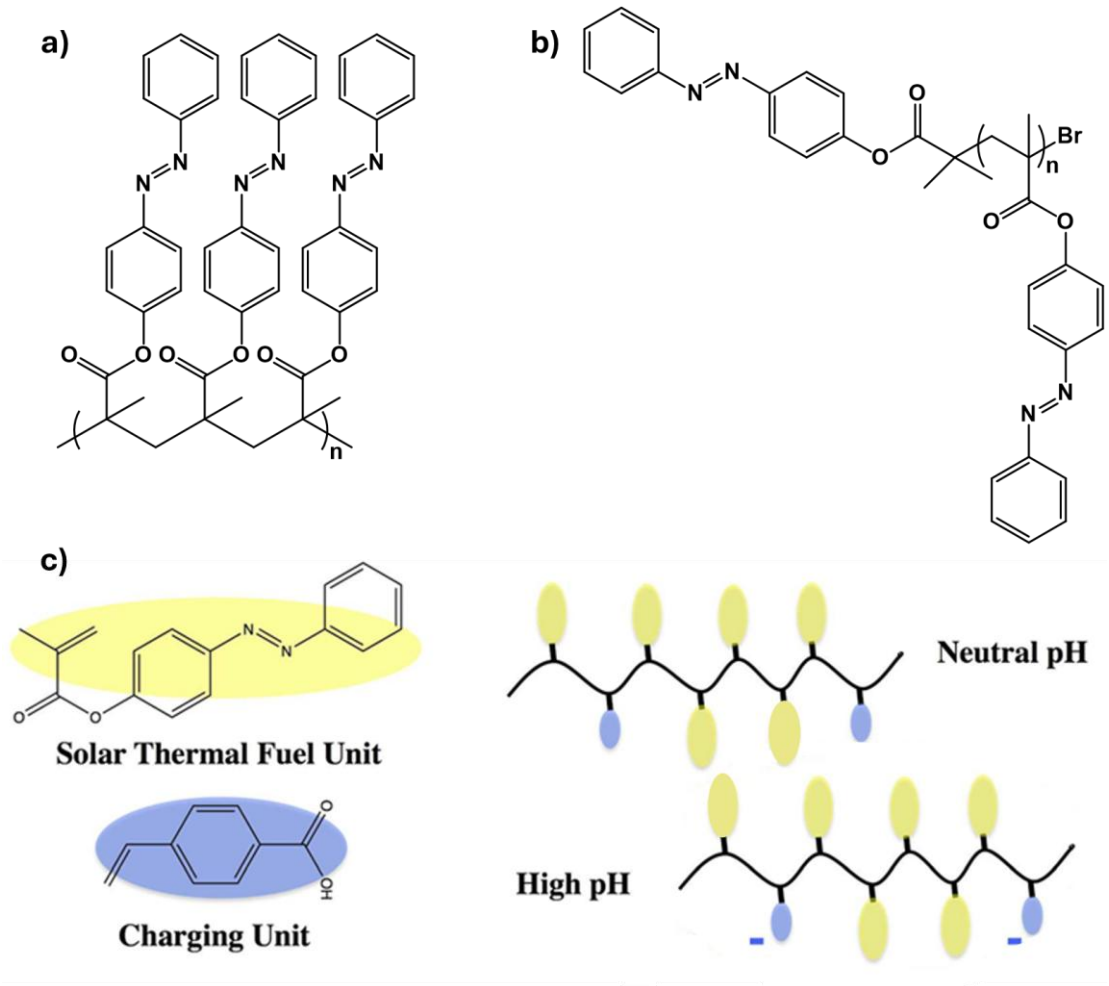

Figure 32. *Examples of polymer-templated AB: a) homopolymer constituted of an aliphatic backbone and AB as pending side chains. Reproduced from*[224]*. b) Polymethacrylate backbone with syndiotacticity, featuring syn ester AB moieties separated by 5 Å. Reproduced from*[226]*. c) Copolymer bearing AB and benzoic acid side chains, enabling deprotonation of the polymer under basic conditions. Figure adapted from*[227]*.*

The second example involves a polymer based on a polymethacrylate backbone bearing AB as side chains (**Figure 32b**). The polymer, obtained via radical polymerization, exhibits high syndiotacticity, with the syn ester AB moieties spaced by 5 Å. This arrangement generates steric effects that destabilize the Z-isomers, thereby enhancing the energy density. Interestingly, the energy density of the polymer film strongly depends on the solvent used during film formation. Tetrahydrofuran (THF) and dichloromethane (DCM) are selected as

excellent solvents for polymer film formation, since good solvents promote polymer chain extension and facilitate strong polymer-polymer interactions. In addition, their low boiling points enable solvent removal at mild temperature, preventing thermal back-isomerization and thus preserving the isomer ratio. Film processed from DCM display an energy density of 110 $kJ.kg^{-1}$, whereas those processed from THF reach 510 $kJ.kg^{-1}$. A similar trend is observed for the solid state back-isomerization kinetics, with $t_{1/2}$ of 49 h (DCM) and 75 h (THF) at R.T. This behavior is attributed to differences in solvation of the dipole formed in the *Z*-isomer. DCM preferentially interacts with the polymer backbone, leaving the dipole poorly solvated. This promotes polymer aggregation, resulting in compact interchain packing with insufficient free volume for π-stacking between AB units. Consequently, cooperative isomerization is hindered, lowering the energy density. In contrast, THF favorably interacts with the dipole, reducing aggregation, increasing the free volume and enabling better oriented π-stacking. By using an optimized DCM/THF mixture, the authors created a film with an energy density of 700 $kJ.kg^{-1}$, illustrating how solvent choice can tune intermolecular interactions and MOST properties.[46,226]

The third example focuses on a copolymer bearing AB and benzoic acid side chains (**Figure 32c**). Under basic conditions, the benzoic acid groups deprotonate, yielding a charged polymer that can be electrodeposited onto conductive substrates such as metal bars or wire meshes. This strategy produces conformal coatings that enable efficient heat transfer from polymer MOST film to the underlying metallic components. Upon irradiation, *E* → *Z* photoisomerization take place, with saturation beginning to appear after 30 min. The PSS is reached after 4 h with a conversion ratio of 43 %. Within the film, the *Z*-isomer displays a $t_{1/2}$ of 75 h, and DSC measurement reveals an energy density of 90 $kJ.kg^{-1}$. The stored energy can be rapidly released as heat through *Z* to *E* isomerization within ten seconds, demonstrating fast and efficient heat output on demand. This work highlights electrodeposition as a powerful approach for integrating AB-polymer-based MOST into diverse solid-state applications without major sacrifice of performance. Nonetheless, challenges remain, particularly the formation of cracks or deformities in thicker film due to shrinkage upon drying. Future research may

therefore focus on designing high molecular weight AB-containing polymers or incorporating suitable binders to improve the mechanical stability while preserving energy storage capacity.[42,227]

Taken together, these three examples highlight the versatility and potential of polymer-templated AB as MOST system. By carefully tuning the monomer structure and the polymer backbone, it is possible to enhance key parameters such as energy density, light absorption efficiency and photoisomerization. Nevertheless, these systems typically exhibit lower energy densities and storage times compared to CNTs or RGO templates. Despite these limitations, their straightforward integration into existing heating devices renders them highly promising candidates for the development of next generation polymer-based MOST systems.[46,225]

Despite considerable research efforts and numerous advances aimed at improving the MOST properties of AB, identifying an optimal candidate that simultaneously satisfies all criteria for an ideal MOST system remains highly challenging. As illustrated by examples discussed above, enhancing one parameter is often achieved at the expense of another. For instance, chemical modifications that induce bathochromic shift in absorption are typically accompanied by reductions in energy density or storage time.[115] Similarly, in the case of template strategy, simultaneously improvements in $t_{1/2}$ and $\Delta H_{storage}$ are frequently counterbalanced by persistence of the main absorption band in the UV region.[149] As a result, only modest PSS values are achieved under sunlight irradiation, since most reported Z-rich PSS rely on artificial laser sources with well-defined wavelength. Nevertheless, a promising direction lies in combining complementary strategy, such as heteroaryl modification with templating methods to design new AB derivatives with enhanced properties. In this context, one of the central objective of the present research is to explored and understand the use of peptoids as an original template to support heteroaryl-AB.

4. WHO YOU GONNA CALL? PEPTOIDS!

Peptoids are fully synthetic, sequence-defined polyamides. As illustrated in **Figure 33**, the primary structure of these N-substituted glycine oligomers differs from peptides by the position of the side chains, which are attached to the nitrogen atom of the amide bond instead of the α-carbon atom. As a result, intramolecular hydrogen bonds between amide moieties are prevented and the absence of stereocenter makes the backbone achiral. Consequently, the structure and functional properties of peptoids are governed primarily by the chemistry of the side chains and the monomer sequence.[228–230] The amide bonds can adopt either a cis or trans conformation, owing to the increased backbone flexibility that results from the absence of H-bond. By contrast, peptides predominantly adopt the trans conformation in order to maximize stabilizing H-bond interactions. The lack of such interactions in peptoids lowers the isomerization barrier of the amide bond rotation, thereby facilitating free rotation and inducing an equilibrium between the two conformations. Nevertheless, this equilibrium can be biased toward one conformation or the other through an appropriate choice of side chains.[231,232]

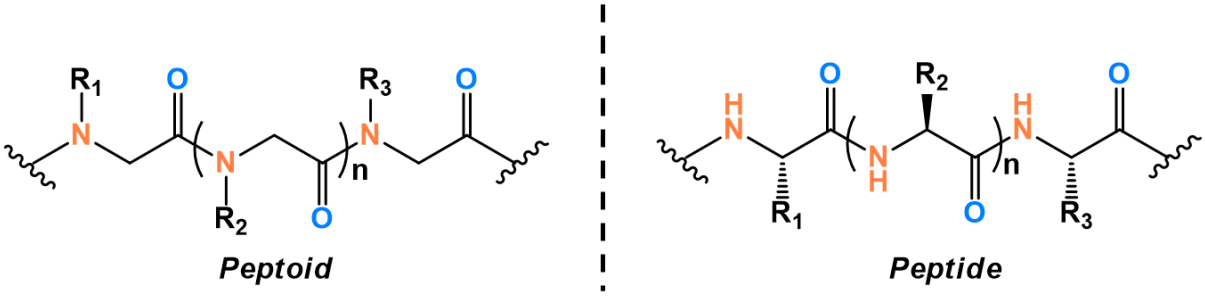

Figure 33. *Structural distinction between peptoid and peptide primary structures.*

Several methods exist for the synthesis of peptoids, which can be achieved either by polymerization or via a step-by-step approach in solution or on solid support. The ring-opening polymerization method is particularly useful when long peptoids chains are required, since the entire polymer can be obtained in a single step. However, this strategy does not allow precise sequence control and results in a broad distribution of polymers with different degrees of polymerization (DP).[233–235] Such heterogeneity is not ideal for MOST investigation since well-defined molecules with unique composition are essential for accurate characterization of

photochemical and thermal properties. To overcome this limitation, step-by-step synthesis is preferred, as it allows the preparation of shorter peptoids with excellent control over the sequence. Among these approaches, solid-support synthesis, inspired by peptide synthesis, offers a clear advantages over solution synthesis, since the latter requires laborious purification steps between each monomer addition.[236,237] Solid-phase peptoid synthesis, first developed by Zuckermann *et al.* in 1992, enables the unit-by-unit assembly of peptoids, yielding tailor-made structures in which each residue can bear a different side chain. This method ensures not only precise sequence control but also accurate control over molecular size, with theoretical dispersity approaching 1.[238,239] Further details on the synthetic procedures employed in this work will be presented in the **Experimental Section**.

5. A GAME OF STRUCTURE

5.1.1 Chain spotting

The primary structure of a peptoid corresponds to its sequence, as defined by the consecutive covalent attachment of the monomer units. To describe this structure, a specific nomenclature adapted to peptoids is required. First, it is necessary to distinguish the two termini of the chain: the N-terminus (Nter) composed of a secondary amine and the C-terminus (Cter) which ends with an amide group (**Figure 34**). Since the peptoid units are exclusively distinguished based on the side chain attached to the nitrogen atom, this feature is used to describe the sequence, written from Nter to Cter. Each unit is denoted N*x*, where N indicates that the side chain is located on the nitrogen atom and *x* is the abbreviation of the side chan. For example, the peptoid illustrated in **Figure 34** contains one unit of (*S*)-phenylethyl (spe) side chain followed by two units bearing tert-butyl (tbu) groups. Its sequence is therefore written as N*spe*N*tbu*N*tbu*. The primary structure of peptoids can be identified by analytical methods such as nuclear magnetic resonance (NMR) or mass spectrometry (MS), which will be discussed in detail later in this manuscript.

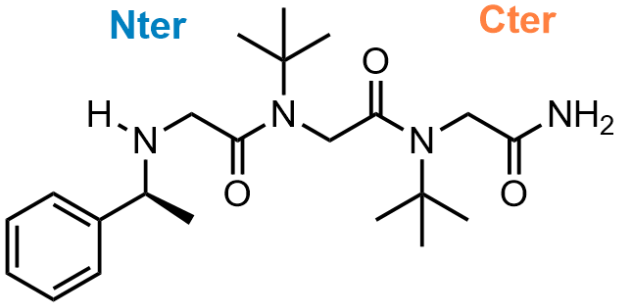

Figure 34. *Primary structure of NspeNtbuNtbu, as presented from Nter to Cter.*

5.1.2 A fold odyssey

The interest of peptoids in the MOST field lies in the fact that they belong to the class of foldamers, meaning they can adopt well-defined secondary structures in solution. Their peptide analogues are well known to form α-helices or β-sheets, stabilized by H-bond networks mediated by trans conformation of their amide bonds.[228,229] In contrast, peptoids lack these backbone H-bond and their folding relies on other stabilizing interactions, such as van der Waals interactions (VDW).[239] An additional structural feature is the cis/trans conformational equilibrium of their amide bonds, which can be tuned by the selection of the side chain(s). Although only a few side chains allow for precise conformational control, they can strongly bias the equilibrium. For examples, the tert-butyl side chain predominantly induces the cis conformation regardless of the solvent (**Figure 35d**), due to steric hindrance that destabilizes the trans from.[240] Conversely, aryl side chains favor the trans conformation (**Figure 35a**), since π-electron repulsion between the aromatic ring and the carbonyl lone pair destabilizes the cis form.[241] However, in most cases, a mixture of cis and trans conformations is detected (**Figure 35b** and **c**), with the trans/cis ratio being also influenced by the solvent.[242,243] Depending on the side chain effect on the amide bond conformations all along the peptoid backbone, peptoids can adopt highly ordered secondary structures through a proper design of their primary sequence and monomer composition. As illustrated in **Figure 36**, the most common conformations are helices and loops, while ribbons or β-sheets are observed less frequently.[239] These structures have been experimentally confirmed using circular dichroism (CD), NMR and in some cases X-ray diffraction.[229,239,244]

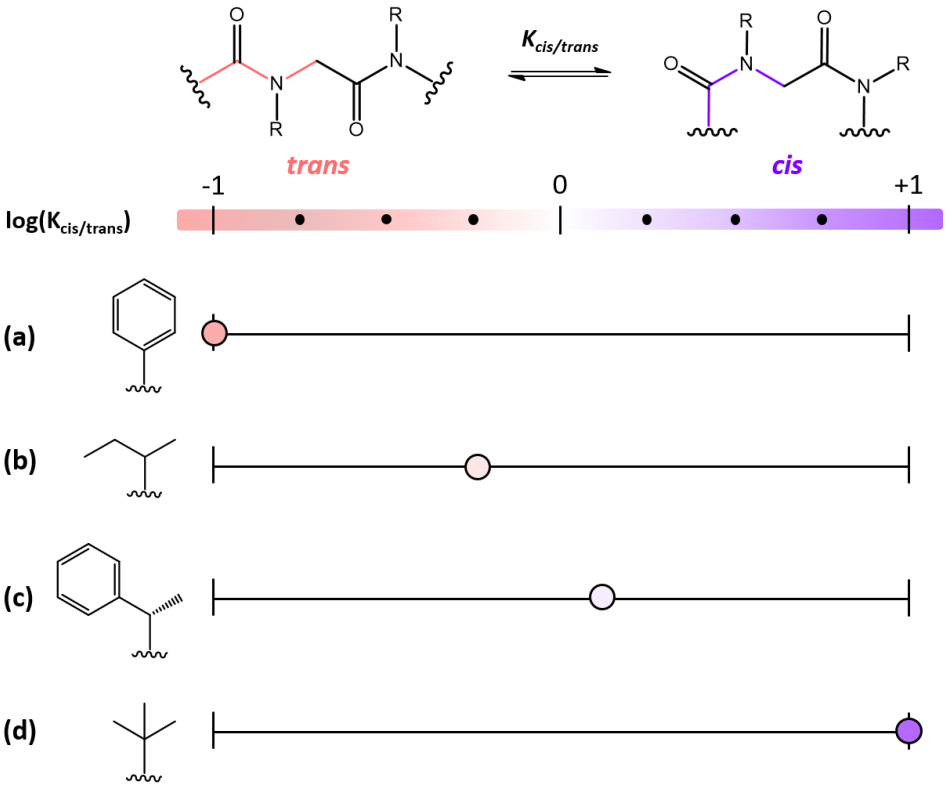

Figure 35. *Representation of the cis/trans ratio through the equilibrium ($K_{cis/trans}$) illustrating the conformational switch between cis and trans amide bonds, measured by NMR in CD_3OD at R.T. the effect of the different side chains is shown: a) N-aryl*[241]*, b) sec-butyl*[243]*, c) (S)-phenylethyl*[243] *and d) tert-butyl*[240]*. Adapted from*[245].

The helical structure in peptoids arises when sterically hindered aromatic side chains are present (**Figure 36a**). Introducing a stereogenic center at the α-position of the nitrogen directs the handedness of the helix: S-configuration leads to a right-handed helix, whereas R-configuration favors a left handed helix. This conformation has been investigated and characterized by techniques such as 2D-NMR, CD, molecular modeling or ion mobility mass spectrometry (IM-MS).[239,246–248] A typical helix-inducing moiety is the S-phenylethyl side chain, which enforces conformational restriction of the amide bonds. Notably, the helical arrangement emerges when 50 % of the side chains are chiral aromatics, generating sufficient steric strain to stabilize the helix. The resulting structure exhibits a pitch of 6.7 Å with three residues per turn, closely resembling a polyproline type I helix.[237,239] To achieve helix formation, a minimum of five monomer units is required in solution and the formatted helix is remarkably robust, showing persistence under severe denaturing conditions such as 8 M urea and elevated

temperature up to 75 °C.[249,250] Other secondary structures including loops, ribbons and β-sheets can also be accessed depending on the sequence and side chain design (**Figure 36b-d**). Interestingly, recent studies have shown that even very short oligomers (dimers or trimers) bearing benzyl side chains can adopt a degree of order, suggesting that structural organization in peptoids may arise earlier than previously discussed.[251]

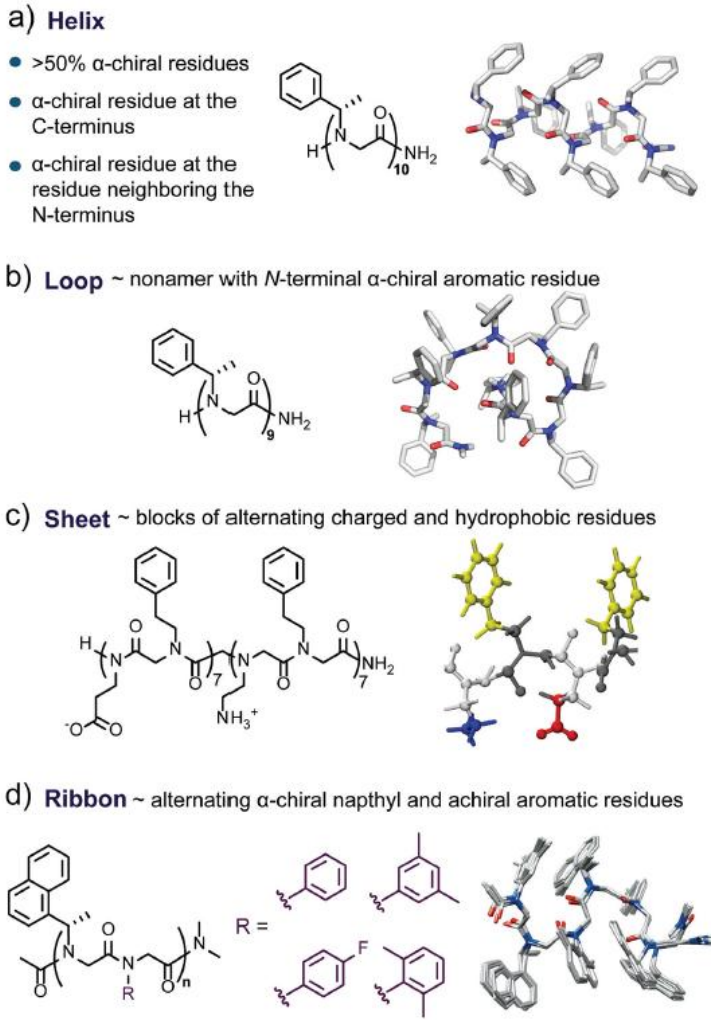

Figure 36.*Secondary structures adopted by peptoids as a function of the sequence and monomer composition: a) helix, b) loop, c) β-sheets and d) ribbon. Figure adapted from*[239]*.*

In summary, exploiting the secondary structure of peptoid molecules as templates for AB represents an elegant strategy to modulate and enhance the MOST properties of the chromophore by tuning the different energy levels of the different isomers through intermolecular interaction.

5.2 LEGEND OF PEPTOID: A LINK TO AZOBENZENE

Due to their structural similarity to peptides, high diversity and notable stability, peptoids find broad applications, *e.g.* in biology, pharmacy, medicine, and catalysis. These properties also make them promising candidates as templates for AB in the MOST field. Their chemical and thermal stabilities support the cyclability of MOST systems, a key requirement for repeated cycles of solar energy storage and heat release. Additionally, if each peptoid unit carries an AB moiety, the peptoid backbone, based on the (N-CH_2-C(=O)-) unit, marginally contributes (56 u per residue) to the overall gravimetric energy density. This is significantly lower than other templates such as CNTs or RGO, where the template accounts for a by far larger mass fraction. The step-by-step solid-phase synthesis of peptoids allows for the creation of tailor-made sequences, opening numerous possibilities for molecular engineering. For instance, different chromophores could be introduced toward a broad solar spectral coverage, H-bonding substituents could also be incorporated for stabilizing the secondary structures, cyclic peptoids are also nowadays tested in our group to exploit cyclic strain effects. Peptoids are soluble in common organic solvents and can be engineered for water solubility, a significant advantage for MOST fluid applications, such as the systems illustrated in **Figure 4**. Finally, the rigid amide backbone together with the stable secondary structures may impart to MOST-based peptoids a templating effect on AB, promoting a highly ordered arrangement. This ordered structure could facilitate interactions between chromophores, potentially modifying the MOST properties.

Based on previous reports and hypotheses discussed above, peptoids show significant potential as templates for AB. To our knowledge, except research already published by our laboratory, peptoid-templated AB structure have not yet been reported in the MOST field. In fact only one paper by Kirshenbaum *et al.* in 2008 reports on AB-anchored peptoids.[241] This work examined whether the grafted AB chromophores could undergo photoisomerization without perturbating the backbone conformation. They investigated peptoids of various lengths, from trimers to heptamers, with a maximum of one AB unit per molecule. The study

concluded that *E* → *Z* and *Z* → *E* photoisomerization are not hindered by the peptoid backbone and that the absorption spectra remain comparable to pristine AB without any shift in the π-π* transition. Interestingly, CD measurements revealed the presence of helical structures for the pentamers and heptamers even upon photoisomerization. Moreover, the $t_{1/2}$ of the metastable isomer is shown to be modulated based on the length of the peptoid backbone. Although this study do not directly address MOST systems, it provides a solid foundation for using peptoids as AB supports to modulate MOST properties.[241]

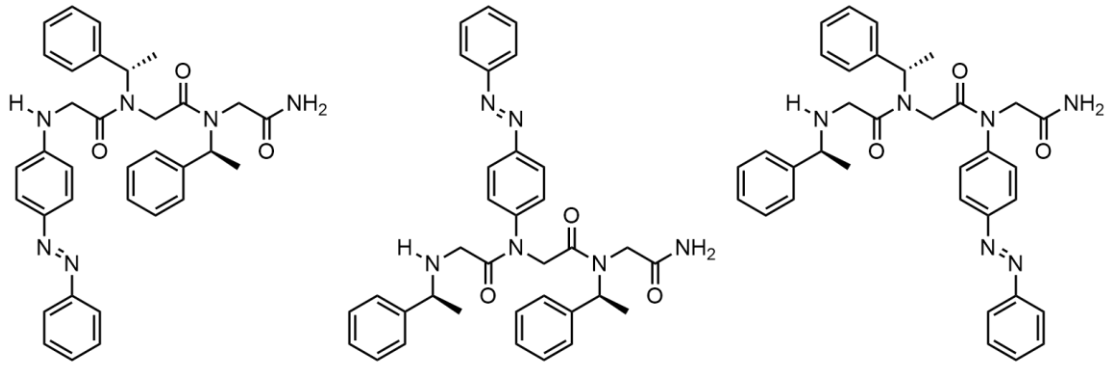

	Nter-AB	Center-AB	Cter-AB
π-π*	391 nm	325 nm	325 nm
$t_{1/2}$	~ms	12 h	14 days
ΔH	n.a	32.2 kJ.mol^{-1}	46.9 kJ.mol^{-1}

Figure 37. *Representation of the structural and principal MOST properties for the three peptoid trimers named Nter-AB for NazoNspeNspe, Center-AB for NspeNazoNspe and Cter-AB for NspeNspeNazo. All the properties were measured in MeOH HPLC at 20 °C. Data from*[114]*.*

In our laboratory, Benjamin Tassignon published a study on three peptoids trimers, each carrying a single AB moiety at different positions, in order to evaluate the influence of the position on the key MOST properties.[114] The three derivatives, referred to as Nter-AB, Center-AB and Cter-AB, are named according to the position of the AB unit on the peptoid backbone (**Figure 37**). The data reveal pronounced site selectivity in terms of MOST behaviors, with the metastable isomer $t_{1/2}$ being the most strongly affected parameter. For Nter-AB, the *Z*-isomer could not be detected, most likely due to an extremely short $t_{1/2}$, which can be attributed to the secondary amine nature of the nitrogen atom bearing the AB residue. In contrast, Cter-AB and

Center-AB display markedly different $t_{1/2}$ of 14 days and 12 h, respectively. These results highlight the importance of the positions on peptoid to design efficient MOST systems. Notably, the exceptionally long $t_{1/2}$ of 14 days for the Cter-AB exceeds that of pristine AB, opening new perspectives for MOST development. In terms of energy storage, Center-AB show a slight decrease compared to pristine AB, whereas Cter-AB maintained storage energy values close to those of unmodified AB. Other MOST characteristics, such as λ_{max} and molar absorptivity are only marginally affected by peptoid incorporation.[114] While these derivatives are not yet optimal MOST candidates, the observed site selectivity imparted by the peptoid backbone paves the way for further studies, such as the incorporation of AB derivatives capable of reaching absorption into the visible region, *e.g.* heteroaryl-AB, which is the central aim of this thesis.

Part 2 - Objectives of the thesis

Objectives of the thesis

Solar energy is increasingly recognized as one of the most promising alternatives to fossil fuels, providing a clean and sustainable power source. Nevertheless, its intermittent availability requires the development of efficient storage and controlled release systems to enable large-scale applications. MOST systems address this challenge by using molecular switches capable of light-induced isomerization into metastable states, thereby storing solar energy in chemical bond for later release. When energy is required, the photoisomer thermally or catalytically reverts to its stable form, releasing the stored energy as heat. The crucial parameters for these systems are listed as followed:

- high gravimetric energy density ;
- absorption in visible for the stable isomer ;
- separated UV-vis spectra for both isomers ;
- quantum yield of photoisomerization close to 1 ;
- thermal stability compatible with solar energy storage ;
- control of energy release ;
- high cyclability ;
- easy to synthesize, cost effective and non-toxic .

Among the various photoswitching systems, AB derivatives, undergoing reversible *E* → *Z* photoisomerization, are among the most extensively studied due to their versatile synthesis, high cyclability and tunable photophysical properties which could allow meeting several properties necessary toward efficient MOST systems by molecular design and organic synthesis. Indeed, they suffer from a low energy storage and strong absorption in the UV region, where both isomers absorption overlap. This overlap leads to an unfavorable photostationary state that limits the overall storage efficiency. To overcome these drawbacks, two strategies will be explored in this thesis as exposed in **Figure 38**: (i) replacing one phenyl

ring with a thiazolyl moiety to redshift the absorption into the visible region, and (ii) grafting AB units at specific positions onto a peptoid backbone to enhance energy storage and sustain the *Z*-isomer half-life time through cooperative effects. By these two strategies, the idea is to improve the properties of AB in the idea to store solar energy.

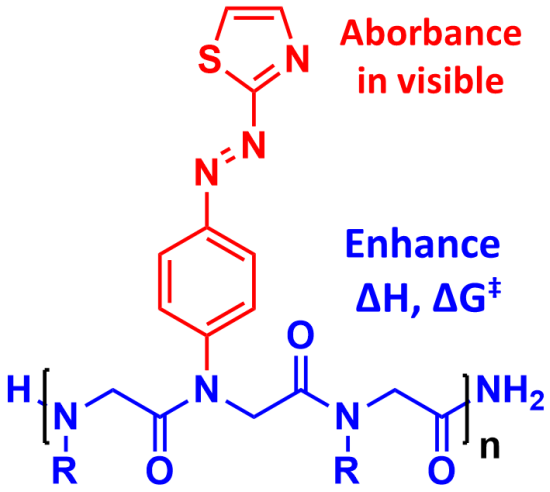

***Figure 38**. Schematic representation of the target peptoids in which the incorporation of thiazolyl units promotes absorption in the visible region, while the peptoid framework contributes to increased energy storage and improved thermal stability.*

The first part of this thesis focuses on the synthesis and structural characterization of various PAT derivatives, employing advanced techniques such as mass spectrometry, nuclear magnetic resonance, and infrared spectroscopy. A significant portion of this section is devoted to evaluating the MOST-relevant properties of these molecular systems, which will serve as foundation for a comparative analysis between monomeric PAT derivatives and their corresponding peptoid forms. Key parameters such as λ_{max}, $\varepsilon_{\lambda max}$, $\Delta H^{\ddagger}$, $\Delta S^{\ddagger}$, $t_{1/2}$ and the percentage of *Z*-isomers at the PSS, when measurable, will be determined. Additionally, this chapter will explore the effects of molecular substitution on these properties, with the goal of identifying the structure-property relationships that could guide the design of more efficient MOST systems.

The second part of this study focuses on the synthesis and characterization of PAT-based peptoids with structural characterization using essentially advanced mass spectrometry

techniques. Alongside, all key MOST properties will be determined for all synthetized peptoids. To design and optimize efficient MOST systems, a series of peptoids with varying architectures will be synthetized. In the first step, three trimeric peptoids incorporating unsubstituted PAT unit and spe residues, varying by the PAT position, will be prepared as reference systems due to their simple structures. Subsequently, substituted-PAT peptoids will be synthetized to further investigate and validate the trends observed for the non-grafted PAT derivatives. A 4-unit peptoid will also be synthetized to explore the influence of chain length on MOST properties. Finally, the effect of the side-chain variation will be examined by incorporating sarcosine and spe residues, allowing for an assessment of how local chemical environments impact the observed photophysical and thermal properties. Beyond conventional MOST parameters, a depth kinetic analysis of the thermal back-isomerization will be performed using LC-MS, enabling the extraction of activation parameters ($\Delta H^{\ddagger}$ and $\Delta S^{\ddagger}$). These data provide critical insight into the underlying mechanisms of thermal back-isomerization and how they are modulated by molecular structure and environment.

The third part of this thesis will focus on the influence of the solvent, which acts as the calorific medium in MOST systems and is expected to play a crucial role in the thermal back-isomerization process. The kinetics of this process will be systematically investigated in a range of solvents to identify potential trends related to solvent polarity and proticity. Subsequently, the study will be narrowed down to four representative solvents, *i.e.* H_2O, MeOH, ACN and toluene, which span a broad range of solvents polarities. Among these, toluene and H_2O define the apolar and polar extremes, respectively, while MeOH and ACN possess comparable polarities but differ in their protic versus aprotic character. The kinetic parameters ($\Delta H^{\ddagger}$ and $\Delta S^{\ddagger}$) will be determined for each solvent, allowing for a detailed comparison and potential correlation between solvent properties and the mechanistic pathway of the thermal back-isomerization. This analysis is intended to clarify how the solvent environment governs the thermal-back-isomerization mechanism in PAT-based MOST systems.

The fourth and final part of this thesis will concern the catalytic activation of the thermal back-isomerization, an essential aspect for achieving controlled and rapid heat release in MOST systems. Since the thermal back-isomerization process typically leads to a progressive release of heat governed by the system $t_{1/2}$, an effective strategy to induce instantaneous energy release involves the use of a catalyst that promotes the *Z* → *E* isomerization. In this context, formic acid will be employed as a catalytic agent to investigate its effect on the back-isomerization kinetics in the four previously studied solvents, allowing comparison of catalytic efficiency across different solvent environments.

Beyond proposing new AB derivatives and peptoid-based templates, this work also aims to highlight the potential of mass spectrometry, a technique not commonly used in the MOST field, as a powerful analytical tool for characterization photoactive systems. By coupling liquid chromatography with mass spectrometry, it becomes possible to separate and individually analyze *E*- and *Z*-isomers, providing quantitative access to key MOST parameters. Moreover, this approach offers a straightforward tool to determine deeper kinetic insights, including activation parameters and reaction mechanisms.

Finally, the comparative analysis of the various peptoid architectures and PAT derivatives will allow the assessment of peptoid backbones as support for enhancing the MOST properties of AB-based chromophores. These findings are expected to pave the way for future developments of hybrid peptoid-AB based systems with optimized energy storage and release characteristics.

Part 3 – Experimental section

Experimental section

All reactants and solvents mentioned in this chapter are commercially available (VWR Chemicals, Chem-Lab, Alfa Aesar, Merck).

The synthesis of azobenzene derivatives via diazonium salt intermediates presents substantial experimental risks, largely due to the inherent instability of these highly reactive species. Aromatic diazonium salts exhibit pronounced thermal sensitivity and a marked propensity for violent decomposition, which is typically accompanied by rapid nitrogen evolution and the generation of highly reactive intermediates. This intrinsic instability, together with the use of toxic and corrosive reagents and the potential formation of hazardous gaseous by-products, requires rigorous control of experimental conditions and the implementation of strict safety protocols, including maintaining reaction temperatures below 0 °C, slow and controlled reagent addition, and conducting all operations within a properly functioning fume hood.

More broadly, the experimental work described in this thesis involves the handling of chemical substances associated with a wide range of intrinsic hazards, including acute and chronic toxicity, corrosivity, flammability, chemical reactivity, and thermal instability. Several experimental procedures involve energetically unstable intermediates, reactive functional groups, and exothermic transformations that may result in uncontrolled heat release, pressure buildup, and hazardous gas evolution. Furthermore, the combination of incompatible reagents, the presence of impurities, or deviations from controlled operating conditions can significantly increase the likelihood of adverse events. Consequently, all experimental activities were conducted under strictly controlled conditions, supported by systematic risk assessment, continuous monitoring of critical parameters, and full compliance with institutional safety regulations, including the mandatory use of appropriate personal protective equipment and adherence to established chemical hygiene practices.

1. HOW I SYNTHESIZED YOUR PHENYLAZOTHIAZOLES

1.1 SYNTHESIS OF SODIUM (PHENYLAMINO)METHANESULFONATE DERIVATIVES

Both sodium (phenylamino)methanesulfonate derivatives were synthesized following the procedure described in section 1.1.1 inspired from synthesis elaborated by Grewal *et al.*[252] Their structures were confirmed by combination of characterization techniques, including ^{1}H NMR spectroscopy, melting point determination, IR spectroscopy and mass spectrometry.

1.1.1 Synthesis of sodium (phenylamino)methanesulfonate (An-prot)

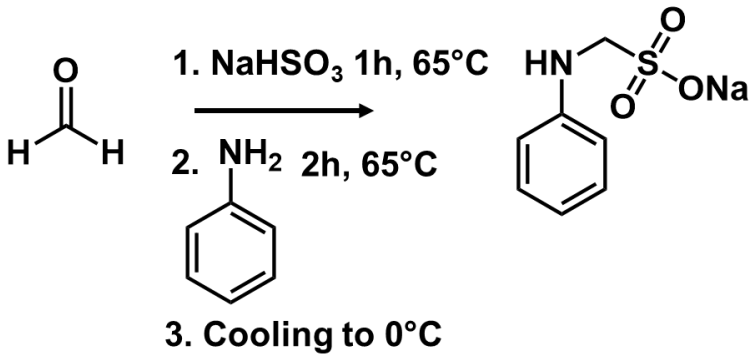

Scheme 1. *Synthesis of An-prot from sodium bisulfite, formaldehyde and aniline.*

A solution of formaldehyde (0.2 mol) in distilled water (80 mL) was prepared, and sodium bisulfite (0.2 mol) was added while stirring. The mixture was heated to 65 °C for 1 hour. Aniline (0.16 mol) was then added dropwise over 15 min to the mixture, which was stirred for an additional 2 hours at 65 °C. After cooling the reaction mixture to approximately 0 °C, a white crystalline solid formed, which was filtered, dried, and used directly in the next step with any further purification. Yield ~ 80%. **m.p.** > 400 °C. ^{1}H-**NMR** (500 MHz, D_2O) : 7.21 ppm (t, 2H), 6.84 ppm (d, 2H), 6.77 ppm (t, 1H), 4.36 ppm (s, 2H). **IR**: 3316 cm^{-1} (stretching N-H), 1601 cm^{-1} (stretching C=C) . **ESI-MS** (-) : *m/z* 186 ($C_7H_8NO_3SNa$).

1.1.2 Synthesis of sodium ((3,5-difluorophenyl)amino)methanesulfonate (F-prot)

Yield ~ 80 %. **m.p.** > 400 °C. 1H-**NMR** (500 MHz, D2O) : 6.46-6.48 ppm (dd, 2H), 6.32-6.36 ppm (tt, 1H), 4.42 ppm (s, 2H). **IR**: 3350 cm^{-1} (stretching N-H), 1597 cm^{-1} (stretching C=C), 1042 cm^{-1} (stretching C-F). **ESI-MS** (-) : m/z 222 ($C_7H_6NO_3F_2S$).

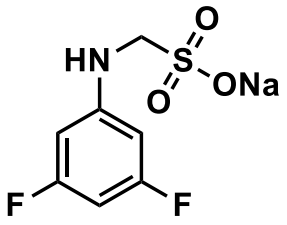

1.2 SYNTHESIS OF AMINO-PHENYLAZOTHIAZOLE DERIVATIVES

Amino-phenylazothiazole (NH_2-PAT) derivatives were synthesized according the procedure inspired by Grewal *et al.* and described in the following sections, with minor adaptations depending on the specific amino-thiazole substituents.[252] For the fluorinated derivatives, the volume of the F-prot solution was adjusted due to higher solubility in MeOH. Concerning the aminobenzothiazole, the compound displayed a very poor solubility in sulfuric acid. Therefore, a mixture of sulfuric acid, acetic acid and water in equal proportions was employed to improve solubility. The structures of the obtained ABs were confirmed by combination of characterization techniques, including ^{1}H NMR spectroscopy, melting point determination, IR spectroscopy and mass spectrometry.

1.2.1 Synthesis of (*E*)-4-(thiazol-2-yldiazenyl)aniline (PAT 1)

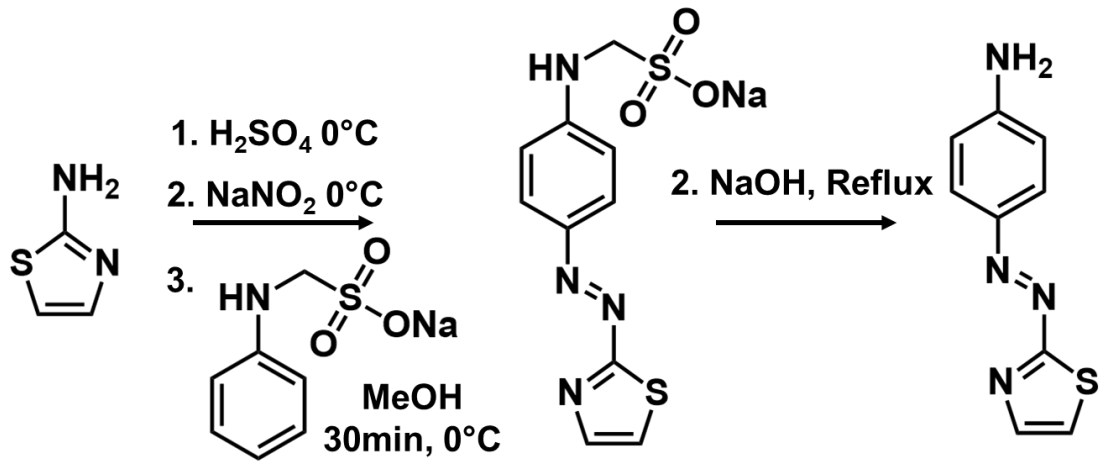

Scheme 2. *Synthesis of PAT 1 from 2-aminothiazole, sodium nitrite and An-prot.*

2-aminothiazole (2.12 g, 21.2 mmol) was dissolved in 80 mL of 50% aqueous sulfuric acid and cooled to 0 °C. Sodium nitrite (1.46 g, 21.2 mmol) was then added slowly, ensuring the temperature remained below 5 °C. After stirring for approximately 45 min, a suspension of An-prot (8.86 g, 42.4 mmol) in 120 mL of cold methanol was added dropwise while maintaining the internal temperature below 5 °C. Following the addition, the reaction mixture was allowed to warm to room temperature, and 80 mL of isopropanol were added dropwise. The resulting precipitate was filtered to yield in a wet dark blue crystals corresponding to the protected PAT 1. These crystals were dissolved in aqueous sodium hydroxide (2 M) and refluxed for 2 hours. After cooling to room temperature, a red solid product was filtered, washed with water, and dried. Yield ~ 75 %. **m.p.** = 190 °C. ^{1}H-**NMR** (500 MHz, $CDCl_3$) : 7.94-7.93 ppm (d,1H), 7.89-7.88 ppm (d, 2H), 7.30-7.29 ppm (d, 1H), 6.74-6.72 ppm (d, 2H), 4.3 ppm (s, 2H). **IR**: 3316-3204 cm^{-1} (stretching N-H), 3077 cm^{-1} (stretching C-H), 1597 cm^{-1} (stretching C=C). **EI-MS** : $C_9H_8N_4S$ m/z 204,0470 (0 ppm). ESI-MS (+) $[M+H]^+$: $C_9H_9N_4S$ *m/z* 205.0550 (1.0 ppm).

1.2.2 (*E*)-4-((5-methylthiazol-2-yl)diazenyl)aniline (PAT 2)

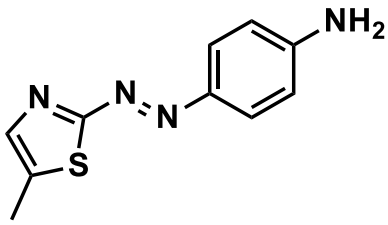

Yield ~ 65 %. **m.p.** = 229 °C. ^{1}H-**NMR** (500 MHz, $CDCl_3$) : 7.86-7.84 ppm (d, 2H), 7.61 ppm (s, 1H), 6.71-6.72 ppm (d, 2H), 4.23 (s, 1H), 2.50 (s, 3H) **IR** : 3319-3202 cm^{-1} (stretching N-H), 1595 cm^{-1} (stretching C=C). **EI-MS**: $C_{10}H_{10}N_4S$ m/z 218,0626 (0.5 ppm). **ESI-MS** (+) $[M+H]^+$: $C_{10}H_{11}N_4S$ *m/z* 219.0707 (1.4 ppm).

1.2.3 (*E*)-4-((4-methylthiazol-2-yl)diazenyl)aniline (PAT 3)

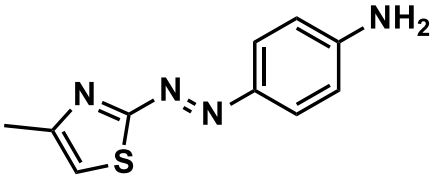

Yield ~ 65 %. **m.p.** = 193 °C. ^{1}H-**NMR** (500 MHz, $CDCl_3$) : 7.87-7.86 ppm (d, 2H), 6.87 ppm (s, 1H), 6.71-6.72 ppm (d, 2H), 4.27 (s, 1H), 2.52 (s, 3H). **IR** : 3316-3196 cm^{-1} (stretching N-H), 1594 cm^{-1} (stretching C=C). **EI-MS** : $C_{10}H_{10}N_4S$ m/z 218,0626 (0.5 ppm). **ESI-MS** (+) $[M+H]^+$: $C_{10}H_{11}N_4S$ *m/z* 219.0704 (0.0 ppm).

1.2.4 Synthesis of (*E*)-3,5-difluoro-4-(thiazol-2-yldiazenyl)aniline (PAT 4)

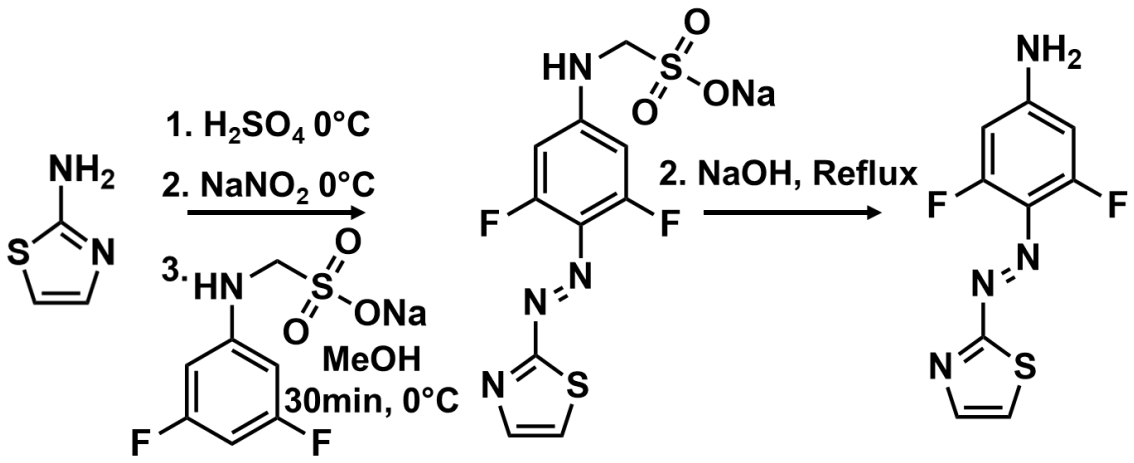

Scheme 3. *Synthesis of PAT 4 from 2-aminothiazole, sodium nitrite and F-prot.*

2-aminothiazole (2.12 g, 21.2 mmol) was dissolved in 80 mL of 50% aqueous sulfuric acid and cooled to 0 °C. Sodium nitrite (1.46 g, 21.2 mmol) was then added slowly, ensuring the temperature remained below 5 °C. After stirring for approximately 45 min, a solution of F-prot (7.8 g, 31.8 mmol) in 80 mL of cold methanol was added dropwise while maintaining the internal temperature below 5 °C. Following the addition, the reaction mixture was allowed to warm to room temperature, and 80 mL of isopropanol were added dropwise. The resulting precipitate was filtered to yield in a wet dark blue crystals corresponding to the protected PAT 4. These crystals were dissolved in aqueous sodium hydroxide (2 M) and refluxed for 2 hours. After cooling to room temperature, a red solid product was filtered, washed with water, and dried. Yield ~ 75 %. **m.p.** = 209 °C. ^{1}H-**NMR** (500 MHz, $CDCl_3$) : 7.97-7.96 ppm (d,1H), 7.34-7.33 ppm (d, 1H), 6.3-6.27 ppm (d, 2H), 4.47 ppm (s, 2H). **IR** : 3352-3208 cm^{-1} (stretching N-H), 1635 cm^{-1} (stretching C=C), 1042 cm^{-1} (stretching C-F). **ESI-MS** (+) $[M+H]^+$: $C_9H_7N_4SF_2$ m/z 241,0359 (0 ppm).

1.2.5 Synthesis of (*E*)-4-(benzothiazol-2-yldiazenyl)aniline (PAT 5)

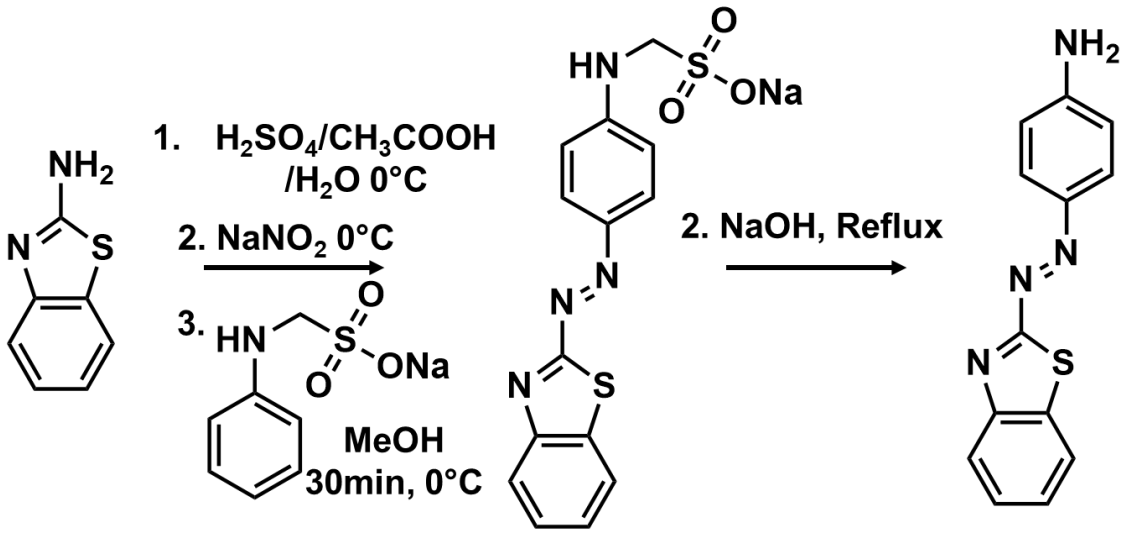

Scheme 4. *Synthesis of PAT 5 from 2-aminobenzothiazole, sodium nitrite and An-prot.*

2-aminobenzothiazole (3.18 g, 21.2 mmol) was dissolved in 90 mL of a mixture of sulfuric acid, acetic acid and water (1:1:1) and cooled to 0 °C. Sodium nitrite (1.46 g, 21.2 mmol) was then added slowly, ensuring the temperature remained below 5 °C. After stirring for approximately 45 min, a suspension of An-prot (8.86 g, 42.4 mmol) in 120 mL of cold methanol was added dropwise while maintaining the internal temperature below 5 °C. Following the addition, the reaction mixture was allowed to warm to room temperature, and 80 mL of isopropanol were added dropwise. The resulting precipitate was filtered to yield wet crystals corresponding to the protected PAT 5. These crystals were dissolved in aqueous sodium hydroxide (2 M) and refluxed for 2 hours. After cooling to room temperature, a red solid product was filtered, washed with water, and dried. Yield ~ 55 %. **m.p.** = 237 °C. ^{1}H-**NMR** (500 MHz, $CDCl_3$) : 8.11-8.09 ppm (d,1H), 7.96-7.94 ppm (d, 2H), 7.86-7.84 (d, 1H), 7.50-7.47 ppm (t, 1H), 7.42-7.39 ppm (t, 1H), 6.75-6.73 (d, 2H), 4.30 ppm (s, 2H). **IR** : 3314-3178 cm^{-1} (stretching N-H), 1598 cm^{-1} (stretching C=C). **ESI-MS** (+) $[M+H]^+$: $C_{13}H_{11}N_4S$ *m/z* 255.0700 (1.6 ppm).

1.3 Synthesis of acetamido-phenylazothiazole derivatives

Acetamido-phenylazothiazole (Ac-PAT) derivatives were synthesized form the corresponding amino-ABs according to the procedure described in the section 1.3.1. The structures of the

resulting ABs were confirmed by combination of characterization techniques, including ^{1}H NMR spectroscopy, melting point determination, IR spectroscopy and mass spectrometry.

1.3.1 Synthesis of (*E*)-N-(4-(thiazol-2-yldiazenyl)phenyl)acetamide (Ac-PAT 1)

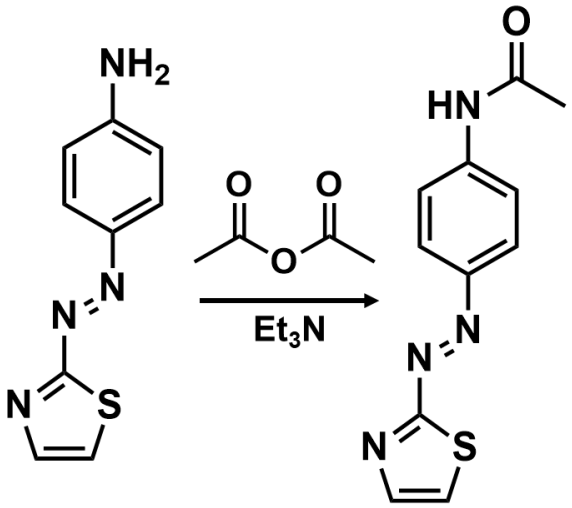

Scheme 5. *Synthesis of Ac-PAT 1 from PAT-1 and acetic anhydride.*

PAT 1 (1 g, 5 mmol) was dissolved in 20 mL of acetic anhydride, and triethylamine (1 mL) was added. The mixture was stirred overnight at R.T. The resulting orange solid was filtered and washed with water. Yield ~ 80 %. **m.p.** = 219 °C. **^{1}H-NMR** (500 MHz, $CDCl_3$) : 8.03-8.02 ppm (d, 1H), 8.01-7.99 ppm (d, 2H), 7.72-7.71 ppm (d, 2H), 7,56 ppm (s, 1H), 7.41-7.40 ppm (d, 1H), 2.25 ppm (s, 3H). **IR**: 3248 cm^{-1} (stretching N-H), 3099 cm^{-1} (stretching C-H), 1672 cm^{-1} (stretching C=O). **EI-MS**: $C_{11}H_{10}N_4OS$ m/z 246,0568 (2,8 ppm). ESI-MS (+) $[M+H]^+$: $C_{11}H_{11}N_4OS$ *m/z* 247.0652 (0.8 ppm).

1.3.2 (*E*)-N-(4-((5-methylthiazol-2-yl)diazenyl)phenyl)acetamide (Ac-PAT 2)

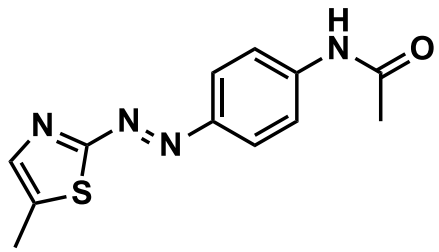

Yield ~ 80 %. **m.p**. = 244 °C. **^{1}H-NMR** (500 MHz, $CDCl_3$) : 7.98-7.96 ppm (d, 2H), 7.70 ppm (s, 1H), 7.69-7.67 ppm (d, 2H), 7,37 ppm (s, 1H), 7,41 ppm (d, 1H), 2.53 ppm (s, 3H), 2.23 (s, 3H). **IR**: 3257 cm^{-1} (stretching N-H), 3055 cm^{-1} (stretching C-H), 1700 cm^{-1} (stretching C=O). **ESI-MS** (+) $[M+H]^+$: $C_{12}H_{13}N_4OS$ *m/z* 261.0811 (0.4 ppm).

1.3.3 (*E*)-N-(4-((4-methylthiazol-2-yl)diazenyl)phenyl)acetamide (Ac-PAT 3)

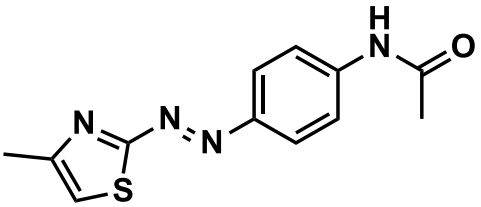

Yield ~ 80 %. **m.p.** = 212 °C. **^{1}H-NMR** (500 MHz, $CDCl_3$) : 8,03 ppm (d, 1H), 8,00 ppm (d, 2H), 7,72 ppm (d, 2H), 7,56 ppm (s, 1H), 7,41 ppm (d, 1H), 2.25 ppm (s, 3H). **IR**: 3245 cm^{-1} (stretching N-H), 3053 cm^{-1} (stretching C-H), 1682 cm^{-1} (stretching C=O). **EI-MS** : $C_{12}H_{12}N_4OS$ m/z 260,0732 (3,8 ppm). **ESI-MS** (+) $[M+H]^+$: $C_{12}H_{13}N_4OS$ *m/z* 261.0811 (0.4 ppm).

1.3.4 (*E*)-N-(3,5-difluoro-4-(thiazol-2-yldiazenyl)phenyl)acetamide (Ac-PAT 4)

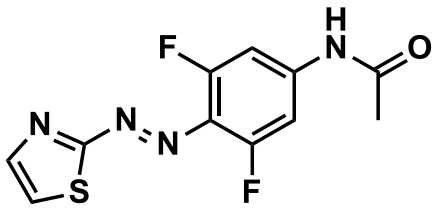

Yield ~ 65 %. **m.p.** = 255 °C. **^{1}H-NMR** (500 MHz, $CDCl_3$) : 8.06-8.05 ppm (d, 1H), 7.45-7.44 ppm (d, 1H), 7.36-7.34 ppm (d, 2H), 2.24 ppm (s, 3H), 2.09 ppm (s, 3H). **IR**: 3104 cm^{-1} (stretching N-H), 2979 cm^{-1} (stretching C-H), 1707 cm^{-1} (stretching C=O). **ESI-MS** (+) $[M+H]^+$: $C_{11}H_9N_4OF_2S$ *m/z* 283.0463 (0.7 ppm).

1.3.5 (*E*)-N-(4-(benzothiazol-2-yldiazenyl)phenyl)acetamide (Ac-PAT 5)

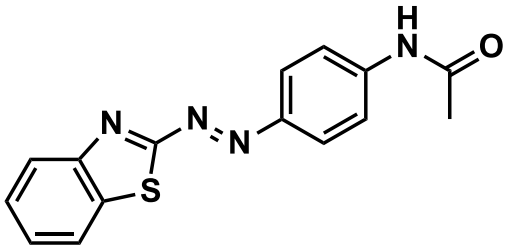

Yield ~ 60 %. **m.p.** = 250 °C. **^{1}H-NMR** (500 MHz, DMSO) : 8.16-8.14 (d,1H), 8.14-8.13 ppm (d, 1H), 8.03-8.01 ppm (d, 2H), 7,90-7.88 ppm (d, 2H), 7.62-7.61-7.59 ppm (t, 1H), 7.58-7.56-7.55 ppm (t, 1H), 2.14 ppm (s, 3H). **IR**: 3176 cm^{-1} (stretching N-H), 2981 cm^{-1} (stretching C-H), 1698 cm^{-1} (stretching C=O). **ESI-MS** (+) $[M+H]^+$: $C_{15}H_{13}N_4OS$ *m/z* 297.0812 (0.7 ppm).

2. THE BIG SYNTHESIS THEORY OF PEPTOIDS

All the sequence-defined peptoids were synthesized by solid phase synthesis inspired by the Zuckermann submonomer method.[238,253] In this approach, a Rink amide resin serves as the solid support, on which the peptoid chain is elongated unit by unit from the C-terminus (Cter) to the N-terminus (Nter). The process relies on the repetition of two successive steps (Scheme 6) : (i) acetylation and (ii) nucleophilic substitution with a primary amine corresponding to the

desired side chain. Two different acetylation strategies were employed; (i) using a mixture of N,N'-diisopropylcarbodiimide (DIC) and bromoacetic acid and (ii) using the most reactive bromoacetyl bromide. The latter has been chosen in some cases to improve the efficiency of the acetylation step. The number of acetylation/substitution iterations determines the final length of the peptoid. In this study, the selected amines are (S)-phenylethylamine (Nspe units), methylamine (Nsar), (E)-4-(thiazol-2-yldiazenyl)aniline (N2tz units), (E)-4-((5-methylthiazol-2-yl)diazenyl)aniline (N5met), (E)-4-((4-methylthiazol-2-yl)diazenyl)aniline (N4met) and (E)-4-(benzothiazol-2-yldiazenyl)aniline (Nbenzo).

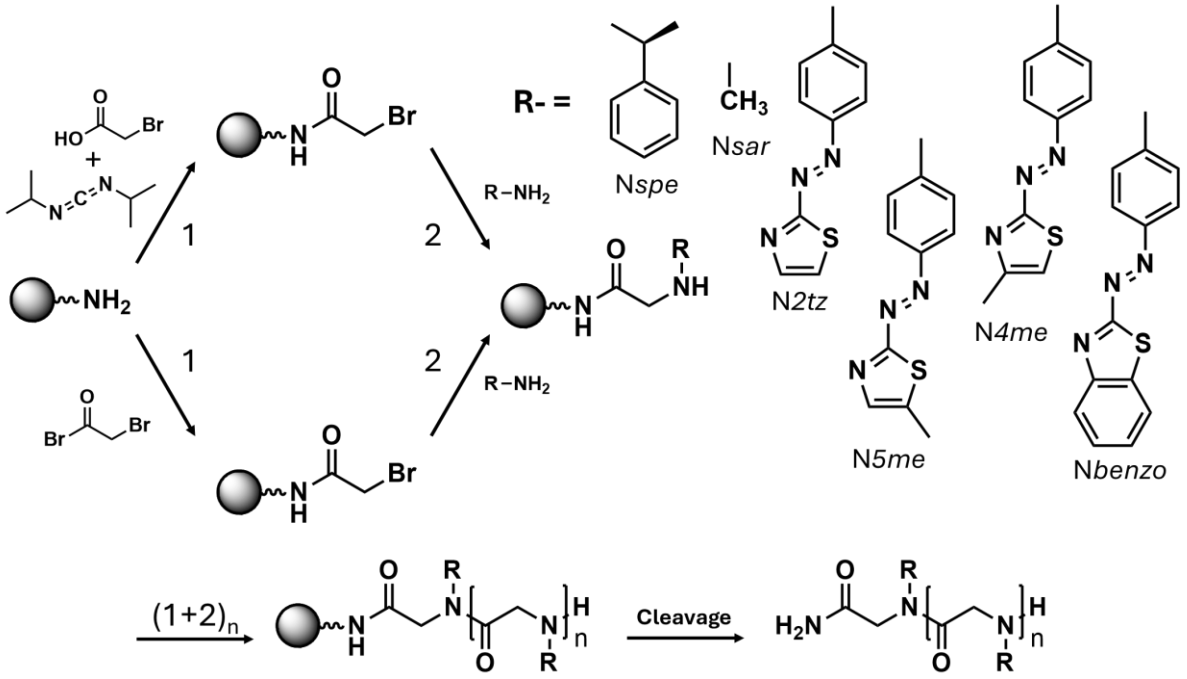

Scheme 6. *Peptoid solid phase submonomer synthesis. The peptoid is built by repetition of bromoacetylation and nucleophilic substitution steps. When the desired length is reached, the peptoid is cleaved from the resin.*

The reaction is manually carried out in a double-walled glass vessel equipped with a three-way valve (**Scheme 7**). This setup enables efficient agitation by nitrogen bubbling through one valve, while temperature of the reaction medium is controlled using a heating circulator that provides hot water circulation within the vessel jacket. Furthermore, solvent and reactants in excess are easily removed by applying a compressed air flux on the upper end using an appropriate valve.

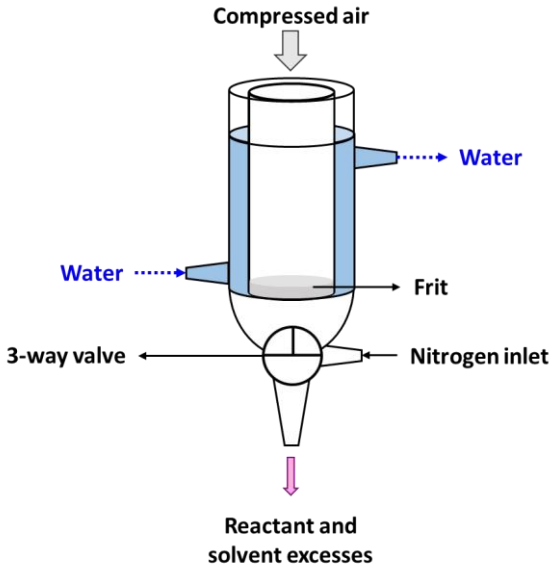

Scheme 7. *Representation of a double-walled glass vessel used for the peptoid solid phase synthesis.*

2.1 GENERAL PROCEDURE FOR THE SOLID-PHASE SYNTHESIS

During this thesis, two different synthetic strategies were used, differing only in the bromoacetylation step. In the first approach, a mixture of N,N'-diisopropylcarbodiimide (DIC) and bromoacetic acid was used while, in the second approach, bromoacetyl bromide was employed. The first step of the synthesis is similar to both strategies and consists in the deprotection of the Rink amide resin. All reactions are carried out at 80 °C in N-methyl-2-pyrrolidone (NMP) as solvent. Solutions of the different reagents are maintained at 80 °C, except for bromoacetic acid and bromoacetyl bromide which are kept at R.T. In practice, in the glass vessel, Rink amide resin (2 g - 100-200 mesh) is swollen with NMP (10 mL) under nitrogen bubbling for 10 min. After evacuation of the solvent, a 20 % solution of 4-methylpiperidine in NMP (10 mL) is added under nitrogen agitation for 10 min to remove the fluorenylmethyloxycarbonyl (Fmoc) protecting group present on the resin. The mixture is then evacuated, followed by three successive washes with NMP (10 ml each). The subsequent steps of the synthesis, which differ between the two strategies, are described in the following sections.[238,241]

2.1.1 Using DIC and bromoacetic acid

For the bromoacetylation step, a solution of DIC (5 mL) and 2 M bromoacetic acid (5 mL) is added to the resin and agitated under nitrogen bubbling for 5 min. After three washes with NMP (10 ml each), the nucleophilic substitution is performed by adding a 2 M solution of the corresponding amine (10 ml). The reaction is maintained for 10 min when using (S)-phenylethyleamine, whereas an extended reaction time at 16 h is required for PAT derivatives due to the lowest nucleophilicity. When PAT derivatives are incorporated in Cter position, the reaction time is further increased to 24 h. Following substitution, the resin is washed three to five times with NMP before repeating the bromoacetylation and nucleophilic substitution steps to generate the desired sequence. Notably, the bromoacetylation step carried out after addition of a PAT derivative is prolonged to 1h30 instead of 5 min due to steric hindrance and poor nucleophilicity of the amine lone pair. After completion of the final step, the resin is washed three times with NMP and subsequently dried three times with DCM (10 ml each).

2.1.2 Using bromoacetyl bromide

For the bromoacetylation step, a 2 M solution of bromoacetyl bromide in NMP (10 mL) is added to the resin and agitated under nitrogen bubbling for 5 min. After three washes with NMP (10 ml each), the nucleophilic substitution is performed by adding a 2 M solution of the corresponding amine (10 ml). The reaction is maintained for 10 min when using (S)-phenylethylamine, whereas an extended reaction time of 16 h is required for PAT derivatives due to its lower nucleophilicity. When PAT derivatives are incorporated in Cter position, the reaction time is further increased to 24 h. Following substitution, the resin is washed three to five times with NMP before repeating the bromoacetylation and nucleophilic substitution steps to generate the desired sequence. Notably, the bromoacetylation step carried out after a PAT derivative is prolonged to 15 min instead of 5 min. Such an adjustment reflects the higher reactivity of bromoacetyl bromide, allowing the step to proceed more rapidly than with the previous method. After completion of the final step, the resin is washed three times with NMP and subsequently dried three times with DCM (10 ml each).

2.2 ACETYLATION OF THE N-TERMINUS AMINE

The acetylation reaction is performed in a double-walled glass vessel, 2 g of the peptoid-grafted resin is swollen in 10 ml of NMP for 10 min under nitrogen bubbling. After removing the solvent, a solution of 2 M DIC (5 ml) and 2 M acetic acid (5 ml) is added and the mixture is agitated overnight under nitrogen bubbling. The resin is subsequently washed three times with 10 ml of NMP and dried by three successive washes with 10 ml of DCM.

2.3 RESIN CLEAVAGE

Peptoid chains are cleaved from the resin either to monitor the progress of the synthesis before subsequent steps (test cleavages) or to obtain the final products for further manipulations and analysis (full cleavages). In the case of test cleavages, a small amount of the resin is treated to release a limited amount of material, which is then directly analyzed by mass spectrometry to confirm the structure before proceeding to further addition of monomers. Full cleavage, on the other hand, is performed on the entire resin batch in order to fully recover the peptoids for characterization of their MOST properties.

2.3.1 Test cleavage

For test cleavages, a small portion of the peptoid grafted resin is suspended in 200 µl of 95:5 trifluoroacetic acid (TFA)/H_2O solution in a glass vial and agitated for 10 min. Then 10 µl of the cleavage solution is diluted in 1 ml of MeOH/H_2O (1:1). 10 µl of this solution are further diluted in 1 ml of MeOH to reach the appropriate concentration for mass spectrometry analysis.

2.3.2 Full cleavage

For full cleavage, the following procedure is described for 1 g of peptoid-grafted resin. The resin is suspended in 10 ml of a 95:5 TFA/H_2O solution and placed under agitation for 10 min. The cleavage mixture is then filtered and the filtrate is basified to around pH 11 with a Na_2CO_3 2 M solution, resulting in peptoid precipitation. The aqueous phase is then extracted three times with 100 ml of organic solvent such as ethyl acetate or isobutanol. The combined organic extracts is washed three times with 200 ml of milli-Q water to remove residual salts. The

resulting organic phase is dried over anhydrous $MgSO_4$ and after solvent evaporation, the peptoid is recovered as a red powder.

2.4 PEPTOID PURIFICATION

Fully cleaved peptoids are purified by flash chromatography on silica gel 60 (particle size 60-200 µm) using DCM/MeOH mixtures as eluents. The purification fractions were evaluated by thin-layer chromatography (TLC) and liquid chromatography coupled to mass spectrometry (LC-MS) analyses, before and after purification.

3. THE FELLOWSHIP OF THE STRUCTURAL CHARACTERIZATION

3.1 NUCLEAR MAGNETIC RESONANCE SPECTROSCOPY

^1H NMR spectra are recorded at R.T (23 °C) on a Bruker AVANCE II 500 spectrometer operating at 500 MHz in the General, Organic and biomedical Chemistry Laboratory (UMONS). Chemical shifts (δ) are reported in parts per million (ppm) relative to tetramethylsilane (TMS) as an internal standard. Samples are prepared at a concentration of 10 $mg.ml^{-1}$ in the appropriate deuterated solvent.

3.2 MASS SPECTROMETRY

To structurally characterize the synthesized PAT, gas chromatography coupled to mass spectrometry (GC-MS) analyses were carried out using a GCT-Premier (Waters), equipped with an electron ionization (EI) source and a Time of Flight (ToF) analyzer. The GC system is equipped with a Phenomenex ZEBRON-ZB-5MS (30 meter x 0.25 mm x 0.25 µm). The thin film of 0.25 µm is composed of a 5 % phenyl-arylene / 95 % dimethylpolysiloxane phase. Helium is used as the carrier gas at a flow rate of 1 $ml.min^{-1}$. Sample solutions are prepared in HPLC-grade hexane at a concentration of 1 $mg.mL^{-1}$ and subsequently diluted 1000-fold. After dilution, 1 µl of the solutions is injected into the GC injector, maintained at 200 °C to ensure the volatilization of the sample. The oven temperature program is set as follows: initial temperature of 30 °C, ramped to 260 °C over 25 min, held at 260 °C for 10 min and finally

returned to 30 °C in 15 min. High-resolution mass spectrometry (HRMS) analyses are performed to determine the elemental composition of the detected ions. Perfluorotributylamine (PFTBA) is used as an external calibrant (lock mass) to ensure accurate mass measurement.

ElectroSpray Ionization Mass Spectrometry (ESI-MS) is employed to characterize the primary structure of the synthesized peptoids. The ESI-MS analyses are performed in positive ionization mode on commercially available instruments, including Waters QToF Premier, Waters QToF US and Waters Synapt G2-S*i*. Typical instrumental parameters employed to maximize the ion signals are summarized in **Table 1**. All MS data were processed using MassLynxTM 4.1 software.

Instrumental parameters	QToF Premier	QToF US	Synapt G2-S*i*
Capillary voltage (kV)	+3.1	+3.1	+3.1
Cone Voltage (V)	30	30	20-30
Source temperature (°C)	80	80	80
Desolvation temperature (°C)	120	120	120
N_2 flow rate for the gas cone ($L.h^{-1}$)	50	50	50
N_2 flow rate for the desolvation ($L.h^{-1}$)	500	500	500
Resolution (NaI solution)	~8500 (m/z 472)	~8000 (m/z 472)	~20 000 (m/z 922)

Table 1. *Typical instrumental parameters used for the molecule characterization with the Waters QToF Premier, QToF US and Waters Synapt G2-Si.*

Sample solutions are prepared in HPLC-grade MeOH at a concentration of 1 $mg.mL^{-1}$. After dilution (1000 x), the solutions are injected into the ESI source using a syringe pump at a flow rate of 5 $\mu L.min^{-1}$.

To confirm the primary structure of the synthesized peptoids, tandem mass spectrometry (MS/MS) experiments are carried out by selecting the mass-to-charge ratio of precursor ions and subjecting them to collisional activation to induce fragmentation. Collision-induced dissociation (CID) experiments correspond to the fragmentation resulting from an energy transfer to the ions upon inelastic collisions with an inert gas (argon). The collision energy is

adjusted for each ion to ensure sufficient fragmentation while maintaining detection of the precursor ions. Further details regarding peptoid fragmentation patterns are provided in the **Results and Discussion** section.

Finally, HRMS analyses are performed to determine the elemental composition of the detected ions. NaI is used as an external calibrant (lock mass) to ensure accurate mass measurement.

3.3 INFRARED SPECTROSCOPY

Infrared spectra are recorded using a compact Fourier Transform Infrared (FT-IR) spectrometer (Bruker model ALPHA – ATR mode). Samples are analyzed in the solid state without further preparation. Spectra are collected in the range of 4000 to 600 cm^{-1}, with a spectral resolution of 2 cm^{-1} and averaging 32 scans for each measurement. The recorded absorption bands are assigned to the main functional groups of the ABs in order to confirm their chemical structure.

3.4 MELTING POINT

The melting points were determined using a capillary tube and a MPA100 Melting Point Apparatus. A small amount of the sample in fine powder is packed into a capillary with a height of 2-3 mm and the capillary is inserted into the preheated block. An initial quick scan (5-10°C.min^{-1}) is performed to estimate the approximate melting temperature range. The final measurement is then carried out at a controlled heating rate of 2 °C.min^{-1}. The melting point is recorded as the temperature at which the sample becomes completely clear and liquid.

4. MOST PROPERTIES HUNTERS

4.1 UV-VIS SPECTROSCOPY

UV-Vis spectra are recorded from 250 nm to 650 nm on a Avaspec-2048 Fiber Optic Spectrometer (Avantes B.V. , Apeldoorn, The Nederlands). VWR® quartz cuvettes with 1 cm optical path length are employed for the measurements. Peptoids and ABs solutions are prepared in the dark at room temperature using HPLC-grade solvents (2-3 mg in 10 ml of

solvent), then this stock solution is diluted to reach final concentration at 5 x 10^{-5} M. UV-Vis spectra are initially recorded in the dark and at room temperature to avoid any unwanted photoisomerization. Molar extinction coefficients at the wavelength of maximum absorbance for peptoids and ABs in the E configuration are determined by measuring absorbance at different concentrations (from 5.0 x 10^{-5} M to 5.4 × 10^{-6} M) and applying the Beer–Lambert law.

$$A = \varepsilon . C . l \qquad (\boldsymbol{Eq.1})$$

where A is the absorbance, ε is the molar extinction coefficient (L.mol^{-1}.cm^{-1}), C is the analyte concentration (mol.L^{-1}) and l is the optical path length (1 cm).

Photochemical *E* → *Z* isomerization is followed by recording UV-vis spectra before and after irradiation using different lamps (see following section **4.2** for irradiation sources).

4.2 IRRADIATION SOURCES

Three different irradiation sources are employed in this work to evaluate the photoisomerization efficiency under different energy inputs. The specific irradiation source used for each experiment is indicated in the legend of the corresponding figures.

- LightningCure LC8 9588-03 (Hamamatsu Photonics) referred as "*visible lamp"* in this study is a Hg-Xe lamp (**Figure 39a**) used at 20 % power, corresponding to a relative irradiance of 900 mW.cm^{-2}. The irradiance is measured at the distance of 1 cm from the output end of the optical fiber (5 mm output diameter).
- LightningCure LC8 9588-02A (Hamamatsu Photonics) named as "*UV lamp*" in this study is a Hg-Xe lamp (**Figure 39b**) used at 20 % power, corresponding to a relative irradiance of 900 mW.cm^{-2}. The irradiance measured at the distance of 1 cm from the output end of the optical fiber (5 mm output diameter). The dispositive is further equipped with a UV transmitting filter (50x50 mm, center wavelength = 325 nm, OptoSigma), its transmission spectrum is shown on **Figure 39c**.

- Experiments under real conditions were performed using direct sunlight as irradiation source. The measurements were performed outdoors on the rooftop of the Mendeleiev building (Av. Victor Maistriau, 23, 7000 Mons, 50°27'53.5"N ; 3°57'25.6"E) under different weather conditions detailed forward in the Results and Discussion part. The corresponding solar irradiation spectrum is presented in **Figure 39d**. This setup allows the evaluation of the system performance under realistic conditions, complementing the controlled laboratory experiments performed with artificial light sources.

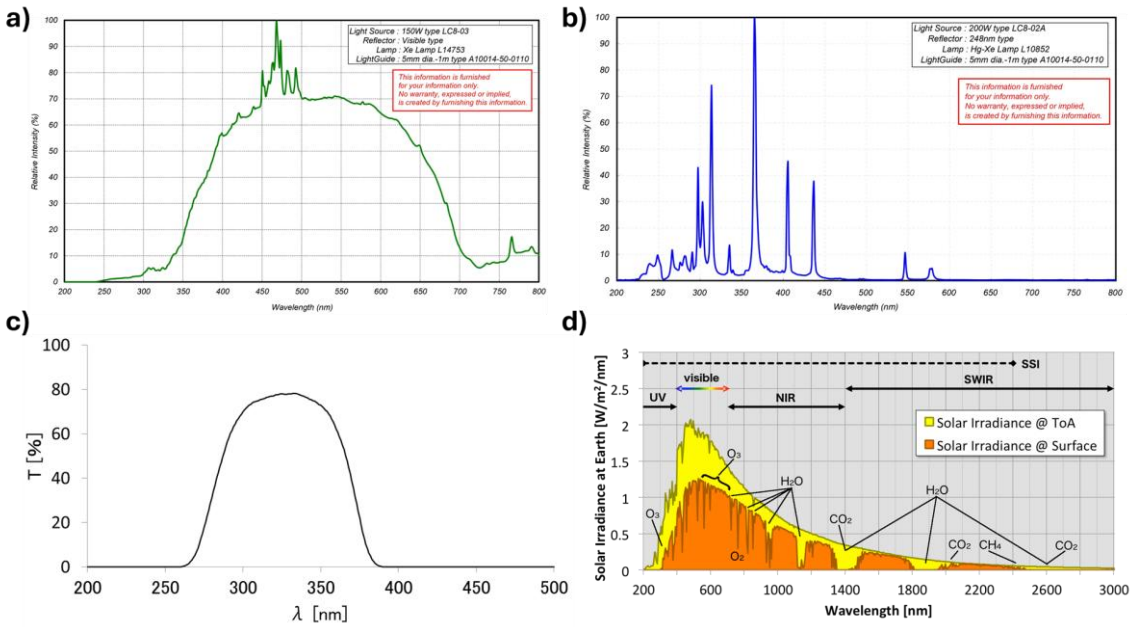

Figure 39. *a) Emission spectrum of the visible lamp (LightningCure LC8 9588-03).*[254] *b) Emission spectra of the UV lamp (LightningCure LC8 9588-02A).*[255] *c) Transmission spectrum of the UV transmitting filter.*[256] *d) Simulated spectral solar irradiance at the top of the atmosphere (ToA) and the Earth's surface. The regions of spectrum where irradiance is absorbed by various atmospheric constituents are indicated, including: ozone (O_3), oxygen (O_2), water vapor (H_2O), carbon dioxide (CO_2), and methane (CH_4).*[257]

4.3 PHOTOISOMERIZATION EXPERIMENTS

LC-MS analyses are performed using an Alliance 2695 HPLC (Waters, UK), equipped with an Agilent Eclipse Plus C_{18} column (4.6×100 mm; 3.5 µm particle size) and coupled to the Waters QToF Premier mass spectrometer. HPLC grade solvents were used. The autosampler temperature is fixed at 20 °C and the column temperature at 25 °C. A linear gradient starting

from 70 % H_2O (with 0.01 % HCOOH)/30 % ACN going to 100 % ACN in 12 min is applied, followed by a column wash phase during 4 min with 100 % ACN and a return to the starting conditions with an equilibrium phase in 4 min. Samples are dissolved in MeOH HPLC grade (1 mg.mL-1 diluted 500X before analysis). Solution irradiation to achieve *E* → *Z* photoisomerization is performed using the irradiation sources described above and LC-MS analyses are repeated at different irradiation times until PSS is reached. Both *E*- and *Z*-isomers are mostly detected as $[M+H]^+$ ions upon electrospray ionization in the positive ionization mode. Extracted ion current (EIC) chromatograms are used for detecting the isomer ions and determining their relative proportions. We here assume that the configuration of the azobenzene chromophore (*E* or *Z*) should not affect the ionization efficiency since the peptoids are systematically protonated on the Nter secondary amines. For both isomers, the corresponding LC-MS ion signals including all isotopic compositions are integrated using the integration algorithm, available under MassLynxTM 4.1 Software.

4.4 THERMAL BACK-ISOMERIZATION

4.4.1 LC-MS analyses

After irradiation of the peptoid solutions and determination of PSS, the vial containing the sample is placed in the HPLC autosampler, where it is stored in the dark under controlled temperature conditions. LC-MS measurements (see **4.3** for details) are repeated at regular intervals on the stored solutions to monitor the kinetics of the Z → E thermal back-isomerization. The relative Z-isomer content is normalized and plotted as a function of storage time. The resulting decay curves obtained are fitted in OriginPro 2019 using a single-exponential decay function, consistent with the well-established first-order kinetics of the thermal back-isomerization of ABs. The fitting equation applied is **Eq.2**.

$$y\,(t) = y_0 + A\,e^{-kt} \qquad (\boldsymbol{Eq.2})$$

where $y\,(t)$ is the normalized *Z*-isomer fraction at time t, y_0 is the offset value for the *Z*-isomer content (fixed at 0 in this case), A is the initial *Z*-isomer content (set at 1) and k (s^{-1}) corresponds

to the first order rate constant. From the fitted values of k, the $t_{1/2}$ of the *Z*-isomer is determined according to **Eq.3**:

$$t_{\frac{1}{2}} = \frac{\ln(2)}{k} \qquad (\boldsymbol{Eq.3})$$

For peptoids containing two ABs units, the thermal back-isomerization kinetics are better described by a biexponential model according to **Eq.4**.

$$y\,(t) = y_0 + A_1\, e^{-k_1 t} + A_2 e^{-k_2 t} \qquad (\boldsymbol{Eq.4})$$

where $y\,(t)$ is the normalized *Z*-isomer fraction at time t, y_0 is the offset value for the *Z*-isomer content (fixed at 0 in this case), k_1 and k_2 (s^{-1}) are the first order rate constants associated to the back-isomerization of each AB moiety, and A_1 and A_2 represent their respective contributions to the overall kinetics. The $t_{1/2}$ of each AB can be directly obtained by applying Eq.5 to the corresponding kinetic constants k_1 and k_2.

To determine the energy of activation (E_a) of the thermal back-isomerization process, the kinetics are monitored by LC-MS measurements at different temperature by adjusting the temperature of the HPLC autosampler (10, 15, 20, 25 and 30 °C). The resulting rate constants are plotted as a function of the inverse of the temperature to construct an Arrhenius plot (**Eq.5**), which provide access to the activation energy of the thermal back-isomerization.

$$k = Ae^{-\frac{E_a}{RT}} \qquad (\boldsymbol{Eq.5})$$

where k is the first order rate constant (s^{-1}), A is the Arrhenius factor, E_a is the energy of activation (J), R is the gas constant and T is the temperature (K).

To gain deeper insight about kinetics parameters, an Eyring-Polanyi plot (**Eq.6**) is also performed. This approach enables extraction of the activation enthalpy ($\Delta H^{\ddagger}$) and activation entropy ($\Delta S^{\ddagger}$), thus providing complementary information about the mechanism of the thermal back-isomerization process.

$$\ln\frac{k}{T} = \left(\ln\frac{k_b}{h} + \frac{\Delta S^{\ddagger}}{R}\right) - \left(\frac{\Delta H^{\ddagger}}{R}\right)\frac{1}{T} \qquad (\boldsymbol{Eq.6})$$

where k (s^{-1}) is the rate constant, T is the temperature (K), k_B is the Boltzmann constant ($1.38*10^{-23}$ $J.K^{-1}$), h is the Planck constant ($6.62*10^{-34}$ J.s), $\Delta S^{\ddagger}$ is the activation entropy ($J.mol^{-1}.K^{-1}$), R is the molar gas constant (8.314 $J.mol^{-1}.K^{-1}$) and $\Delta H^{\ddagger}$ is the activation enthalpy ($kJ.mol^{-1}$).

4.4.2 UV-vis spectroscopy

LC-MS analyses typically operate on timescales of several minutes to detect the different isomers, which limits their applicability for AB derivatives exhibiting very fast thermal back-isomerization ($t_{1/2}$ of few seconds to minutes). To overcome this limitation, UV-vis spectroscopy provides a more suitable alternative for monitoring rapid kinetics, typically with the use of an Avaspec-2048 Fiber Optic Spectrometer, as it enables acquisition of a UV-vis spectrum each second. However, this method only allows determination of the $t_{1/2}$ of the *Z*-isomer, but not the PSD. In practice, a spectrum is first recorded before irradiation to identify the maximum of the π-π* transition band. The sample is then irradiated using the selected light source and the spectra are collected at fixed time intervals. The absorption at the λ_{max} is normalized between its minimum (after irradiation) and its maximum (before irradiation). By plotting the normalized absorbance as a function of time, the kinetics constant for the *Z* → *E* thermal back-isomerization can be extracted. In this setup, measurements were performed at R.T only, since the dispositive is not equipped with a system to control the sample temperature. Consequently, kinetic parameters ($\Delta H^{\ddagger}$ and $\Delta S^{\ddagger}$) could not be derived from this method. It is worth noting that in UV-vis experiments, the kinetic constant is determined from the reappearance of the *E*-isomer, while, for LC-MS analyses, the disappearance of the *Z*-isomer is rather monitored. However, both approaches yield identical rate constants, differing only in the monitored species.

4.4.3 Solvent effects

The thermal back-isomerization of ABs from *Z*- to *E*-isomer is strongly influenced by the nature of the solvent. Solvent polarity, proticity and even viscosity affect the activation barrier of the thermal back-isomerization and, consequently, the $t_{1/2}$ of the *Z*-isomer. Since this process is concomitantly impacted by several parameters, it is really difficult to define a single descriptor that accounts for all solvent effects at once. In this context, the use of empirical polarity parameters such as the Dimroth and Reichardt parameter ($E_T(30)$) offers a representative approach to describe the overall solvent effect. This parameter is based on absorption of betaine 30 (B30) (**Figure 40a**), a solvatochromic dye whose absorption maximum is highly sensitive to the solvent environment, as illustrated in **Figure 40b**.[258] The $E_T(30)$ (kcal.mol^{-1}) value of a solvent can be calculated according to **Eq.7** :

$$E_T(30) = 0.239 * N_a hc\nu_{max} = 2.8591 * 10^{-3} * \nu_{max} = \frac{28591}{\lambda_{max}} \qquad (\boldsymbol{Eq.7})$$

In **Eq.7**, *h* denotes Planck's constant (6.626*10^{-34} J·s), c is the speed of light in vacuum (2.998*10^{8} m/s), and N_a is Avogadro number (6,022 140 76*10^{23} mol^{-1}). The factor 0.239 accounts for the conversion from joules to kilocalories. The term ν_{max} (cm^{-1}) or its reciprocal λ_{max} (nm) corresponds to the wavenumber or wavelength, respectively, of the maximum absorption band of B30.

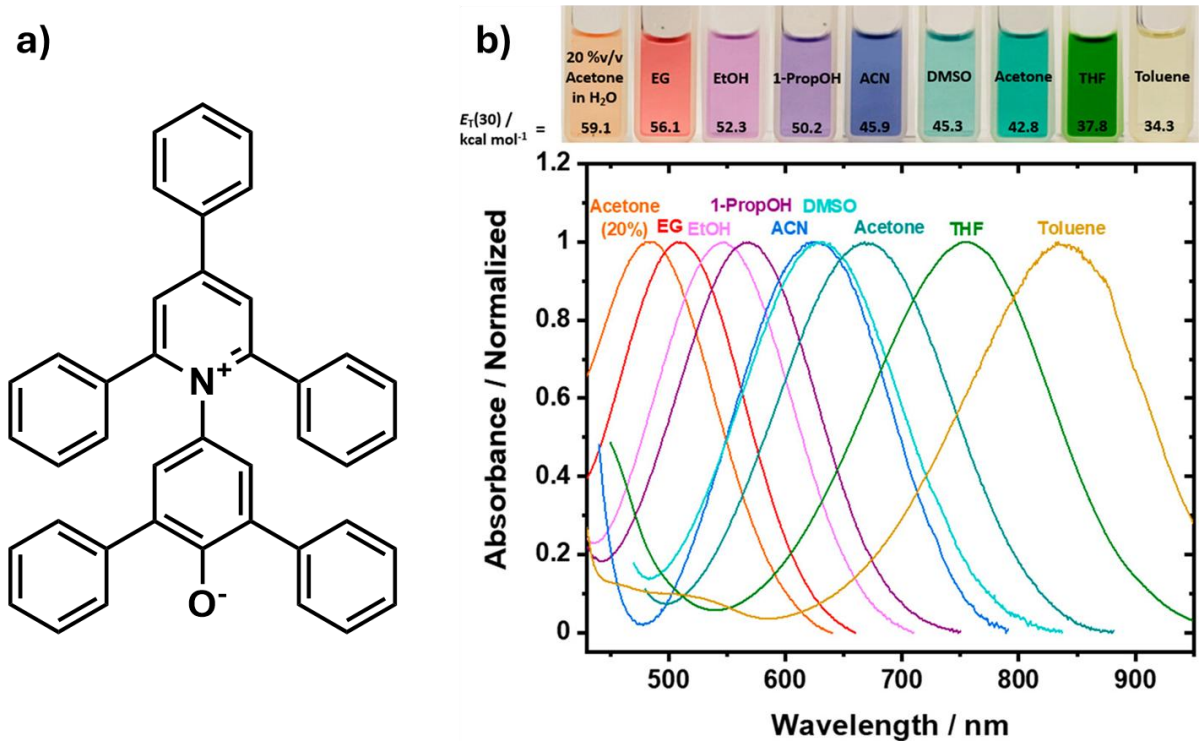

Figure 40. *a) Molecular structure of the B30 in its zwitterionic form adapted from*[259]*. b) Normalized absorption band of the B30 dissolved in nine different solvents. From left to right: 20 % acetone/H_2O, ethylene glycol (EG), EtOH, 1-propanol (1-PrOH), ACN, dimethyl sulfoxide (DMSO), THF and toluene. The corresponding $E_T(30)$ values are indicated, showing a progressive redshift of the absorption band with decreasing solvent polarity. Numeric values of $E_T(30)$ and $E_T^N(30)$ measured at 293 K are reported in Table 2.*[258]

To facilitate comparison across different solvents, the raw values of $E_T(30)$ values are often normalized according to **Eq.8**, where TMS ($E_T(30)$ = 30.7) and H_2O ($E_T(30)$ = 63.1) are taken as reference solvents corresponding to lowest and highest polarity values, respectively. This normalization yields a dimensionless parameters $E_T^N(30)$ ranging from 0 for the least polar solvents to 1 for the most polar solvents, which allows a more straightforward comparison of solvent effects on the thermal back isomerization rate of ABs.[260]

$$E_T^N(30) = \frac{E_T(solvent) - E_T(TMS)}{E_T(H_2O) - E_T(TMS)} = \frac{E_T(solvent) - 30.7}{32.4} \qquad (\boldsymbol{Eq.8})$$

For the purpose of this thesis, different solvents have been selected and their corresponding $E_T(30)$ and $E_T^N(30)$ values are reported in **Table 2**, based on reference data available in literature.

Solvent	λ_{max} (nm)	$E_T(30)$ $(kcal.mol^{-1})$	$E_T^N(30)$
TMS	931	30.7	0.00
Toluene	843	33.9	0.10
Ethyl acetate (EtAc)	750	38.1	0.23
Chloroform ($CHCL_3$)	731	39.1	0.26
DCM	702	40.7	0.31
Acetone	677	42.2	0.35
ACN	627	45.6	0.46
Isobutanol (Isobut)	654	43.7	0.40
1-propanol (1-PrOH)	564	50.7	0.62
2-propanol (2-PrOH)	581	49.2	0.57
EtOH	550	51.9	0.65
MeOH	516	55.4	0.76
H_2O	453	63.1	1.00

Table 2. *λ_{max} values of B30 in the thirteen solvents measured at 293 K. Numeric values of $E_T(30)$ and $E_T^N(30)$ taken from literature.*[260]

However, for mixture of solvents, reference values are generally not available in the literature and must therefore be experimentally determined. To establish these values, betaine 30 is first dissolved in the solvent mixture at a concentration of 1 $mg.ml^{-1}$ and then diluted to approximately 5.10^{-5} $mol.l^{-1}$. The λ_{max} of the resulting solution is measured in the same way as described in section **4.1**. The λ_{max} values are then introduced into **Eq.7** and **Eq.8** to calculate the corresponding $E_T(30)$ and $E_T^N(30)$ values, respectively. In this thesis, the solvent mixtures investigated include MeOH/H_2O (1:3, 1:1 and 3:1), MeOH/ACN (1:1) and ACN/H_2O (1:1). For validation of the method, the $E_T(30)$ of the pure solvents were also experimentally determined under identical conditions, in addition to those of solvent mixtures.[261]

4.4.4 Catalytic activation

In order to gain deeper insight in the thermal back-isomerization process, the catalytic activation of *Z* → *E* back-isomerization was investigated. In this approach, formic acid was employed as a catalytic additive, as protonation of the N=N bond is expected to lower the activation barrier and thereby accelerate the thermal relaxation.[262] To evaluate solvent effects on this catalytic activation, four solvents of different polarities and proticities (toluene, ACN, MeOH and H_2O) were selected. The experiments were carried out using the peptoid N*spe*N*spe*N2*tz*, and small amounts of formic acid were added to the samples before kinetic monitoring. The thermal back-isomerization was then followed by LC-MS measurements under the same experimental conditions as described in section **4.2.1**, enabling direct comparison of the catalytic efficiency across solvents.

Part 4 – Results and Discussion

Results and discussion

As outlined in the thesis objectives (Chapter 2), this section is organized into four parts:

- *Synthesis, structural characterization and MOST properties evaluation of PATs:* this part introduces the different PAT derivatives studied in this thesis with a brief structural characterization. Their MOST properties (λ_{max}, $\varepsilon_{\lambda max}$, $\Delta H^{\ddagger}$, $\Delta S^{\ddagger}$, $t_{1/2}$ and PSD) will be determined to assess the influence of the substitution patterns and to compare the impact of peptoid backbone on these properties.
- *Synthesis, structural characterization and MOST property evaluation of peptoids:* the targeted peptoids will be presented alongside the optimized synthetic protocols. A more detailed structural characterization will be carried out, with MS and MS-MS analysis to confirm the peptoid primary structures. The MOST properties of the peptoids will be determined and compared with those of the non-grafted PAT.
- *Solvent effects on the thermal back-isomerization:* since thermal back-isomerization is a key parameter for efficient MOST system, this section will investigate the influence of the solvent on this process for selected PATs and two peptoids (N*spe*N*spe*N*2tz* and N*spe*N*2tz*N*spe*). For the peptoids, a deeper investigation will be conducted, including the determination of the kinetic parameters in different solvents.
- *Catalytic activation of the thermal back-isomerization:* evaluation of the acid-catalyzed back isomerization of N*spe*N*spe*N*2tz Z*-isomer using formic acid in different solvents.

1. THE FIFTH PHENYLAZOTHIAZOLES

1.1 SYNTHESIS AND STRUCTURAL CHARACTERIZATION

Several PAT derivatives were synthesized during this work, with detailed protocols provided in sections **1.2** and **1.3** of the **Experimental part**. Two main types of PATs were synthesized: NH_2-PAT and Ac-PAT derivatives shown on **Figure 41**. The NH_2-PAT derivatives were

obtained via azo coupling reaction involving the formation of a diazonium salt inspired by a protocol by Grewal *et al*.[252] In this process, the aminothiazole derivatives were first dissolved in water under acidic conditions at 0°C and sodium nitrite was added to generate the diazonium salt. The appropriate coupling agent was then introduced to form the N=N bond. Subsequently, the NH_2-PAT derivatives were deprotected under basic conditions to regenerate the free amine group, which is required for their incorporation into peptoid. The Ac-PAT derivatives were prepared by acetylating the amine group of the NH_2-PAT using acetic anhydride in the presence of triethylamine. These acetylated derivatives are crucial for comparison with the PAT-grafted peptoids, as they allow assessment of the impact of the peptoid backbone on the MOST properties. This is particularly relevant since the PAT units are connected to the peptoid backbone through an amide bond.

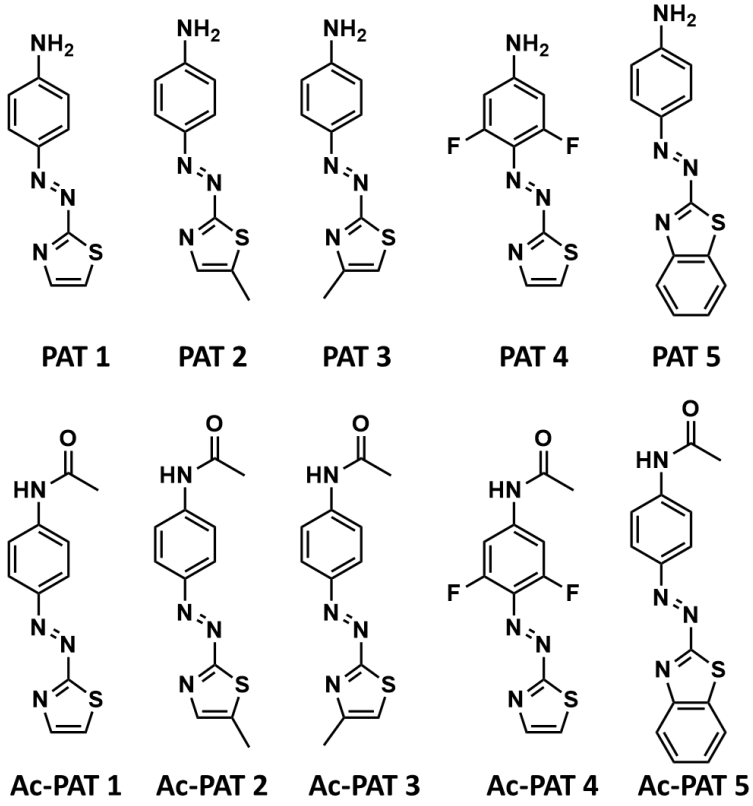

Figure 41. *Representation of the 10 PAT derivatives synthesized in this work, along with their abbreviated names.*

The structural characterization of the synthesized PAT derivatives was carried out using HRMS, MS/MS, IR, m.p. and H^1 NMR analyses. Detailed descriptions of these

characterizations are provided in sections 1.2 and 1.3 of the **Experimental part**. The complete sets of MS, HRMS, MS-MS, IR and H^1 NMR spectra for all PAT derivatives are included in the **Appendix part**.

1.2 DETERMINATION OF MOST PROPERTIES

The determination of the MOST properties of these molecular systems represents a major part of this study as this will constitute the basis of the comparative study, *i.e.,* monomers vs peptoids. As a first step, the properties of the NH_2-PAT derivatives will be examined, followed by those of the Ac-PAT derivatives. These properties are measured in solution in MeOH as the reference solvent. The initial properties determined are the λ_{max} and $\varepsilon_{\lambda max}$, which reveal the absorption wavelength (UV or visible range) and the efficiency of the absorption. Subsequently, parameters such as $t_{1/2}$, PSD, $\Delta H^{\ddagger}$ and $\Delta S^{\ddagger}$ will be measured.

1.2.1 NH_2-PAT derivatives

1.2.1.1 E-isomer spectroscopic properties

The UV-vis spectra of the NH_2-PAT derivatives are shown in **Figure 42a**, while the corresponding λ_{max} and $\varepsilon_{\lambda max}$ values are summarized in **Table 3**. PAT 1, the unsubstituted derivative, exhibits a maximum absorption at 463 nm corresponding to the π-π* transition which represents an absorbance in the visible region. PAT 2 and 3, which bear methyl substituents at position 5 and 4, respectively, display absorption maxima similar to PAT 1, around 465 nm. This result is consistent with the limited electronic effect of the methyl group, which does not significantly alter the conjugation within the system and therefore induces minor shifts in absorption. In contrast, PAT 4 corresponding to PAT 1 substituted with fluorine in the ortho positions of the N=N bond, shows a hypsochromic shift, with the absorption maximum blueshifted to 420 nm. This behavior can be attributed to a decrease in molecular planarity caused by the fluorine atom, leading to a blueshift of the π-π* transition, in agreement with previous observations for halogenated AB.[155] Another key feature of the UV-vis absorbance profile of PAT 4 is the detection of a second band, *i.e.* a shoulder, that will be demonstrated

hereafter using LC-MS analysis to be related to the presence of a side-product. For PAT 5, where conjugation is extended through the addition of a phenyl group on the thiazolyl moiety, the absorption maximum is redshifted to 490 nm. The reduction of the π-π* gap in this derivative results directly from the increased conjugation. It should also be noted that the n-π* transition of the NH_2-PAT derivatives could not be clearly resolved due to overlap with the π-π* transition, which is strongly bathochromically shifted.

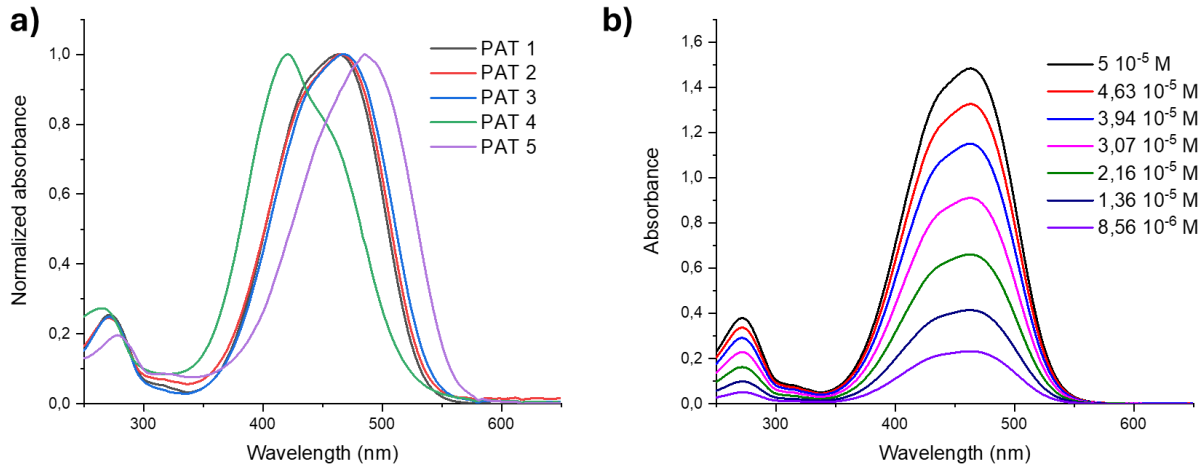

Figure 42. *a) UV-vis spectra (normalized absorbance) of NH_2-PAT derivatives in MeOH. b) UV-vis spectra of PAT 1 in MeOH at different concentrations ranging from 5 10^{-5} M to 8.56 10^{-6} M.*

The molar extinction coefficients were determined in MeOH for all the PAT derivatives using Beer-Lambert's law. For PAT 1, ε at 463 nm is 2.93 10^4 $L.mol^{-1}.cm^{-1}$, as illustrated in **Figure 42b** which shows the UV-vis spectra at different concentrations. For the substituted derivatives, ε values are higher, ranging from 2.88 10^4 $L.mol^{-1}.cm^{-1}$ for PAT 4 to 5.57 10^4 $L.mol^{-1}.cm^{-1}$ for PAT 5. The particularly high value observed for PAT 5 can be attributed to the extended aromatic conjugation, as such a structural modification typically leads to a redshift of the absorption but also to an increase of the ε value.

1.2.1.2 Photo- and back-isomerization processes

Regarding the photoisomerization process, since NH_2-PAT derivatives absorb in the visible region, the *visible lamp* is used for irradiation. For PAT 1, no change is observed in the UV-vis

spectrum before and after irradiation (**Figure 43a**). This indicates that the $t_{1/2}$ of the *Z*-isomer is too short to be detected, *i.e.*, less than one second. Similar results are obtained for PAT 2, PAT 3 and PAT 5, where no detectable photoisomerization occurs.

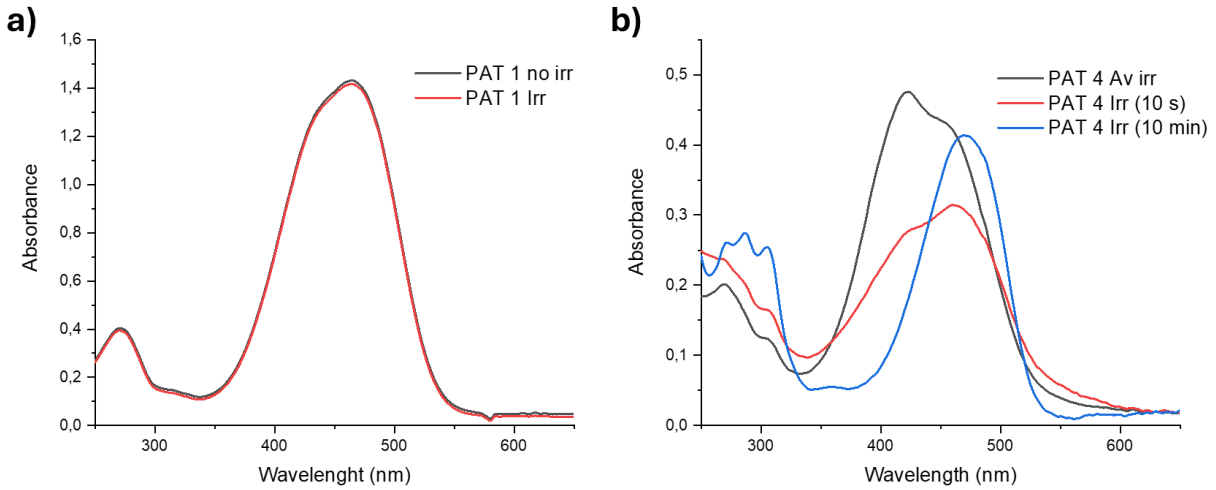

Figure 43. *a) UV-vis spectra of PAT 1 before and after irradiation, showing no significant change in absorption (MeOH, 5 10^{-5} M). b) UV-vis spectra of PAT 4 in MeOH recorded before, after 10 s and after 10 min of irradiation, with the emergence of a new absorption band at 480 nm.*

In contrast, PAT 4 exhibits a clear photoisomerization as shown in the UV-vis spectra in **Figure 43b**. By plotting the absorbance at 420 nm over time (**Figure 44a**), the $t_{1/2}$ of the *Z*-isomer was determined to be 1.65 s. Although this value remains very low, it highlights the influence of the fluorine substituents, which increase the stability of the *Z*-isomer, consistent with observations for halogen-substituted AB.[155]

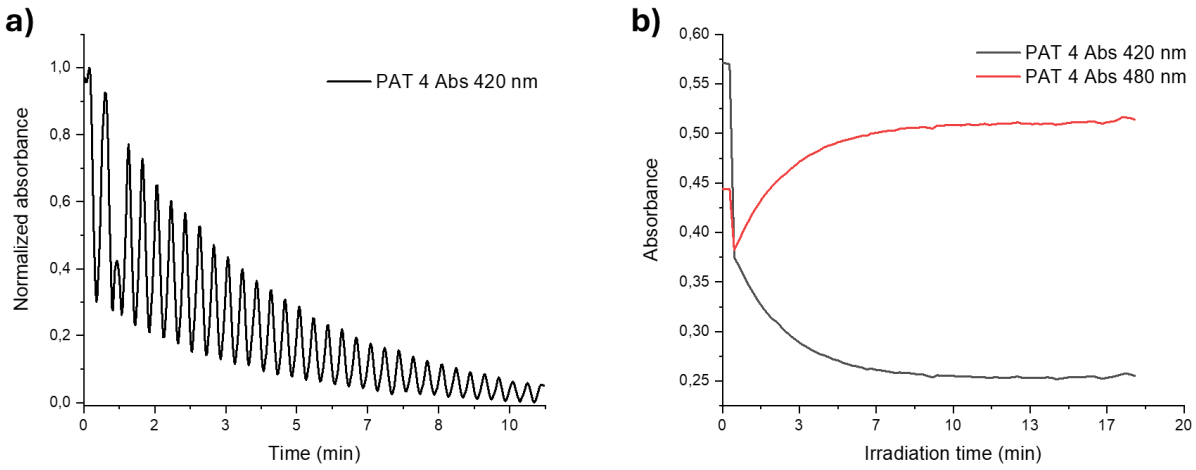

Figure 44. *a) Evolution of the normalized absorbance of PAT 4 at 420 nm under successive photo- and back-isomerization in MeOH, showing a significant 5 % degradation per cycle. b) Evolution of the absorbance in MeOH at 420 nm and 480 nm as a function of the irradiation time.*

However, repeated photoisomerization and thermal back-isomerization cycles revealed progressive degradation, with approximately 5 % loss per cycle, as shown on **Figure 44a**. In the UV-vis spectra (**Figure 43b**), a new absorption band emerged at 480 nm. Monitoring the signals at both 420 nm and 480 nm as function of irradiation time (**Figure 44b**) shows that the decrease at 420 nm is directly counterbalanced by the appearance of the 480 nm band, suggesting that PAT 4 degrades into an unknown species.

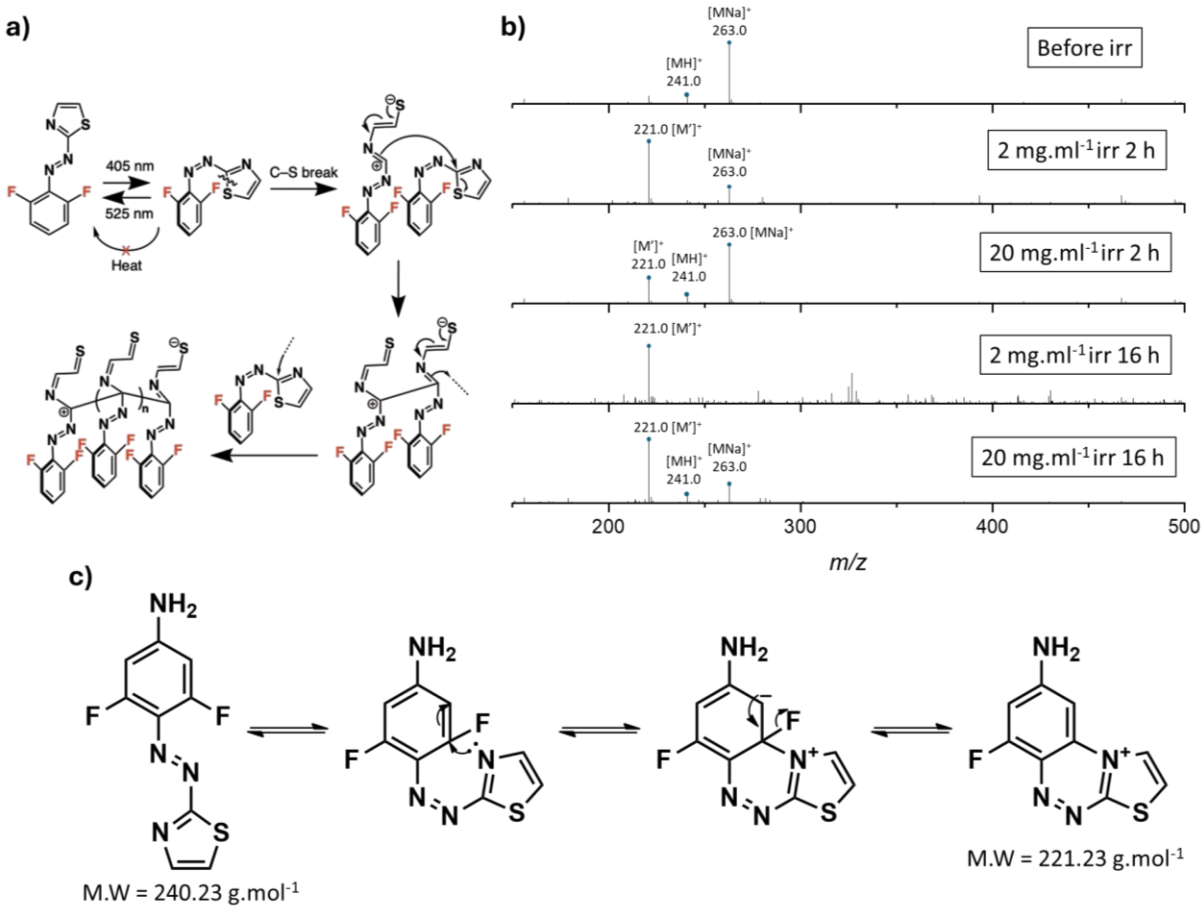

Figure 45. *a) Mechanism proposed by Hashim et al. illustrating the oligomerization of PAT-F_2 triggered by cleavage of a C-S bond. Figure from*[263]*. b) MS spectra of PAT 4 in DMSO at two different concentrations (2 mg.ml^{-1} and 20 mg.ml^{-1}), recorded before irradiation and after 2 h and 16 h of irradiation. c) Proposed degradation mechanism of PAT 4 proceeding via an intermolecular addition-elimination pathway.*

Upon further examination of the literature, a study by Hashim *et al.* in 2024 on fluorine-substituted PAT derivatives reported similar degradation behavior under irradiation.[263] The authors proposed a degradation mechanism based on oligomerization of the PAT derivatives, as illustrated in **Figure 45a**. This pathway involves an initial C-S bond cleavage, which triggers oligomerization and leads to the formation of zwitterionic oligomers. Although such a C-S bond scission appears rather unlikely, we sought to verify or refute this proposed pathway by performing MS analyses (**Figure 45b**). To this end, two DMSO solutions of PAT 4 were prepared at different concentrations (2 mg.ml^{-1} and 20 mg.ml^{-1}) to investigate the concentration dependence of the degradation process. Prior to irradiation, MS spectra of both solutions are

similar, displaying primarily the protonated (*m/z* 241) and sodium adducts (*m/z* 263) of PAT 4. After 2 h of irradiation, a new signal at *m/z* 221 appeared and became the predominant peak in the 2 $mg.ml^{-1}$ solution, whereas in the more concentrated solution, the sodium adduct of PAT 4 remained the major species. After 16 h of irradiation, the PAT 4 signal has completely disappeared in the dilute solution, while it is still detectable at higher concentration, certainly due to a too short (16 h) irradiation time at this concentration. The new peak at *m/z* 221 corresponds to a mass loss of 20 relative to the protonated PAT 4, which is consistent with an addition-elimination (add/elim) mechanism (**Figure 45c**) in which fluoride is substituted by the nucleophilic nitrogen atom of the thiazolyl moiety. The identity of the resulting cation is confirmed by HRMS, giving *m/z* 221.0297 ($C_9H_6N_4SF$) with an error of 0.5 ppm, supporting the proposed structure. No signal corresponding to oligomeric species was detected, suggesting that the degradation proceeds predominantly through an intermolecular cyclization via the add/elim mechanism rather than oligomerization. This degradation pathway will be further investigated for Ac-PAT 4 by LC-MS analyses.

1.2.2 Ac-PAT derivatives

1.2.2.1 E-isomer spectroscopic properties

After the investigation of NH_2-PAT derivatives, attention was next directed to the Ac-PAT series. The UV-vis spectra of the Ac-PAT are shown in **Figure 46a**. Ac-PAT 1 displays a π-π* absorption band at 392 nm, positioned at the frontier of the visible region. Compared to the NH_2-PAT derivatives, the absorption maxima of the Ac-PAT derivatives are shifted to lower wavelengths, ranging from 386 nm for Ac-PAT 4 to 410 nm for Ac-PAT 5. Both Ac-PAT 2 and Ac-PAT 3 exhibit absorption maxima at 400 nm, which represents only a modest improvement relative to Ac-PAT 1. The n-π* transition could not be distinguished, as in the case of NH_2-PAT derivatives, due to partial overlap with the π-π* band. Again a second band, at ~480 nm, is detected for Ac-PAT 4 at higher wavelength, mimicking somehow the behavior of the non-acetylated counterpart, PAT 4.

The ε of the Ac-PAT derivatives were determined in MeOH using Beer-Lambert's law. For Ac-PAT 1, $\varepsilon_{\lambda max}$ is 2.56 10^4 L.mol^{-1}.cm^{-1}, while the other derivatives exhibit higher values, ranging from 2.74 10^4 L.mol^{-1}.cm^{-1} for Ac-PAT 4 to 4.42 10^4 L.mol^{-1}.cm^{-1} for Ac-PAT 5. Overall, Ac-PAT show lower ε values compared to their NH_2-PAT counterparts. Nevertheless, the substituted Ac-PAT derivatives display both redshifted absorption and higher ε values than Ac-PAT 1, suggesting that substitution enhances spectroscopic properties, making them more suitable as MOST systems. These results indicate that Ac-PAT derivatives hold greater potential than NH_2-PAT for solar energy storage applications. However, further investigations are required to confirm this hypothesis, particularly regarding their photoisomerization behavior and thermal back-isomerization kinetics, which will be examined in the following section.

1.2.2.2 Photo- and back-isomerization processes

The photoisomerization of the Ac-PAT derivatives was monitored using UV-vis spectroscopy, as shown in **Figure 46b**, for the typical case of Ac-PAT 1 with a strong absorption band with a maximum at around 392 nm being observed prior to irradiation, which decreases upon irradiation. However, with this approach, it is challenging to accurately determine PSD and *Z*-isomer $t_{1/2}$, since ε are not known.

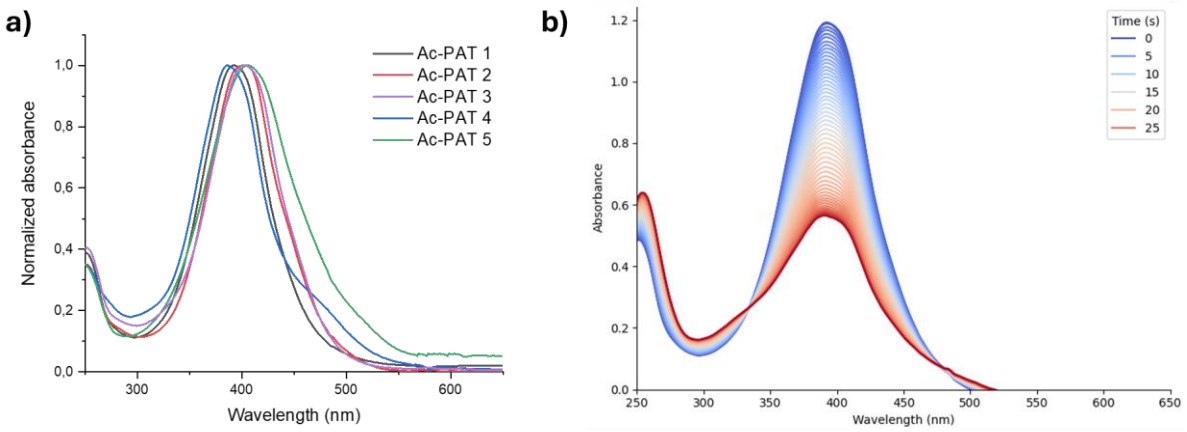

Figure 46. *a) Normalized UV-vis absorption spectra of Ac-PAT derivatives in MeOH. b) Time dependent evolution of Ac-PAT 1 during irradiation in MeOH (c ≈ 5 10^{-5} M). Curves progress from blue to red with increasing irradiation time, indicating photoisomerization.*

To overcome this limitation, LC-MS analyses were employed, as they allow the quantification of the relative proportions of the *E*- and *Z*-isomers, provided that both isomers exhibit similar ionization efficiencies. For Ac-PAT 1, the extracted chromatograms of the *m/z* 247 ions (protonated Ac-PAT1 – $[M+H]^+$) obtained before and after irradiation are shown in **Figure 47a**. The upper chromatogram (before irradiation) shows only the *E*-isomer, while the lower chromatogram (after irradiation) shows less than 10 % of *Z*-isomer. This low proportion is likely due to thermal back-isomerization occurring on the column during the LC separation, as also indicated by the *Z*-isomer signal tailing from the *Z*-isomer toward the *E*-isomer peaks. Two factors may explain this result: (i) the *Z*-isomer could be thermally unstable within the timescale of LC-MS analysis with injection and elution times exceeding its $t_{1/2}$; or (ii) the elution solvent mixture (ACN/H_2O) could influence the stability of the *Z*-isomer, an aspect further discussed in this thesis in the section dealing with solvent effects. Similar LC-MS analyses were performed on all Ac-PAT derivatives, leading to the same outcome, with the exception of Ac-PAT 4 as demonstrated hereafter. All the extracted chromatograms for each Ac-PAT derivatives are available in the **Appendix**, section **1.4**.

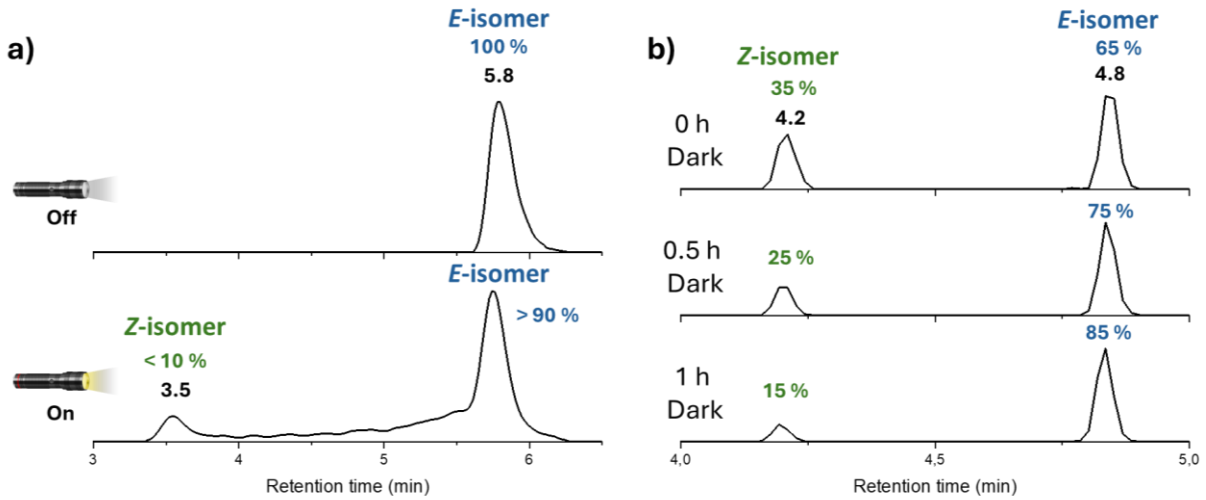

Figure 47. *a) LC-MS analysis (EIC chromatograms of the $[M+H]^+$ ions at m/z 247) of Ac-PAT 1 in MeOH before and after irradiation with the visible lamp. b) LC-MS analysis (EIC chromatograms of the $[M+H]^+$ ions at m/z 283) of Ac-PAT 4 in MeOH after different storage times in the dark in the LC-MS autosampler at 20 °C and in MeOH.*

For Ac-PAT 4, LC-MS analyses were carried out with analysis performed every 15 min to enable a time evolution monitoring. By extracting the EIC of the *m/z* 283 ions ($[M+H]^+$), the chromatogram shown on **Figure 47b** was obtained and the *E*- and *Z*-proportions were determined and normalized. Plotting the normalized *Z*-isomer content as a function of storage time and fitting the data with a decreasing exponential allows the extraction of the kinetic constant for the thermal back-isomerization (**Figure 48a**); a $t_{1/2}$ = 53 min is hence obtained for Ac-PAT 4. However, the exponential fit is slightly irregular, deviating from expected profile as shown on **Figure 48b**. Considering that PAT 4 was already known to degrade after multiple photo- and back-isomerization cycles, a similar process is suspected here.

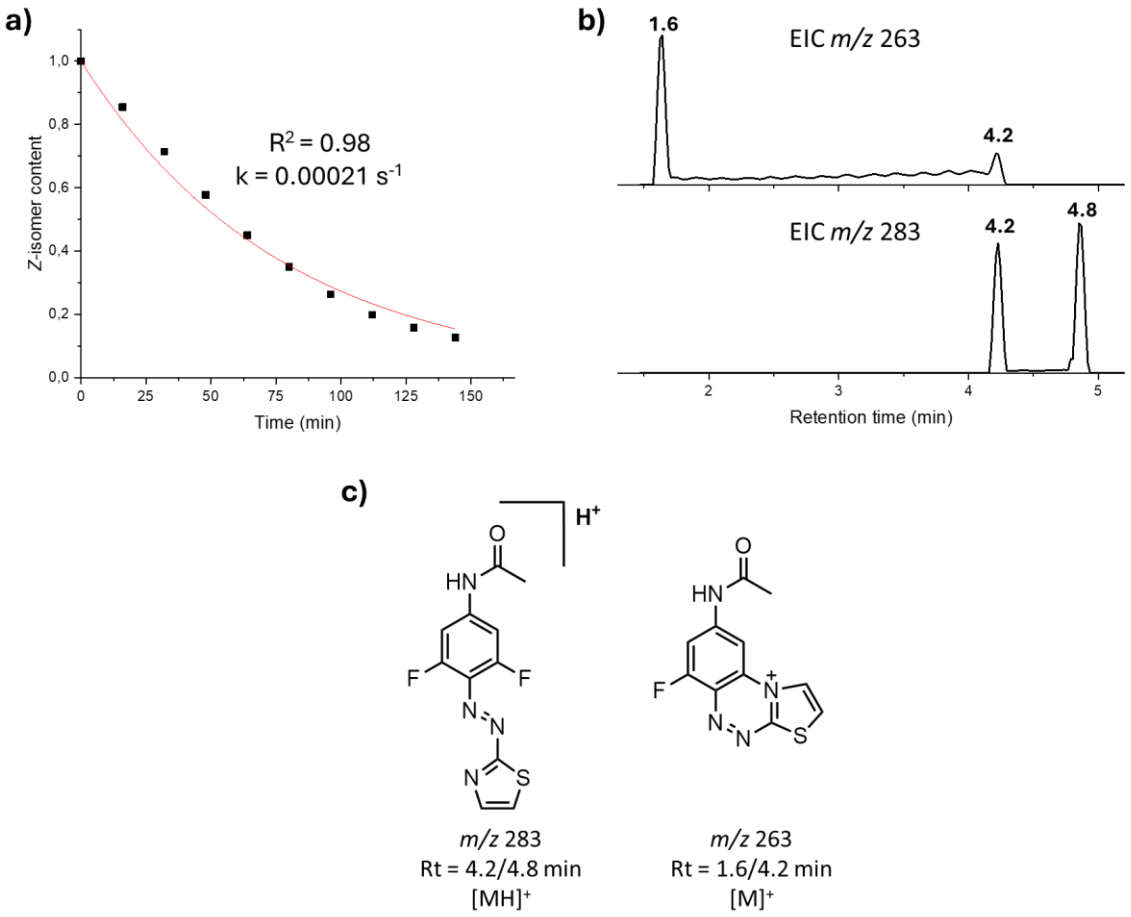

***Figure 48**. a) Monitoring of the thermal Z → E back isomerization kinetics by LC-MS analyses of Ac-PAT 4 : normalized absorbances plotted against time revealing first-order exponential decays (MeOH at 20 °C). b) LC-MS analysis (EIC chromatograms of the $[M+H]^+$ ions at m/z 283 and of the $[M]^+$ ions at m/z 263) of Ac-PAT 4 in MeOH after 10 min irradiation with the visible lamp. b) Structure of the m/z 283 and m/z 263 ions.*

Indeed, further investigation of the chromatograms revealed the appearance of a new peak at 1.6 min, corresponding to *m/z* 263 ions, formally corresponding to a 19 mass unit loss from the neutral molecule (**Figure 48c**). This new signal is observed to trail toward the *Z*-isomer peak at 4.2 min, suggesting that degradation occurs specifically from the *Z*-form. Closer analysis leads to the conclusion that this degradation results from an intramolecular nucleophilic add/elim, in which fluoride is substituted by the nucleophilic nitrogen atom of the thiazole ring generating a bicyclic cationic species. This process is strongly favored in the *Z*-form due to the special proximity of these atoms, as shown in **Figure 48b**. Since LC column employed was a C_{18} reversed-phase column, it is logical that the *m/z* 263 signal is observed at a shorter retention time. The low retention indicates a weak interaction between the compound and the hydrophobic stationary phase, likely due to the +1 charge of the molecule, resulting in an elution time close to the column dead time. Such a degradation of the *Z*-isomer generated upon photoisomerization is irreversible making the fluorinated PAT derivatives unsuitable for efficient solar energy storage and PAT 4 will not be considered for further peptoid incorporation in this thesis.

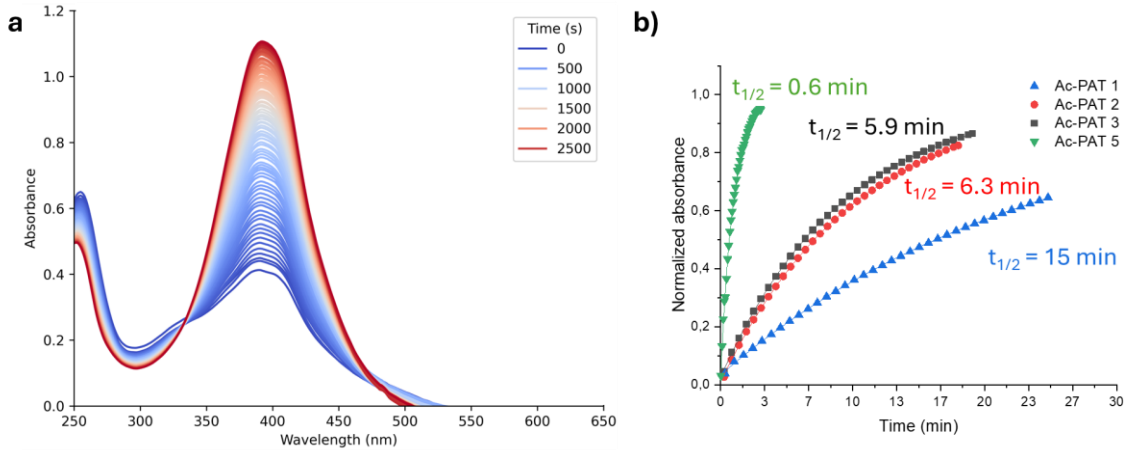

Figure 49. *a) Time dependent evolution of Ac-PAT 1 during thermal back-isomerization in MeOH ($c \approx 5\ 10^{-5}$ M). Curves progress from blue to red with increasing storage time in the dark at R.T. b) Monitoring of the thermal Z → E back isomerization kinetics by UV-vis spectroscopy of Ac-PAT derivatives. Normalized absorption plotted against time showing a first-order exponential growth (MeOH at R.T).*

UV-vis spectroscopy was further employed to average the *Z*-isomer $t_{1/2}$, despite the ε values of the Ac-PAT isomers not being available. The method consists of monitoring the maximum absorbance of each derivative after irradiation as exposed for Ac-PAT 1 in **Figure 49a**. The recorded absorbances are normalized between the minimum (after irradiation) and the maximum (before irradiation) values. Plotting this normalized absorbance as function of time and fitting the data with growing exponential function allows extraction of the kinetic constant for the thermal back-isomerization, as shown in **Figure 49b**. For Ac-PAT 1 in MeOH, the $t_{1/2}$ of the *Z*-isomer is established at approximately 15 min. In contrast, the substituted derivatives exhibit significantly shorter $t_{1/2}$ ranging from 0.6 min for Ac-Pat 5 to approximately 6 min for Ac-PAT 2 and Ac-PAT 3. One notable exception is Ac-PAT 4, which displays a noticeably longer $t_{1/2}$ = 53 min.

UV-vis spectroscopy were carried out exclusively at R.T, since the experimental setup is not equipped with a temperature-control system. Consequently, kinetic parameters ($\Delta H^{\ddagger}$ and $\Delta S^{\ddagger}$) could not be determined using this method. To compare the $t_{1/2}$ obtained by UV-vis spectroscopy and LC-MS analyses, we assume that UV-vis monitoring the growth of the *E*-isomer (growing exponential) and LC-MS analyses monitoring the decay of the *Z*-isomer (decreasing exponential), describe the same kinetics process, yielding identical rate constants.

The approximate $t_{1/2}$ values obtained in MeOH for all Ac-PAT derivatives are summarized in **Table 3**.

1.3 INTERMEDIATE CONCLUSION

As a conclusion for this section, five NH_2-PAT derivatives were successfully synthesized, with adjustments to the synthetic protocols depending on the aminothiazole substitution pattern. These compounds were subsequently acetylated to mimic the acetyl linkage present in peptoids, enabling comparison of their properties with PAT-grafted peptoids and evaluation of the influence of the peptoid backbone. Regarding their properties, NH_2-PAT derivatives generally absorb in the visible region with relatively high ε values at λ_{max}. However, their

Z-isomers exhibit low thermal stability, with $t_{1/2}$ below one second for all compounds except PAT 4. Although PAT 4 displays apparent enhanced stability, it actually undergoes degradation after several photo- and back-isomerization cycles. For Ac-PAT derivatives, the absorption is blueshifted and ε values are lower compared to their amino analogues, though absorption remains close to the visible region with acceptable intensity. Substitution appears to improve spectroscopic properties, as all substituted derivatives display increased absorption and higher ε values. In terms of thermal stability, the *Z*-isomer $t_{1/2}$ range from 0.6 min to 15 min, still too short for efficient solar energy storage. The exception is Ac-PAT 4, which shows a $t_{1/2}$ of 53 min, but similarly to its amino counterpart, it suffers from degradation through intermolecular nucleophilic substitution. Compared to pristine AB, the PAT derivatives exhibit enhanced absorption in the visible region and display higher $\varepsilon_{\pi\text{-}\pi^*}$ values, indicating improved photoactive properties. However, thermal stability of the *Z*-isomers is significantly reduced, down to approximately 15 min for PAT 1, and even lower for other derivatives. All the values are summarized in **Table 3**.

	NH_2-PAT			Ac-PAT		
	$\lambda_{\pi\text{-}\pi^*}$ (nm)	$\varepsilon_{\pi\text{-}\pi^*}$ ($L.mol^{-1}.cm^{-1}$)	$t_{1/2}$ (s)	$\lambda_{\pi\text{-}\pi^*}$ (nm)	$\varepsilon_{\pi\text{-}\pi^*}$ ($L.mol^{-1}.cm^{-1}$)	$t_{1/2}$ (min)
1	463	(2.93 ± 0.02) 10^4	< s	392	(2.56 ± 0.03) 10^4	15.0 ± 0.1
2	465	(4.07 ± 0.23) 10^4	< s	400	(3.61 ± 0.05) 10^4	6.3 ± 0.1
3	465	(3.71 ± 0.21) 10^4	< s	400	(3.74 ± 0.14) 10^4	5.9 ± 0.1
4	420	(2.88 ± 0.15) 10^4	1.65 ± 0.1	386	(2.74 ± 0.05) 10^4	53.4 ± 0.1
5	490	(5.57 ± 0.05) 10^4	< s	410	(4.42 ± 0.02) 10^4	0.6 ± 0.02

Table 3. *Summary of the relevant MOST parameters for NH_2-PAT and Ac-PAT determined in MeOH: $\lambda_{\pi\text{-}\pi^*}$ is the maximum absorption wavelength, $\varepsilon_{\pi\text{-}\pi^*}$ is the molar extinction coefficient at maximum of absorption and $t_{1/2}$ is the metastable isomer half-life time at R.T (Ac-PAT 1, 2, 3 and 5) or 20 °C (Ac-PAT 4).*

1.4 APPENDICES

Appendix 1. *IR spectra of the different molecules synthetized during this work*

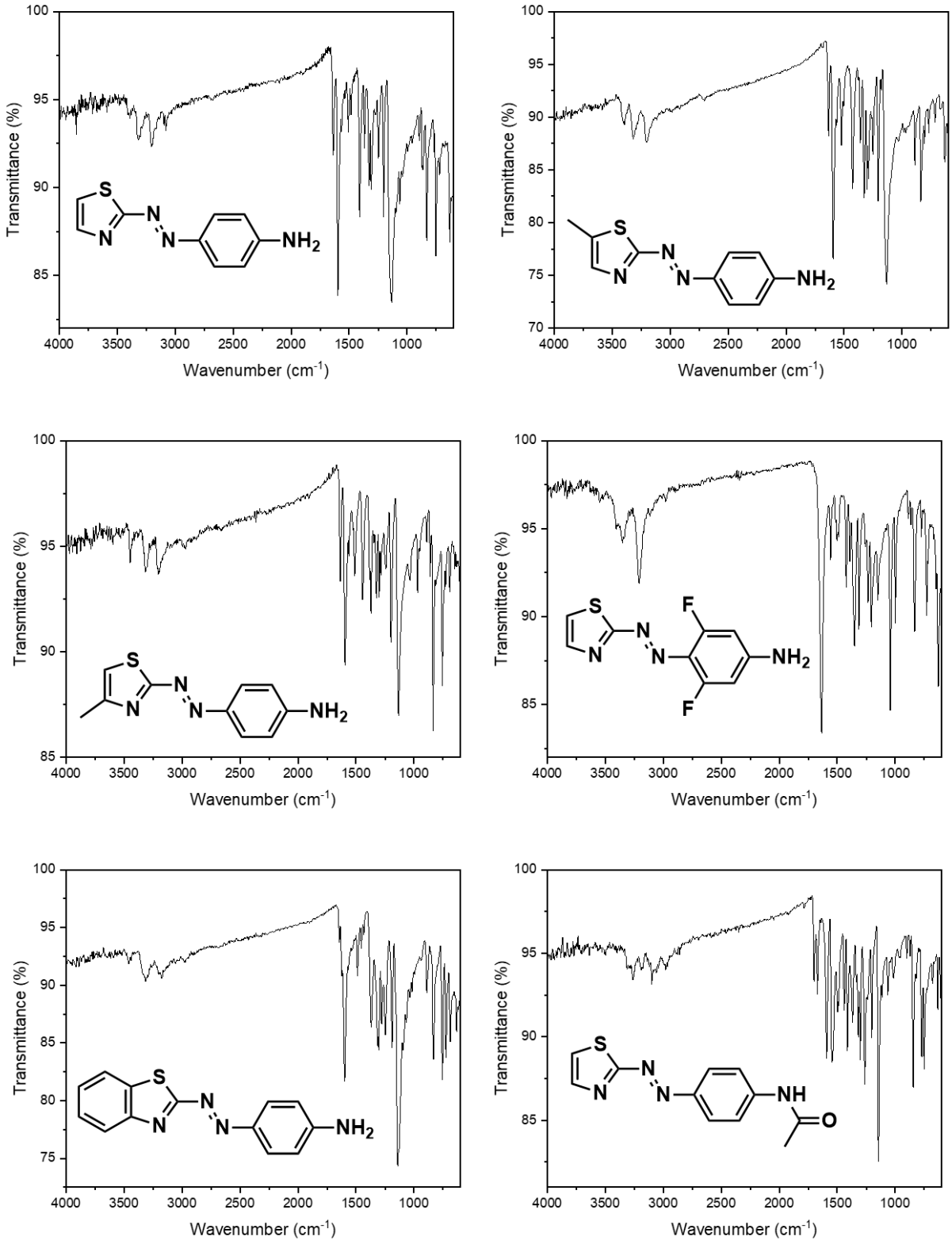

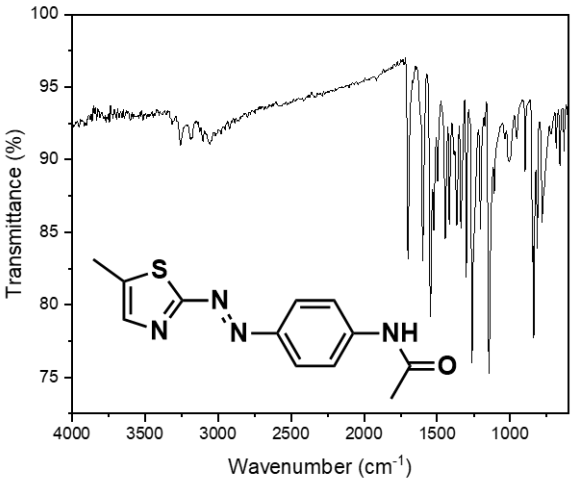
Transmittance (%)
Wavenumber (cm-1)
S
N
N
N
NH
O

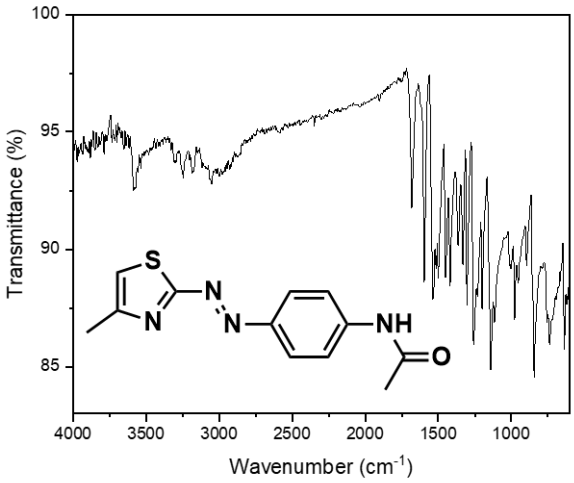
Transmittance (%)
Wavenumber (cm-1)
S
N
N
N
NH
O

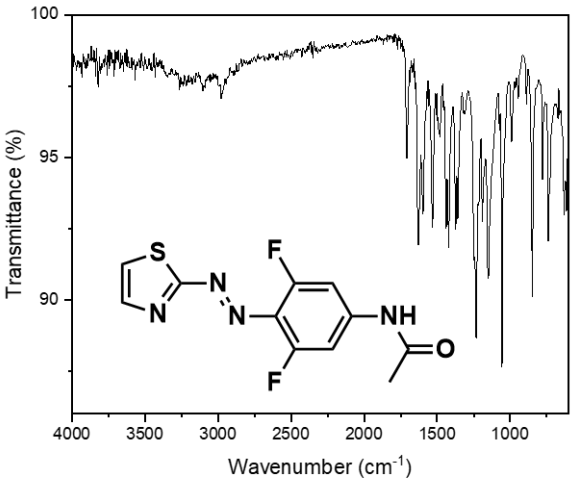
Transmittance (%)
Wavenumber (cm-1)
S
N
N
N
F
F
NH
O

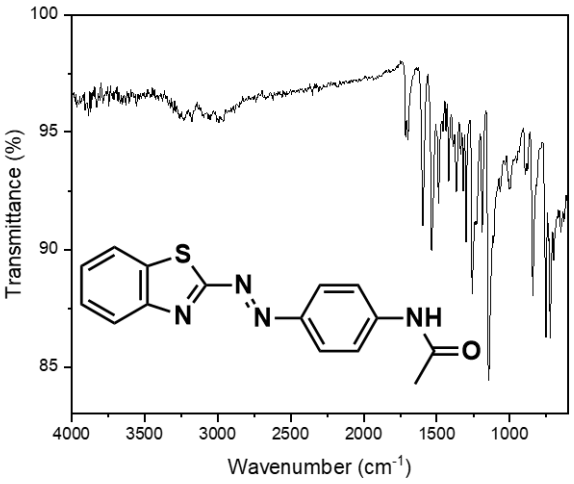
Transmittance (%)
Wavenumber (cm-1)
S
N
N
N
NH
O

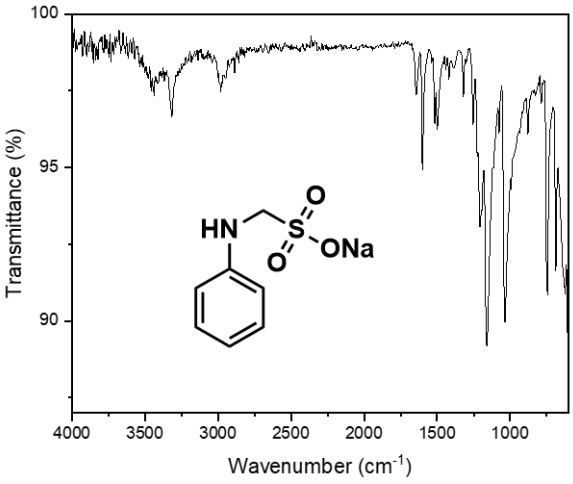
Transmittance (%)
Wavenumber (cm-1)
HN
S
O
O
ONa

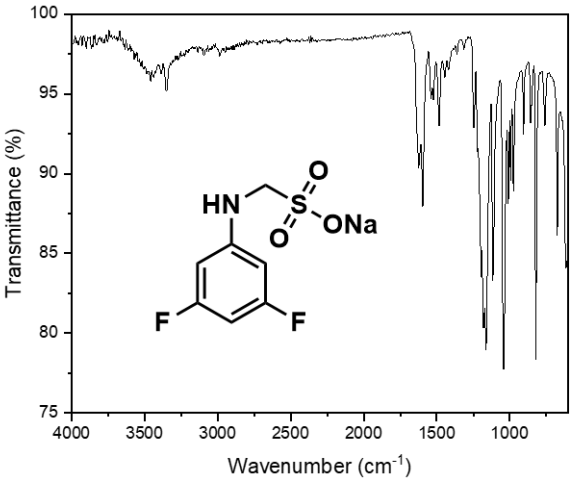
Transmittance (%)
Wavenumber (cm-1)
HN
S
O
O
ONa
F
F

Appendix 2. *^{1}H-NMR (500 MHz) spectra of the different molecules synthetized during this work in D_2O, DMSO or $CDCl_3$.*

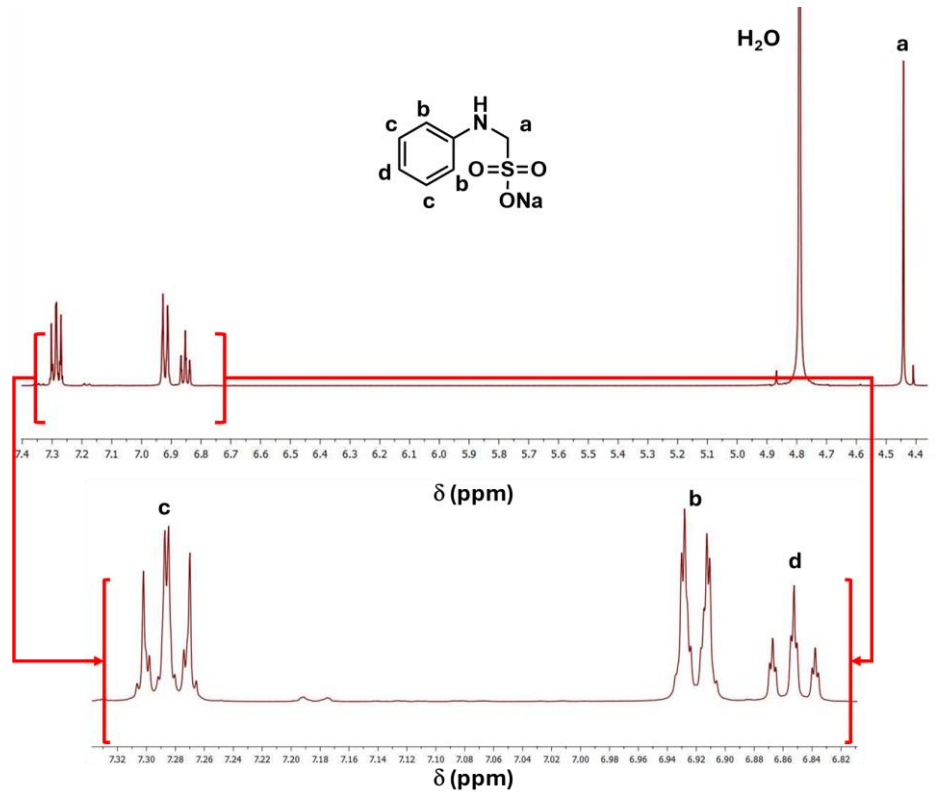

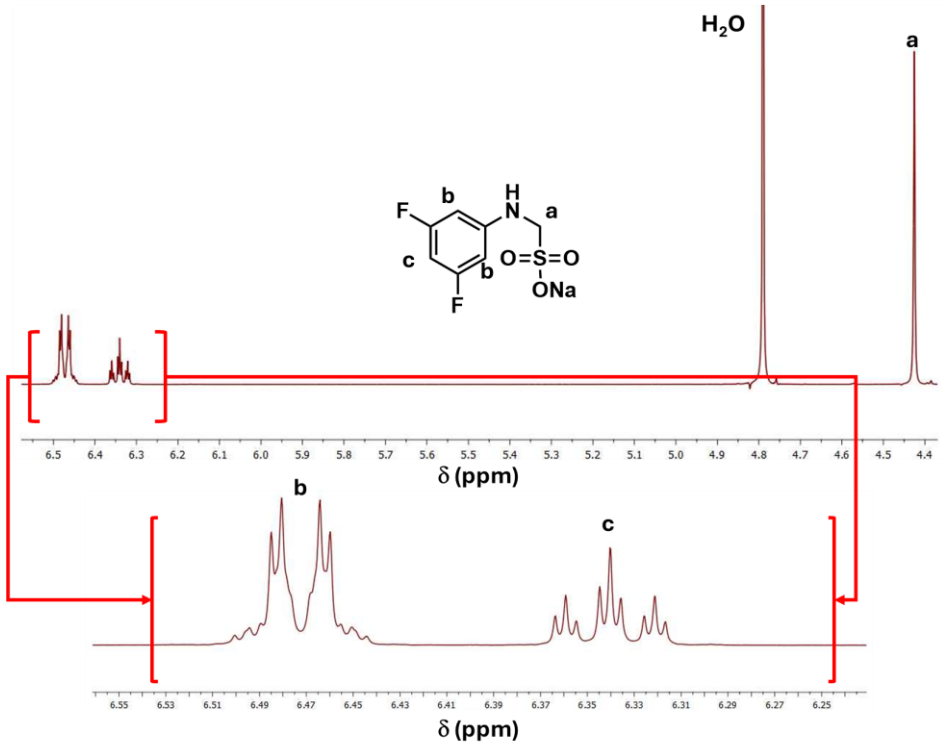

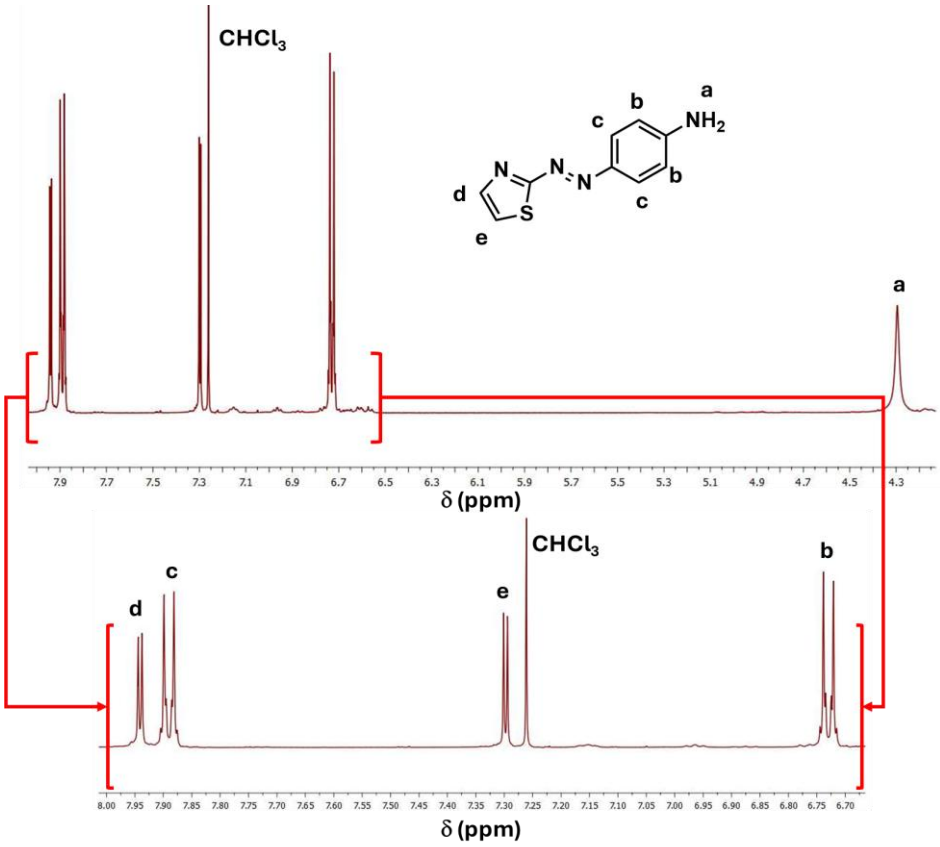
CHCl3
a
b
c
NH2
d
e
δ (ppm)
CHCl3
b
c
d
e
δ (ppm)

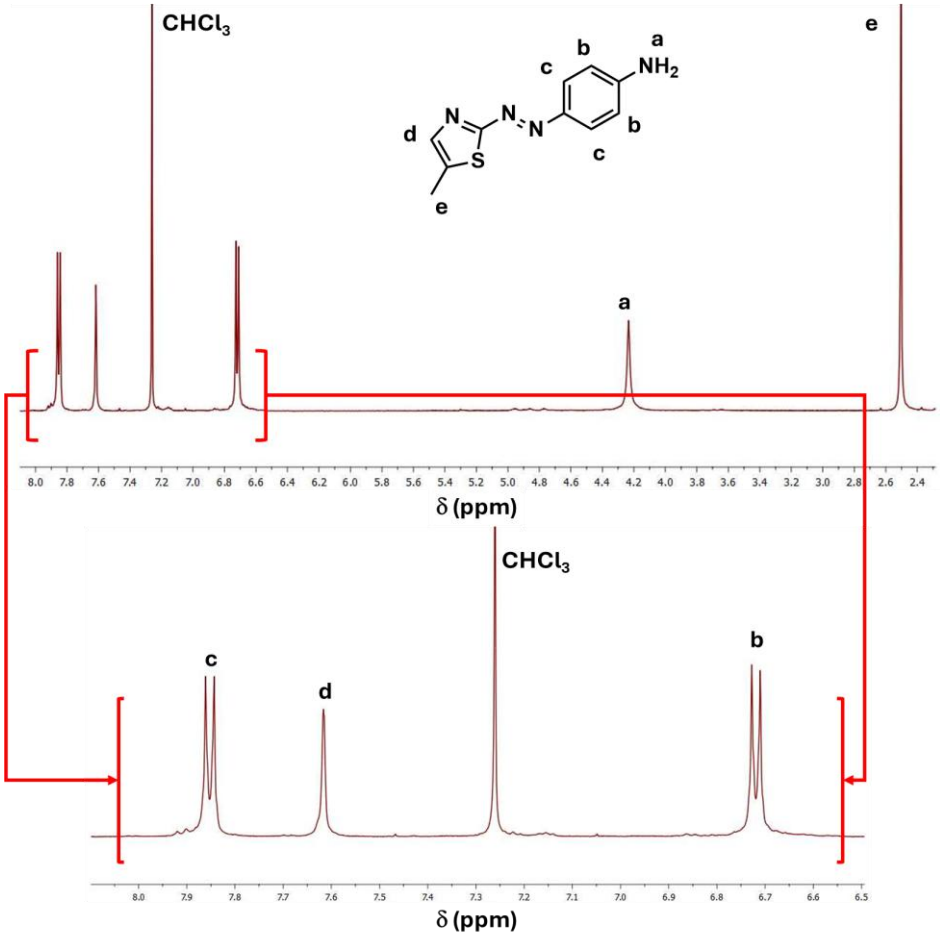
CHCl3
e
a
b
c
NH2
d
e
δ (ppm)
CHCl3
b
c
d
δ (ppm)

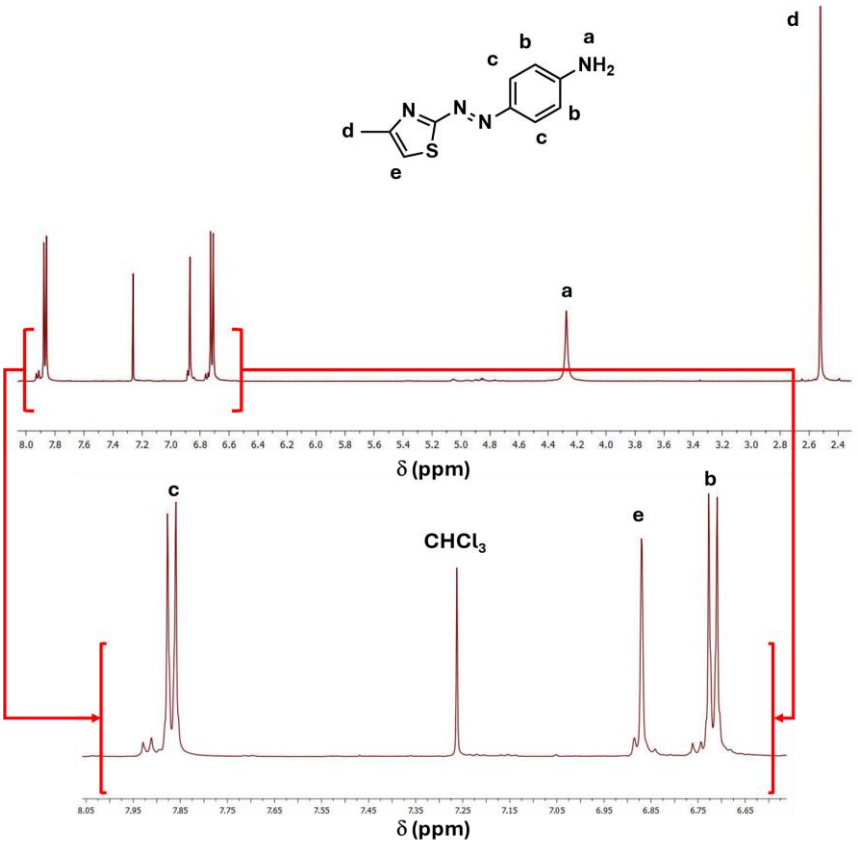
d
a
c
b
a
NH2
c
b
N
N
N
d
S
c
e
a
δ (ppm)
c
b
e
CHCl3
δ (ppm)

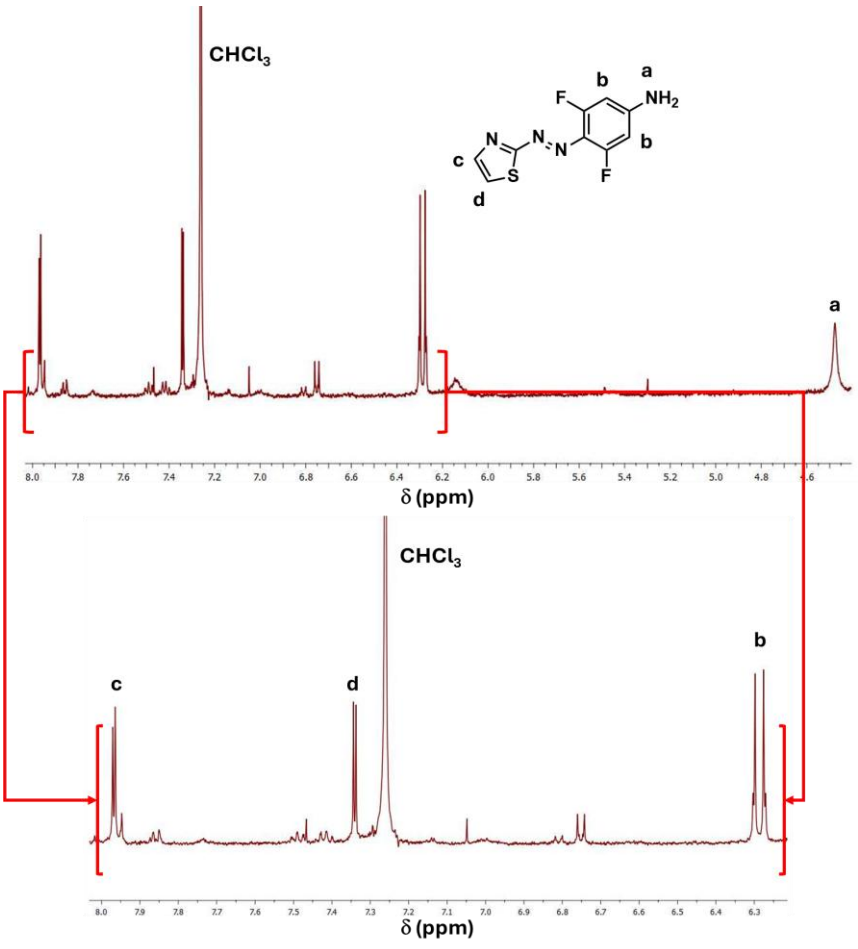
CHCl3
b
a
F
NH2
N
N
b
c
S
F
d
a
δ (ppm)
CHCl3
b
c
d
δ (ppm)

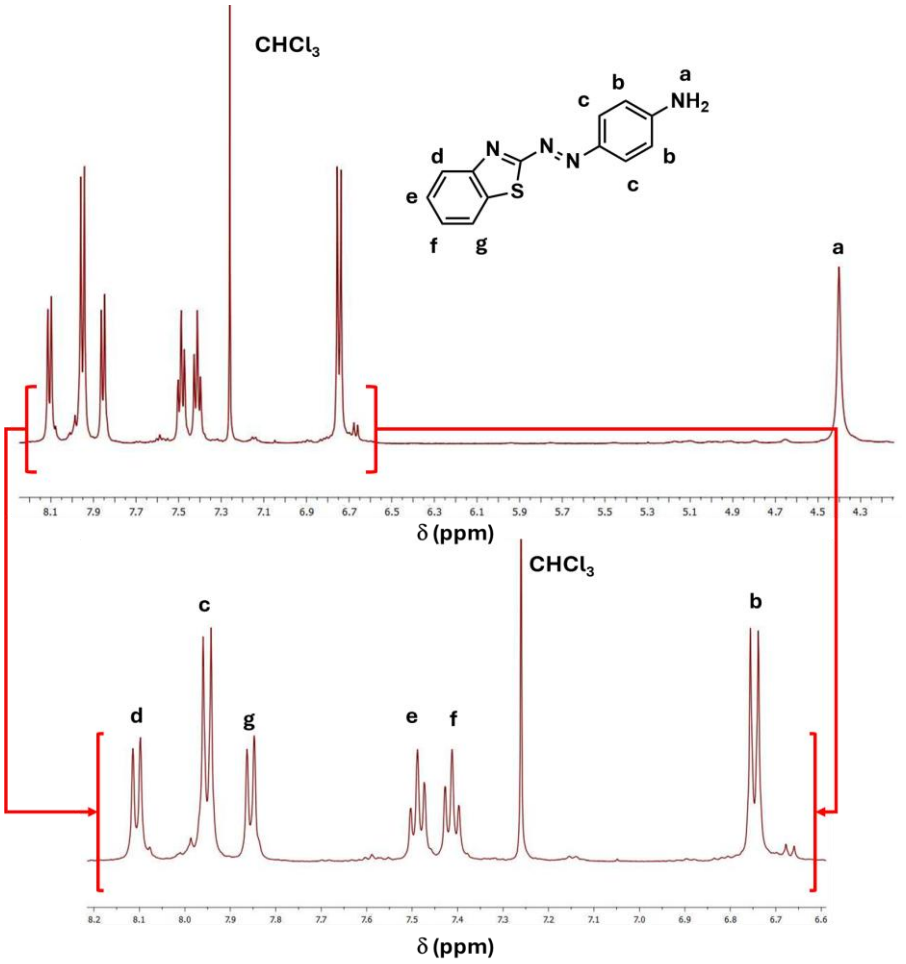
CHCl3
a
b
c
NH2
d
e
f
g
δ (ppm)
CHCl3
c
b
d
g
e
f
δ (ppm)

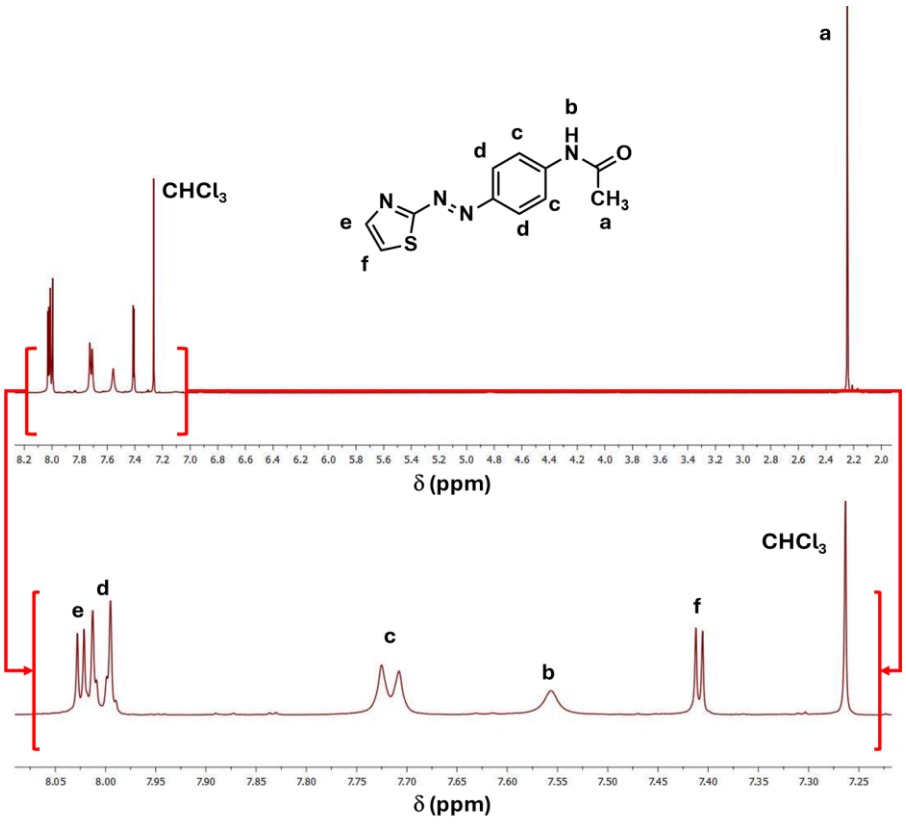
a
b
H
N
O
CH3
c
d
e
f
CHCl3
δ (ppm)
CHCl3
e
d
c
b
f
δ (ppm)

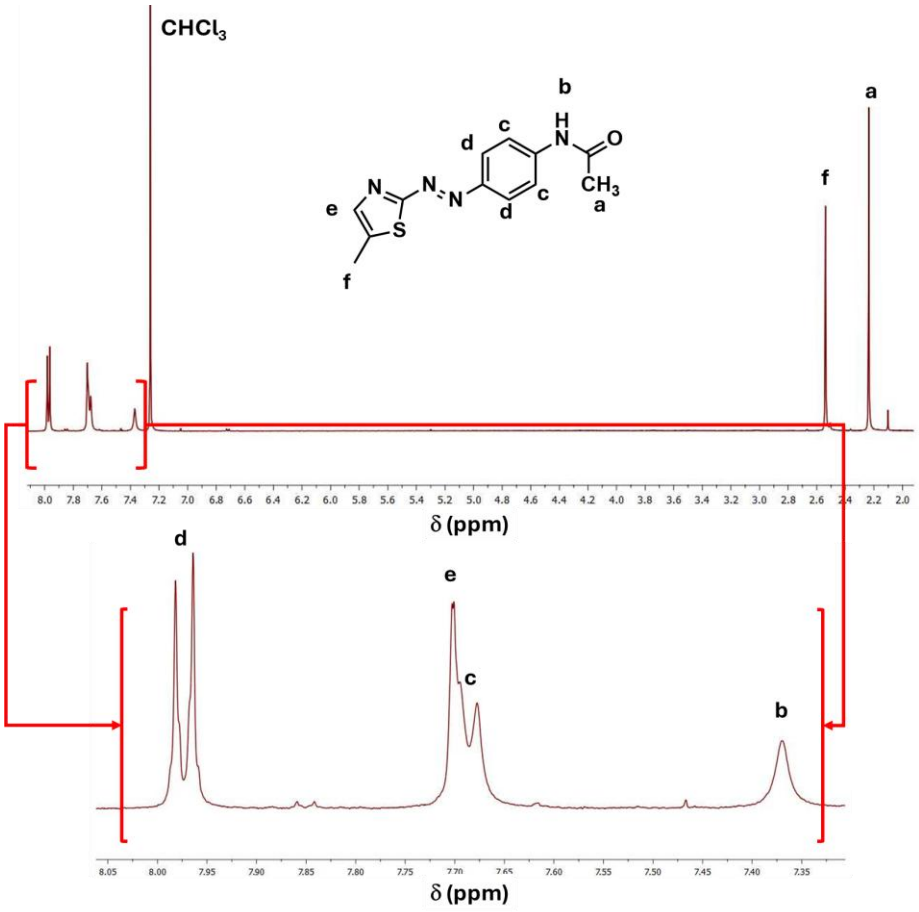
CHCl3
b
H
N
O
c
d
a
CH3
N
N
N
e
S
f
f
a
d
c
d
e
c
b
δ (ppm)

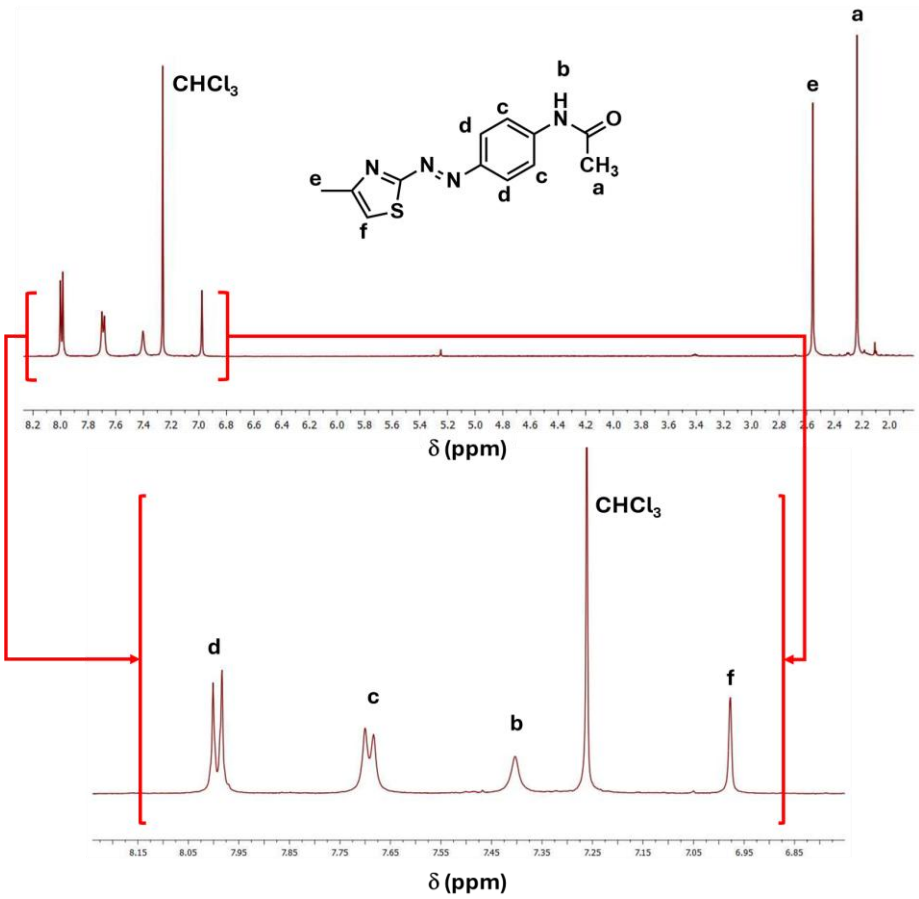
a
CHCl3
b
H
N
O
e
c
d
CH3
N
N
N
e
S
a
f
d
c
CHCl3
d
c
b
f
δ (ppm)

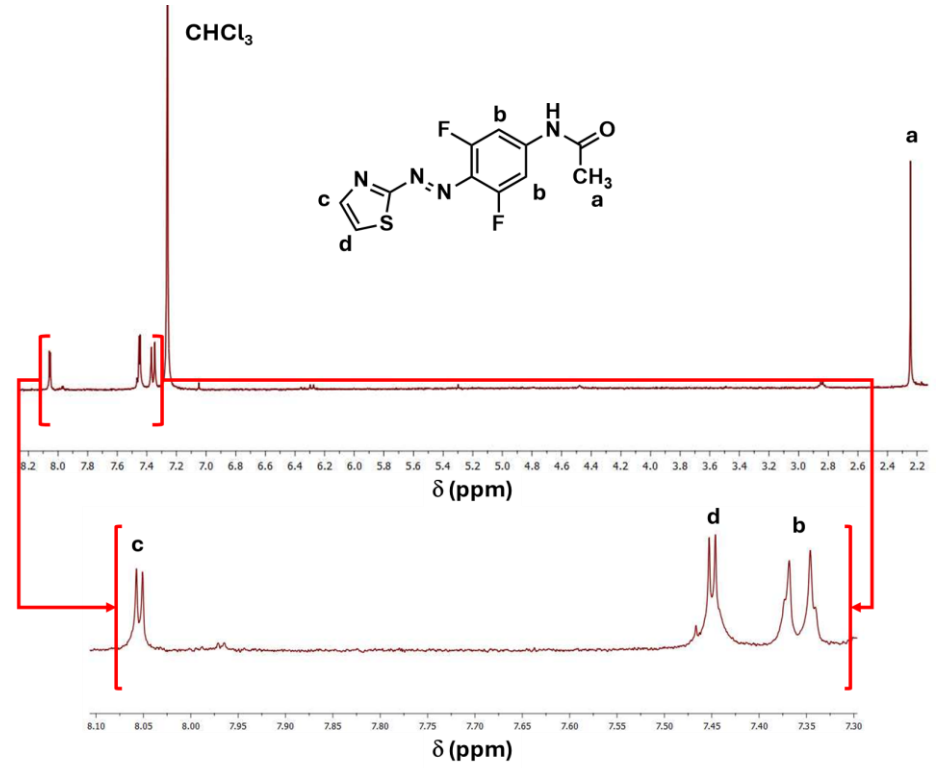
CHCl3
F
b
H
N
O
a
N
N
N
CH3
c
b
a
S
F
d
δ (ppm)
c
d
b
δ (ppm)

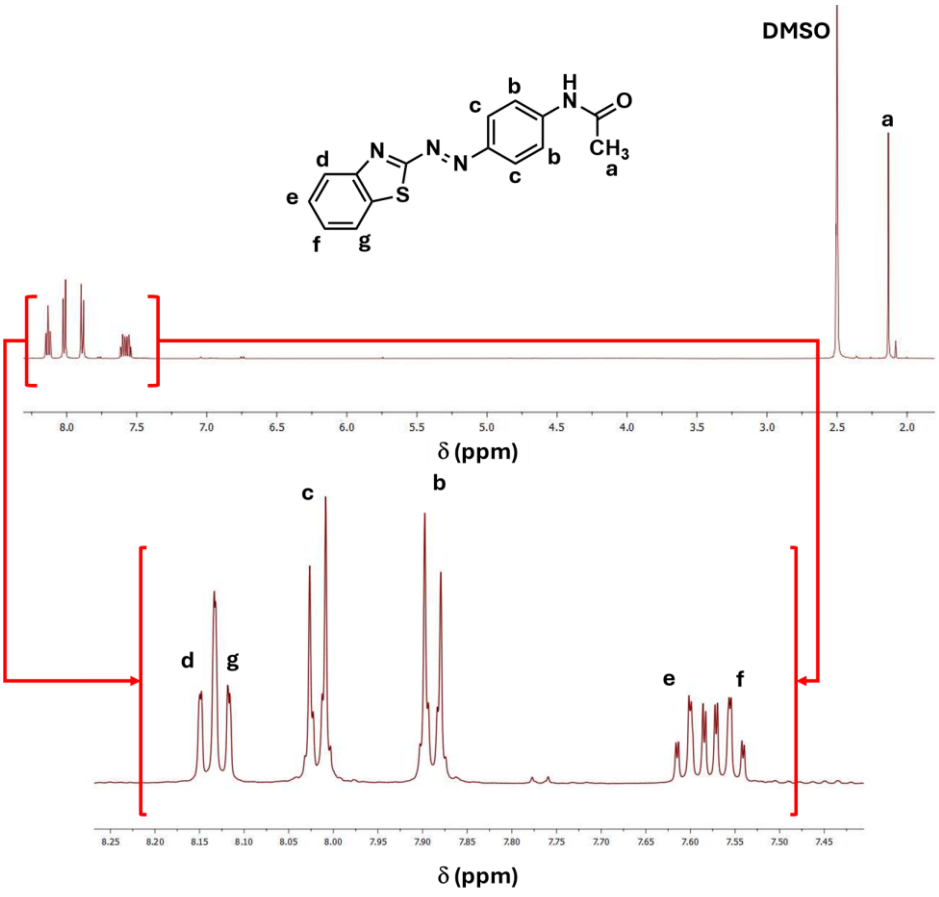
DMSO
b
H
N
c
O
a
d
N
N
CH3
b
c
e
S
f
g
δ (ppm)
c
b
d
g
e
f
δ (ppm)

Appendix 3. *ESI-MS (+) (Waters Synapt G2-Si): MS spectra (upper spectrum) and MS/MS spectra (bottom spectrum) for each PAT synthetized. MS/MS performed on $[M+H]^+$ with E_{col} = 12 eV.*

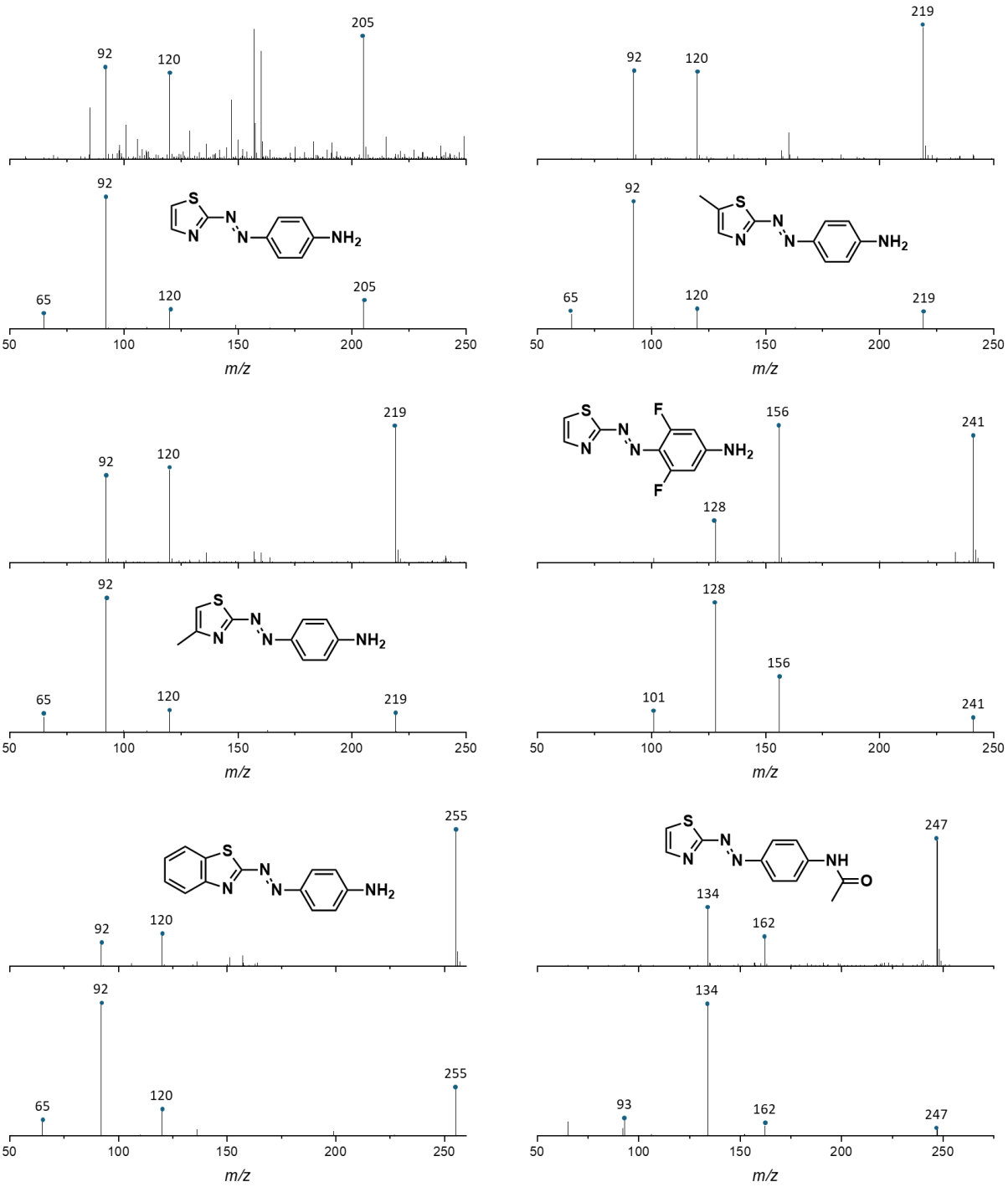

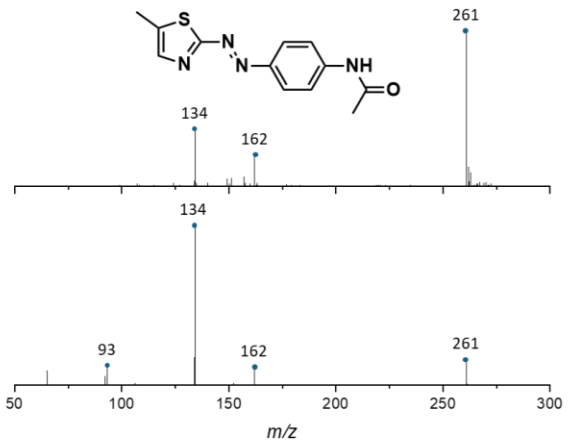
261
134
162
134
93
162
261
50
100
150
200
250
300
m/z

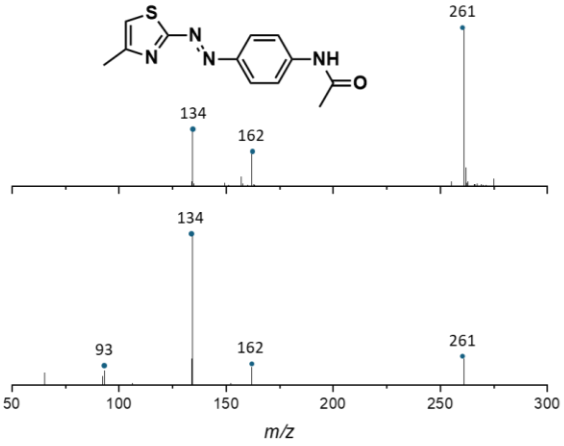
261
134
162
134
93
162
261
50
100
150
200
250
300
m/z

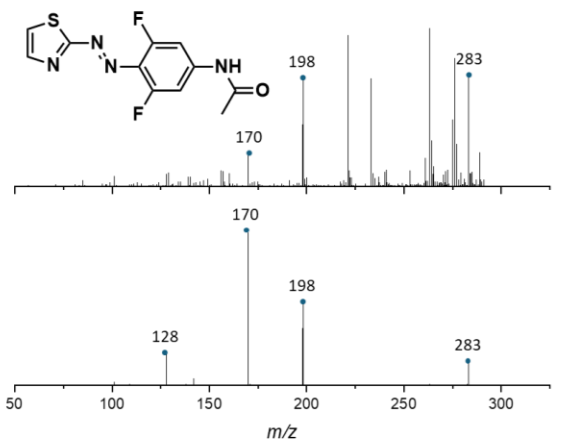
F
198
283
170
170
198
128
283
50
100
150
200
250
300
m/z

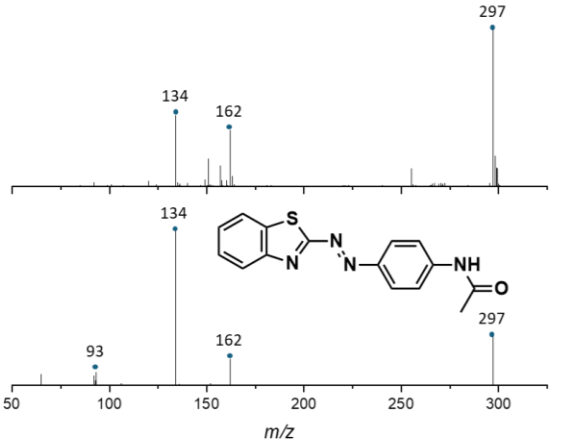
297
134
162
134
93
162
297
50
100
150
200
250
300
m/z

Appendix 4. *Molecular weights, compositions, and exact mass measurements determined by HRMS on a Waters Synapt G2-Si mass spectrometer for the different PAT synthetized.*

PAT	M.W ($g.mol^{-1}$)	Elemental composition	Calculated mass	Experimental mass	Error (ppm)
PAT 1	204.25	$C_9H_9N_4S$	205.0548	205.0550	1.0
PAT 2	218.28	$C_{10}H_{11}N_4S$	219.0704	219.0707	1.4
PAT 3	218.28	$C_{10}H_{11}N_4S$	219.0704	219.0704	0.0
PAT 4	240.23	$C_9H_7N_4F_2S$	241.0359	241.0359	0.0
PAT 4 cyclic	221.23	$C_9H_6N_4FS$	221.0297	221.0296	0.5
PAT 5	254.31	$C_{13}H_{11}N_4S$	255.0704	255.0700	1.6
Ac-PAT 1	246.29	$C_{11}H_{11}N_4OS$	247.0654	247.0652	0.8
Ac-PAT 2	260.31	$C_{12}H_{13}N_4OS$	261.0810	261.0811	0.4
Ac-PAT 3	260.31	$C_{12}H_{13}N_4OS$	261.0810	261.0809	0.4
Ac-PAT 4	282.27	$C_{11}H_9N_4OF_2S$	283.0465	283.0463	0.7
Ac-PAT 4 cyclic	263.27	$C_{11}H_8N_4OFS$	263.0403	263.0404	0.4
Ac-PAT 5	296.35	$C_{15}H_{13}N_4OS$	297.0810	297.0812	0.7

Appendix 5. *Determination of the molar extinction coefficients for each PAT derivatives in MeOH from the linear fit of absorbance versus concentration according to the Beer-Lambert law.*

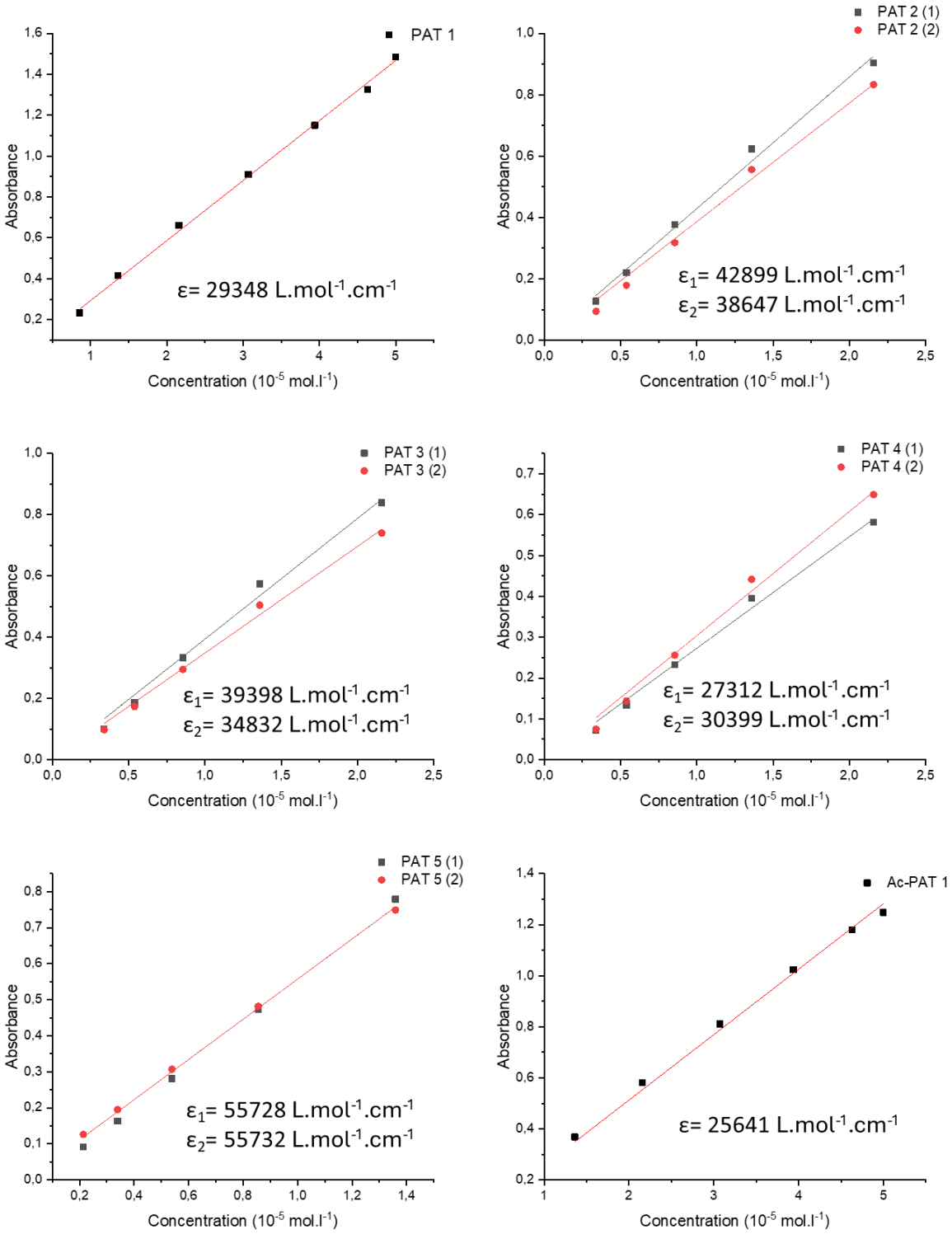

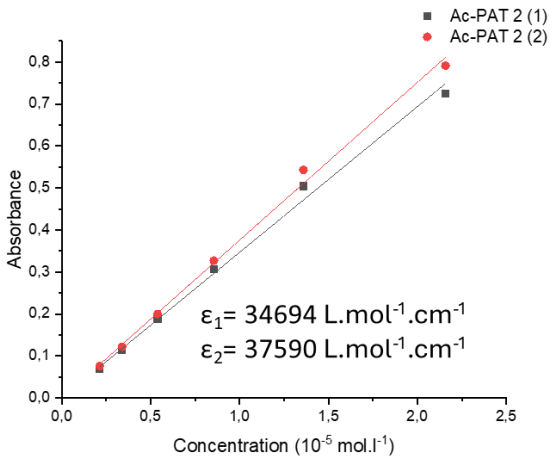
Ac-PAT 2 (1)
Ac-PAT 2 (2)
Absorbance
Concentration (10^{-5} mol.l^{-1})
ε_1= 34694 L.mol^{-1}.cm^{-1}
ε_2= 37590 L.mol^{-1}.cm^{-1}

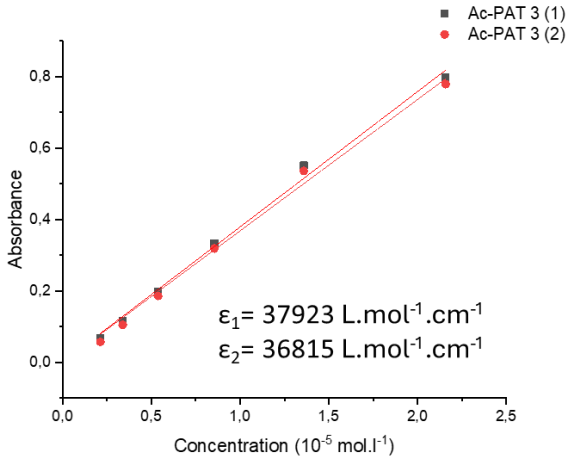
Ac-PAT 3 (1)
Ac-PAT 3 (2)
Absorbance
Concentration (10^{-5} mol.l^{-1})
ε_1= 37923 L.mol^{-1}.cm^{-1}
ε_2= 36815 L.mol^{-1}.cm^{-1}

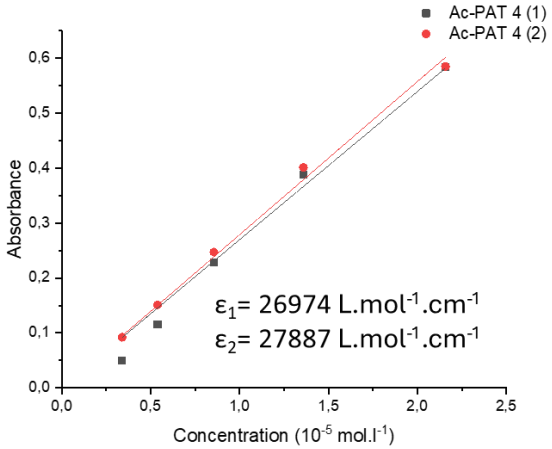
Ac-PAT 4 (1)
Ac-PAT 4 (2)
Absorbance
Concentration (10^{-5} mol.l^{-1})
ε_1= 26974 L.mol^{-1}.cm^{-1}
ε_2= 27887 L.mol^{-1}.cm^{-1}

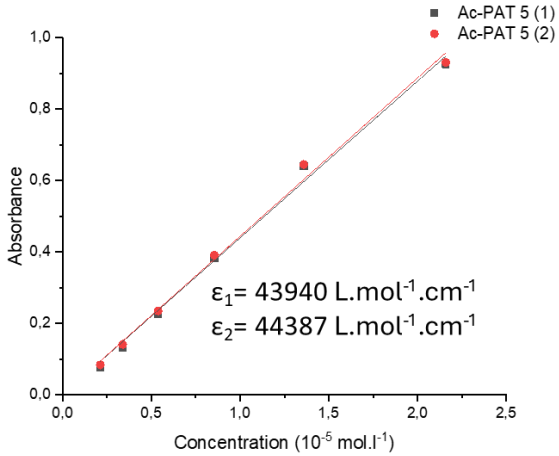
Ac-PAT 5 (1)
Ac-PAT 5 (2)
Absorbance
Concentration (10^{-5} mol.l^{-1})
ε_1= 43940 L.mol^{-1}.cm^{-1}
ε_2= 44387 L.mol^{-1}.cm^{-1}

Appendix 6. *UV-vis spectra of substituted PAT before and after irradiation (MeOH, 5 10^{-5} M). The black curves correspond to PAT derivatives before irradiation, the red curves correspond to PAT derivatives after irradiation.*

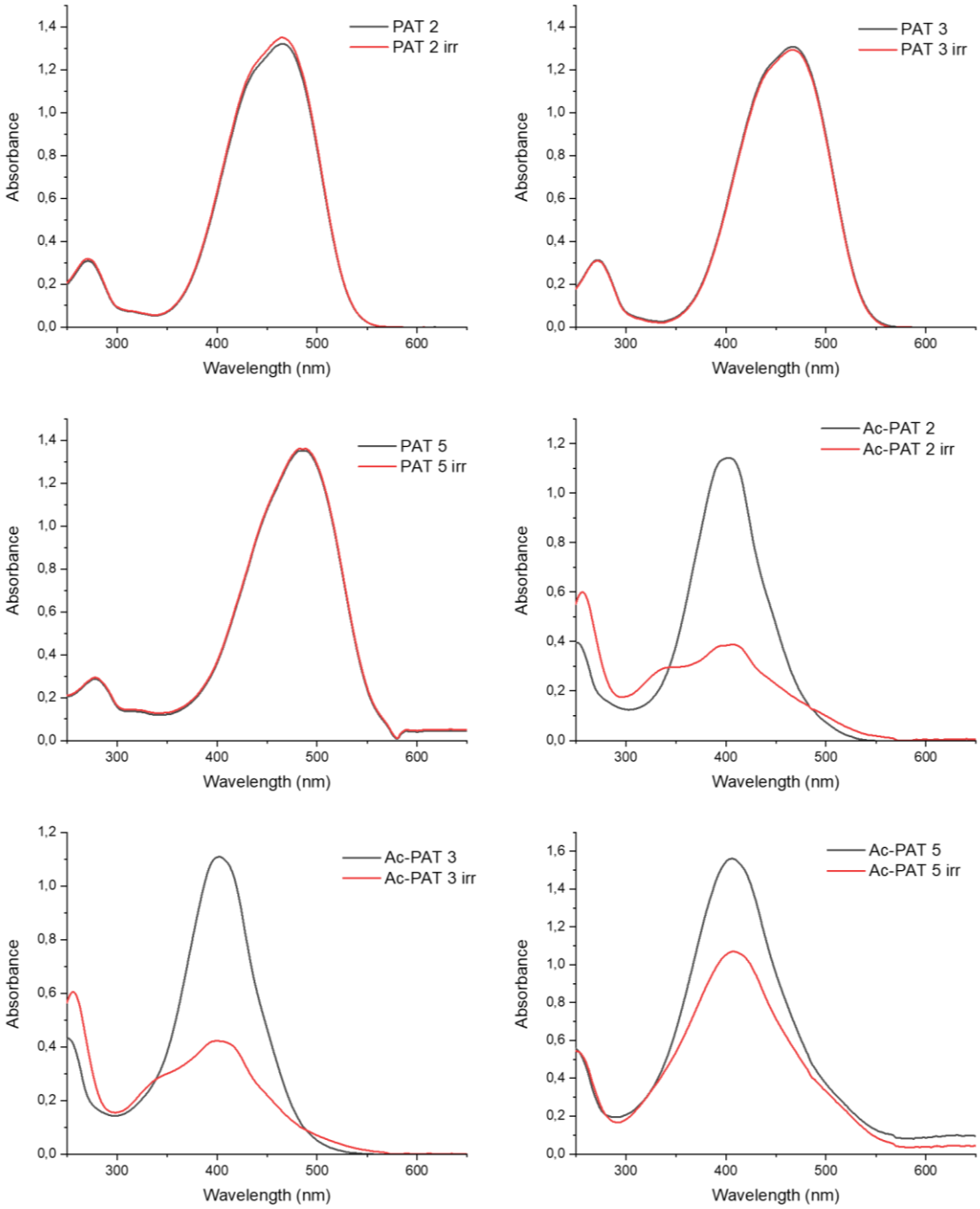

Appendix 7. *LC-MS analysis (EIC chromatograms of the $[M+H]^+$ ions) of Ac-PAT 2, Ac-PAT 3 and Ac-PAT 5 in MeOH before and after irradiation with the visible lamp.*

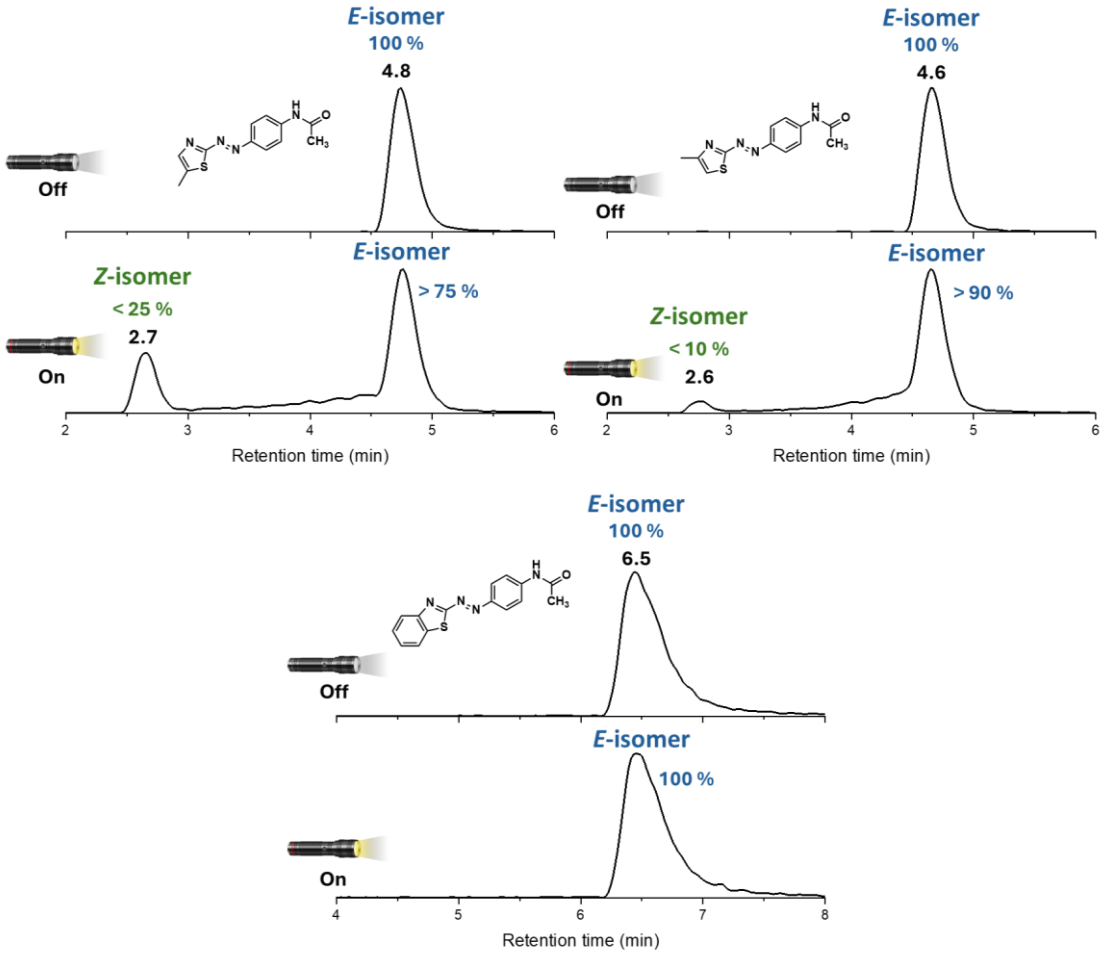

2. THE CURIOUS CASE OF PEPTOIDS

2.1 SYNTHESIS AND STRUCTURAL CHARACTERIZATION

As detailed in the **Experimental section**, the different peptoids were synthesized via solid phase synthesis following the submonomer method originally developed by Zuckermann.[238,253] Since one of the objectives of this work is to evaluate the influence of the peptoid backbone and its structural organization on the MOST properties of PAT derivatives, hybrid peptoid structures incorporating (S)-phenylethylamine (spe), methylamine (sar) and PAT-based side chains were designed and synthetized. The spe side chain was selected for two main reasons: (i) its potential to engage in π-π interaction with the PAT chromophore and (ii) its well-known ability to promote the formation of secondary helical conformation in solution. In contrast, the sar side chain lacks the ability to participate in such interaction or to induce structural organization. Before studying longer peptoids bearing multiple chromophores, it is necessary to evaluate the interaction between the peptoid backbone and PAT residue on short sequences, typically 3-unit peptoids.

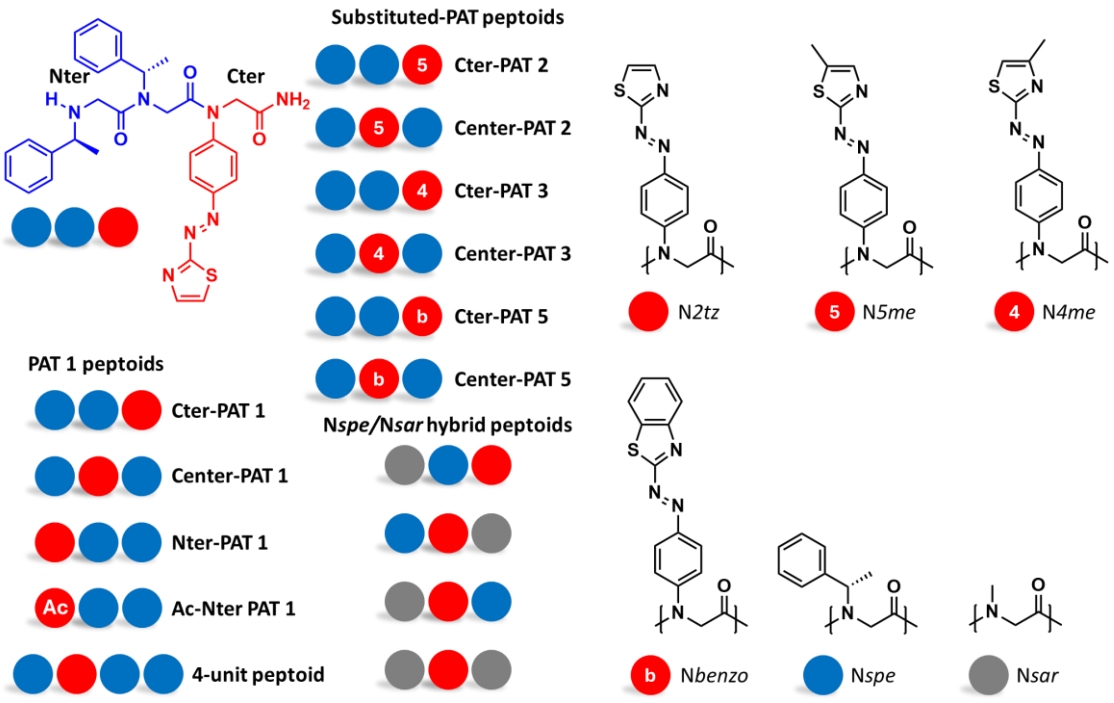

Figure 50. *Ball formalism of the 15 peptoids (14 trimers and 1 tetramer) synthetized in this work with the structure of the NspeNspeN2tz peptoids as a typical example.*

Using the protocol established by Tassignon *et al.* for the incorporation of AB into peptoids, as described in the **Experimental section**, 15 peptoids were synthetized.[114] During this thesis, additional optimizations were carried out to improve the overall yield of the peptoid synthesis. Peptoids associating PAT 1 and Nspe/Nsar were synthetized using the original method, which employes a mixture of bromoacetic acid and DIC for the bromoacetylation step. In contrast, the substituted-PAT peptoids were synthetized using an optimized method based on bromoacetyl bromide for the bromoacetylation step. In this context, the bromide acts as a better leaving group than the diisopropyl urea, resulting in improved reaction efficiency.

PAT 1 peptoids were synthetized to investigate whether the peptoid backbone enhances the intrinsic properties of PAT 1. To this end, three 3-unit isomers were prepared, differing only in the position of the PAT 1 unit within the sequence. These regioisomers, *i.e.* N*spe*N*spe*N*2tz*, N*spe*N*2tz*N*spe* and N*2tz*N*spe*N*spe*, are named according to the position of PAT 1, respectively Cter-PAT 1, Center-PAT 1 and Nter-PAT 1 (**Figure 50**). A ball formalism is also established to allow a better visualization of the peptoids sequence, see also **Figure 50**. In the Nter-position, PAT 1 is linked to the peptoid backbone through a secondary amine, whereas in the Center- and Cter-positions, the linkage occurs via an amide bond. The Center-PAT 1 is flanked by two spe side chains, which could influence its properties through potential π-π interactions, but could also introduce steric hindrance. In contrast, the Cter-PAT 1 position is more sterically free and less affected by π-π interaction.

Substituted-PAT units (see **Figure 50**) were also introduced at a later stage of the research to confirm the trends previously observed with their Ac-PAT counterparts, which displays enhanced spectroscopic properties but reduced thermal stability as described in the previous section. Finally, the stabilization effects of the peptoid backbone and side chains were investigated through the synthesis of hybrid peptoids incorporating PAT, N*sar*/N*spe* residues.

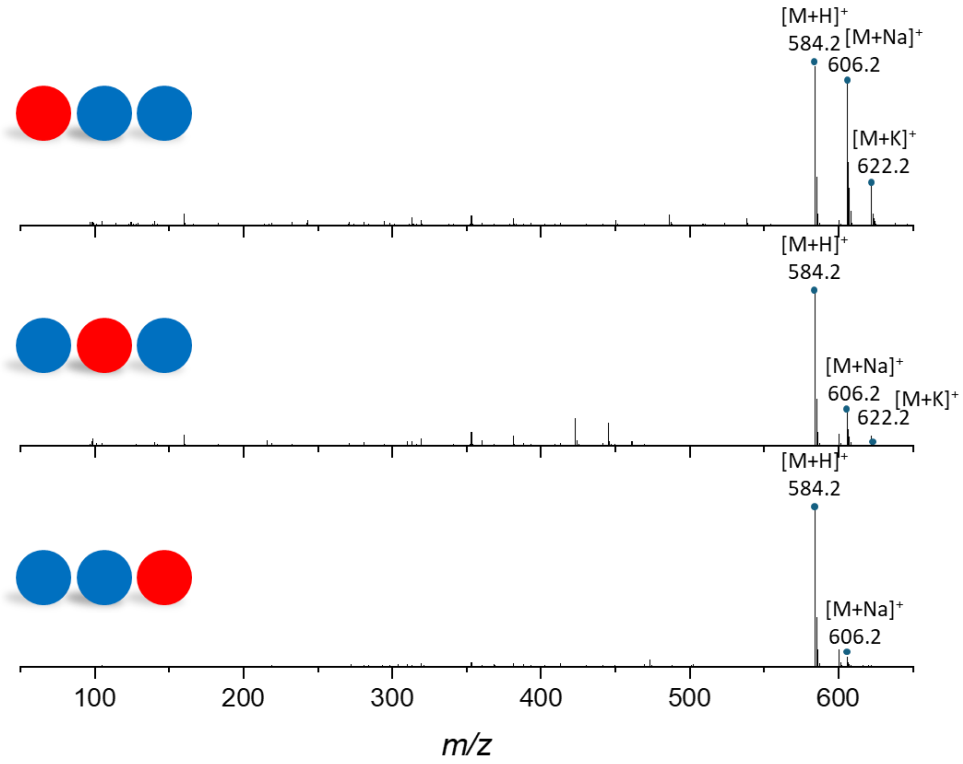

Figure 51. *ESI-MS (Waters Synapt G2-Si) spectra of the purified peptoids, ions corresponding to N2tzNspeNspe (top), NspeN2tzNspe (middle) and NspeNspeN2tz (bottom) can be found on the spectra under protonated form, sodium adduct and potassium adduct.*

As confirmed by the corresponding ESI-MS spectra on **Figure 51**, the expected peptoids were obtained, with the detection of the protonated (*m/z* 584), sodium-adduct (*m/z* 606) and potassium-adduct (*m/z* 622) ions. The exact mass measurements (**Table 4**) further support the successful synthesis of the three peptoid isomers, which appear to be relatively pure given the absence of shorter oligomers. However, these single-stage mass spectra provide data only on the molecular composition of the peptoid not on their sequence. Since the three compounds are positional isomers, they share the same molecular mass and therefore appear at identical *m/z* in the spectra (**Figure 51**). To gain insight into the primary structures of these peptoid ions, MS/MS experiments were performed.

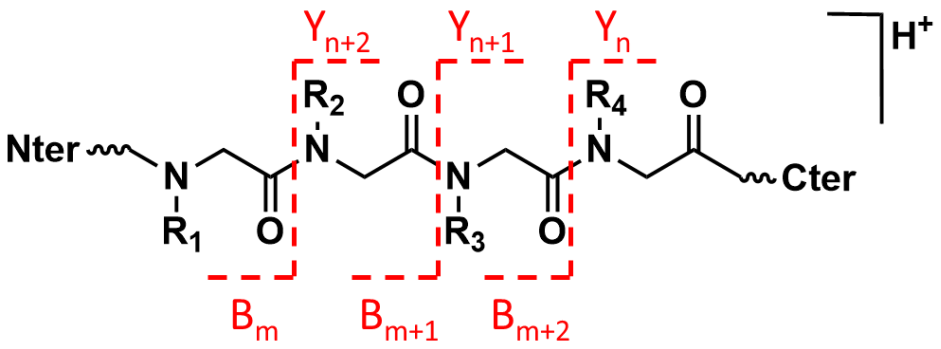

Figure 52. *B/Y fragmentation of protonated peptoids. The cleavage occurs between the nitrogen and the carbonyl of the peptoid (R denotes the side chain). Scheme adapted from*[264]*.*

As detailed in the **Experimental section** (Section 3.2.), CID experiments provide structural information by inducing structure-specific fragmentation of precursor ions through inelastic collisions with neutral gas. The resulting fragment ions are characteristic of the precursor ion primary structures. In the present study, peptoid fragmentations mainly occur through amide bond cleavages, allowing the sequence of the peptoid ions to be determined by analyzing the mass differences between consecutive peaks in the MS/MS spectra. Before interpreting these spectra, it is essential to understand the fragmentation mechanism involved. Due to their structural similarity to peptides, the fragmentation formalism used for peptoids ions is analogous to that of peptide ions.[265,266] The predominant fragmentation pathway observed in peptoids, known as B/Y fragmentation, occurs between the carbonyl and the nitrogen atom of the amide bond. This process yields two complementary fragment ions: B-ions, which retain the Nter extremity and Y ions, which contain the Cter extremity (**Figure 52**).[264]

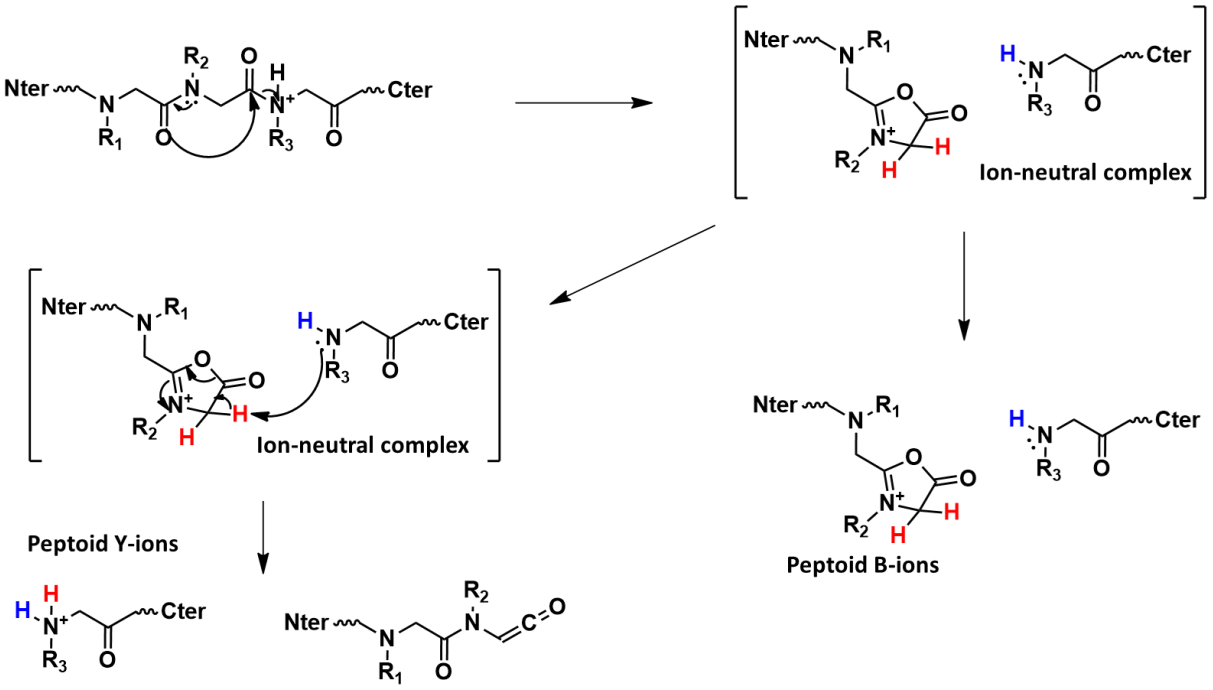

Scheme 8. *Collision-induced dissociation of protonated peptoids: general mechanism of the B/Y fragmentation. (R denotes the side chain). Scheme adapted from*[264].

The general mechanism of B/Y fragmentation is illustrated on **Scheme 8** and involves the mobile proton model (MPM) which is well-established for peptide fragmentation.[267–269] In the first step, upon collisional activation, the proton migrates from the most basic site of the molecule to the amide nitrogen atom of the backbone. This proton transfer significantly weakens the amide C-N bond and increases the electrophilicity of the carbonyl carbon. Consequently, the oxygen atom of the preceding amide group can perform a nucleophilic attack, leading to the cleavage of the backbone C-N bond and the formation of an ion-neutral complex (INC). From this intermediate complex, two types of fragments ions can be generated. When the positive charge is retained by the cyclic species, B-fragment ions are detected. Alternatively, if a proton transfer occurs between the cyclic ion and the neutral counterpart, Y-fragment ions are produced.[264]

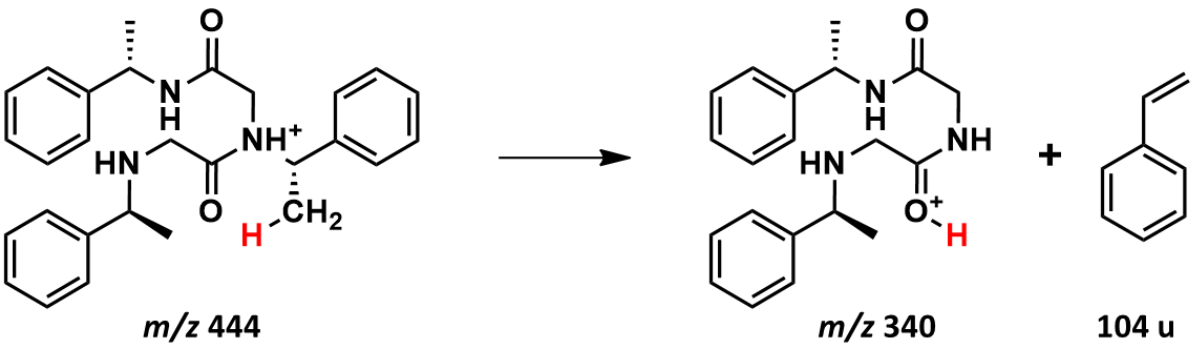

Scheme 9. *Collision-induced dissociation of protonated peptoids: example of the SCL mechanism for protonated peptoid with sequence NspeNspeNspe (m/z 444), leading to fragment ions at m/z 340 upon styrene loss. Scheme adapted from*[270].

In addition to the B/Y fragmentation, two other peptoid fragmentations can occur in peptoids, namely the Side-Chain Loss (SCL) reaction and the A/Y fragmentations.[264,270] As illustrated on **Scheme 9**, the SCL process is particularly favored for spe side chain and proceeds via a concerted rearrangement initiated from the protonated amide nitrogen of the peptoid backbone. This rearrangement leads to the elimination of a styrene (corresponding to a loss of 104 mass units), resulting in a charged peptoid ion lacking one spe side chain.[270]

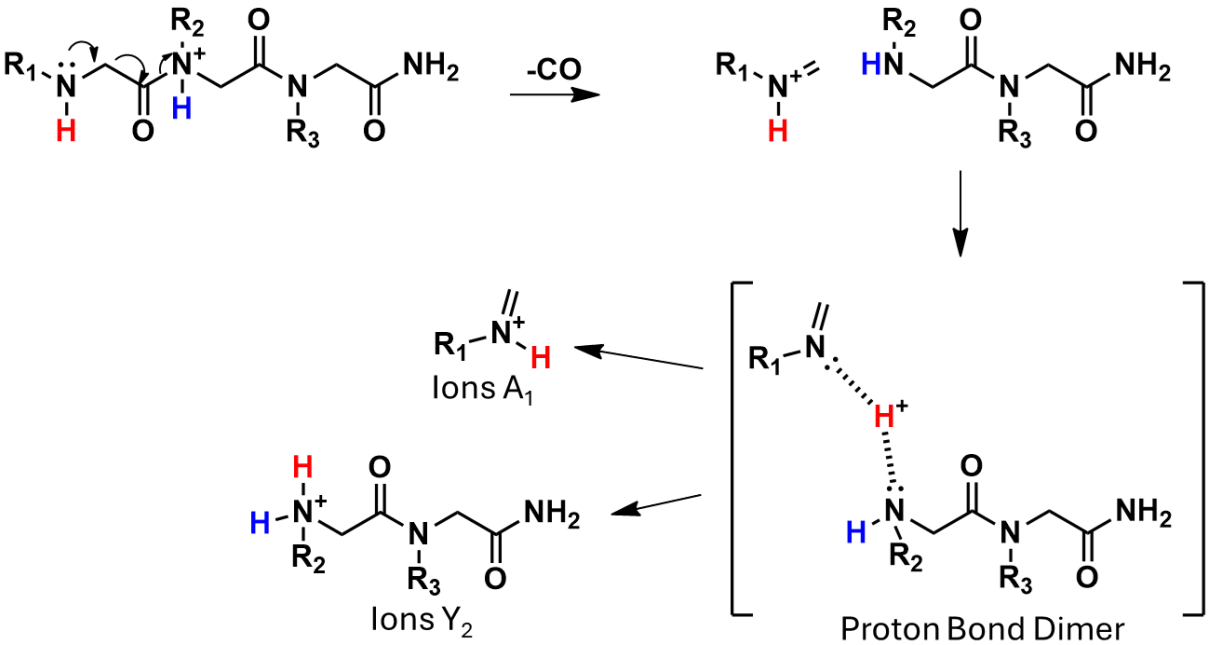

Scheme 10. *Collision-induced dissociation of protonated peptoids: general mechanism of the A/Y fragmentation. (R denotes the side chain). Scheme adapted from*[264].

Finally, regarding the A/Y fragmentation pathway, upon protonation of an amide nitrogen atom, the rearrangement is initiated from the Nter unit, leading to the loss of a carbon monoxide (CO) molecule (**Scheme 10**). This process generates a transient intermediate know as a "Proton Bound Dimer" (PBD), which associates an imine fragment with the truncated peptoid, as illustrated in **Scheme 10**. Depending on the proton affinity (PA) of both species, this PBD intermediate can dissociate via two competing pathways: it may yield an iminium ion (A-fragment ion) or a protonated truncated peptoid (Y-fragment ion).[264] As with B/Y fragmentation, analysis of the consecutive A/Y fragmentations provides valuable information for determining the sequence of peptoid ions.

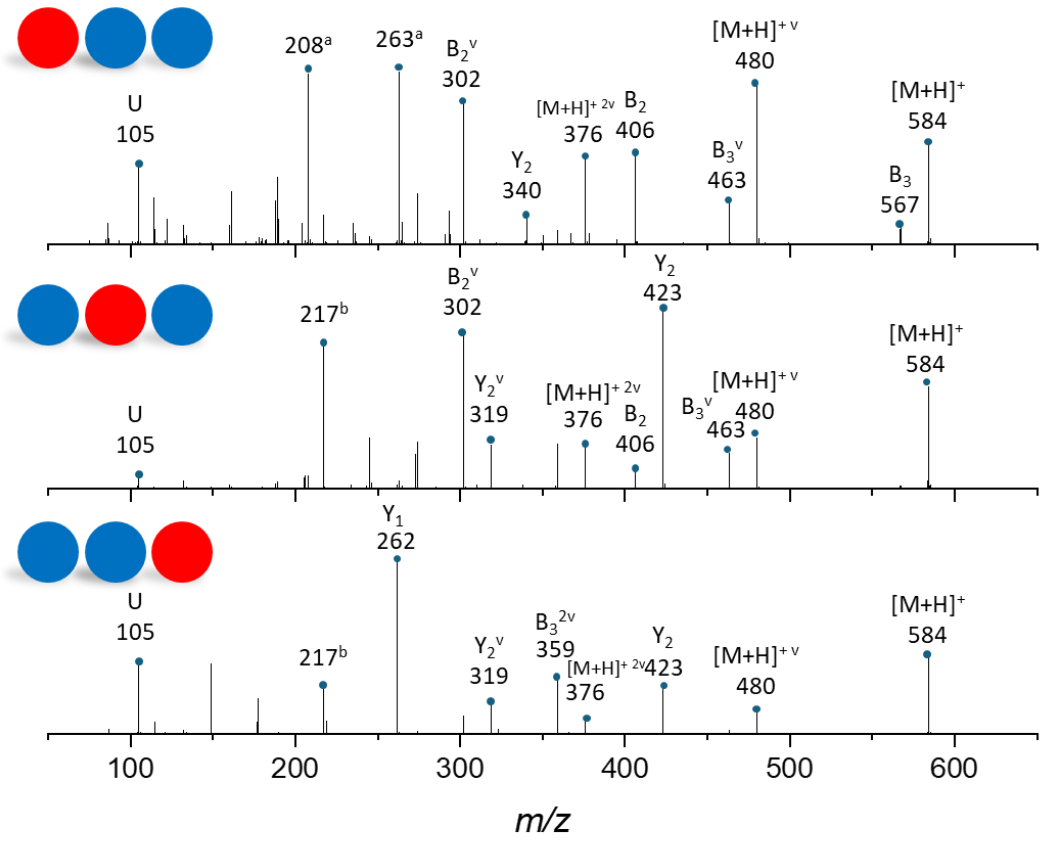

Figure 53. *ESI-MS/MS (Waters Synapt G2-Si) CID spectra of m/z 584 ($[M+H]^+$) ions corresponding to protonated N2tzNspeNspe (top), NspeN2tzNspe (middle) and NspeNspeN2tz (bottom). Spectra were recorded with collision energy (E_{col}) of 17 eV. [a] Fragmentation of the thiazole group, likely due to generation of a relatively stable thiazolyl-carbene species. [b] Fragment corresponding to successive B/Y and A/Y fragmentation.*

By applying these fragmentation mechanisms to interpret the MS/MS spectra of the three isomeric peptoid (**Figure 53**), the sequence of each positional isomer could be confirmed. In these spectra, the different fragments are denoted as X_n^{zV}, where X represents the fragment type (A,B or Y), n indicates the position of the fragment along the peptoid backbone, V designates the loss of one or more spe side chains and z corresponds to the number of lost spe units. For example, the ions labeled Y_2^{2V} correspond to the Y_2 fragment that has undergone the loss of two spe side chains. Finally, in each MS/MS spectrum, the U ion detected at *m/z* 105 corresponds to protonated styrene, which is formed via the SCL mechanism.

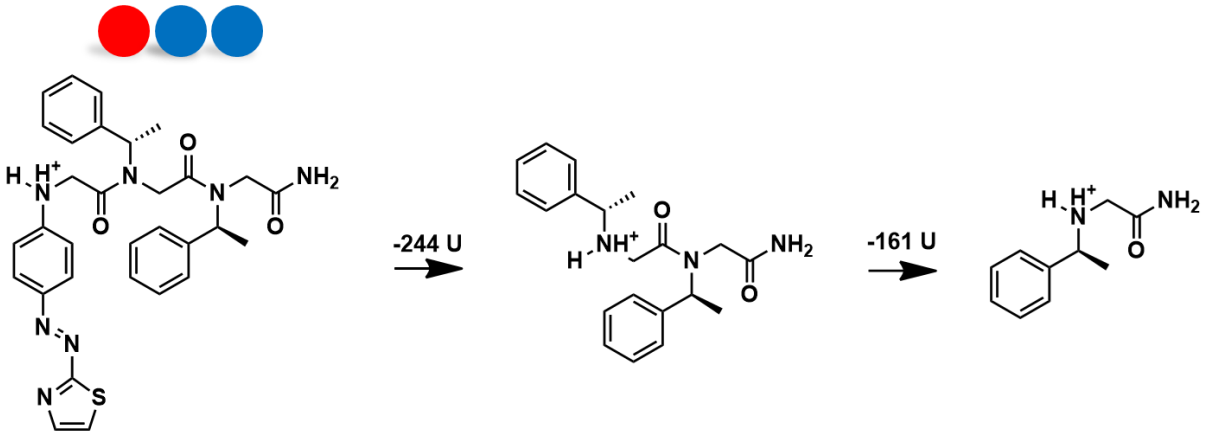

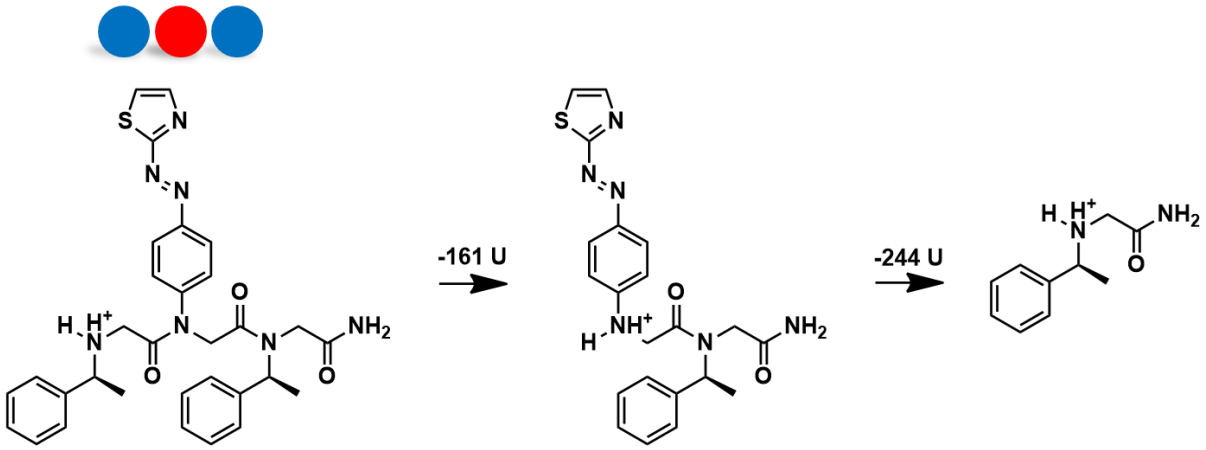

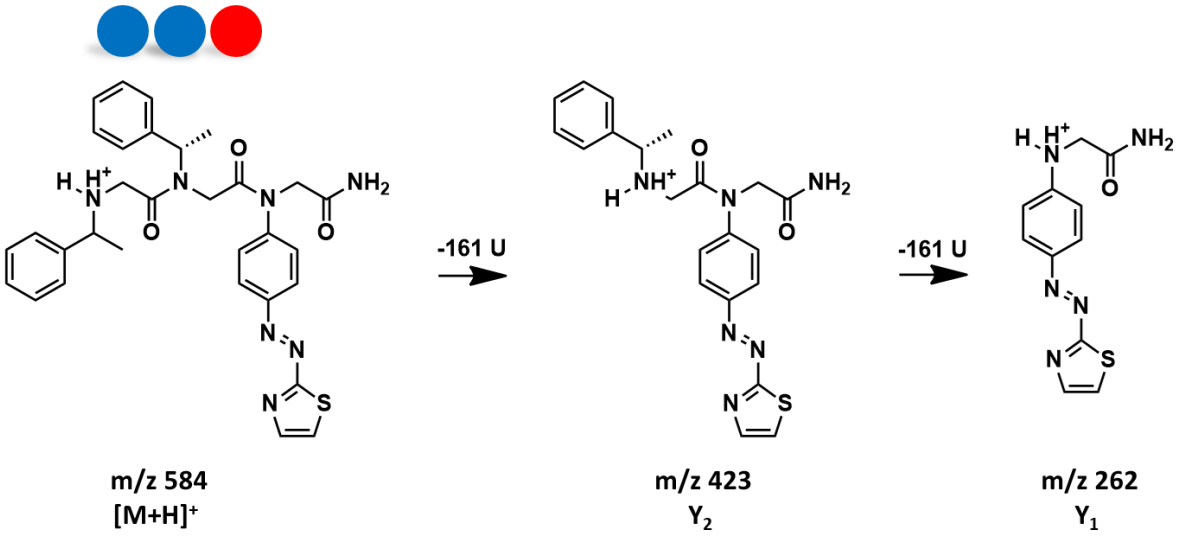

Scheme 11. *Collision-induced dissociation of protonated peptoids : sequence of Y-fragments for ions corresponding to protonated N2tzNspeNspe (top), NspeN2tzNspe (middle) and NspeNspeN2tz (bottom).*

In the three MS/MS spectra shown on **Figure 53**, the primary structure of each peptoid is confirmed by the sequence of Y-fragment ions observed on the spectra, as illustrated on **Scheme 11**. Furthermore, the assignment of most of the fragment ions based on the targeted structures confirms the sequences and allows distinguishing the positional isomers.

The additional peptoids presented on **Figure 50** were all synthesized and characterized using the same methodology. However, to maintain readability and avoid redundancy, the complete MS and MS/MS data for these compounds are not shown here, all corresponding spectra are provided in the **Appendix**.

PAT-peptoids	M.W ($g.mol^{-1}$)	Elemental composition	Calculated mass	Experimental mass	Error (ppm)
	583.70	$C_{31}H_{34}N_7O_3S$	584.2444	584.2448	0.7
	583.70	$C_{31}H_{34}N_7O_3S$	584.2444	584.2455	1.9
	583.70	$C_{31}H_{34}N_7O_3S$	584.2444	584.2457	2.2
	625.74	$C_{33}H_{36}N_7O_4S$	626.2549	626.2551	0.3
	744.90	$C_{41}H_{45}N_8O_4S$	745.3284	745.3288	0.5
	597.73	$C_{32}H_{36}N_7O_3S$	598.2600	598.2590	1.7
	597.73	$C_{32}H_{36}N_7O_3S$	598.2600	598.2587	2.2
	597.73	$C_{32}H_{36}N_7O_3S$	598.2600	598.2590	1.7
	597.73	$C_{32}H_{36}N_7O_3S$	598.2600	598.2584	2.7
	633.76	$C_{35}H_{36}N_7O_3S$	634.2600	634.2605	0.8
	633.76	$C_{35}H_{36}N_7O_3S$	634.2600	634.2603	0.5
	493.58	$C_{24}H_{28}N_7O_3S$	494.1974	494.1976	0.4
	493.58	$C_{24}H_{28}N_7O_3S$	494.1974	494.1971	0.6
	493.58	$C_{24}H_{28}N_7O_3S$	494.1974	494.1976	0.4
	403.46	$C_{17}H_{22}N_7O_3S$	404.1505	404.1519	3.5

Table 4. *Ball formalism structures, molecular weights, elemental composition and exact mass measurements realized by HRMS on Waters Synapt G2-Si for the fifteen peptoids synthetized.*

2.2 DETERMINATION OF MOST PROPERTIES

The determination of the MOST properties of these molecular systems represents a major part of this study as this will constitute the basis of the comparative study, *i.e.* monomers vs peptoids. As a first step, the properties of the PAT 1 peptoids will be examined, followed by those of the substituted-PAT peptoids. These properties are measured in solution in MeOH as the reference solvent. The initial properties determined are the λ_{max} and $\varepsilon_{\lambda max}$, which reveal the

absorption wavelength (UV or visible range) and the efficiency of the absorption. Subsequently, parameters such as $t_{1/2}$, PSD, $\Delta H^{\ddagger}$ and $\Delta S^{\ddagger}$ will be measured.

2.2.1 E-isomer spectroscopic properties

The UV-vis spectra of the PAT 1 peptoids are presented in **Figure 54a**, and the corresponding λ_{max} and $\varepsilon_{\lambda max}$ values are summarized in **Table 5**. For Cter-PAT 1 and Center-PAT 1, the UV-vis spectra closely resemble to pristine AB, exhibiting distinct π-π* (~375 nm vs 320 nm) and n-π* (~480 nm vs 440 nm) transitions. A bathochromic shifts of 55 nm is observed, attributed to the presence of the thiazolyl group.[128] The redshift of the n-π* transition compared to pristine AB arises from the incorporation of a heteroaryl group, which alters the energy of the n-orbital, thereby shifting the n-π*transition toward longer wavelengths.[188] Compared to Ac-PAT 1, a clear separation of the two absorption bands is observed; however this improvement is accompanied by a slight hypsochromic shift of the π-π* band from 392 nm to 375 nm, indicating that incorporation into the peptoid backbone negatively affects the λ_{max} compared to the acetylated counterparts. This behavior was also previously reported by Tassignon *et al.*, who observed that AB-peptoids exhibit a lower λ_{max} than acetylated-AB[114], likely due to steric hindrance imposed by the peptoid backbone which reduces the planarity of the E-isomer resulting in lower absorption maximum. For Nter-PAT 1, the π-π* and n-π* transitions overlap producing a broad band around 465 nm, corresponding to a bathochromic shift of 90 nm compared to Cter-PAT 1 and Center-PAT 1 analogues. This behavior closely mimics PAT 1 behavior, as expected for amino-AB derivatives.[128]

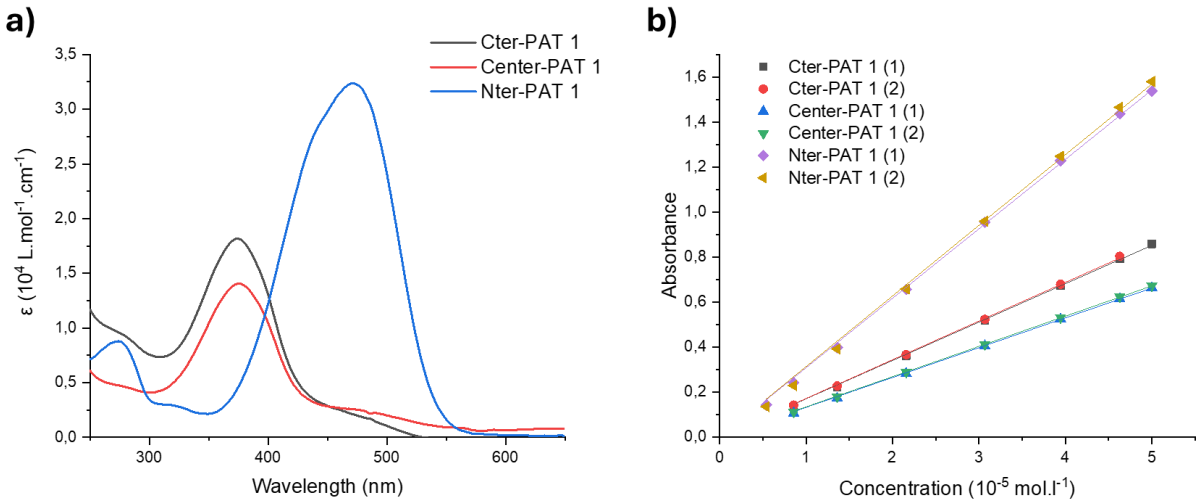

Figure 54. *a) UV-vis spectra of PAT 1 peptoid derivatives in MeOH at a concentration of 5 10^{-5} mol.l^{-1}. The blue curve corresponds to Nter-PAT 1, the red curve to Center-PAT 1 and the black curve corresponds to Cter-PAT 1. b) Determination of the molar extinction coefficients for each PAT 1 peptoid in MeOH from the linear fit of absorbance versus concentration according to the Beer-Lambert law, with concentration ranging from 5 10^{-5} mol.l^{-1} to 8.56 10^{-6} mol.l^{-1}.*

The molar extinction coefficients for the π-π* transitions were determined using Beer-Lambert law as illustrated on **Figure 54b**. For Cter-PAT 1 and Center-PAT 1, the ε values are 1.71 10^4 and 1.33 10^4 L.mol^{-1}.cm^{-1}, respectively. These values are slightly lower than that of Ac-PAT 1 (2.56 10^4 L.mol^{-1}.cm^{-1}); in other words, the incorporation of PAT unit into a peptoid backbone somewhat reduces the ε values. Nevertheless, the incorporation of PAT within a peptoid scaffold marginally affects the overall UV-vis properties compared to pristine PAT (PAT without any substitution), as the values recorded for the latter in ACN (λ_{max}= 363 nm and ε_{max}= 1.97 10^4 L.mol^{-1}.cm^{-1}) are quite similar to those observed for the Cter-PAT 1 and Center-PAT 1 chromophores in MeOH.[191] For Nter-PAT, the ε value is 3.11 10^4 L.mol^{-1}.cm^{-1} indicating no significant deviation from the PAT 1, in this case showing that the incorporation at Nter does not alter the absorption properties.

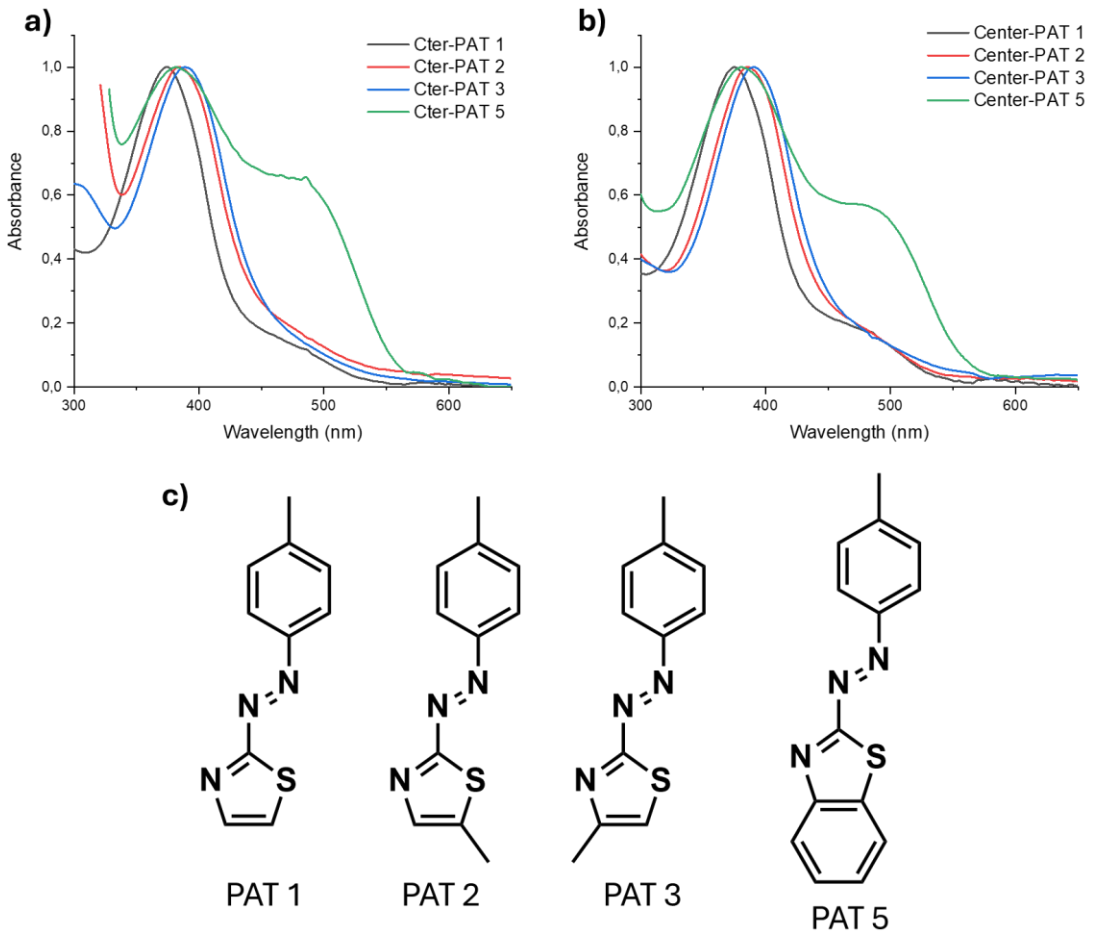

Figure 55. *a) Normalized UV-vis spectra of the Cter-PAT peptoids in MeOH. The black curve corresponds to Cter-PAT 1, the red curve to Cter-PAT 2, the blue curve to Cter-PAT 3 and the green curve to Cter-PAT 5. b) Normalized UV-vis spectra of the Center-PAT peptoids in MeOH. The black curve corresponds to Center-PAT 1, the red curve to Center-PAT 2, the blue curve to Center-PAT 3 and the green curve to Center-PAT 5. c) Reminder of the substituted PAT structure.*

Regarding the substituted-PAT peptoids, only Cter and Center derivatives were synthetized. The UV-vis spectra of the different PAT-based peptoids are shown in **Figure 55**. Peptoids bearing substituted PAT display absorption maxima at 385, 390 and 380 for PAT 2, PAT 3 and PAT 5 peptoids, respectively. The position of the PAT along the backbone (Cter and Center position) does not influence the absorption band. Overall, substitution leads to a bathochromic shift of 5 to 15 nm, indicating an enhancement in visible light absorption. Interestingly, the PAT 2 and PAT 3 peptoids, which are positional isomers, exhibit slightly different absorption maxima, with a 5 nm redshift observed for the PAT 3 derivatives. Another noteworthy observation concerns the PAT 5 peptoids: while the NH_2- and Ac-PAT monomeric analogues

exhibit the highest absorption maxima, incorporation into peptoid scaffold results in a decrease in λ_{max}. This behavior is likely due to steric hindrance within the peptoid structure, which may disrupt the planarity of the PAT chromophore, thereby increasing the π-π* energy gap and blueshifting the absorption maximum. In the UV-vis spectra of PAT 5 peptoids, n-π* transition appears relatively intense compared to the other derivatives. This could also arise from the distorted planarity of the molecule, which enhances the overlap between the n- and π*-orbitals, making the transition less forbidden compared to typical AB derivatives. Unfortunately, due to time constraints, purification of the substituted PAT peptoids was not completed, therefore, their ε values were not determined.

2.2.2 Photoisomerization process

UV-vis spectroscopy was first employed as a direct method to confirm the occurrence of photoisomerization. **Figure 56** shows the UV-vis spectra recorded in MeOH before and after 1 min of irradiation. For the different PAT 1 peptoids, two distinct behaviors were observed. The first behavior is associated to Cter-PAT 1 (**Figure 56a**) and Center-PAT 1 (**Figure 56b**) which exhibit a decrease of the absorbance at 375 nm upon irradiation. This decrease is attributed to the *E* → *Z* photoisomerization, leading to the formation of the *Z*-isomer. In contrast, Nter-PAT 1 (**Figure 56c**) displays not noticeable spectral change before, during, or after irradiation. This indicates that both the photoisomerization and thermal back-isomerization processes occur on a timescale faster than 1 s, which is beyond the temporal resolution of our setup. Since the ε values of the *Z*-isomers are unknown, it is not possible to accurately determine parameters such as PSD and the *Z*-isomers $t_{1/2}$. To address this limitation, an LC-MS approach was employed for further characterization, as described in the following section. Finally given that Nter-PAT 1 does not exhibit measurable photoisomerization within the experimental timescale, its photoisomerization and thermal back-isomerization processes were not further investigated by UV-vis spectroscopy or LC-MS analysis.

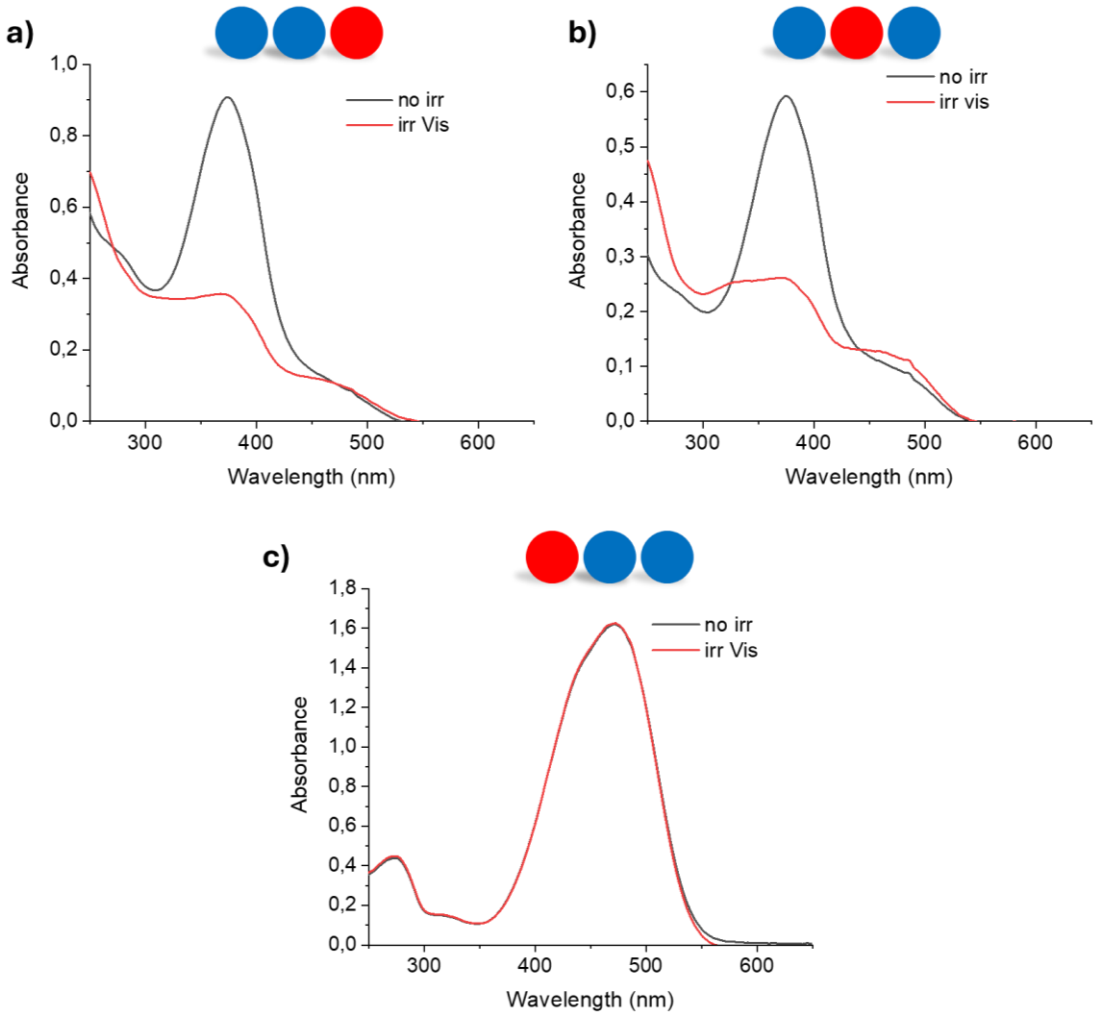

Figure 56. *UV-vis spectra of a) Cter-PAT 1, b) Center-PAT 1 and c) Nter-PAT 1 before and after irradiation in MeOH (5 10^{-5} mol.l^{-1}). The black curves correspond to PAT 1 peptoids before irradiation, the red curves correspond to PAT 1 peptoids after irradiation.*

Figure 57 presents the results of the photoisomerization of the Center-PAT 1 and Cter-PAT 1 under UV or vis irradiation in MeOH as monitored using LC-MS experiments. For both congeners, the PSS are reached within 30 seconds of irradiation as shown on **Figure 57c**. To ensure consistency across all measurements, an irradiation time of 1 min was arbitrarily chosen for subsequent analyses under identical experimental conditions. From these data, the PSD were determined to be 41% (UV) and 66 % (visible) for Center-PAT 1, and 42 % (UV) 69 % (visible) for Cter-PAT 1. It is worth noting that the UV (270-380 nm) and vis (350-700 nm) light sources both emit strongly around 350 nm, which coincides with the π-π* transition of the PAT chromophores (375 nm). However, the UV light emission only marginally overlaps with

this transition, which accounts for the lower proportion of *Z*-isomers observed at the PSS under UV irradiation (**Figure 57a-b**). The position of the PAT chromophore whether at the Cter- or center-position of the peptoid backbone does not significantly influence the overall photoisomerization process, as the PSS are reached, for both Cter-PAT 1 and Center-PAT 1, within approximately 30 s to similar extent, PSD ~66-69 %. Given the higher efficiency of the visible light source, visible irradiation was selected for all subsequent experiments throughout this study.

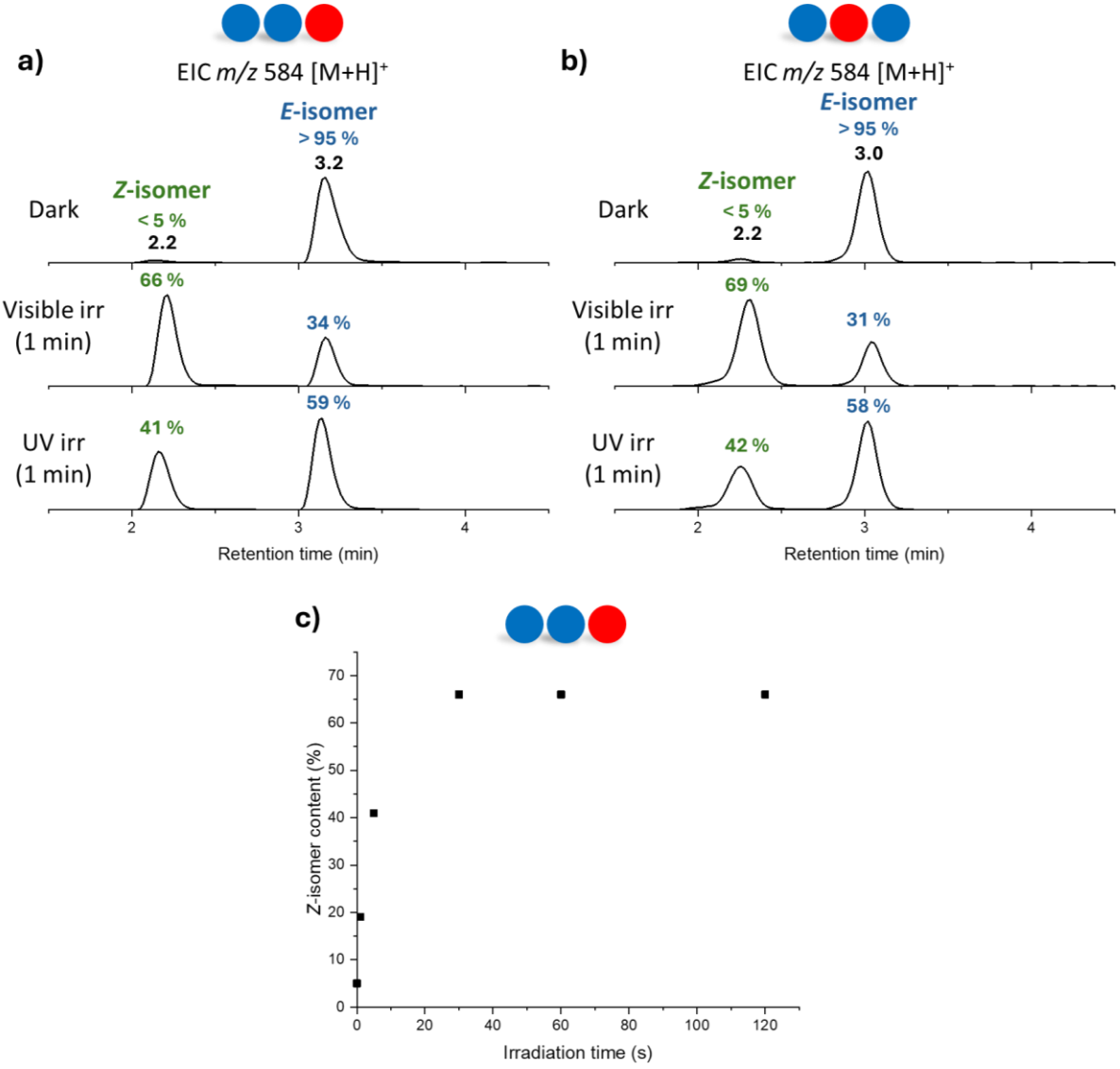

Figure 57. *a) LC-MS analysis (EIC chromatograms of the $[M+H]^+$ ions at m/z 584) of Cter-PAT 1 in MeOH under different irradiation sources: before irradiation (upper) visible irradiation (middle) and UV irradiation (bottom). b) LC-MS analysis (EIC chromatograms of the $[M+H]^+$ ions at m/z 584) of Center-PAT 1 in MeOH under different irradiation sources: before irradiation (upper) visible irradiation (middle)*

and UV irradiation (bottom). c) Z-isomer content in function of the irradiation time under visible lamp for the Cter-PAT 1 in MeOH. Where PSS appears after 30 s of irradiation.

We finally conducted solar irradiation experiments under real-life conditions on Cter-PAT 1 as a representative compound. A methanolic solution of Cter-PAT 1 was exposed to sunlight between 12:00 to 13:00 under various weather conditions (**Figure 58**). The first experiment was performed on October 16, 2024, during a partly sunny and cloudy day (T = 21 °C and UV index = 2/10). The second experiment took place on October 21, 2024, under rainy conditions (T = 13 °C, UV index = 1/10). The final experiment was carried out on September 16, 2025, during a fully sunny day (T = 29 °C and UV index of 5/10). In all cases, the samples were irradiated on the rooftop of the UMONS chemistry building (50°27'53.5"N ; 3°57'25.6"E), and LC-MS analyses were immediately performed following irradiation. During the last experiment, a time-resolved follow-up of the photoisomerization process revealed that the PSS is reached within 30 s of solar irradiation (**Figure 58b**). This rapid photoisomerization is particularly promising for MOST energy storage, as it demonstrates the system ability to efficiently harvest and store solar energy in a short timescale. Overall, solar irradiation proved to be highly effective in triggering the photoisomerization process, with a Z-isomer content of 66 % at the PSS under the tested conditions. Interestingly, these results also confirm that the visible-light sources used in laboratory experiments provides a realistic mimic of solar irradiation under specific conditions. This emphasizes that MOST studies should ideally be conducted under broadband irradiation, rather than using monochromatic light sources, to better reproduce real soler exposure conditions.

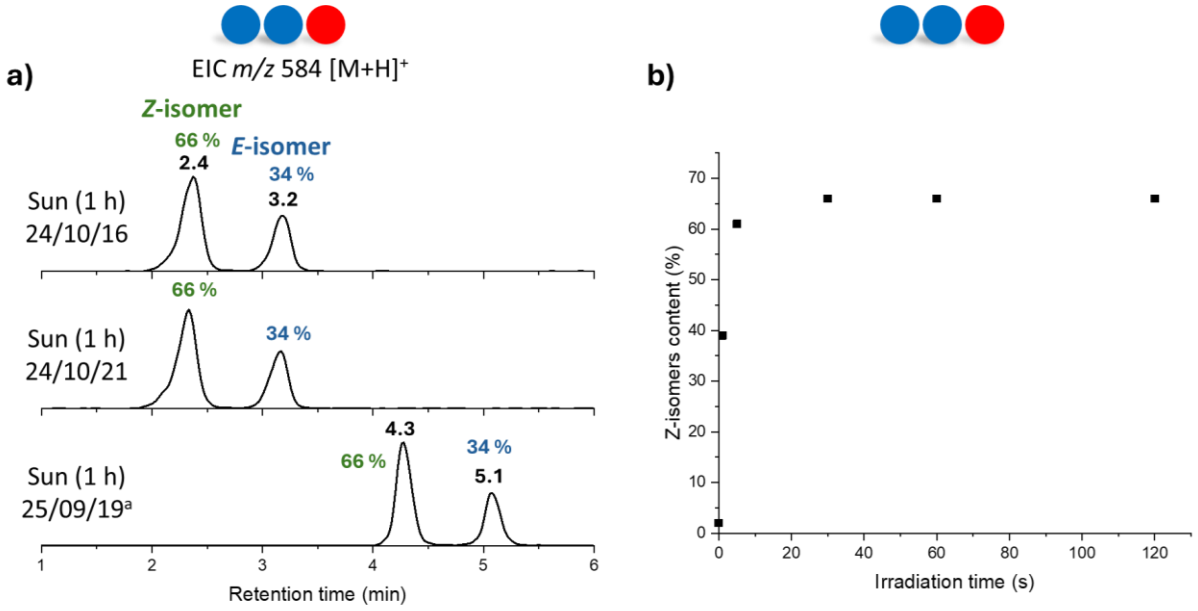

Figure 58. *a) LC-MS analysis (EIC chromatograms of the $[M+H]^+$ ions at m/z 584) of Cter-PAT 1 in MeOH under different sunlight irradiation conditions: cloudy October 16, 2024, partly sunny and cloudy day (upper), October 21, 2024, rainy conditions and September 16, 2025, fully sunny day. b) Z-isomer content in function of the irradiation time under sunlight for the Cter-PAT 1 in MeOH. The PSS is reached within 30 s of solar irradiation. [a] LC-MS analyses was performed using a different LC-MS method compared to the other EIC chromatograms.*

Regarding the photoisomerization of the different substituted-PAT peptoids, similar trends to those observed for PAT 1 peptoids were found for PAT 2 and PAT 3 peptoids, with no difference between the Cter- and center-positions and PSD at 70 % for both PAT. However, in the case of PAT 5 peptoids, the PSD were determined at only 56 % and 61 % Center-PAT 5 and Cter-PAT 5, respectively. This decrease in PSD compared to other derivatives likely results from steric restrictions imposed by the peptoid backbone and the side chains, which may destabilize the Z-isomer and hinder efficient photoisomerization. All chromatograms featuring the relative proportions of the *E*- and *Z*-isomers are provided in the **Appendix**. Having established a clear understanding of the photoisomerization process, the next step in this study involves investigating the thermal back-isomerization behavior of these systems.

2.2.3 Thermal back-isomerization process

After having reached the PSS, both solutions were stored in the dark at 293 K (within the sample manager of the Waters Alliance 2695) and the *Z* → *E* back isomerization was monitored over time through automatic periodic sampling and LC-MS analysis (**Figure 59**).

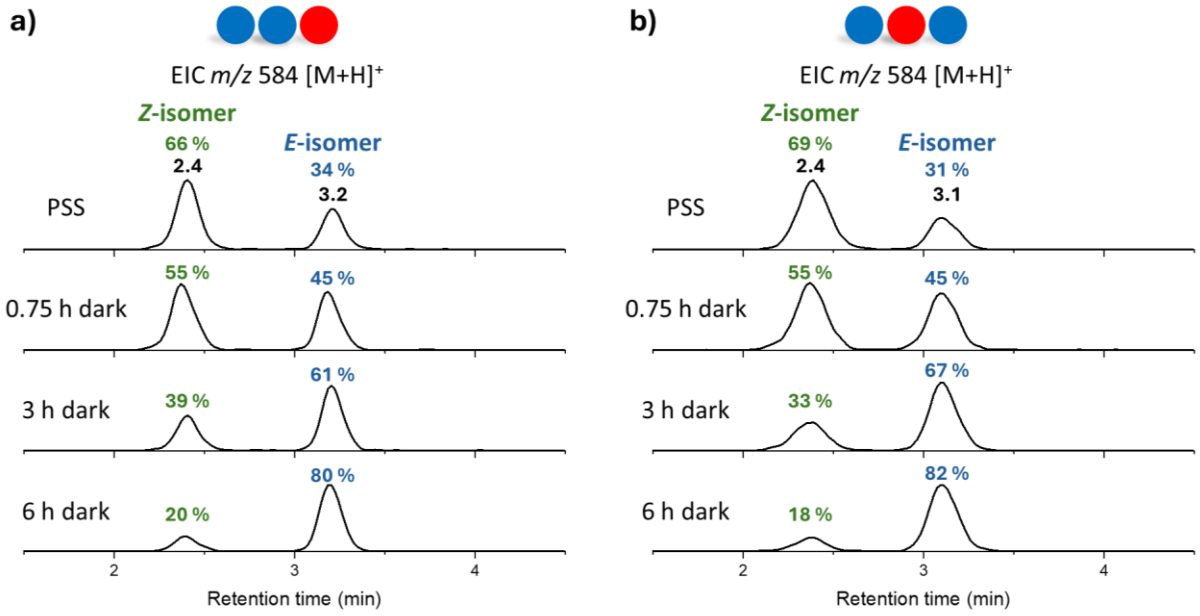

Figure 59. *a) LC-MS analysis (EIC chromatograms of the $[M+H]^+$ ions at m/z 584) of Cter-PAT 1 back-isomerization with sampling at different storage times in the dark in the LC-MS autosampler at 20 °C and in MeOH. b) LC-MS analysis (EIC chromatograms of the $[M+H]^+$ ions at m/z 584) of Center-PAT 1 back-isomerization with sampling at different storage times in the dark in the LC-MS autosampler at 20 °C and in MeOH.*

The thermal back-isomerization process is slightly slower for Center-PAT 1 compared to Cter-PAT 1, as 90 % of the *Z*-isomers revert to the E-isomer after approximately 11h for Cter-PAT 1 and 9 for Center-PAT 1 at 20 °C. Since the thermal back-isomerization of AB derivatives typically follows first-order kinetics, the corresponding rate constant and $t_{1/2}$ were determined by applying an exponential fit to the LC-MS data (**Figure 60**). The extracted $t_{1/2}$ values at 20 °C are 3.6 h and 3.1 h for Cter-PAT 1 and Center-PAT 1 respectively.

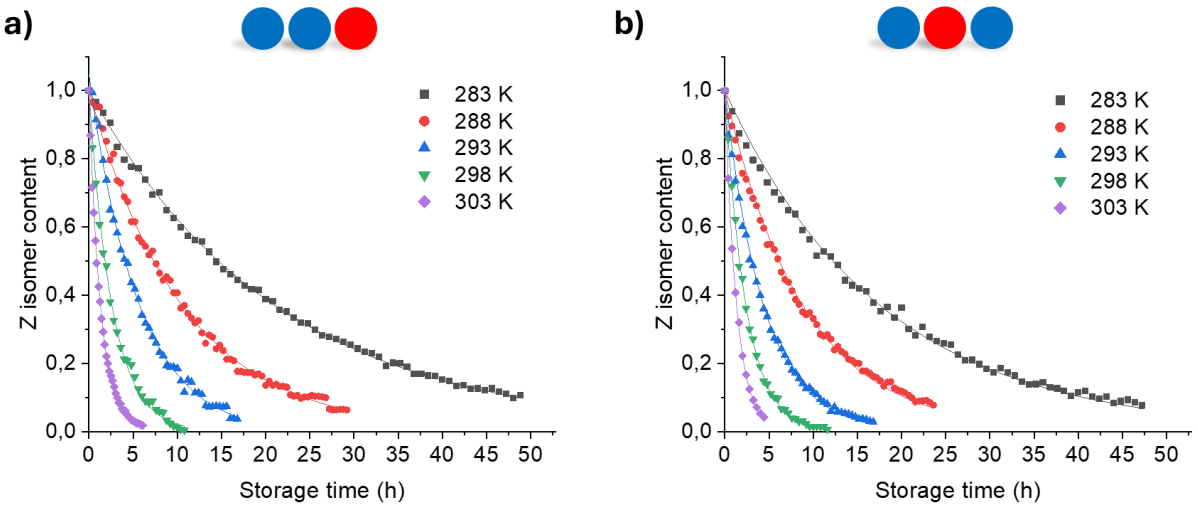

Figure 60. *Monitoring of the thermal Z → E back-isomerization kinetics by LC-MS analyses at various temperatures ranging from 283 K to 303 K in 5-degree increments for Cter-PAT 1 (a) and Center-PAT 1 (b). Normalized Z-isomer content plotted against the time showing a first-order exponential decay in MeOH.*

These $t_{1/2}$ values are significantly lower compared to those reported by Tassignon *et al.* for AB-containing peptoids, where the Cter-AB (N*spe*N*spe*N*azb*) and Center-AB (N*spe*N*azb*N*spe*) derivatives exhibited remarkably different $t_{1/2}$ of 14 days and 12 h respectively, revealing a pronounced site-selective stabilization of the *Z*-isomer.[114] Such a behavior is typical of hetero-substituted AB, which most of the time display bathochromic shifts toward the visible region but often at the cost of reduced thermal stability of the *Z*-isomer, owing to push-pull electronic effects. Nevertheless, since Ac-PAT 1 exhibits a $t_{1/2}$ of only 15 min at R.T, anchoring PAT chromophore onto peptoid backbone clearly enhances the *Z*-isomer stability. However, compared to pristine PAT as reported by Reimann et al. ($t_{1/2}$ = 5.3 h, ACN, 20 °C), incorporating PAT into a peptoid scaffold appears to negatively impact the MOST performances, with reduced *E* → *Z* conversion at the PSS, increase MW and reduced $t_{1/2}$. However, it should be noted that the photoisomerization of pristine PAT was conducted under monochromatic irradiation (405 nm) optimizing the *E* → *Z* conversion, whereas the experiments presented here employed a broadband light source, more representative of real solar conditions. Additionally, differences in solvent polarity (ACN in Reimann study versus MeOH in ours) may also contribute to the observed disagreements. These effects will be

discussed with more details in the following section, which focuses on the solvent influence on the photo- and thermal back-isomerization of PAT derivatives.

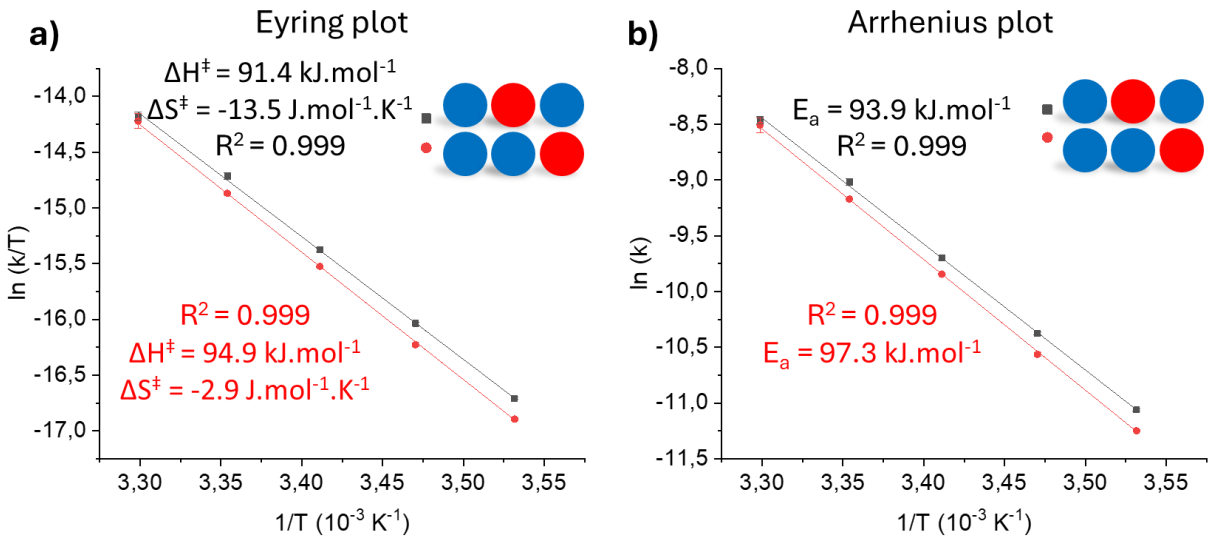

Figure 61. *Eyring-Polanyi plot based on the rate constants extracted from the kinetics at different temperatures for Cter-PAT 1 and Center-PAT 1 (LC-MS procedure). Kinetics parameters are presented for Cter-PAT 1 in red and Center-PAT 1 in black. d) Arrhenius plot based on the rate constants extracted from the kinetics at different temperatures for Cter-PAT 1 and Center-PAT 1. Activation energies are presented for Cter-PAT 1 in red and Center-PAT 1 in black.*

Kinetics experiments were further conducted at various temperatures ranging from 283 K to 303 K in 5-degree increments, for Cter-PAT and Center-PAT (**Figure 60**). From these experiments, the $t_{1/2}$ of the Z isomers were determined at each temperature, and the resulting data were used to construct Eyring (**Figure 61a**) and Arrhenius plots (**Figure 61b**). These plots enable the extraction of the kinetics parameters, including $\Delta H^{\ddagger}$, $\Delta S^{\ddagger}$, and E_a (see **Table 5**). For Cter-PAT 1, the activation enthalpy ($\Delta H^{\ddagger}$) and entropy ($\Delta S^{\ddagger}$) were measured at 94.9 kJ mol^{-1} and -2.9 $J.mol^{-1}.K^{-1}$, respectively. Similarly, for Center-PAT 1, $\Delta H^{\ddagger}$ and $\Delta S^{\ddagger}$ were determined at 91.4 $kJ.mol^{-1}$ and -13.5 $J.mol^{-1}.K^{-1}$, respectively. The Eyring approach offers an advantage over Arrhenius analysis, as it provides access to activation entropy, a key parameter recently demonstrated by Reimann *et al.*[37] to help elucidation the back-isomerization mechanism. Depending on the molecular structure, the E → Z thermal back-isomerization of AB can proceed through either a rotation (type II) or inversion pathway, each characterized by distinct entropy signature: strongly negative $\Delta S^{\ddagger}$ values are associated with rotation, whereas values

close to zero indicate inversion.[37] The strongly negative value for $\Delta S^{\ddagger}$ typically observed for type II rotation arises from the intermediacy of a triplet state, which significantly reduces the overall entropy of activation.[37] Therefore, when comparing our results with those of pristine AB and pristine PAT (**Table 5**), which both display significantly negative $\Delta S^{\ddagger}$ values consistent with a rotation pathway, the near-zero or positive $\Delta S^{\ddagger}$ values obtained for Cter-PAT 1 and Center-PAT 1 suggest that their thermal back-isomerization proceeds predominantly through an inversion mechanism. This behavior likely arises from steric and electronic constraints imposed by the spe side chains, which hinders the free rotation around the N=N bond.

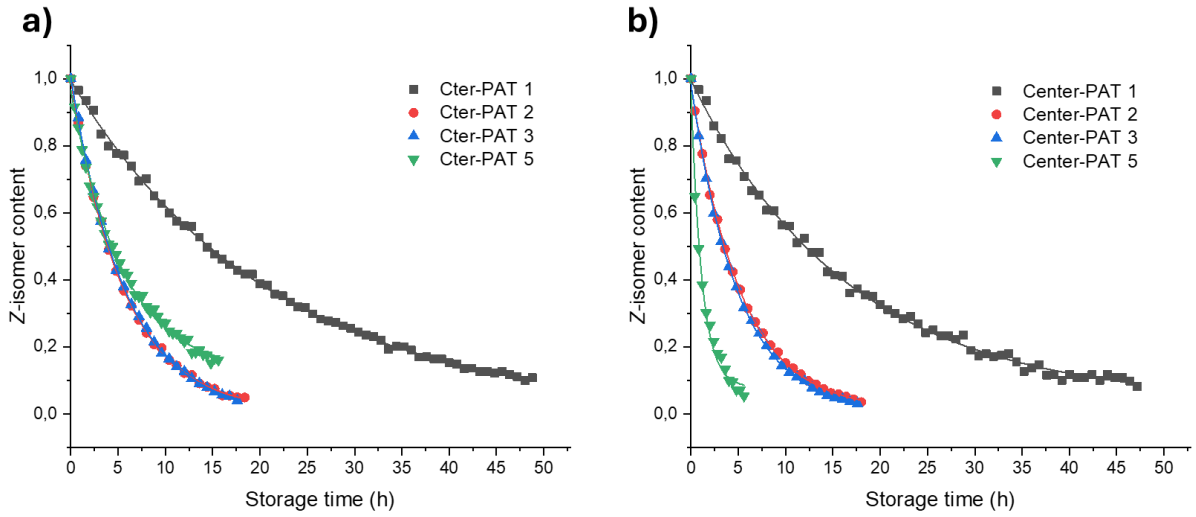

Figure 62. *Monitoring of the thermal Z → E back-isomerization kinetics by LC-MS analyses at 10 °C for Cter-PAT peptoids (a) and Center-PAT peptoids (b). Normalized Z-isomer content plotted against the time showing a first-order exponential decay in MeOH.*

Regarding the substituted-PAT peptoids, the thermal stability of the Z-isomer is significantly weaker for all derivatives compared to the PAT 1 peptoids, this result being the same for both the Cter- and Center-positions. **Figure 62** presents the corresponding kinetics profiles recorded at 10°C, as the substituted derivatives exhibit $t_{1/2}$ too short to be accurately measured at 20 °C using LC-MS analysis. Regarding $t_{1/2}$ values of the substituted derivatives, the same trend as observed for the PAT 1 peptoids is maintained: the Cter-position exhibits longer $t_{1/2}$ than the Center-position. For the Cter-PAT peptoids, all the $t_{1/2}$ values fall within a similar range, around 3.9 h. In contrast, a significant decrease in $t_{1/2}$ is observed for Center-PAT 5, which can

be attributed to the steric hindrance induced by the spe side chains neighboring the PAT 5 chromophores. This effect is further amplified by the presence of the bulky benzothiazole ring in PAT 5, which is considerably larger than the methylthiazole groups present in the PAT 2 and PAT 3. Unfortunately, due to time constraints, the kinetics parameters ($\Delta H^{\ddagger}$, $\Delta S^{\ddagger}$ and E_a) of these derivatives were not determined in this study. Nevertheless, it would be highly interesting to investigate in future work how the nature and position of the substituents on the PAT core influence these kinetics parameters. All the values of $t_{1/2}$ are available in **Table 5**.

2.2.4 Acetylation of Nter-PAT 1

Positioning the PAT chromophore at the Nter extremity proved unsuitable for solar energy storage applications due to the extremely short $t_{1/2}$ observed. This instability primarily arises from the presence of a residual secondary amine group on the chromophores, distinguishing this position from the two others, where the PAT units are connected through amide bond. To address this issue, the secondary amine was converted into an amide via acetylation, as illustrated on **Scheme 12**. It was therefore anticipated that this new derivative, hereafter referred as Ac-Nter PAT 1, would exhibit a measurable $t_{1/2}$ for the *Z*-isomer.

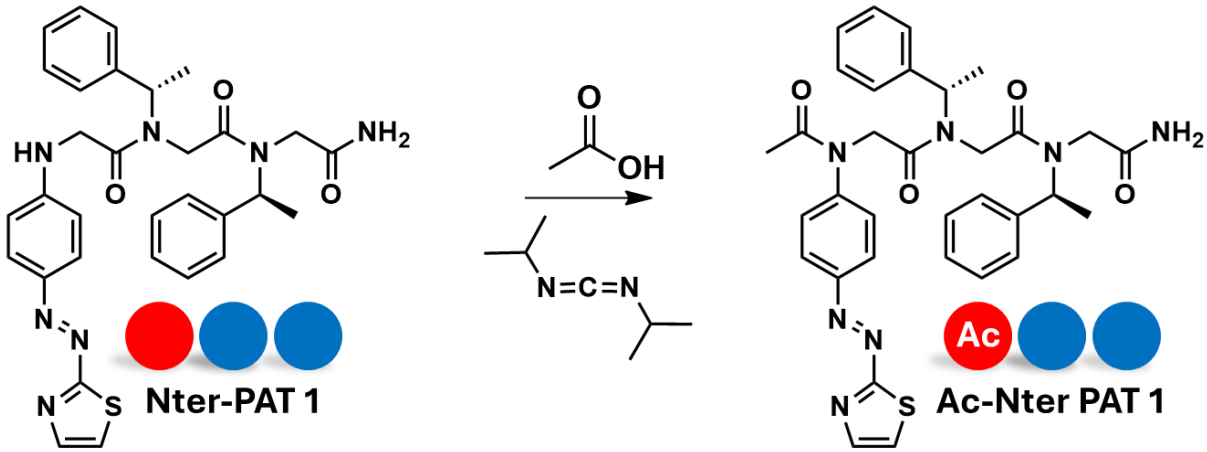

Scheme 12. *Acetylation of the Nter-PAT 1 using bromoacetic acid and DIC to produce Ac-Nter PAT 1*

As shown on **Figure 63a**, Ac-Nter PAT 1 exhibits a pronounced blueshift (85 nm) of the π-π* transition compared to Nter-PAT 1, resulting from acetylation of the Nter amine and thereby restoring the typical AB-like optical behavior. However, despite multiple purification attempts,

an absorption band characteristic of Nter-PAT 1 remains visible, indicating incomplete separation. This is likely due to the very similar polarity of the two compounds and the known tendency of PAT derivatives to diffusing on chromatographic columns (tailing), making the isolation of closely related species particularly challenging.

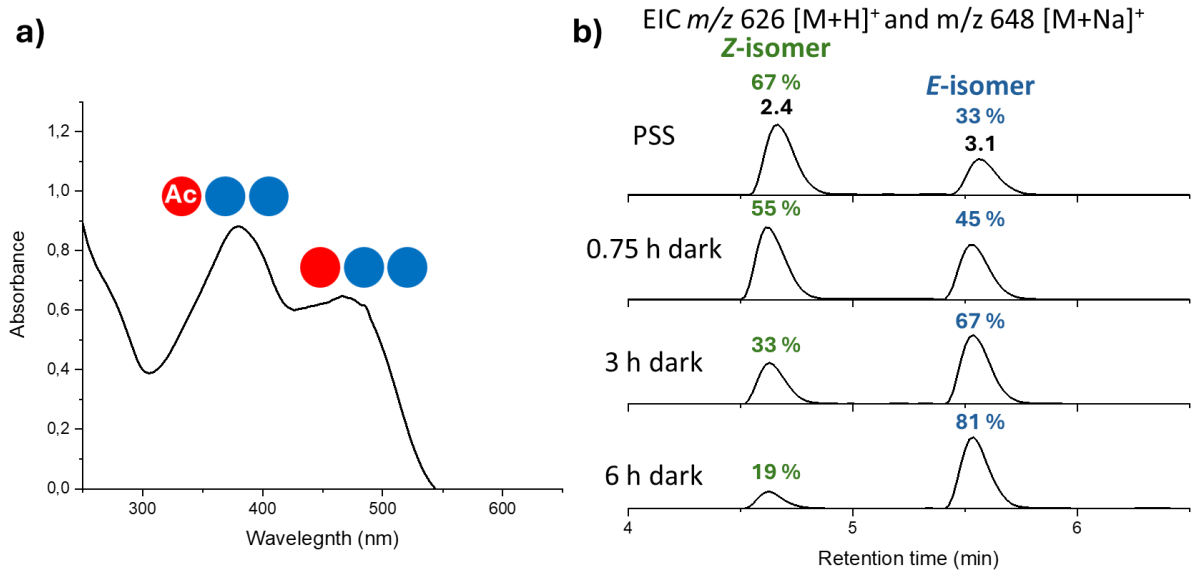

Figure 63. *a) UV-vis spectra of Ac-Nter PAT 1 in MeOH at a concentration of 5 10^{-5} mol.l^{-1}. Two bands are observed corresponding to Nter-PAT 1 and Ac-Nter PAT 1. b)) LC-MS analysis (combination of EIC chromatograms of the $[M+H]^+$ ions at m/z 626 and the $[M+Na]^+$ ions at m/z 648 of Ac-Nter PAT 1 after different storage times in the dark in the LC-MS autosampler at 20 °C and in MeOH.*

Although the compound was not obtained in pure form, a major advantage of LC-MS analysis is that the proportion of each isomer can still be accurately determined, regardless of the residual presence of Nter-PAT 1. **Figure 63b** displays the evolution of the *E*/*Z*-isomer proportions. It is worth noting that the EIC chromatograms presented here correspond to a combination of protonated and sodium adduct species ($[M+H]^+$ and $[M+Na]^+$). Since the free secondary amine is no longer available for protonation upon acetylation, a non-negligeable proportion of sodium adducts is detected in the ESI-MS mass spectrum. Upon visible-light irradiation of the methanolic solution, a PSS composed of 67 % of *Z*-isomer is achieved. This clearly demonstrates the benefit of modifying the Nter unit, as the Z-isomer could not be detected for the non-acetylated Nter-PAT 1 (see **Figure 56c**). The $t_{1/2}$ of Ac-Nter-PAT 1 is 3.2 h at 20 °C, which is slightly weaker than those determined for Cter- and Center-PAT 1.

Nevertheless, the key advantage of this derivative lies in its absorption properties, showing a slight 5 nm redshift compared to its non-acetylated counterpart, making it a promising candidate for MOST applications.

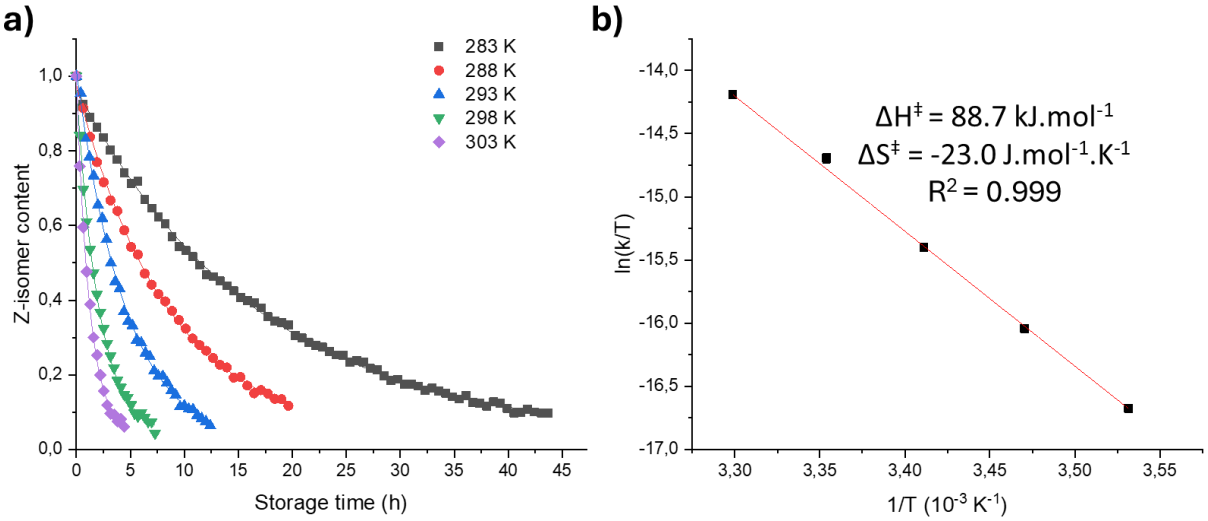

Figure 64. *a) Monitoring of the thermal Z → E back-isomerization kinetics by LC-MS analyses at various temperatures ranging from 283 K to 303 K in 5-degree increments for Ac-Nter PAT 1. Normalized Z-isomer content plotted against the time showing a first-order exponential decay in MeOH. b) Eyring-Polanyi plot based on the rate constants extracted from the kinetics at different temperatures for Ac-Nter PAT 1, with presentation of the kinetic parameters.*

Once again, kinetic experiments were conducted at various temperatures ranging from 283 K to 303 K in 5-degree increments (**Figure 64a**). From these experiments, the $t_{1/2}$ values of the *Z*-isomers were determined at each temperature, and the resulting data were used to construct Eyring (**Figure 64b**) and Arrhenius (**Appendix**) plots. These plots enable the extraction of the kinetics parameters with $\Delta H^{\ddagger}$ of 88.7 kJ mol^{-1} and $\Delta S^{\ddagger}$ of -23.0 $J.mol^{-1}.K^{-1}$. Interestingly, the significant negative value of the activation entropy indicates a notable mechanistic change in the thermal back-isomerization pathway. Unlike the Cter- and Center-PAT 1, which undergo inversion driven isomerization, Ac-Nter PAT 1 appears to follow a rotation pathway. This mechanistic shift may arise from the structural and electronic effects introduced by the Nter-acetylation, which modifies the local environment and steric constraints around the AB-group.

2.2.5 NspeN2tzNspeNspe derivative

The NspeN2tzNspeNspe peptoid named here 4-unit peptoid was synthetized to investigate the influence of introducing an additional spe side chain on the spectroscopic and thermal properties. In this context, the addition of spe units modifies the balance between steric hindrance and electrostatic interactions, potentially leading to altered properties. The UV-vis spectrum of this compound, shown on **Figure 65a**, exhibits a maximum absorption at 480 nm, corresponding to a slight 5 nm redshift compared to the PAT 1 3-unit peptoids.

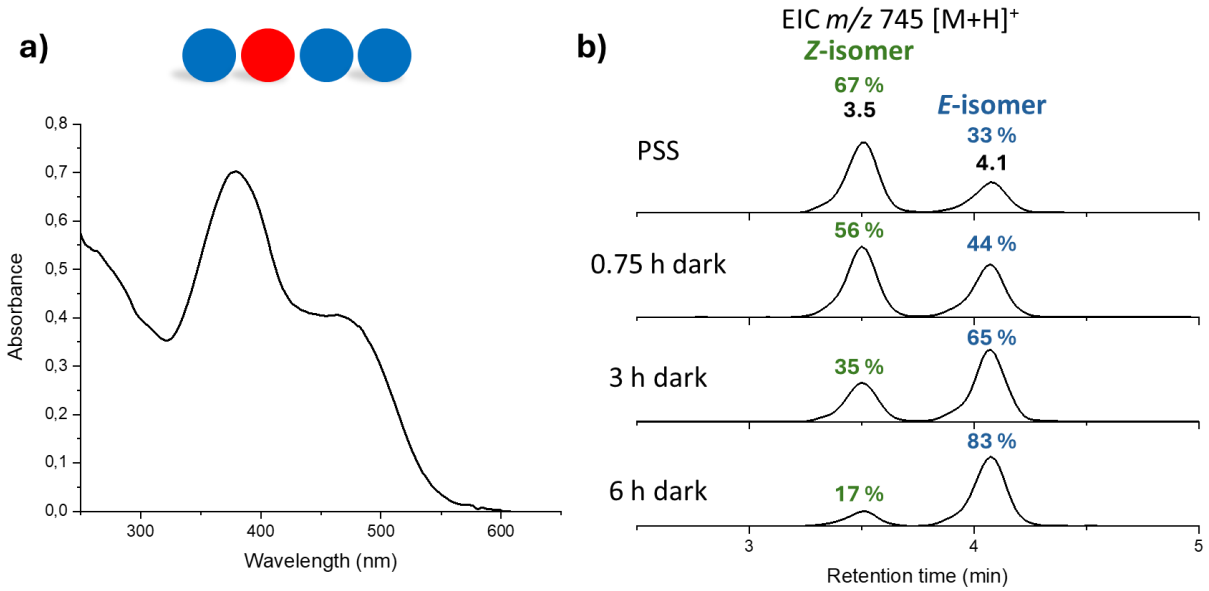

Figure 65. *a) UV-vis spectra of the 4-unit peptoid in MeOH at a concentration of 5 10^{-5} mol.l^{-1}. b) LC-MS analyses (EIC chromatograms of the $[M+H]^+$ ions at m/z 745) after different storage times in the dark in the LC-MS autosampler at 20 °C and in MeOH.*

Figure 64b displays the evolution of the *E*/*Z*-isomer proportions with the EIC chromatograms presented here correspond to protonated species ($[M+H]^+$). Upon visible-light irradiation of the methanolic solution, a PSS composed of 67 % *Z*-isomer is reached. The $t_{1/2}$ of the 4-unit peptoid is 3.0 h at 20 °C, which is slightly lower than those of (3-unit) Cter- and Center-PAT 1. Nevertheless, similarly to Ac-Nter-PAT 1, the key advantage of this derivative lies in its absorption properties, showing a 5 nm redshift compared to its non-acetylated counterpart.

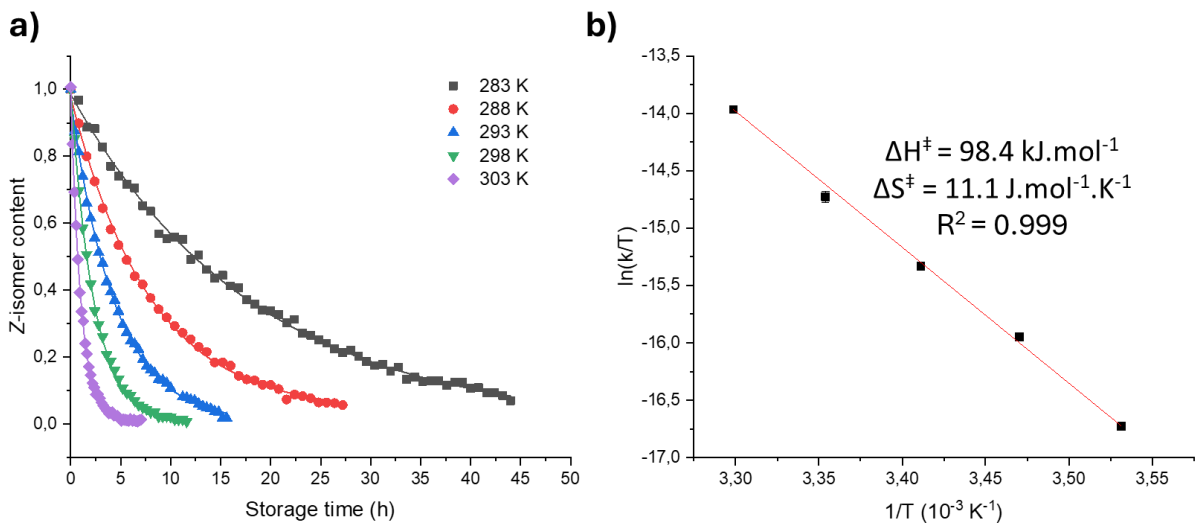

Figure 66. *a) Monitoring of the thermal Z → E back-isomerization kinetics by LC-MS analyses at various temperatures ranging from 283 K to 303 K in 5-degree increments for the 4-unit peptoid. Normalized Z-isomer content plotted against the time showing a first-order exponential decay in MeOH. b) Eyring-Polanyi plot based on the rate constants extracted from the kinetics at different temperatures for the 4-unit peptoid, with presentation of the kinetics parameters.*

Once more, kinetics experiments were performed at various temperatures ranging from 283 K to 303 K in 5-degree increments (**Figure 66a**). From these experiments, the $t_{1/2}$ values of the *Z*-isomers were determined at each temperature, and the resulting data were used to construct Eyring (**Figure 66b**) and Arrhenius (**Appendix**) plots. These analyses allow determining the kinetic parameters, yielding $\Delta H^{\ddagger}$ of 98.4 kJ mol^{-1} and $\Delta S^{\ddagger}$ of 11.1 $J.mol^{-1}.K^{-1}$. Interestingly, a clearly positive value of activation entropy is obtained for the first time, leaving no doubt about the mechanism of thermal back-isomerization. Following Reimann *et al.*[37], this corresponds to an inversion mechanism. The presence of an additional spe side chain compared to other PAT 1 peptoids, thus modifies the local structuration of the peptoid backbone, introducing steric hindrance restricts the special freedom required for a rotation pathway. As a result, the back-isomerization proceeds preferentially via the inversion pathway, which is less sterically demanding.

2.2.6 N*spe*/N*sar* hybrid peptoids

To investigate the impact of spe side chains, hybrid peptoids containing both sar and spe residues were synthetized. Their chemical structures are provided in the **Appendix**, and their schematic ball representation is shown in **Figure 50**, where grey spheres denote sar side chains, blue spheres correspond to spe side chains , and red spheres indicate the PAT 1 unit. For these compounds, only the thermal behavior was investigated using LC-MS analyses to explore their back-isomerization kinetics and related thermodynamic parameters.

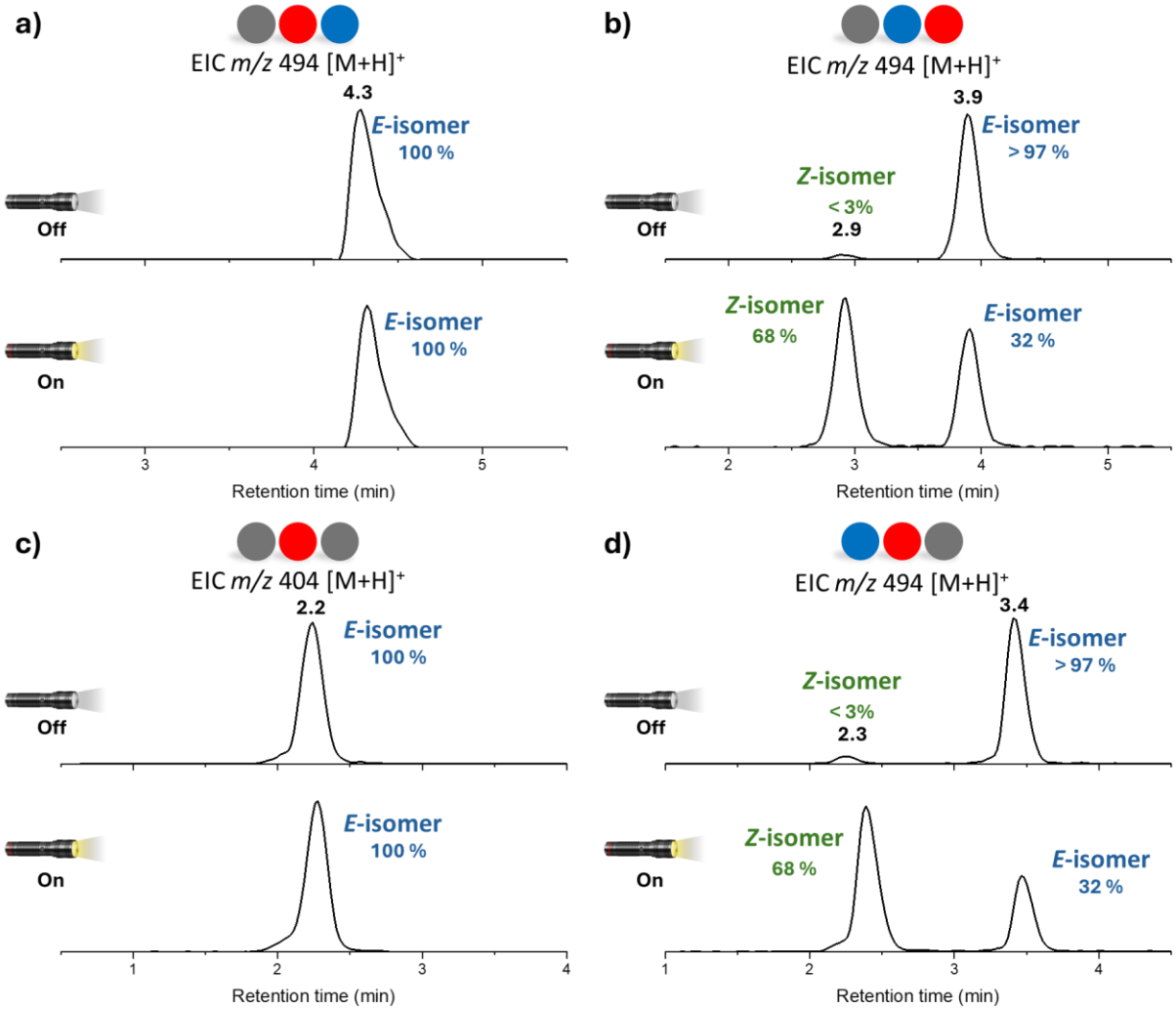

Figure 67. *LC-MS analyses (EIC chromatograms of the [M+H]⁺ ions) of NsarN2tzNspe (a), NsarNspeN2tz (b), NsarN2tzNsar (c) and NspeN2tzNsar in MeOH before irradiation (upper) and after visible irradiation (bottom).*

Thermal stability of the different *Z*-isomers was evaluated by recording LC-MS analysis at 20 °C in MeOH. Two distinct behaviors were observed among the compounds. Upon irradiation, the *Z*-isomers of N*spe*N2*tz*N*sar* (**Figure 67d**) and N*sar*N*spe*N2*tz* (**Figure 67b**) are detected together with the *E*-isomers, whereas for N*sar*N2*tz*N*sar* (**Figure 67c**) and N*sar*N2*tz*N*spe* (**Figure 67a**), no Z-isomer could be detected after visible-light irradiation. Interestingly, the position of the sar side appears to determine this behavior. When a spe residue is located to the left of the PAT unit within the peptoid sequence, the thermal stability of the PAT moiety is sufficient to allow detection of a *Z*-isomer and to measure $t_{1/2}$. In contrast, when the sar side chain occupies this position, no photoisomerization is observed by LC-MS. This suggests that a strong stabilization of the *Z*-isomer may occur when a spe side chain is adjacent to the PAT unit, potentially due to π-interactions between the aromatic groups. In the case of the sar side chain, such an interaction is absent, and the less bulky side chain (limited to a methyl substituent) may further reduce any stabilizing effect, leading to the lack of observable photoisomerization.

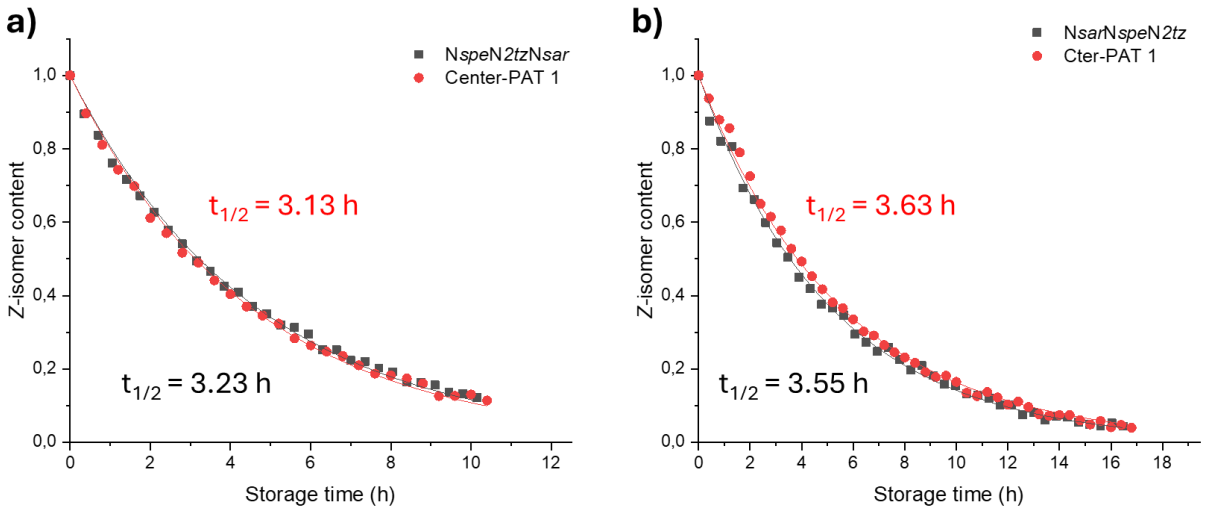

Figure 68. *Monitoring of the thermal Z → E back-isomerization kinetics by LC-MS analyses at 20 °C for Cter-PAT 1 and NspeN2tzNspe couple (a) and Cter-PAT 1 and NsarNspeN2tz couple (b). Normalized Z-isomer content plotted against the time showing a first-order exponential decay in MeOH.*

The back isomerization kinetics of the two hybrid peptoids detected as Z isomers were analyzed at 20°C and compared to those of Cter-PAT 1 and Center-PAT 1, *i.e.* their

homologues containing two spe side chains (**Figure 68**). For the N*sar*N*spe*N2*tz* and Cter-PAT 1 couple, the measured $t_{1/2}$ values amount to 3.55 h and 3.63 h, respectively. The slightly lower value for the hybrid peptoid is not significant enough to suggest any notable destabilization resulting from the replacement of one spe side chain by a sar unit. Similarly, for the Center-PAT 1 and N*spe*N2*tz*N*sar* couple, $t_{1/2}$ values of 3.13 h and 3.23 h are obtained, respectively. Here, a minor increase in the hybrid peptoid $t_{1/2}$ is observed but again, this variation is too small to draw any solid conclusion. Overall, these results indicate that the substitution of one spe side chain by a sar one does not significantly affect the thermal stability of the PAT containing peptoids at 20 °C. However, further investigation is required to confirm these observations and better understand the influence of side chain composition on the system stability.

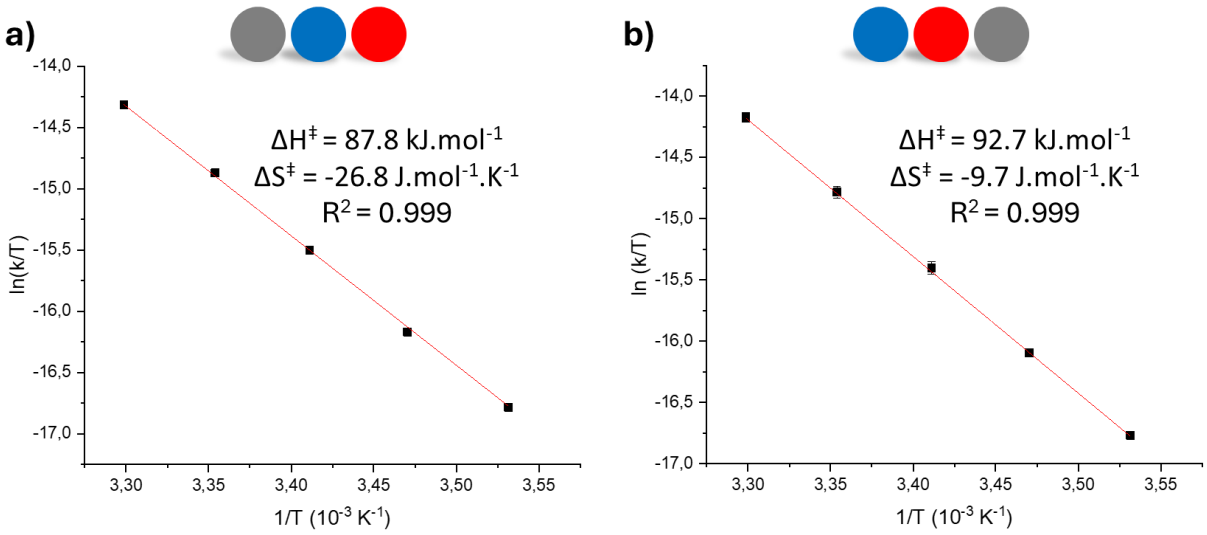

Figure 69. *Eyring-Polanyi plot based on the rate constants extracted from the kinetics at different temperatures for NsarNspeN2tz (a) and NsepN2tzNsar (b), with presentation of the kinetic parameters*

Kinetic experiments were performed at various temperatures ranging from 283 K to 303 K in 5-degree increments. The $t_{1/2}$ values of the *Z*-isomers were determined at each temperature (**Appendix**), and the resulting data were used to construct the Eyring plots shown in **Figure 69a** for N*sar*N*spe*N2*tz* and in **Figure 69b** for N*spe*N2*tz*N*sar*. The corresponding Arrhenius plots are provided in the **Appendix**. These analyses enable the determination of the different kinetic parameters associated to the thermal back-isomerization process. For

N*spe*N2*tz*N*sar*, an activation entropy of - 9.7 J.mol^{-1}.K^{-1} is obtained, compared to - 13.5 J.mol^{-1}.K^{-1} for Center-PAT 1. Although a slight increase in activation entropy is observed, this variation is not significant enough to suggest a change in the mechanism, which remains the inversion pathway. In contrast, for the N*sar*N*spe*N2*tz,* the activation entropy significantly decreases to - 26.8 J.mol^{-1}.K^{-1}, compared to - 2.9 J.mol^{-1}.K^{-1} for Cter-PAT 1. Such a noticeable reduction in entropy suggests a possible mechanistic shift from an inversion pathway to a rotation pathway, in accordance with the criteria proposed by Reimann *et al*.[37] This change may stem from the loss of the spe side chain, which appears to influence both the stabilization of the Z-isomer and the pathway of the thermal back-isomerization. Interestingly, even though the substitution of spe by sar occurs two positions away from the PAT unit, it still impacts the reaction mechanism. This finding underscores the critical role of the side-chain composition and the sequence in modulating the MOST properties of peptoid-based systems and highlights the potential for fine-tuning molecular behavior through targeted structural modifications.

2.3 INTERMEDIATE CONCLUSION

As a conclusion for this section, we have demonstrated the site selectivity afforded by the different positions of the peptoid backbone, *i.e.,* the Nter, Cter and central positions, by determining the MOST properties of the corresponding peptoids in methanolic solutions. The dependence on backbone length was also shown to significantly influence the properties, as illustrated by introducing a 4-unit peptoid. The spectroscopic properties of the different derivatives are particularly noteworthy, with absorption maxima ranging from 375 nm to 390 nm, *i.e*., at the boundary of the visible region. This feature has a direct impact on the photoisomerization process, which proceeds efficiently under sunlight irradiation, making a clear improvement over the pristine AB. Regarding the thermal stability of the *Z*-isomers, all synthetized peptoids exhibit significantly higher $t_{1/2}$ compared to their Ac-PAT counterparts, confirming that the peptoid backbone induces a stabilizing effect on the *Z*-isomers. For all cases, the Cter-PAT peptoids display longer $t_{1/2}$ than their Center-PAT analogues, highlighting

the positional influence on isomer stability. Furthermore, acetylation of the Nter-PAT 1 successfully restored measurable and exploitable MOST properties, which is highly encouraging for further molecular design. Finally, through the determination of activation entropy, the mechanisms of thermal back-isomerization were elucidated and attributed to either rotation or inversion pathways, depending on the structure of the peptoids. The study of the hybrid peptoids bearing both sar and spe side chains highlights the strong influence of side-chain composition and positioning on the MOST properties of PAT-based systems. The results demonstrate that even subtle structural modifications, such as replacing a spe unit with a sar residue, can significantly affect the thermal back-isomerization behavior, either by altering the stability of the Z-isomer or by shifting the reaction mechanism from inversion to rotation. All corresponding quantitative data supporting these conclusions are summarized in **Table 5**.

	$\lambda_{\pi-\pi^*}$ (nm)	$PSD_{visible}$ (%)	$t_{1/2}$ 10 °C (h)	E_a (kJ.mol^{-1})	$\Delta H^{\ddagger}$ (kJ.mol^{-1})	$\Delta S^{\ddagger}$ (J.mol^{-1}.K^{-1})	$\Delta G^{\ddagger}$ 20 °C (kJ.mol^{-1})
Pristine AB[a]	320	25[c]	105 days	98.6	94.9	- 44	108.1
Pristine PAT[b]	364	85	18.81	87.9	85.4	- 38.40	96.7
	465	/	< 1 s	/	/	/	/
	375	69	12.3	93.86	91.4	- 13.5	95.40
	375	66	14.8	97.32	94.9	- 2.9	95.75
	380	67	11.9	91.13	88.7	- 23.0	95.42
	380	67	12.5	100.72	98.4	11.1	95.20
	385	70	3.9	/	/	/	/
	385	70	3.6	/	/	/	/
	390	70	4.0	/	/	/	/
	390	70	3.4	/	/	/	/
	380	56	3.8	/	/	/	/
	380	61	1.0	/	/	/	/
	/	68	13.3	90.31	87.8	-26.8	95.69
	/	68	13.0	95.10	92.7	-9.7	95.53

Table 5. *Summary of the relevant MOST parameters for PAT peptoids determined in MeOH: $\lambda_{\pi-\pi^*}$ is the maximum absorption wavelength, $PSD_{visible}$ is the proportion of Z-isomer at the PSS, $t_{1/2}$ is the metastable isomer half-life time at 10 °C, E_a is the activation energy calculated using Arrhenius plot, $\Delta H^{\ddagger}$ is the activation enthalpy of the thermal back-isomerization, $\Delta S^{\ddagger}$ is the activation entropy of the thermal back-isomerization, $\Delta G^{\ddagger}$ is the Gibbs free energy of the thermal back-isomerization. [a] Data in ACN from[37]. [b] Data in ACN with 405 nm irradiation from[191]. [c] Photoisomerization yield under unfiltered sunlight irradiation (simulated AM1.5 sunlight) from[148].*

2.4 APPENDICES

Appendix 8. *Structures of the synthetized peptoids*

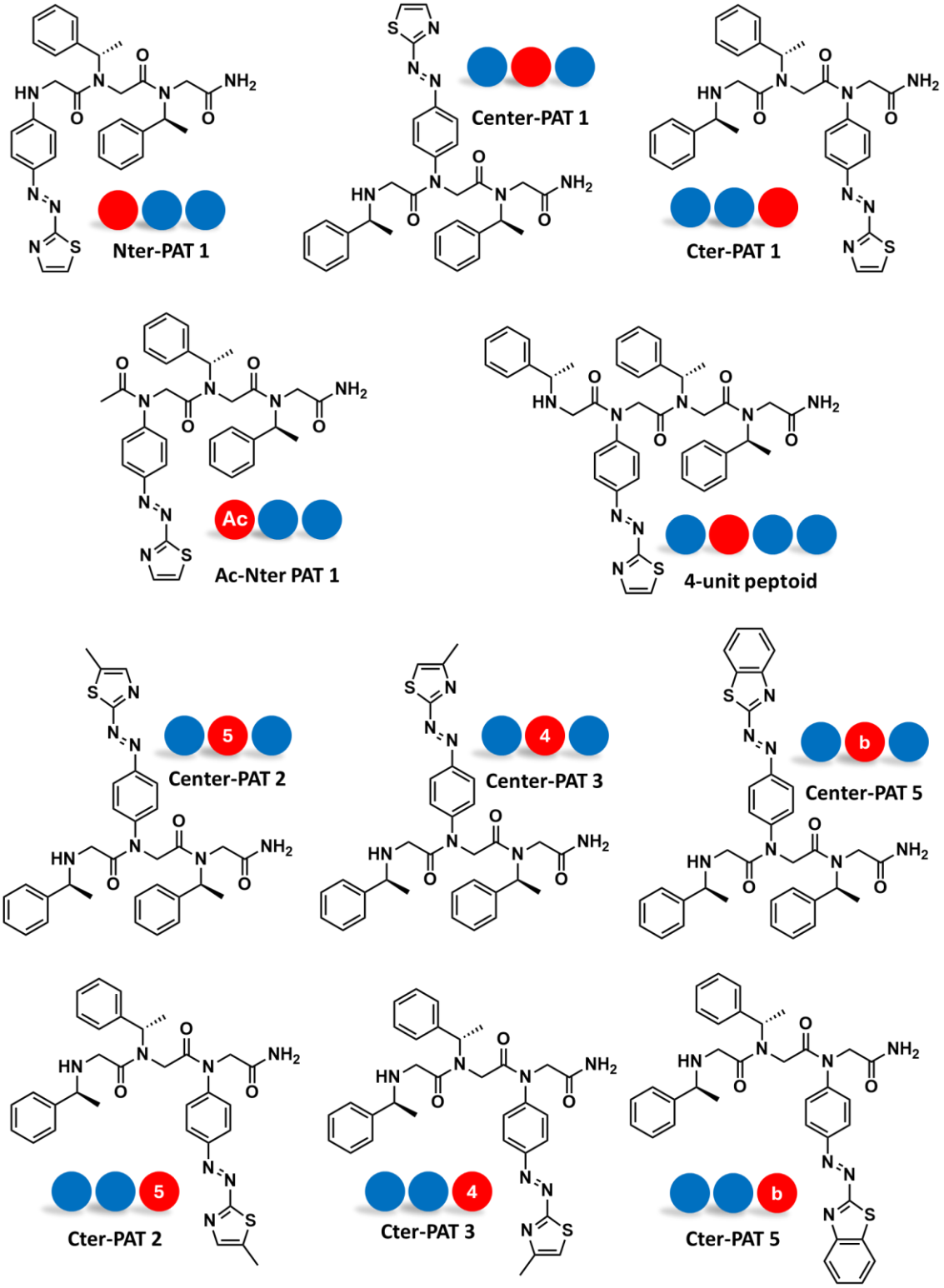

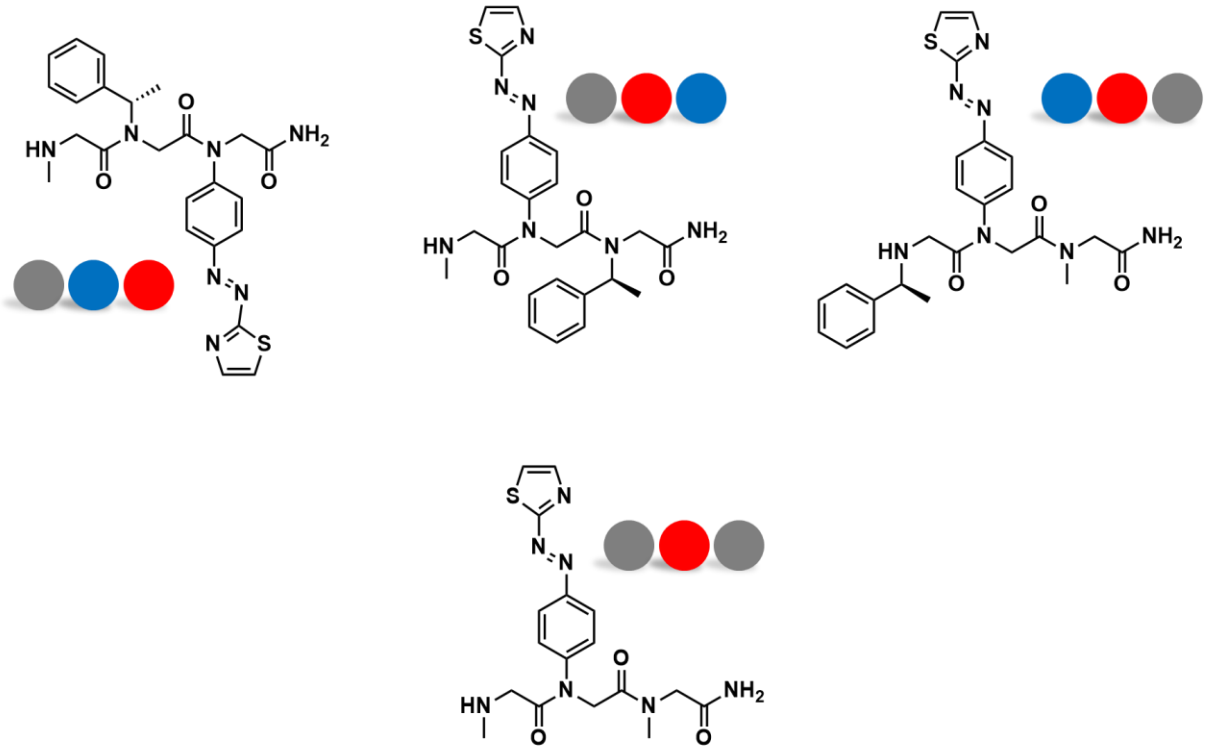

Appendix 9. *ESI-MS (+) (Waters Synapt G2-Si): MS/MS spectra for each PAT-based peptoid synthetized. MS/MS performed on $[M+H]^+$ with the corresponding E_{col}.*

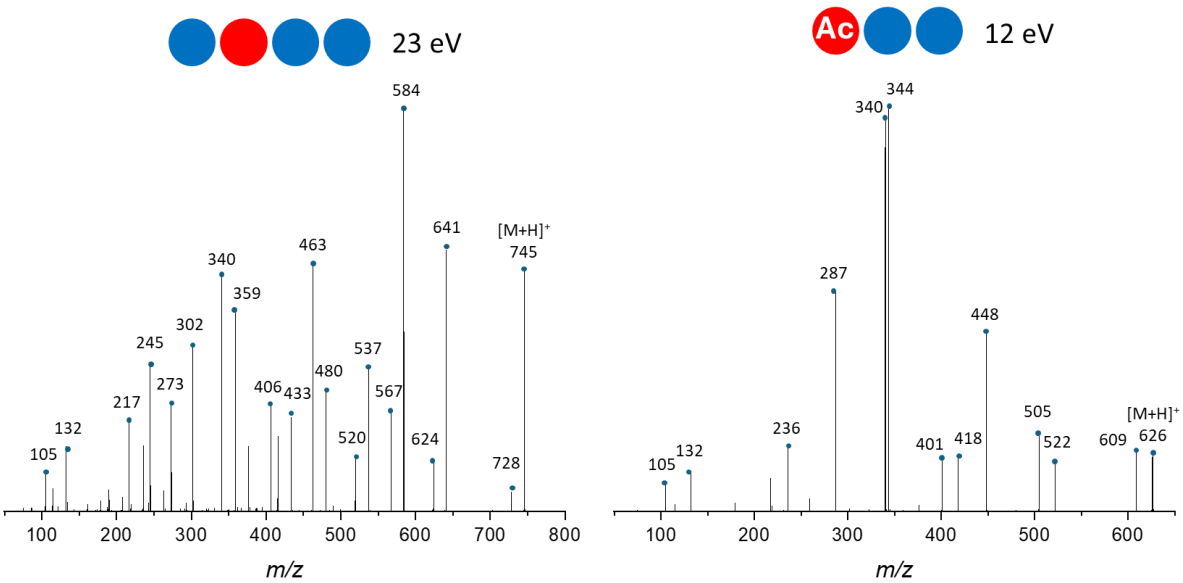

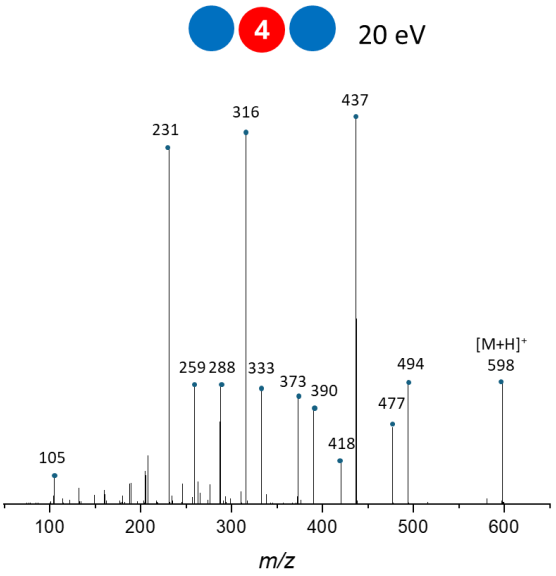
4
20 eV
105
231
259
288
316
333
373
390
418
437
477
494
[M+H]+
598
100
200
300
400
500
600
m/z

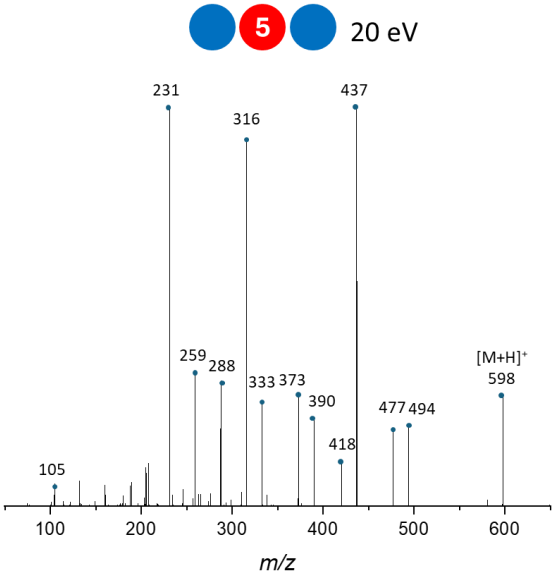
5
20 eV
105
231
259
288
316
333
373
390
418
437
477
494
[M+H]+
598
100
200
300
400
500
600
m/z

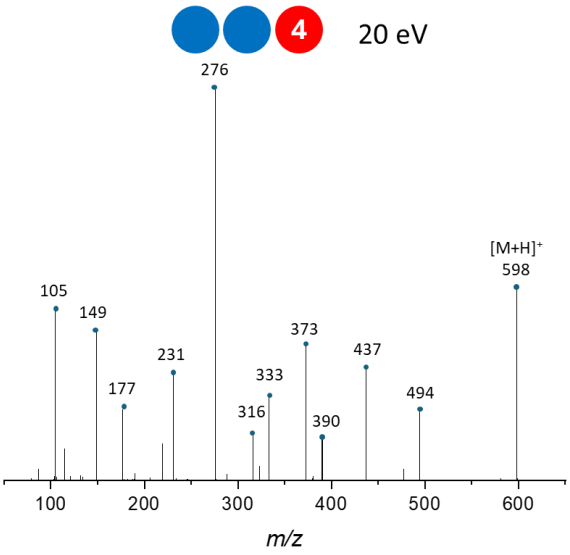
4
20 eV
105
149
177
231
276
316
333
373
390
437
494
[M+H]+
598
100
200
300
400
500
600
m/z

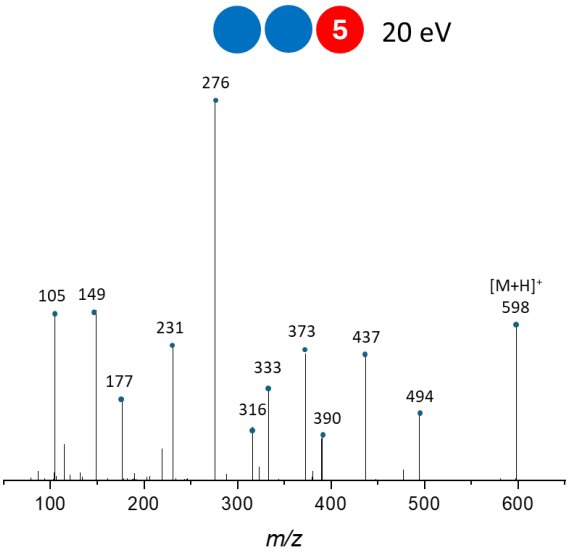
5
20 eV
105
149
177
231
276
316
333
373
390
437
494
[M+H]+
598
100
200
300
400
500
600
m/z

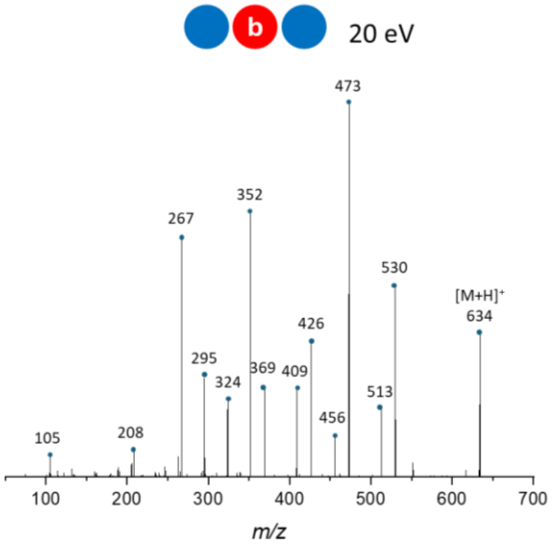
b
20 eV
105
208
267
295
324
352
369
409
426
456
473
513
530
[M+H]+
634
100
200
300
400
500
600
700
m/z

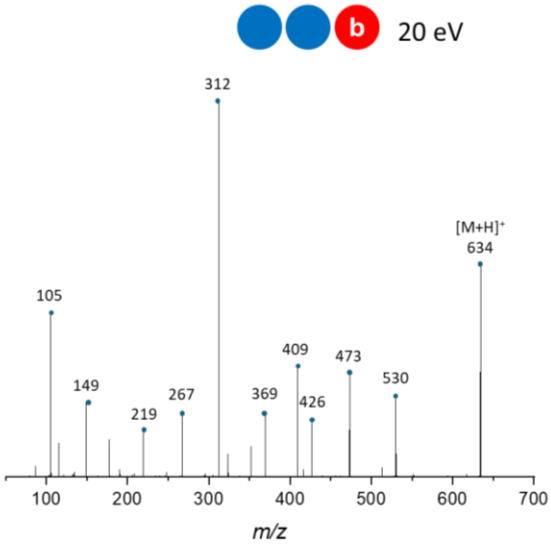
b
20 eV
105
149
219
267
312
369
409
426
473
530
[M+H]+
634
100
200
300
400
500
600
700
m/z

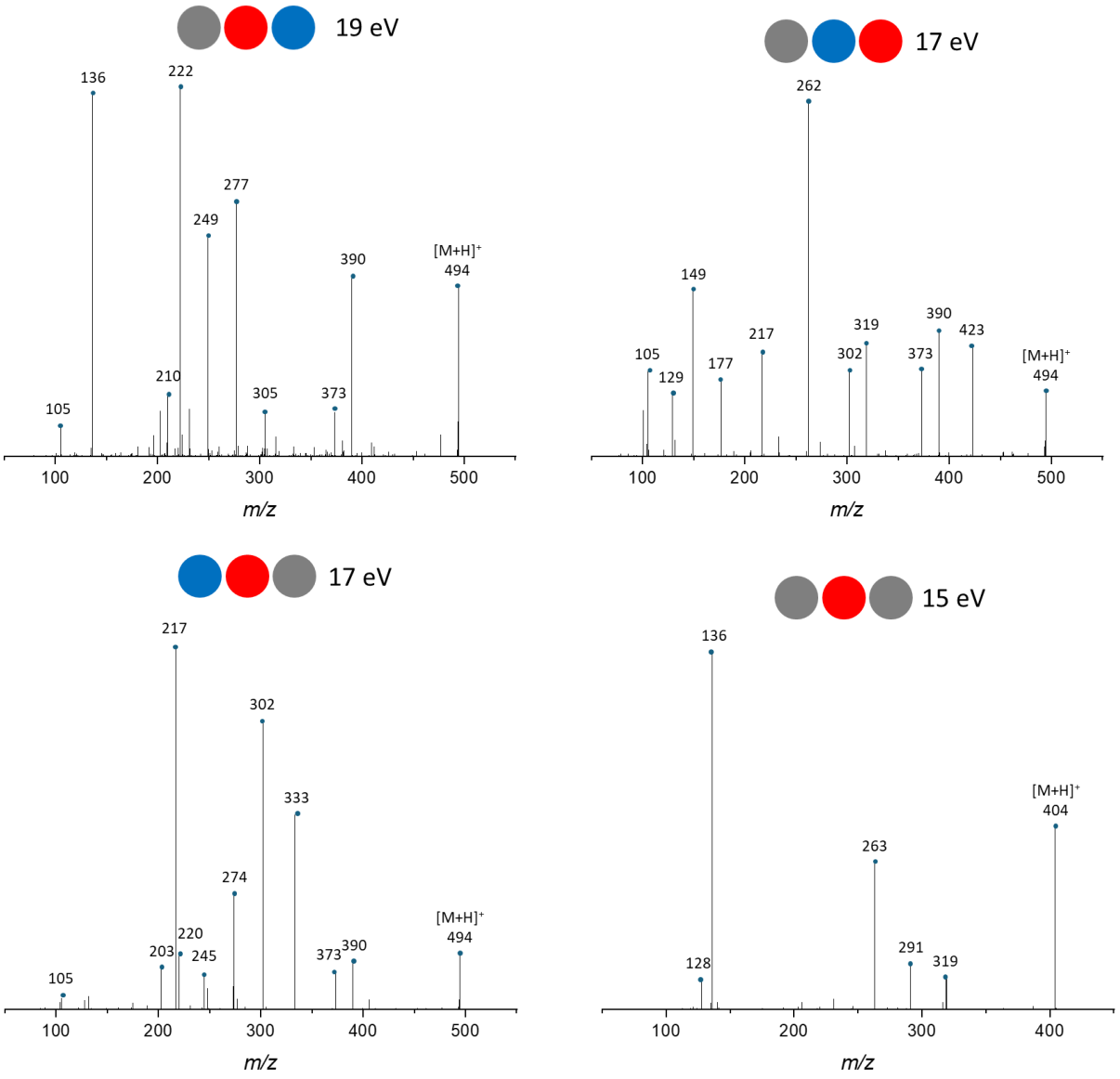

Appendix 10. *Monitoring of the thermal Z → E back-isomerization kinetics by LC-MS analyses at various temperatures ranging from 283 K to 303 K in 5-degree increments for hybrids peptoids in MeOH.*

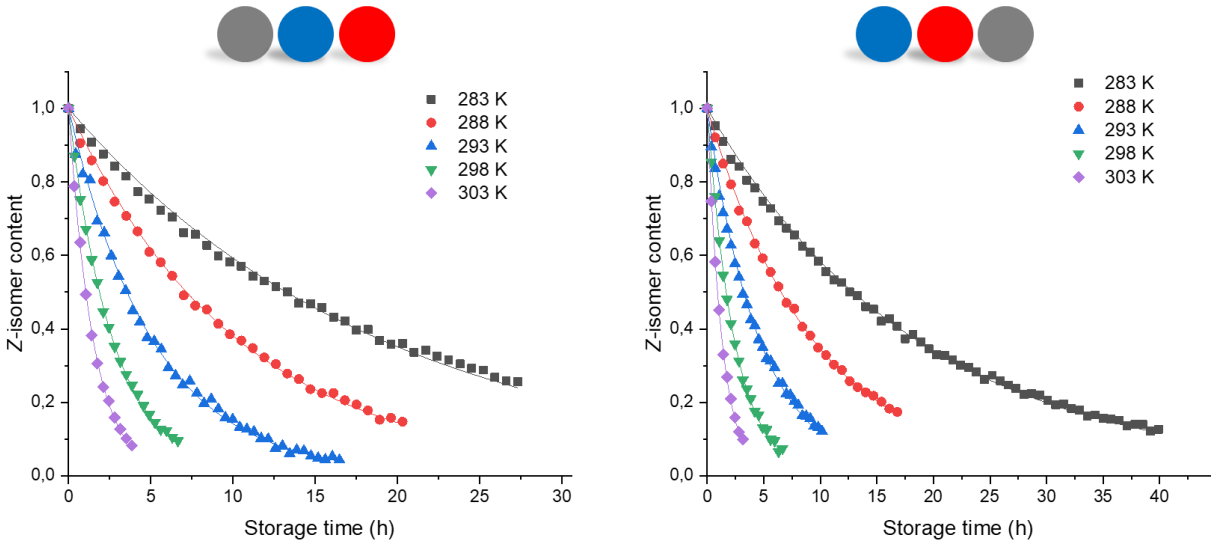

Appendix 11. *Summary of the relevant thermal parameters for PAT peptoids determined in MeOH: k_{avg} is the average kinetic constant, $t_{1/2}$ is the metastable isomer half-life time, $\Delta H^{\ddagger}$ is the activation enthalpy, $\Delta S^{\ddagger}$ is the activation entropy, $\Delta G^{\ddagger}$ is the Gibbs free energy.*

	T (°C)	k_{avg} (10^{-5} s^{-1})	$t_{1/2}$ (h)	$\Delta H^{\ddagger}$ ($kJ.mol^{-1}$)	$\Delta S^{\ddagger}$ ($J.mol^{-1}.K^{-1}$)	$\Delta G^{\ddagger}$ 20 °C ($kJ.mol^{-1}$)
Cter-PAT 1	10	1.30 ± 0.01	14.78 ± 0.22	94.90 ± 0.64	- 2.88 ± 2.19	95.75 ± 1.28
	15	2.58 ± 0.05	7.46 ± 0.18			
	20	5.30 ± 0.03	3.63 ± 0.03			
	25	10.39 ± 0.11	1.85 ± 0.03			
	30	20.17 ± 0.01	0.96 ± 0.09			
Center-PAT 1	10	1.57 ± 0.02	12.25 ± 0.18	91.44 ± 0.83	- 13.49 ± 2.88	95 40 ± 1.67
	15	3.13 ± 0.04	6.16 ± 0.13			
	20	6.14 ± 0.10	3.13 ± 0.08			
	25	12.12 ± 0.39	1.59 ± 0.07			
	30	21.07 ± 0.74	0.91 ± 0.04			
Ac-Nter PAT 1	10	1.62 ± 0.01	11.86 ± 0.08	88.69 ± 0.32	- 22.95 ± 1.05	95.42 ± 0.62
	15	3.11 ± 0.05	6.19 ± 0.10			
	20	6.00 ± 0.10	3.21 ± 0.05			
	25	12.37 ± 0.50	1.56 ± 0.06			
	30	20.81 ± 0.01	0.92 ± 0.01			
4-unit peptoid	10	1.54 ± 0.02	12.52 ± 0.17	98.45 ± 0.70	11.07 ± 2.33	95.20 ± 0.71
	15	3.42 ± 0.12	5.64 ± 0.20			
	20	6.45 ± 0.23	2.99 ± 0.11			
	25	11.98 ± 0.60	1.61 ± 0.08			
	30	26.04 ± 0.30	0.74 ± 0.01			
N*sar*N*spe*N2*tz*	10	1.45 ± 0.03	13.25 ± 0.41	87.84 ± 0.37	- 26.80 ± 1.28	95.69 ± 0.75
	15	2.74 ± 0.09	7.04 ± 0.29			
	20	5.43 ± 0.01	3.55 ± 0.01			
	25	10.38 ± 0.33	1.86 ± 0.08			
	30	18.39 ± 0.07	1.05 ± 0.01			
N*spe*N2*tz*N*sar*	10	1.48 ± 0.02	13.03 ± 0.30	92.67 ± 0.65	- 9.73 ± 2.26	95.53 ± 1.31
	15	2.95 ± 0.01	6.53 ± 0.01			
	20	5.99 ± 0.30	3.23 ± 0.24			
	25	11.31 ± 0.55	1.71 ± 0.12			
	30	21.19 ± 0.78	0.91 ± 0.05			

Appendix 12. *Arrhenius plot based on the rate constants extracted from the kinetics at different temperatures for the 4-unit peptoid, Ac-Nter PAT 1, NsarNspeN2tz and NspeN2tzNsar with their corresponding activation energies.*

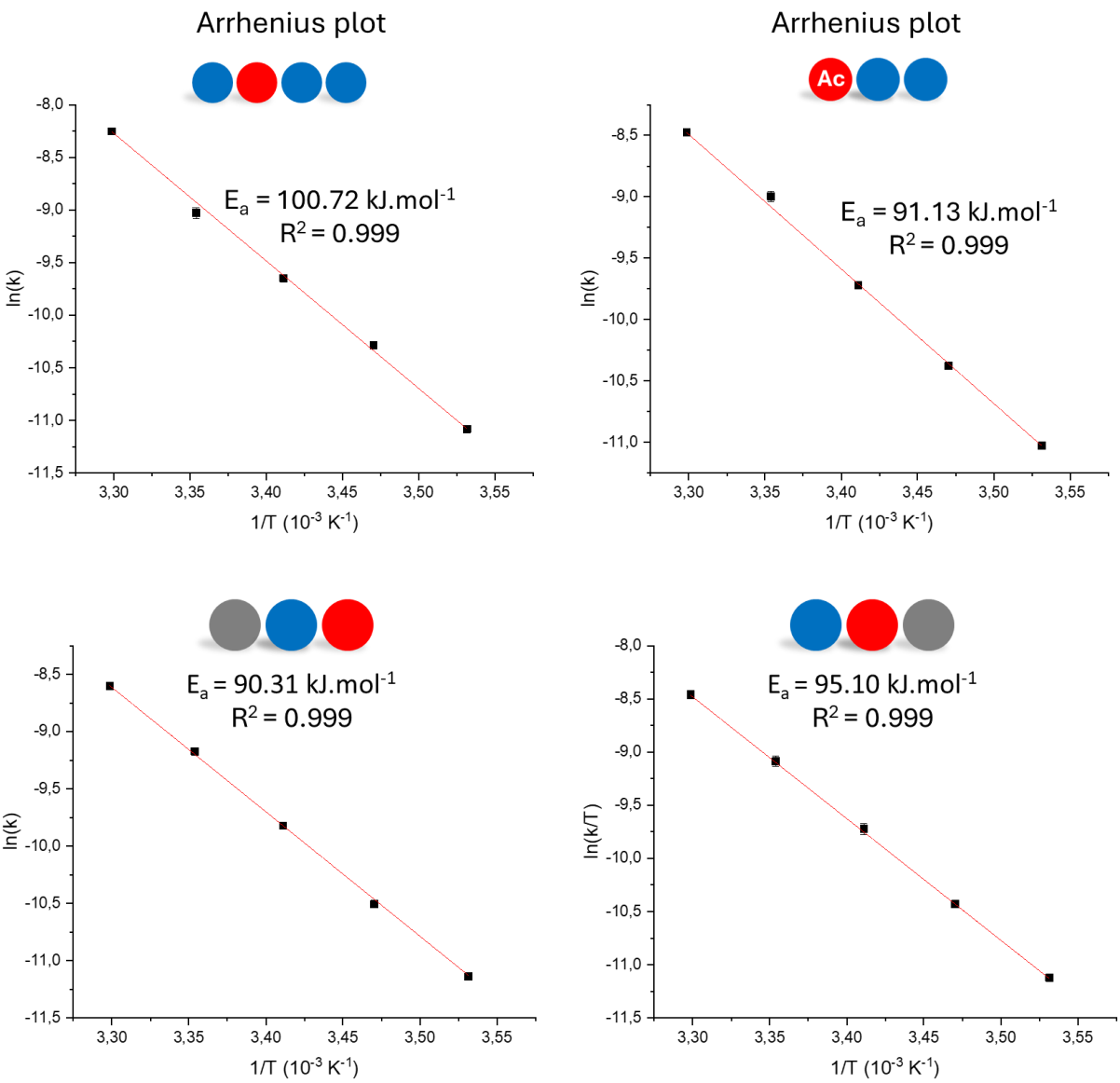

3. THE SILENCE OF THE SOLVENTS

The solvent, which represents the calorific medium of the MOST system, is likely to play a significant role in the thermal back-isomerization process. The objective of this section is to highlight this influence by determining the corresponding kinetic parameters in order to assess whether the observed behavior can be correlated with specific solvent properties. Initially, the focus was placed on examining solvent polarity. However, solvent polarity is a rather complex concept that cannot be fully described by a single parameter such as proton affinity, dielectric constant or dipole moment. To better reflect the complexity of real systems, we therefore decided to consider an empirical solvent parameter that encompasses several of these aspects simultaneously. Empirical parameters are particularly valuable in this context, as they provide an overall measure of solvent behavior by integrating multiple underlying physicochemical contributions.

3.1 SOLVENT POLARITY CALIBRATION

During this thesis, the Dimroth-Reichardt parameter was employed to describe solvent polarity.[258] This parameter is based on the influence of the solvent on the UV-vis absorption of betaine 30 (B30), also known as Reichardt dye, whose structure is shown in **Figure 70a**. The pronounced shifts observed in the charge-transfer band arise from different stabilization/destabilization of the polar ground state of B30 compared to the less polar excited state.[258] Consequently, highly polar solvents stabilize the ground state more effectively through solvation, leading to a strongly negative solvatochromic effect. The absorption maximum of the dye ranges from 438 nm in the most polar solvents to 881 nm in the most apolar ones, making this probe suitable across a wide range of solvent polarities. The $E_T(30)$ parameter is calculated according to **Eq.7** (see **Experimental** section) based on the maximum of the charge-transfer band. To establish a dimensionless polarity scale, Reichardt later introduced the normalized polarity scale[271], $E_T^N\ (30)$, which allows relative comparison between solvents positioned at the borders of the $E_T(30)$ scale, namely H_2O and TMS.[258]

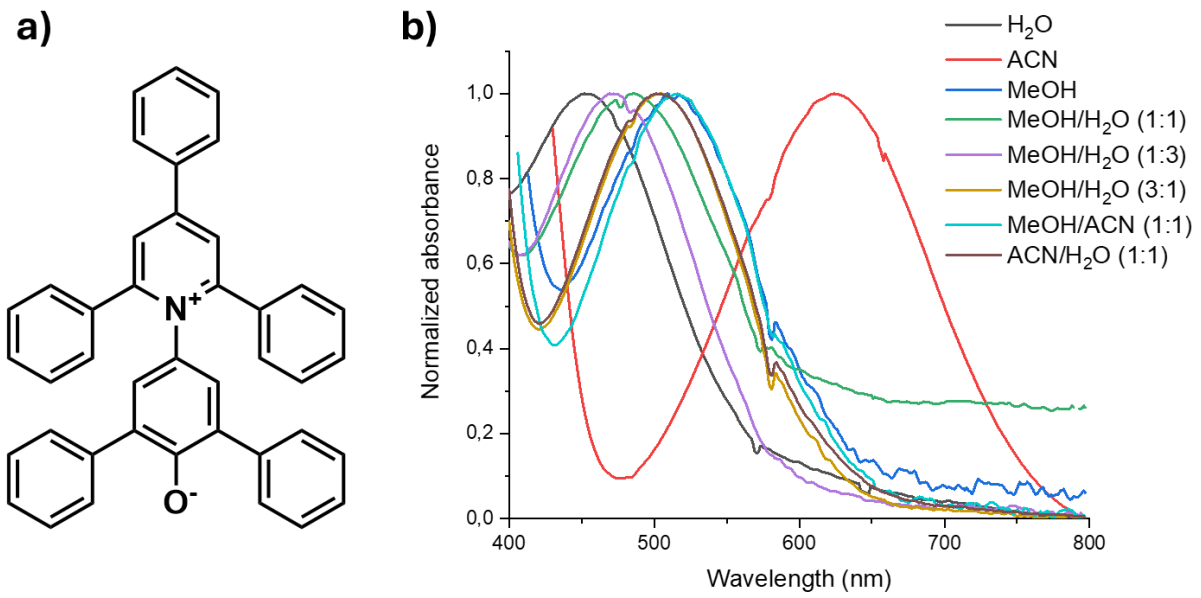

Figure 70. *Dimroth-Reichardt method to assess solvent polarity: a) Molecular structure of B30 in its zwitterionic form adapted from*[259]*. b) Normalized absorption profiles of B30 dissolved in 8 different solvents : H_2O, MeOH/H_2O (1:3), MeOH/H_2O (1:1), MeOH/H_2O (3:1), ACN/H_2O (1:1), MeOH, MeOH/ACN (1:1) and ACN. Numeric values of $E_T(30)$ and $E_T^N(30)$ measured at R.T are reported in Table 6.*

The $E_T(30)$ values for pure solvents are well-documented in the literature. However, data for solvent mixtures is scarcely or inconsistently reported. Since our study aims to examine how solvent composition influences $t_{1/2}$, we also measured several solvent mixtures, *i.e.* MeOH/H_2O ((1:3), (1:1) and (3:1)), MeOH/ACN (1:1) and ACN/H_2O (1:1). To determine the corresponding $E_T(30)$ values, UV-vis spectra were recorded (**Figure 70b**). To validate the reliability of the method, the $E_T(30)$ values for pure MeOH, ACN and H_2O were also measured and compared with the literature reported reference values.

Solvents	λ_{max} (nm)	$E_T(30)$ (kcal.mol^{-1})	$E_T^N(30)$	$E_T(30)^a$ (kcal.mol^{-1})
H_2O	452	63.3	1.004	63.1
MeOH	510	56.1	0.783	55.4
ACN	624	45.8	0.467	45.6
MeOH/H_2O (1:3)	469	61.0	0.934	/
MeOH/H_2O (1:1)	485	59.0	0.872	/
MeOH/H_2O (3:1)	504.5	56.7	0.802	/
MeOH/ACN (1:1)	516	55.4	0.763	/
ACN/H_2O (1:1)	501	57.1	0.814	/

Table 6. *Dimroth-Reichardt method to assess solvent polarity: λ_{max} values of B30 in the 8 solvents measured at R.T with numeric values of $E_T(30)$ and $E_T^N(30)$.[a] $E_T(30)$ obtained from*[260]*.*

Table 6 presents the $E_T(30)$ values obtained for different solvents. A very good agreement is observed between the measured values for pure solvents and those reported in the literature, confirming the reliability of the methodology used. Therefore, the $E_T(30)$ values determined for the solvent mixture in this work can be confidently compared with literature data. Interestingly, for MeOH/H_2O mixtures, a linear correlation (see **Appendix**) is observed between the solvent composition and the corresponding $E_T(30)$ values, in line with previous reports.[272] In contrast, mixtures containing ACN (either with MeOH or H_2O) do not follow this linear trend. Instead, the $E_T(30)$ values obtained for these mixtures are closer to those of MeOH and H_2O, showing a rather good exponential correlation. This behavior suggests that solvent proticity plays a key role in determining the absorption maximum of the B30. For both ACN-containing mixtures, additional solvent ratios would be required to confirm this hypothesis, but this is beyond the scope of our study.

3.2 THERMAL BACK-ISOMERIZATION IN DIFFERENT SOLVENTS

Combining the $E_T^N(30)$ values calculated in this work and those available in the literature, it is now possible to investigate the influence of solvent polarity on the thermal back-isomerization process. This study will first focus on the Ac-PAT derivatives, with the thermal-back-isomerization monitored at R.T by UV-vis spectroscopy. In a second step, the solvent effects

will be examined for Cter-PAT 1 and Center-PAT 1 at 20 °C using LC-MS analyses. From a practical standpoint, the samples were dissolved directly in the solvent under investigation. In cases where the compound exhibited limited solubility, a stock solution in MeOH (for protic solvent) and ACN (for aprotic solvent) was prepared and added in a proportion below 1 % (v/v) to the analysis medium, assuming that such a limited addition does not influence drastically the thermal back-isomerization kinetics.

3.2.1 Ac-PAT derivatives

Figure 70 displays the kinetic constants of Ac-PAT 1 (**Figure 71a**), Ac-PAT 2 (**Figure 71b**), Ac-PAT 3 (**Figure 71c**) and Ac-PAT 5 (**Figure 71d**) in H_2O (squares), MeOH (Circle), ACN (triangles) and toluene (stars) as a function of the polarity parameter. It is observed that, compared to MeOH, the $t_{1/2}$ values obtained in H_2O are significantly lower, decreasing to 11 min for Ac-PAT 1 and approximately 3.7 min for Ac-PAT 2 and Ac-PAT 3. The lowest value is observed for Ac-PAT 5, for which photoisomerization is undetectable in H_2O, suggesting an extremely fast thermal-back-isomerization with $t_{1/2} < 1$ s.

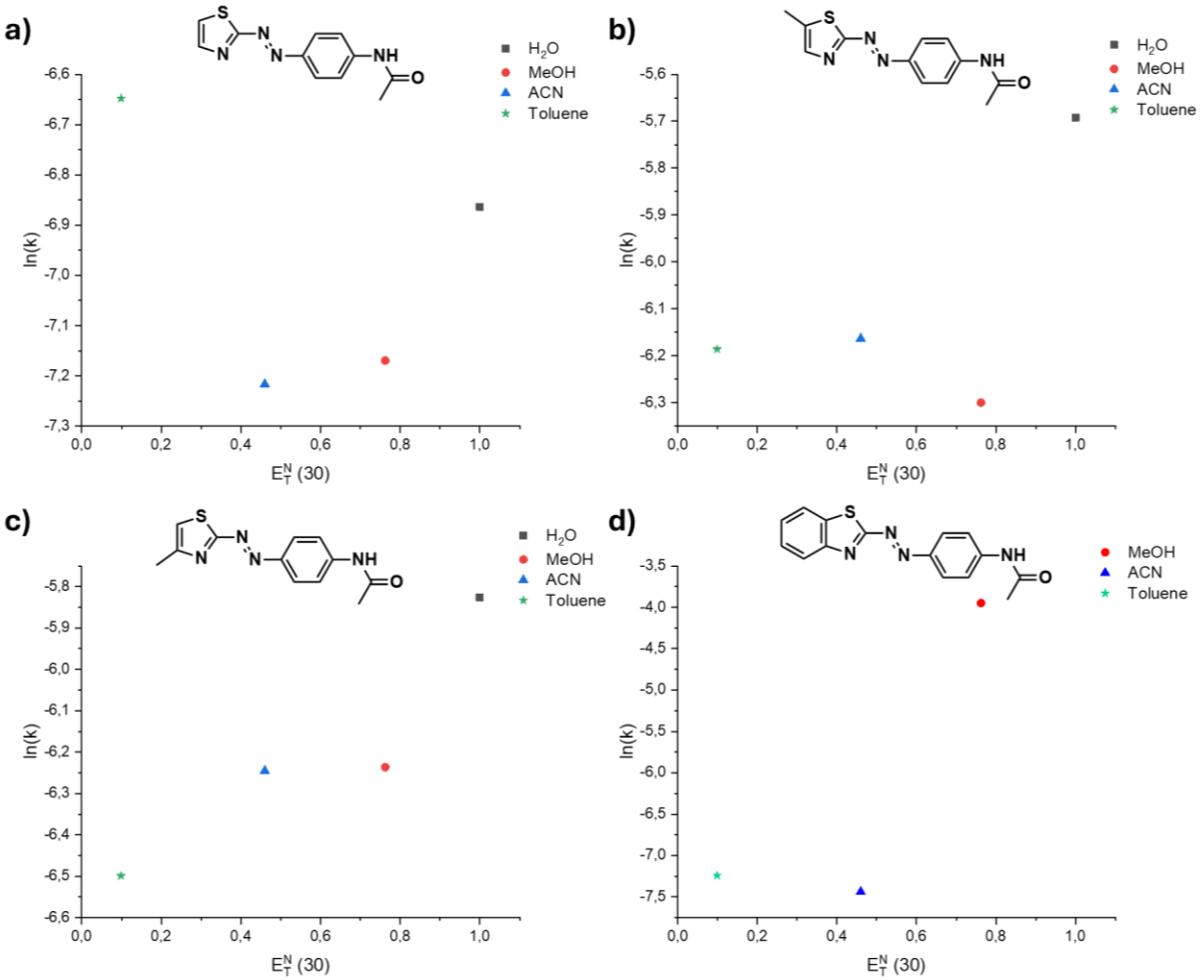

Figure 71. *Dimroth-Reichardt plot gathering the kinetic constants in H_2O (squares), MeOH (circles), ACN (triangles) and toluene (stars) plotted against the E_T^N (30) parameter for Ac-PAT 1 (a), Ac-PAT 2 (b), Ac-PAT 3 (c) and Ac-PAT 5 (d).*

Concerning ACN, the $t_{1/2}$ values obtained for Ac-PAT 1, Ac-PAT 2 and Ac-PAT 3 are similar to those measured in MeOH. However, for Ac-PAT 5, a drastic increase is observed in ACN with a $t_{1/2}$ of 19.6 min corresponding to a 33-fold increase compared to MeOH. In toluene, Ac-PAT 1 exhibits a 50% reduction of the $t_{1/2}$ compared to MeOH, while Ac-PAT 2 shows no significant variation. In contrast, Ac-PAT 3 presents a slight increase in thermal stability, with $t_{1/2}$ of 7.8 min. Once again, Ac-PAT 5 displays a remarkable enhancement, with a 27-fold increase in $t_{1/2}$ compared to MeOH. All the $t_{1/2}$ values are summarized in **Table 7**.

R.T	$t_{1/2}$ H_2O (min)	$t_{1/2}$ MeOH (min)	$t_{1/2}$ ACN (min)	$t_{1/2}$ Toluene (min)
Ac-PAT 1	11.07 ± 0.37	15.01 ± 0.14	15.74 ± 0.26	8.92 ± 0.27
Ac-PAT 2	3.54 ± 0.54	6.29 ± 0.14	5.49 ± 0.17	5.63 ± 0.27
Ac-PAT 3	3.92 ± 0.01	5.90 ± 0.11	5.96 ± 0.08	7.67 ± 0.03
Ac-PAT 5	< 1 s	0.60 ± 0.02	19.69 ± 0.85	16.17 ± 0.91

Table 7. *$t_{1/2}$ values obtained at R.T for Ac-PAT derivatives in H_2O, MeOH, ACN and toluene.*

The only clear trend observed across all the derivatives studied is the drastic reduction of $t_{1/2}$ values in H_2O compared to other solvents. The next step is to examine whether anchoring the PAT chromophore onto a peptoid backbone influences this solvent-dependent behavior observed for the various Ac-PAT derivatives.

3.2.2 PAT 1 peptoids

The back-isomerization reaction was investigated in 17 different solvents or solvent mixtures for Cter-PAT 1. The study was further limited to only four representative solvents, *i.e.* H_2O, MeOH, ACN and toluene, as these cover a broad panel of solvent polarities. Among them, toluene and H_2O represent the apolar and highly polar limits, respectively, while MeOH and ACN are comparably polar but differ in their protic/aprotic nature. The kinetic constants obtained in each solvent were plotted as a function of the polarity parameter (**Figure 72**). In this representation, protic solvents and their mixtures are shown as square symbols, aprotic solvents as circles, and protic/aprotic mixtures as stars.

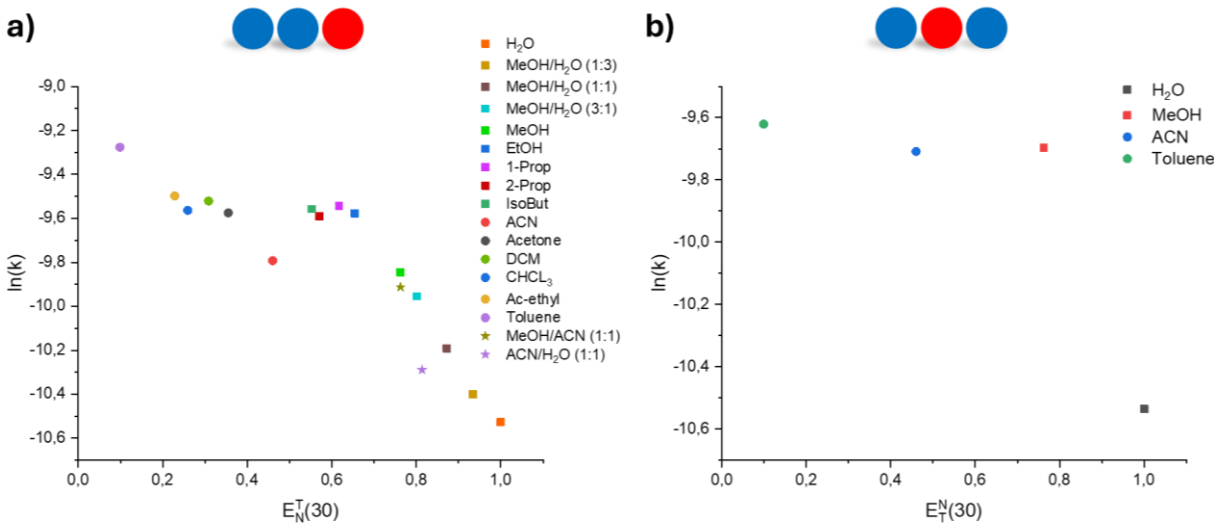

Figure 72. *a) Dimroth-Reichardt plot showing the kinetic constants of Cter-PAT 1 in various solvents: protic and mixture of protic solvents (squares), aprotic solvents (circles) and mixture of protic/aprotic solvents (stars) plotted against* $E_T^N\ (30)$ *parameter. b) Dimroth-Reichardt plot showing the kinetic constants of Center-PAT 1 in* H_2O*, MeOH, ACN and toluene plotted against the* $E_T^N\ (30)$ *parameter.*

For Cter-PAT 1 (**Figure 72a**), two distinct regions can be identified: the aprotic solvents are clustered on the left side of the plot, while protic solvents are grouped on the right-hand side. Interestingly, mixtures of protic solvents also appear on the right-hand side, emphasizing that solvent proticity plays a key role in the thermal back-isomerization process. The results show that the highest $t_{1/2}$ value is obtained in H_2O (7.0 h), whereas the lowest is observed in toluene (2.2 h). By comparison, MeOH gives an intermediate value of 3.6 h, indicating that the $t_{1/2}$ in H_2O is roughly twice as long. This finding is particularly encouraging from an application standpoint, as H_2O is non-toxic, cheap and environmentally friendly solvent. Remarkably, this trend is the opposite of what was observed for the Ac-PAT derivatives, where H_2O led to a much shorter $t_{1/2}$. This inversion suggests that the thermal back-isomerization mechanisms differ between Ac-PAT derivatives and Cter-PAT 1 peptoid. A plausible explanation lies in the molecular size and structural complexity of the systems: the smaller Ac-PAT derivatives are likely more sensitive to solvent interactions, whereas the larger peptoid frameworks may experience different stabilization or destabilization in the structure of either the *E*- and *Z*-isomer or in the transition state, ultimately leading to distinct thermal back-isomerization kinetics.

20 °C	$t_{1/2}$ H_2O (h)	$t_{1/2}$ MeOH (h)	$t_{1/2}$ ACN (h)	$t_{1/2}$ Toluene (h)
Cter-PAT 1	7.05 ± 0.13	3.63 ± 0.03	3.68 ± 0.24	2.20 ± 0.15
Center-PAT 1	7.25 ± 0.05	3.13 ± 0.06	3.17 ± 0.05	2.90 ± 0.06

Table 8. *$t_{1/2}$ values obtained at 20 °C for Cter-PAT 1 and Center-PAT 1 in H_2O, MeOH, ACN and toluene.*

Concerning Center-PAT 1, a similar trend is observed, with the largest $t_{1/2}$ obtained in H_2O and the weakest in toluene. However, the difference between ACN and toluene is less pronounced, as their $t_{1/2}$ values are relatively close. In contrast, the gap between H_2O and MeOH is more significant than that observed for Cter-PAT 1, indicating that Center-PAT 1 is more sensitive to solvent proticity. All the values of $t_{1/2}$ for Cter-PAT 1 and Center PAT 1 are summarized in **Table 8**.

3.3 DETERMINATION OF KINETIC PARAMETERS

To investigate in more details the solvent-dependent trends, and to elucidate the mechanism(s) of thermal back-isomerization, the kinetics were measured at different temperatures in order to extract the corresponding activation parameters. The temperature-dependent kinetic data for both PAT 1 peptoids are provided in the **Appendix**. The Eyring plots for Cter-PAT 1 and Center-PAT 1 are shown in **Figure 73a** and **73b**, respectively, while the Arrhenius plots are presented in the **Appendix** section.

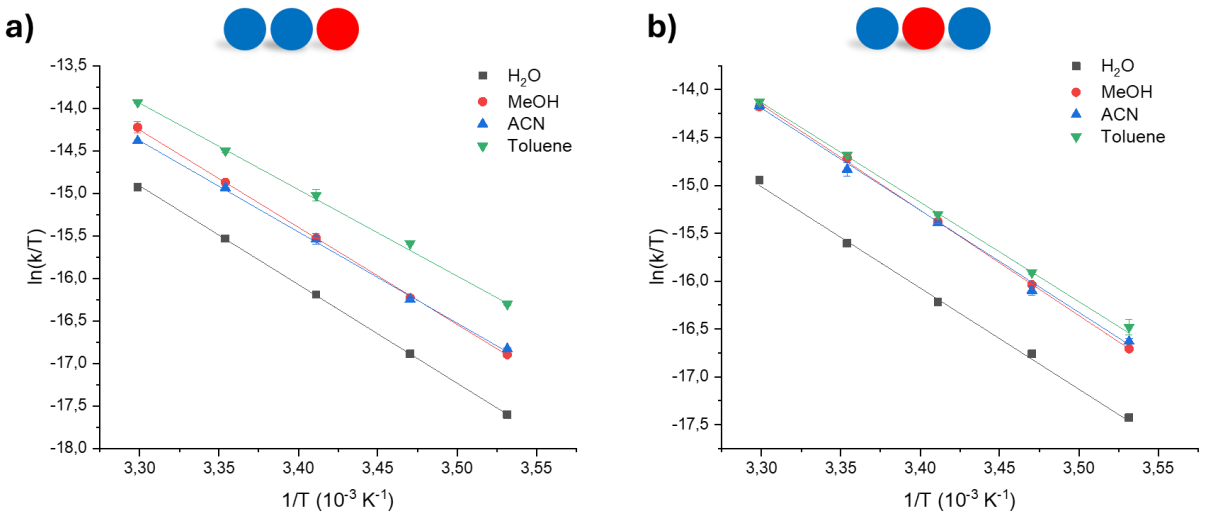

Figure 73. *Eyring-Polanyi plot based on the rate constants extracted from the kinetics at different temperatures for Cter-PAT 1 (a) and Center-PAT 1 (b) (LC-MS procedure) in various solvents: H_2O (black), MeOH (red), ACN (blue) and toluene (green).*

The enthalpies and entropies of activation for both systems in the different solvents are summarized in **Table 9**. For Cter-PAT 1, the entropy of activation obtained in H_2O is comparable to that measured in MeOH, but significantly more negative entropy values are observed in ACN and toluene. This suggests that the thermal back-isomerization proceeds through different mechanisms depending on the solvent: an inversion pathway in protic solvents (H_2O and MeOH) and a rotation pathway in aprotic solvents (ACN and toluene), according to the classification proposed by Reimann *et al.*[37] This mechanistic shift can be rationalized by the proticity of the solvent, since hydrogen-bond in protic media may restrict molecular motion and favor inversion, while the lack of such interaction in aprotic solvents allows greater conformational freedom, enabling rotation. It should be noted that the rotation type I pathway is also possible, which corresponds to rotation process but without passing through triplet state. This process exhibits activation entropy values intermediate between those of the inversion and rotation type II mechanisms. However, this pathway is relatively uncommon, as the triplet state, when accessible, is generally the preferred route for the back-isomerization process.

	$\Delta H^{\ddagger}$ (kJ.mol^{-1})	$\Delta S^{\ddagger}$ (J.mol^{-1}.K^{-1})	$\Delta G^{\ddagger}_{20°C}$ (kJ.mol^{-1})	E_a (kJ.mol^{-1})
Cter-PAT 1 (H_2O)	96.35 ± 0.34	- 3.57 ± 1.2	97.39 ± 0.70	98.74 ± 0.33
Cter-PAT 1 (MeOH)	94.90 ± 0.64	- 2.9 ± 2.2	95.75 ± 1.28	97.32 ± 0.65
Cter-PAT 1 (ACN)	89.01 ± 1.65	- 23.4 ± 5.6	95.86 ± 3.28	91.46 ± 1.65
Cter-PAT 1 (Toluene)	84.44 ± 1.06	- 34.8 ± 3.6	94.64 ± 2.12	86.88 ± 1.05
Center-PAT 1 (H_2O)	87.87 ± 2.45	- 32.4 ± 8.4	97.37 ± 4.91	90.30 ± 2.47
Center-PAT 1 (MeOH)	91.44 ± 0.83	- 13.5 ± 2.9	95.40 ± 1.67	93.86 ± 0.82
Center-PAT 1 (ACN)	88.58 ± 1.73	- 23.3 ± 5.9	95.39 ± 3.46	91.01 ± 1.74
Center-PAT 1 (Toluene)	86.35 ± 0.77	- 30.1 ± 2.6	95.18 ± 1.52	88.80 ± 0.77

Table 9. *Kinetic parameters for Cter-PAT 1 and Center-PAT 1 in H_2O, MeOH, ACN and toluene.*

For Center-PAT 1, drastic differences are observed compared to Cter-PAT 1. In MeOH, a $\Delta S^{\ddagger}$ of -13.5 J.mol^{-1}.K^{-1} is obtained, representing the least negative and thus the highest value recorded for this system. In this case, the previous explanation based on solvent proticity does not hold, since all the solvents investigated exhibit negative activation entropies, suggesting that the thermal back-isomerization proceeds predominantly via a rotation pathway. To confirm these hypotheses, theoretical modeling and simulations would be valuable to further clarify the reaction mechanism.

It is also worth noting that the activation energy obtained from Arrhenius plot are systematically higher than enthalpies of activation estimated from Eyring plots, with discrepancies of approximately 2-3 kJ.mol^{-1}. Although both parameters are expected to represent the same kinetic parameters, the thermal energy required for the back-isomerization process, this systematic deviation can have non-negligeable consequences. Even this difference may appear minor, in the context of thermal back-isomerization, such variations can lead to two- to threefold differences in the calculated $t_{1/2}$ values. Consequently, the Eyring plot appears to provide a more accurate and realistic description of the experimental reality, as its derived parameters show better agreement with the $t_{1/2}$ values obtained experimentally.

3.4 CONCORDANCE BETWEEN GAS AND LIQUID PHASES

An interesting observation can be made for Cter-PAT 1 when examining **Figure 72a**, which shows a linear evolution of the kinetic constants as a function of E_T^N (30) between 0.75 to 1.00. This is further exemplified in **Figure 74** that presents the kinetic constants in H_2O/MeOH solvent mixtures plotted against the corresponding polarity parameter.

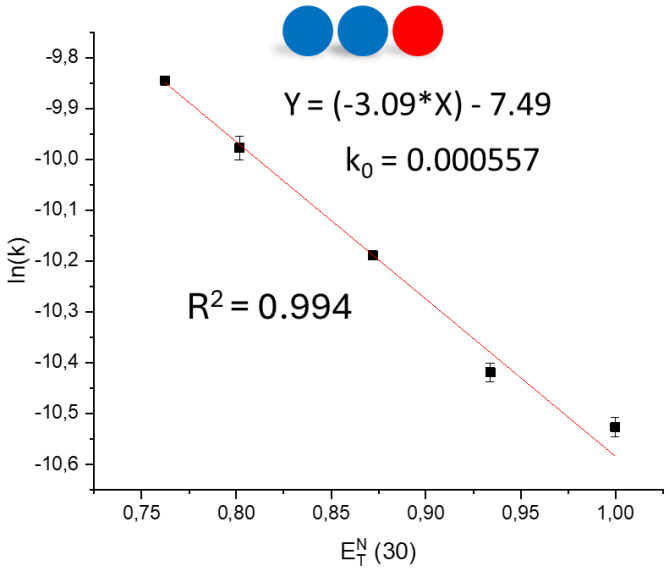

Figure 74. *Dimroth-Reichardt plot showing the kinetic constant of Cter-PAT 1 in H_2O/MeOH mixtures plotted against E_T^N (30) parameter.*

Applying a linear fit to these data points allows the determination of the intercept of the linear regression, which theoretically corresponds to the most apolar solvent possible. From this extrapolation, a kinetic constant of 5.57 10^{-4} s^{-1} ($t_{1/2}$ = 21 min) is obtained. This result is remarkably close to that recently determined in the lab for the gas-phase thermal back-isomerization extrapolated at 20 °C (5.17 10^{-4} s^{-1}, $t_{1/2}$ = 22 min)[273], note that the extreme vacuum within the mass spectrometer can be compared as an apolar solvent. By measuring the kinetic constant of AB derivatives in H_2O/MeOH mixtures of varying composition and plotting them as a function of the $E_T(30)$ parameter, it may be possible to establish a bridge between the condensed-phase and the gas-phase behaviors of the thermal back-isomerization. Further investigations are currently under progress to establish the limit of such a comparison.

3.5 INTERMEDIATE CONCLUSION

The investigation of the solvent influence on the thermal back-isomerization of PAT derivatives revealed that solvent polarity/proticity plays a crucial role in the stabilization or destabilization of the *E*/*Z*-isomers and their transition state. For Ac-PAT derivatives, H_2O significantly accelerates the back-isomerization compared to MeOH, whereas ACN leads to comparable $t_{1/2}$ values among the different tested compounds. Interestingly, this behavior contrasts with that observed for the PAT 1 peptoids, where both Cter- and Center-PAT 1 display approximately double $t_{1/2}$ values in H_2O relative to MeOH. For Cter-PAT 1, aprotic solvents appear to promote a rotation mechanism for the thermal-back-isomerization, while protic solvents favor an inversion pathway. In contrast, Center-PAT 1 exhibits highly negative activation entropies in all tested solvents, indicating that the rotation mechanism predominates regardless of the solvent nature. These results suggest that no universal behavior can be established, as the thermal-back-isomerization mechanism is strongly system-dependent and must be determined individually for each derivative/solvent combination.

The linear correlation observed for kinetic constants of Cter-PAT 1 in MeOH/H_2O mixtures plotted against the polarity parameter further suggests a possible continuity between liquid- and gas-phase behaviors. Such hypothesis should be verified by evaluating kinetic constants of H_2O/MeOH mixtures for additional PAT peptoids. Overall, these findings underline the sensitive interplay between solvent properties, molecular structure, and isomerization pathway, offering valuable insights for the rational design and optimization of MOST systems through solvent engineering.

3.6 APPENDICES

Appendix 13. *Correlation between the $E_T(30)$ polarity parameters and the proportion of H_2O or MeOH in MeOH/H_2O, MeOH/ACN and ACN/H_2O mixtures.*

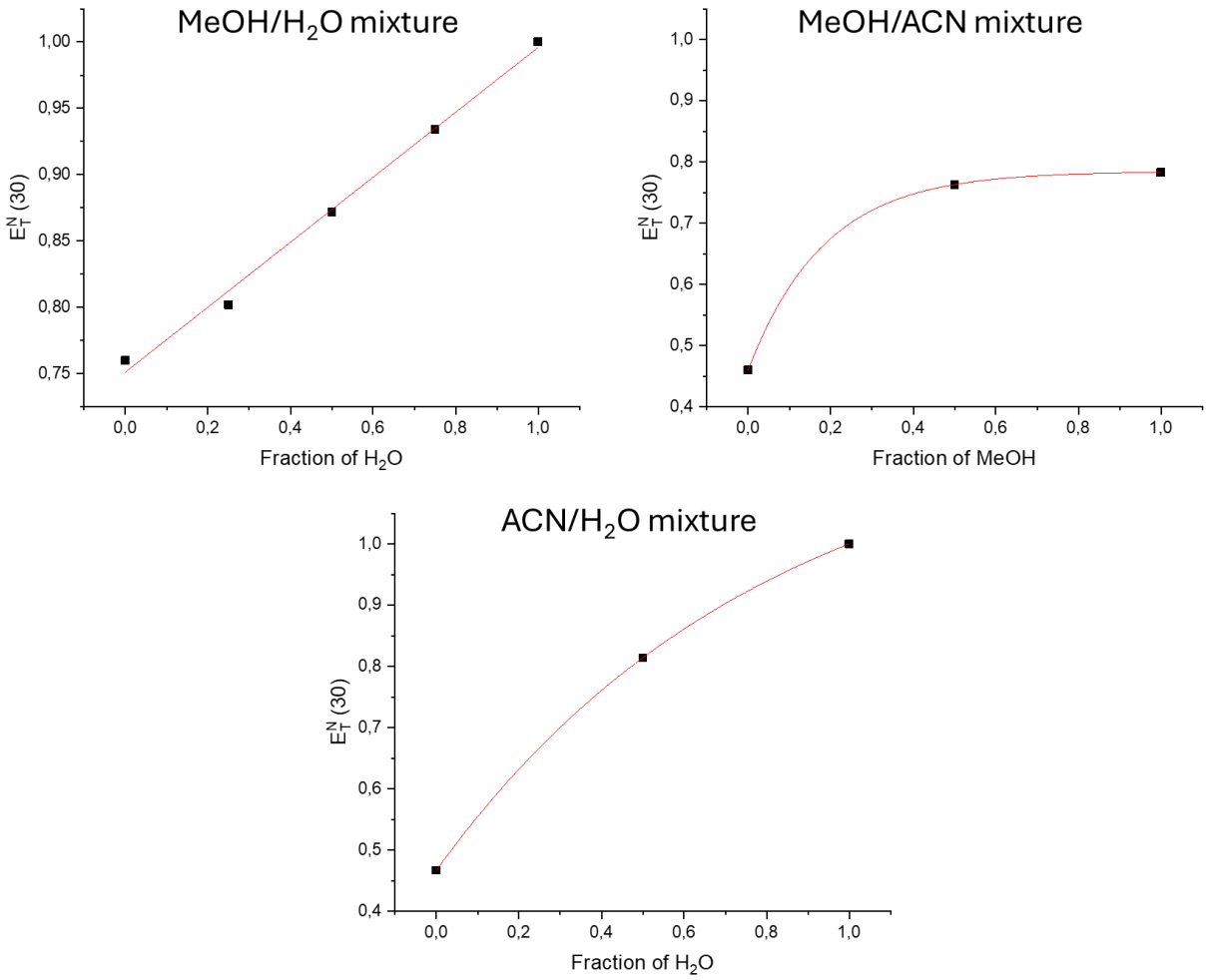

Appendix 14. *Monitoring of the thermal Z → E back isomerization kinetics by UV-vis spectroscopy of Ac-PAT derivatives in MeOH, H_2O, ACN and toluene.*

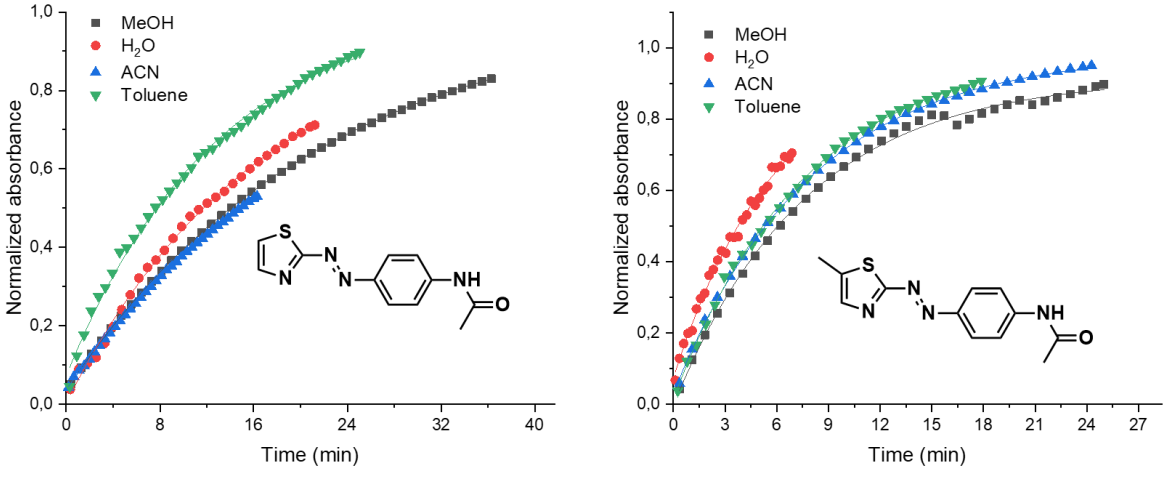

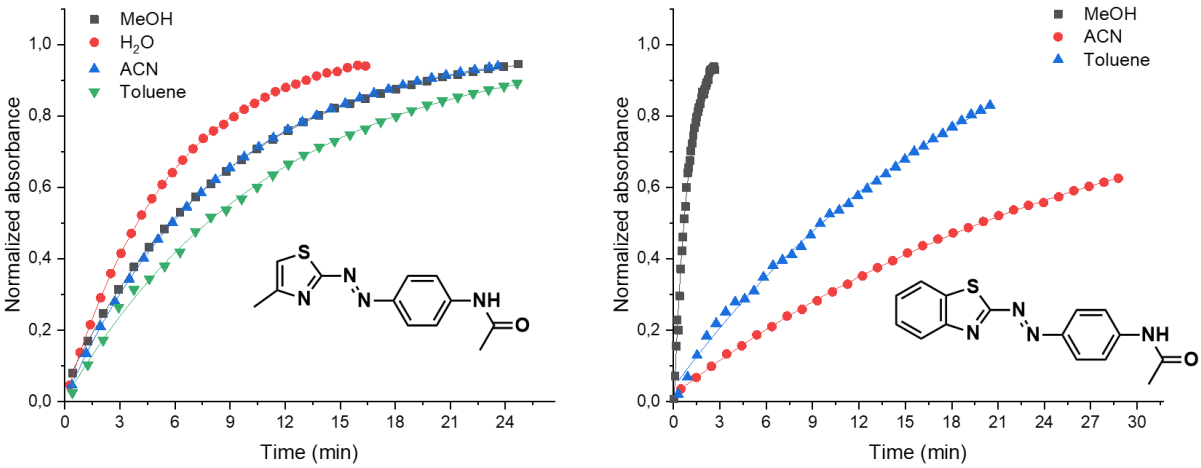

Appendix 15. *Monitoring of the thermal Z → E back-isomerization kinetics by LC-MS analyses at 20 °C for Cter-PAT 1 and Center-PAT 1 in various solvents. Normalized Z-isomer content plotted against the time showing a first-order exponential decay.*

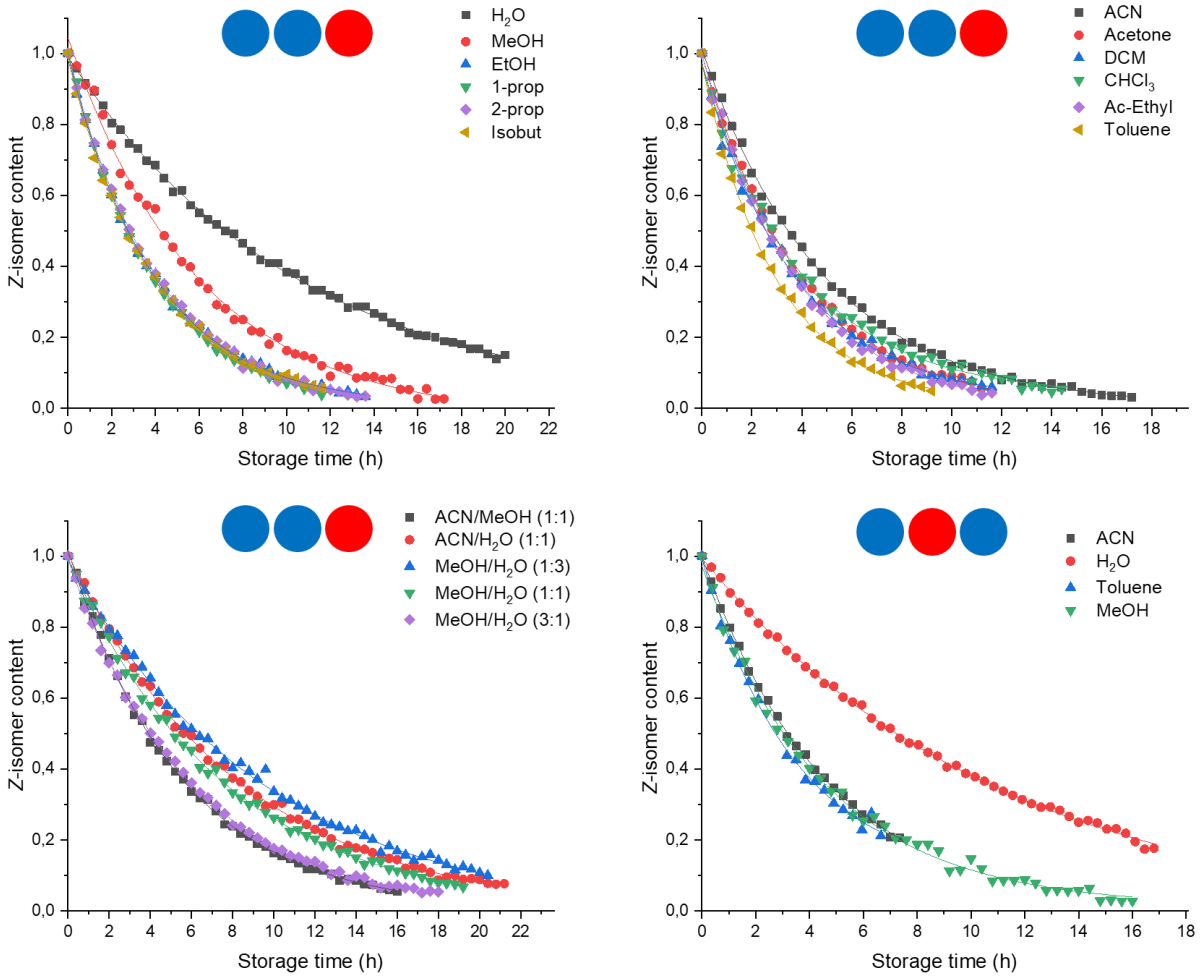

Appendix 16. *Kinetic constants and $t_{1/2}$ values obtained for Cter-PAT 1 and Center-PAT 1 at 20 °C in various solvents, along with their corresponding $E_T^N(30)$.*

20°C	k (10^{-5} s^{-1})	$t_{1/2}$ (h)	$E_T^N(30)$
			
H_2O	2.73 ± 0.05	7.05 ± 0.13	1.00
MeOH	5.30 ± 0.03	3.63 ± 0.03	0.76
EtOH	6.93 ± 0.04	2.78 ± 0.02	0.65
1-prop	7.16 ± 0.03	2.69 ± 0.01	0.62
2-prop	6.83 ± 0.03	2.81 ± 0.01	0.57
Isobut	7..07 ± 0.05	2.72 ± 0.02	0.40
ACN	5.25 ± 0.34	3.68 ± 0.24	0.46
Acetone	6.94 ± 0.04	2.77 ± 0.02	0.35
DCM	7.33 ± 0.10	2.63 ± 0.03	0.31
$CHCl_3$	7.14 ± 0.25	2.74 ± 0.10	0.26
Ac-ethyl	7.50 ± 0.05	2.57 ± 0.02	0.23
Toluene	8.78 ± 0.59	2.20 ± 0.15	0.10
ACN/H_2O (1:1)	3.40 ± 0.02	5.66 ± 0.03	0.81
ACN/MeOH (1:1)	4.95 ± 0.02	3.89 ± 0.02	0.76
MeOH/H_2O (1:3)	2.99 ± 0.06	6.45 ± 0.12	0.93
MeOH/H_2O (1:1)	3.76 ± 0.01	5.12 ± 0.01	0.87
MeOH/H_2O (3:1)	4.64 ± 0.11	4.15 ± 0.10	0.80
	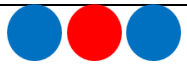		
H_2O	2.66 ± 0.02	7.25 ± 0.05	1.00
MeOH	6.14 ± 0.10	3.13 ± 0.08	0.76
ACN	6.08 ± 0.10	3.17 ± 0.05	0.46
Toluene	6.63 ± 0.13	2.90 ± 0.06	0.10

Appendix 17. *Monitoring of the thermal Z → E back-isomerization kinetics by LC-MS analyses at various temperatures ranging from 283 K to 303 K in 5-degree increments for Cter-PAT 1 and Center-PAT 1 in H2O, ACN and toluene.*

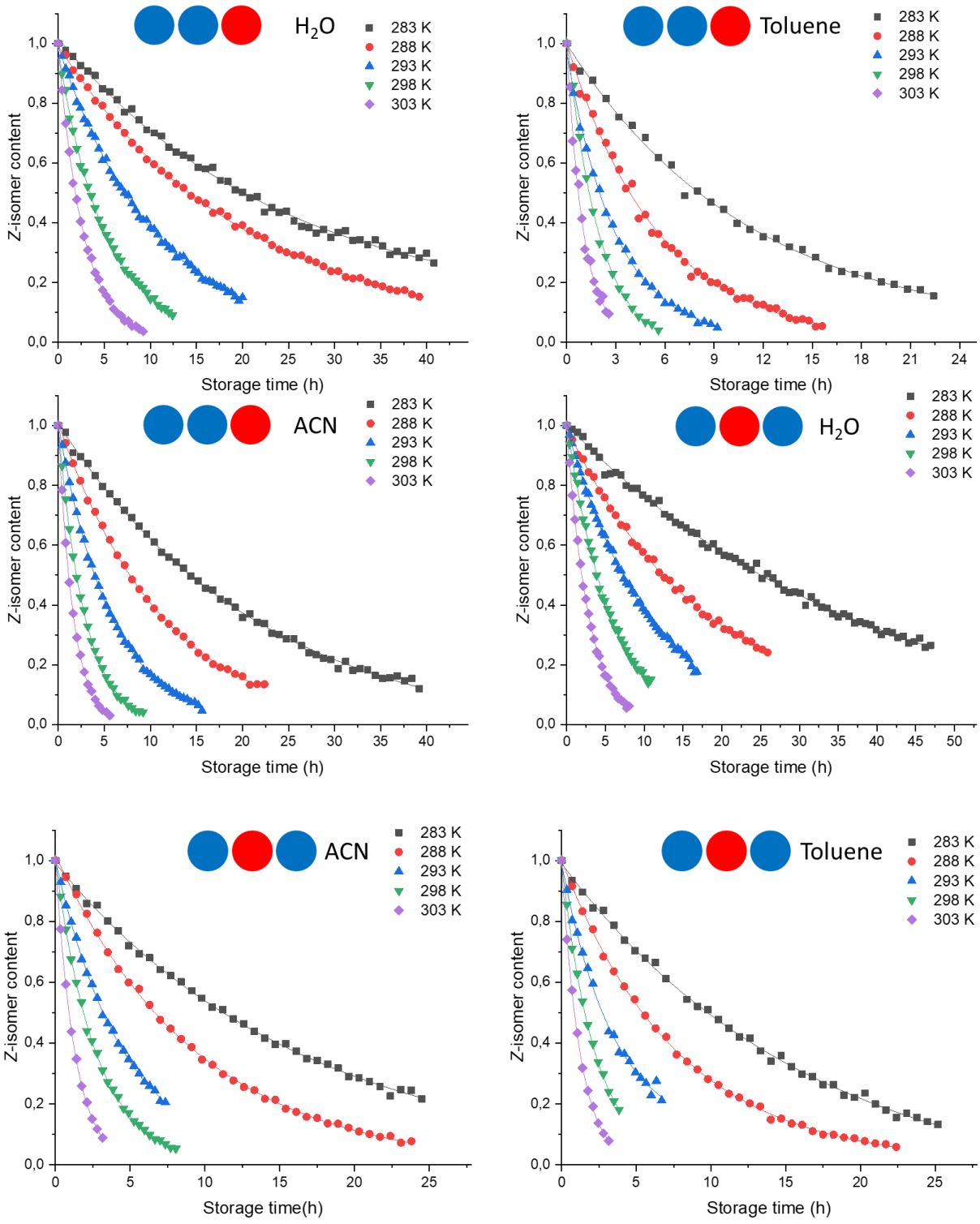

Appendix 18. *Summary of the relevant thermal parameters for Cter-PAT 1 determined in MeOH, H_2O, ACN and toluene: k_{avg} is the average kinetic constant, $t_{1/2}$ is the metastable isomer half-life time, $\Delta H^{\ddagger}$ is the activation enthalpy, $\Delta S^{\ddagger}$ is the activation entropy, $\Delta G^{\ddagger}$ is the Gibbs free energy.*

	T (°C)	k_{avg} (10^{-5} s^{-1})	$t_{1/2}$ (h)	$\Delta H^{\ddagger}$ ($kJ.mol^{-1}$)	$\Delta S^{\ddagger}$ ($J.mol^{-1}.K^{-1}$)	$\Delta G^{\ddagger}$ 20 °C ($kJ.mol^{-1}$)
MeOH	10	1.30 ± 0.01	14.78 ± 0.22	94.90 ± 0.64	- 2.88 ± 2.19	95.75 ± 1.28
	15	2.58 ± 0.05	7.46 ± 0.18			
	20	5.30 ± 0.03	3.63 ± 0.03			
	25	10.39 ± 0.11	1.85 ± 0.03			
	30	20.17 ± 0.01	0.96 ± 0.09			
H_2O	10	0.645 ± 0.001	29.84 ± 0.06	96.35 ± 0.34	- 3.57 ± 1.21	97.39 ± 0.70
	15	1.34 ± 0.01	14.40 ± 0.04			
	20	2.73 ± 0.05	7.05 ± 0.13			
	25	5.36 ± 0.10	3.59 ± 0.07			
	30	9.96 ± 0.23	1.93 ± 0.04			
ACN	10	1.39 ± 0.02	13.81 ± 0.16	89.02 ± 1.65	- 23.36 ± 5.56	95.86 ± 3.28
	15	2.54 ± 0.02	7.58 ± 0.06			
	20	5.25 ± 0.34	3.68 ± 0.24			
	25	9.74 ± 0.05	1.98 ± 0.01			
	30	17.19 ± 0.09	1.12 ± 0.01			
Toluene	10	2.36 ± 0.02	8.17 ± 0.06	84.44 ± 1.06	- 34.78 ± 3.63	94.64 ± 2.12
	15	4.89 ± 0.10	3.94 ± 0.08			
	20	8.78 ± 0.59	2.20 ± 0.15			
	25	15.06 ± 0.38	1.28 ± 0.03			
	30	27.03 ± 0.26	0.71 ± 0.01			

Appendix 19. *Summary of the relevant thermal parameters for Center-PAT 1 determined in MeOH, H_2O, ACN and toluene: k_{avg} is the average kinetic constant, $t_{1/2}$ is the metastable isomer half-life time, $\Delta H^{\ddagger}$ is the activation enthalpy, $\Delta S^{\ddagger}$ is the activation entropy, $\Delta G^{\ddagger}$ is the Gibbs free energy*

	T (°C)	k_{avg} (10^{-5} s^{-1})	$t_{1/2}$ (h)	$\Delta H^{\ddagger}$ ($kJ.mol^{-1}$)	$\Delta S^{\ddagger}$ ($J.mol^{-1}.K^{-1}$)	$\Delta G^{\ddagger}$ 20 °C ($kJ.mol^{-1}$)
MeOH	10	1.57 ± 0.02	12.25 ± 0.18	91.44 ± 0.83	- 13.49 ± 2.88	95 40 ± 1.67
	15	3.13 ± 0.04	6.16 ± 0.13			
	20	6.14 ± 0.10	3.13 ± 0.08			
	25	12.12 ± 0.39	1.59 ± 0.07			
	30	21.07 ± 0.74	0.91 ± 0.04			
H_2O	10	0.766 ± 0.01	25.15 ± 0.34	87.86 ± 2.45	- 32.41 ± 8.39	97.37 ± 4.91
	15	1.52 ± 0.06	12.71 ± 0.55			
	20	2.66 ± 0.02	7.25 ± 0.05			
	25	4.98 ± 0.16	3.87 ± 0.12			
	30	9.81 ± 0.15	1.96 ± 0.03			
ACN	10	1.70 ± 0.05	11.34 ± 0.32	88.58 ± 1.73	- 23.25 ± 5.89	95.39 ± 3.46
	15	2.94 ± 0.14	6.57 ± 0.33			
	20	6.08 ± 0.10	3.17 ± 0.05			
	25	10.79 ± 0.78	1.79 ± 0.12			
	30	21.37 ± 0.43	0.90 ± 0.02			
Toluene	10	1.97 ± 0.16	9.26 ± 0.69	86.35 ± 0.77	- 30.12 ± 2.58	95.18 ± 1.52
	15	3.55 ± 0.07	5.43 ± 0.10			
	20	6.63 ± 0.13	2.90 ± 0.06			
	25	12.53 ± 0.21	1.54 ± 0.03			
	30	22.21 ± 0.27	0.87 ± 0.01			

Appendix 20. *Arrhenius plot based on the rate constants extracted from the kinetics at different temperatures for Cter-PAT 1 and Center-PAT 1 with their corresponding activation energies in H_2O (black), ACN (red) and toluene (blue).*

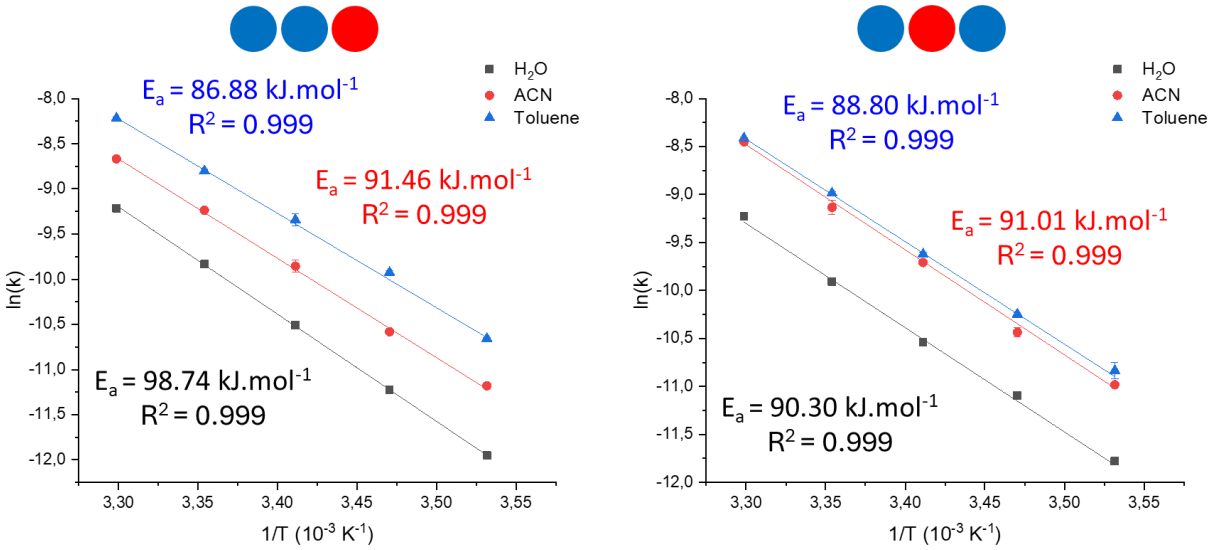

4. TOO FAST TO RELAX, TOO FURIOUS TO STAY: CATALYTIC ACTIVATION

Another important aspect to consider is that the heat release occurs progressively throughout the thermal back-isomerization process, depending on the $t_{1/2}$ of the system. In other words, the stored thermal energy is generally released gradually over time rather than instantaneously upon demand. While this behavior is disadvantageous for applications such as circulating heat exchangers, where rapid heat delivery is required, it could be advantageous for continuous heat output devices, such as window coatings or floor-heating systems. To achieve a controlled and instantaneous energy release, the use of a catalyst capable of promoting the "instantaneous" *Z* → *E* back-isomerization becomes essential. In this work, the catalytic induction of the back-isomerization was explored using an acidic catalyst, with formic acid selected as a model system. Acid-catalyzed processes are known to effectively accelerate the thermal back-isomerization through protonation of the N=N bond, which facilitates the conversion by promoting a rotation mechanism, as previously demonstrated by Rickhoff *et al*.[121,262,274]

As discussed in **section 3.2**, the mechanism of thermal back-isomerization depends strongly on the solvent nature by impacting the activation entropy, in nice agreement with the work of Reimann *et al.*[37] In aprotic solvents (ACN and toluene), the reaction preferentially follows a rotation type II mechanism, characterized by highly negative activation entropy values. In contrast, in protic solvents (H_2O and MeOH), the process likely proceeds via an inversion pathway, consistent with the near-zero activation entropies obtained. Although a rotation type I pathway is also theoretically possible, characterized by intermediate activation entropy values, it is much less frequently observed.[37]

The central question now becomes: how does acid catalysis influence the back-isomerization mechanism in different solvents, and can a solvent-dependent trend be established? To address this, kinetic studies of the thermal back-isomerization of Cter-PAT 1 were performed in various solvents (H_2O, MeOH, ACN and toluene), using increasing equivalents of formic acid to evaluate how catalytic conditions affect the back-isomerization rates and mechanisms.

Figure 75 presents the kinetic profiles of the Cter-PAT 1 relaxation in MeOH with increasing amounts of formic acid, ranging from 1 % to 10 % (v/v in 1.5 ml of MeOH). Contrary to expectations, no significant catalytic acceleration of the thermal back-isomerization is observed, even at the highest acid concentration tested. This result indicates that formic acid is not an effective catalyst for promoting the back-isomerization of Cter-PAT 1 in methanolic solution.

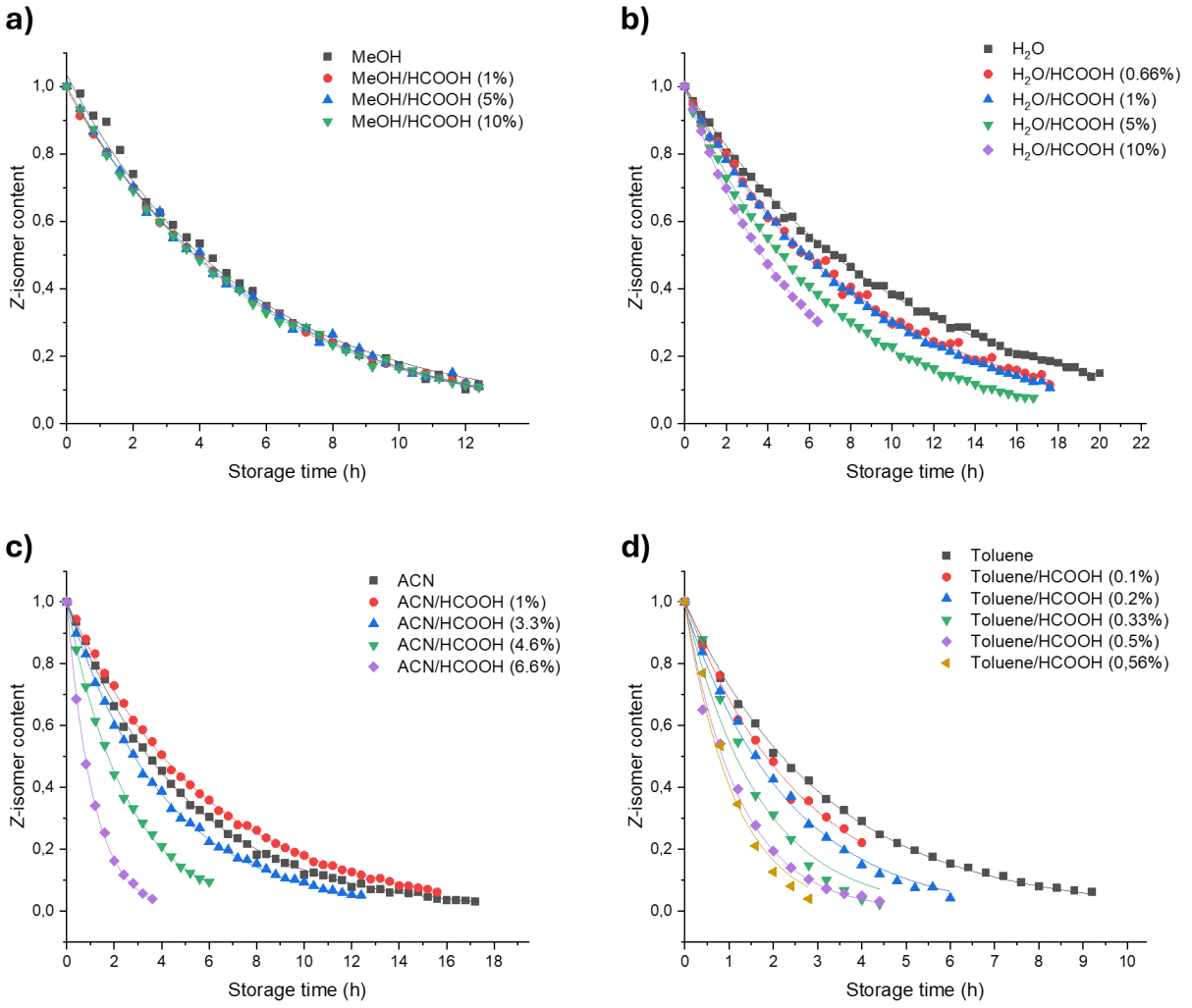

Figure 75. *Monitoring of the thermal Z → E back-isomerization kinetics by LC-MS analyses under various proportions of HCOOH at 20 °C for the Cter-PAT 1. Normalized Z-isomer content plotted against the time showing a first-order exponential decay in MeOH (a), H_2O (b), ACN (c) and toluene (d).*

Regarding the others solvents (H_2O, ACN and toluene), all exhibit a noticeable acceleration of the thermal back-isomerization upon addition of formic acid. In ACN, a slight increase in $t_{1/2}$ is observed at 1 % HCOOH. Note that the catalytic kinetic measurements were performed only

once making the interpretation of weak differences irrelevant. At higher acid concentrations, a clear decrease in $t_{1/2}$ is detected, confirming that formic acid effectively catalyzes the back-isomerization in ACN. In H_2O, a reduction of the $t_{1/2}$ is already evident at low HCOOH content (0.66 %), resulting in highly efficient catalysis. In toluene, the catalytic effect is even more pronounced, with accelerated back-isomerization observed for acid concentration as low as 0.1-0.56 %.

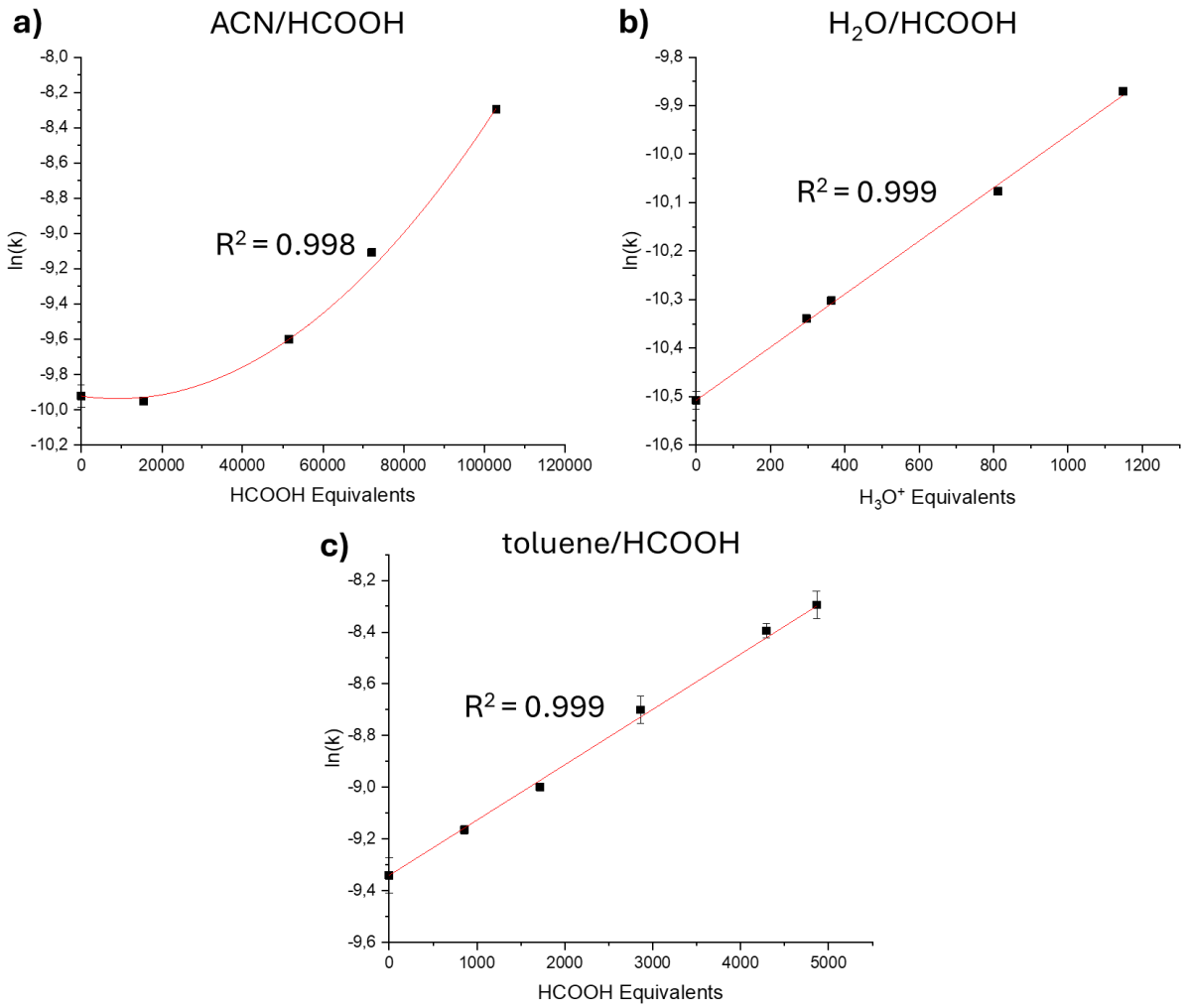

Figure 76. *Kinetic constants plotted as a function of HCOOH equivalents to illustrate the efficiency of the catalytic system in different solvents: ACN (a), H_2O (b) and toluene (c). HCOOH equivalents are here determined based on the HCOOH/peptoid molar ratios.*

Figure 76 displays the evolution of the kinetic constants as a function of the HCOOH equivalents for Cter-PAT 1. It is important to note that, in H_2O, HCOOH behaves as a weak acid. Therefore, the effective acidity of the medium is governed by H_3O^+, which represents the

strongest acid species in H_2O. For this reason, the kinetics constants in H_2O are plotted against the equivalents of H_3O^+ rather than HCOOH. Two distinct trends are observed: (i) linear correlations are determined in toluene and H_2O, and (ii) a nonlinear evolution is measured in ACN. Regarding the linear correlations, a steeper slop indicates a more efficient catalytic effect. In this context, the catalyst appears to be more effective in H_2O than in toluene. Although the relationship in ACN deviates from linearity, higher acid concentrations are required to significantly decrease $t_{1/2}$, suggesting that catalysis is less efficient in ACN compared to the other solvents. It should be underlined that these interpretations remained mostly qualitative.

Figure 77 features the structure of Cter-PAT 1, highlighting the various potential protonation sites relevant to the formic acid-induced catalytic effect. Protonation can, in principle, occur at multiple positions within the molecule. However, the most basic site will be preferentially protonated. Depending on which site is protonated, distinct effects on the thermal back-isomerization process may arise, as detailed in the following discussion.

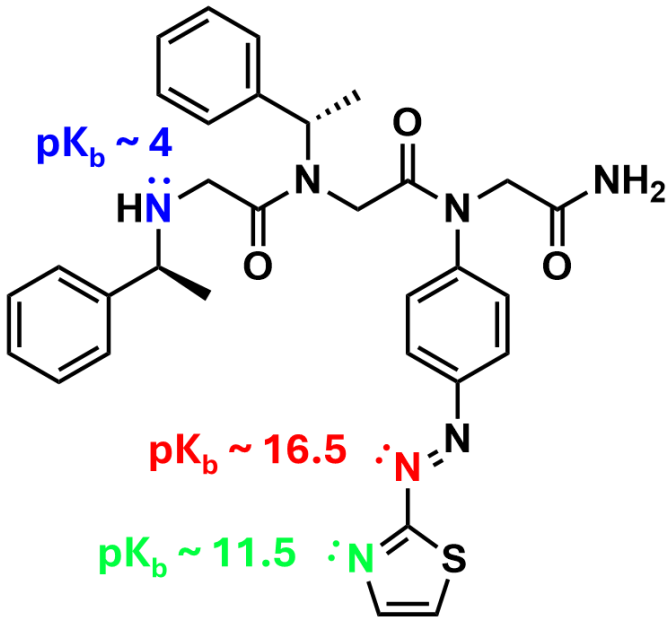

Figure 77. *Structure of Cter-PAT 1 with the corresponding pK_b of the 3 principal protonation sites ranging from the most to the less basic: Nter extremity (pK_b ~ 4)[275], N-thiazole lone pair (pK_b ~ 11.5)[276] and N=N lone pair (pK_b ~ 16.5)[277].*

The most basic site, and therefore the first akin to undergo protonation, is the Nter extremity of the peptoid (see blue nitrogen in **Figure 77**). Protonation at this position may locally affect the conformation of the peptoid backbone. However, since the PAT chromophore is located at the opposite end of the molecule, this protonation is unlikely to significantly influence the back-isomerization behavior of the PAT unit.

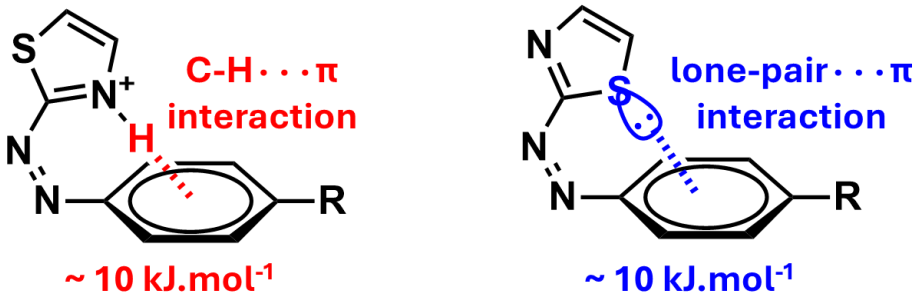

Figure 78. *Schematic representation of the two T-shape conformation accessible to the Z-isomer of protonated PAT derivative: one stabilized by a C-H···π interaction and the other by a lone-pair···π interaction, each with an approximate stabilization energy of 10 kJ.mol-1.*[188,210]

The second most basic site within the peptoid is the nitrogen atom of the thiazole moiety, with estimated pK_b of 11.5 (see red nitrogen in **Figure 77**).[276] Protonation at this site could have more pronounced effect on the back-isomerization process due to its close proximity to the N=N bond. Indeed, protonation of the nitrogen could enable the formation of a potential C-H···π interaction (**Figure 78**). From an energetic standpoint, the C-H···π and the lone-pair···π interaction (already present to stabilize PAT) exhibits comparable stabilization energies.[188,210] Consequently, although both interactions are feasible, the overall kinetics of the back-isomerization process are unlikely to be significantly affected by the emergence of the C-H···π interaction.

The final and least basic protonation site within the peptoid is the N=N bond itself. Despite the being weakest basic site, it is the most chemically relevant for catalytic activation. Protonation of the N=N bond reduces the electron density on the nitrogen atom, thereby weakening the N=N double bond. This bond weakening lowers the activation barrier for the thermal back-isomerization, leading to an acceleration of the Z → E isomerization process. Notably, this

catalytic mechanism is only effective when the isomerization pathway proceeds via a rotation pathway.[262]

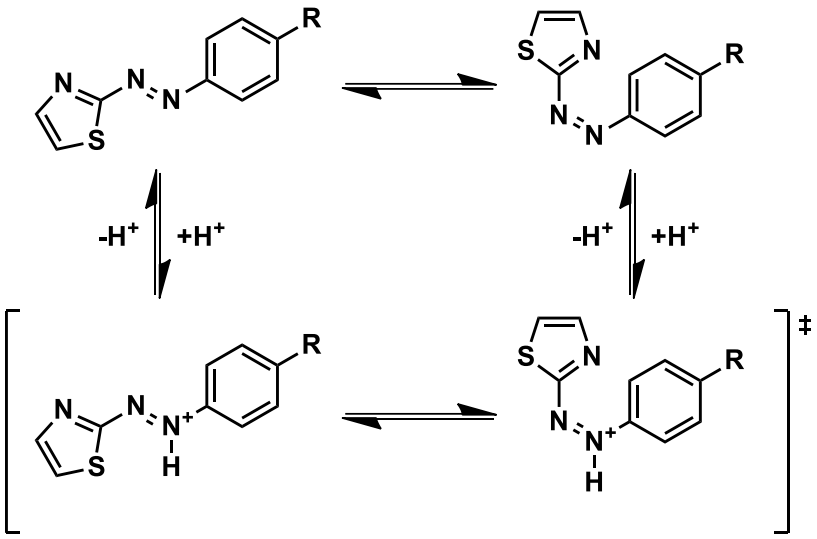

Scheme 13. *Isomerization mechanism of the thermal back-isomerization of protonated PAT derivatives, adapted from*[262]*.*

As illustrated in **Scheme 13,** once the PAT unit is protonated, the back-isomerization occurs rapidly. However, in our system, the process is not instantaneous, suggesting that the rate-limiting step is the protonation of the N=N bond. Since other, more basic sites are present on the peptoid, protonation of the N=N bond is less favorable and occurs infrequently. This could explain why relatively high equivalents of formic acid are required to observe a noticeable acceleration in the back-isomerization rate. Moreover, the protonated PAT species may exhibit a non-negligible lifetime, implying that multiple species could participate in the reaction. This would lead to complex kinetics, potentially with higher orders, as possibly observed for Cter-PAT 1 in ACN. Such stabilization of protonated AB species has already been reported by Rickhoff *et al.* for methoxy-substituted ABs, supporting this mechanistic hypothesis.[262]

Considering all these findings, the observed acceleration of the thermal back-isomerization in ACN and toluene appears consistent with the proposed mechanisms, as previously discussed through the activation entropies. In these two solvents, the dominant back-isomerization pathway is expected to be rotation, making them more responsive to protonation-induced

catalysis. Notably, in toluene, being a completely apolar and aprotic solvent, the medium cannot stabilize the formation of charged species resulting from the dissociation of formic acid into $HCOO^-$ and H^+. Consequently, the catalytic species in toluene likely corresponds to a non-dissociated complex involving the peptoid and HCOOH. This complex would influence the relative energies of the *Z*- and *E*-isomers as well as the transition state, possibly leading to a more intricated back-isomerization mechanism than in polar media.

In MeOH, the absence of any catalytic acceleration is also consistent with expectations, since the reaction is believed to proceed via an inversion mechanism. This interpretation is further support by Robert et al., who reported no change in the rate constant when using NH_4I, a compound known to promote singlet to triplet intersystem crossing and thus to accelerate the rotation type II pathway.[273]

The case of H_2O is more complex, as an acceleration of the back-isomerization is observed despite previous evidence suggesting an inversion pathway. Two hypotheses could explain this behavior. First, the mechanism in H_2O might actually proceed via a rotation type I pathway (occurring exclusively on the singlet state), which would be consistent with the near-zero activation entropy and the observed increase in the isomerization rate. Alternatively, under acidic conditions, protonation may reduce the rotational barrier sufficiently to make it lower than the inversion barrier, causing a mechanistic switch toward the rotational pathway.

In conclusion, it remains challenging to define clear and universal trends for these systems due to the multiple potential protonation sites and the complex interplay between solvent environment and protonation effects. Therefore, these catalytic experiments are not sufficient to unambiguously confirm the back-isomerization mechanism in each solvent, as protonation itself may alter the reaction pathway. To gain a deeper insight into the catalytic influence and its mechanistic implications, kinetics analyses under catalytic conditions at different temperatures should be performed. Determining the activation parameters ($\Delta H^‡$ and $\Delta S^‡$) under these conditions would provide valuable perspectives for future investigations.

Part 5 – Conclusions and perspectives

Conclusions and perspectives

1. A BRIEF HISTORY OF MOST

Molecules that undergo light-induced isomerization to metastable isomers can be used to store solar energy. Such systems are known as MOlecular Solar Thermal systems. Exposing photoswitching molecules to sunlight generates high energy photoisomers whose lifetime is considered as a key criterion for storage purposes. When energy is needed, the photoisomer is converted back to the stable form, releasing the excess energy under the form of heat. AB with their E → Z photoisomerization are among the most widely studied molecular photoswitches although properties such as storage enthalpy, half-life time and optical properties need to be improved.

Two strategies were considered in this thesis to optimize AB-based chromophores for MOST applications; *i.e.* (i) the substitution of one phenyl group by a thiazole moiety to red shift the absorption of the chromophores in the visible region, and (ii) the grafting of AB residue(s) at selected positions along a polymer backbone to enhance the storage enthalpy and the metastable isomer half-life time via cooperating effects. This work thus aimed to explore and improve MOST systems based on PAT derivatives and integrating them within peptoid scaffolds. The research combined organic synthesis, spectroscopic characterization, kinetic analyses and mechanistic interpretation to establish the structure-properties relationships governing photoisomerization efficiency, energy storage and thermal back-isomerization dynamics. Moreover, the study demonstrated the potential of advanced MS techniques, particularly LC-MS, as powerful and underutilized tool in the investigation of MOST systems.

In the first part, five NH_2-PAT derivatives were successfully synthetized through optimized reaction adapted to the substituted patterns of the aminothiazole precursors. These compounds were subsequently acetylated to reproduce the acetyl linkage of peptoids, thereby allowing meaningful comparison with PAT-grafted peptoids. The spectroscopic properties

revealed that the NH_2-PAT derivatives absorb efficiently in the visible region, exhibiting relative high molar extinction coefficients at λ_{max}. However, the thermal stability of their *Z*-isomers was generally low, with $t_{1/2}$ below one second for all compounds except PAT 4. Although PAT 4 *Z*-isomer seemed thermally more stable, it appeared to undergo degradation upon repeated photo- and back-isomerization cycles. Ac-PAT derivatives display blueshifted absorption bands and slightly lower ε values, while maintaining significant absorption in the visible region. Substitution on the thiazole ring improved spectroscopic properties, enhancing both λ_{max} and ε values. Nevertheless, the thermal stability of the *Z*-isomers for all the Ac-PAT derivatives remains too short for efficient solar energy storage, with $t_{1/2}$ values ranging grom 0.6 min to 15 min, except for Ac-PAT 4 ($t_{1/2}$ = 53 min), which similarly degrade upon cycling reaction. Compared to pristine AB, PAT derivatives demonstrated improved absorption in the visible region, confirming their potential as MOST candidate. However, their low thermal stability highlights the need for additional strategies to prolong the *Z*-isomer $t_{1/2}$.

The second part of this thesis focused on the design, synthesis and characterization of PAT-grafted peptoids. By systematically varying the position of the PAT unit along the peptoid backbone (Nter-, Center- and Cter-positions), as well as the chain length (4-unit peptoid), the influence of the molecular architecture on MOST properties was elucidated. All the PAT-peptoids exhibited absorption maxima between 375 and 390 nm, at the edge of the visible region, thereby enabling efficient photoisomerization under natural sunlight, a significant improvement over pristine-AB. Importantly, all PAT-peptoids showed markedly increase thermal stability compared to Ac-PAT analogues, confirming that the peptoid framework provides a stabilizing effect. Among the position isomers, the Cter-PAT derivatives always display longer $t_{1/2}$ values than their Center-PAT analogues, emphasizing the role of the position on the *Z*-isomer stability. Acetylation of the Nter-PAT 1 restores measurable and exploitable $t_{1/2}$ compared to the Nter-PAT 1 homologues which displayed no photoisomerization. Activation entropies determined from kinetic analyses further revealed the mechanistic diversity of the thermal back-isomerization, proceeding either via inversion or rotation pathways depending on

the specific peptoid architecture. The synthesis and analysis of hybrid peptoids bearing both sar and spe side chains further underlined the structural sensitivity of these systems. Even subtle modifications, such as substituting a single spe unit with sar, led to notable variations in Z-isomer stability and mechanistic behavior, with some hybrids exhibiting a mechanistic shift from inversion to rotation. This emphasizes the critical role of sequence and side-chain composition in tuning MOST properties and suggests a promising avenue for molecular-level optimization of thermal energy storage materials.

The third part of this work addressed the solvent effect on the thermal back-isomerization kinetics. We demonstrated that solvent polarity and proticity have a pronounced impact on the kinetics and mechanism of thermal back-isomerization. While Ac-PAT derivatives exhibit faster back-isomerization in H_2O than in MeOH, PAT-peptoids showed the opposite trend, with longer $t_{1/2}$ values in H_2O. For Cter-PAT 1, aprotic solvents favorize a rotation mechanism, whereas protic solvents promote inversion pathway. In contrast, Center-PAT 1 displays consistently negative activation entropies, indicating a predominant rotation pathway across all solvents. These findings confirm that the back-isomerization process is highly system-dependent, governed by both the molecular framework and the solvent environment. The observed linear correlation between kinetic constants of Cter-PAT 1 in MeOH/H_2O mixtures and solvent polarity further suggests a possible continuity between liquid- and gas-phase behavior, though this hypothesis requires further validation with additional derivatives.

The fourth and final part explored the catalytic activation of the thermal back-isomerization process, essential for controlled and instantaneous energy release. The use of formic acid as an acid activator was investigated in various solvents. While acceleration of the back-isomerization was observed in most solvents (toluene, ACN and H_2O), no catalytic enhancement occurred in MeOH. The results suggest that multiple protonation sites within the peptoid can alter the reaction pathway and kinetics, complicating mechanistic interpretation. To elucidate these effects, future studies should determine activation parameters under catalytic conditions at varying temperatures.

Overall, this thesis provides a comprehensive study of PAT-based molecular solar thermal systems, spanning molecular design, structural characterization, solvent and catalytic effects, and mechanistic insights. Beyond the development of new photoactive architectures, this work demonstrates that mass spectrometry is a powerful analytic tool, particularly LC-MS, for the determination of kinetic parameters and the subsequent mechanistic elucidation of MOST systems. The conclusions drawn from this work pave the way toward rationally engineered photoresponsive materials capable of optimizing light absorption, energy storage, and controlled heat release for sustainable solar energy applications.

2. MOST RELOADED

This work demonstrates the high potential of PAT-based peptoids as promising candidates for MOST energy storage systems. Accordingly, several perspectives naturally emerge from this study. A first and relatively straightforward direction would be the investigation of additional PAT derivatives in order to further elucidate the relationship between molecular substitution and the resulting photochemical properties.

Another important perspective concerns the determination of the storage enthalpy, which could not be addressed within the scope of this thesis due to time constraints. This investigation could be carried out using complementary experimental approaches. DSC would provide access to the energy difference between the two isomers in the solid state. However, since this value may be influenced by solvent effect, an alternative method based on calorimetry could be employed by triggering back-isomerization through catalytic activation to induce rapid energy release and measurement. This approach would allow the direct measurement of the energy difference between the *E*- and *Z*-isomers and is currently under investigation in our laboratory.

Most of the experimental analyses performed in this thesis were conducted at low concentrations, typically 5.10^{-5} mol.l^{-1} or below. While appropriate for spectroscopic and MS characterization, such dilute conditions are not fully representative of the operational

requirements of MOST systems, for which higher concentrations are expected to maximize energy storage density. Consequently, an important future direction would be the re-evaluation of key properties, such as thermal stability, at higher concentrations in order to determine whether increased concentrations positively or negatively affect the system performances.

Another direct perspective involves a more detailed investigation of the thermal back-isomerization mechanisms of the different peptoids studied in this work. Establishing correlations between experimental observations and theoretical calculations would provide valuable mechanistic insight. This effort could be extended to the solvent effects observed in this thesis by performing additional LC-MS analyses to extract kinetic parameters in various solvents. Such data would help to validate the proposed mechanistic hypothesis of an inversion pathway in protic solvents and a rotation pathway in aprotic solvents. Complementary theoretical studies would constitute a highly valuable component of this investigation.

Finally, further development and evaluation of prototype devices would be essential to assess the real-world performance and technological viability of these systems. In parallel, continued fundamental investigations could explore new molecular architectures, including the co-incorporation of AB and PAT units within the same peptoid scaffold, an approach that is only slightly explored during the present work.

2.1 AB/PAT HYBRIDS PEPTOIDS

Two hybrid derivatives incorporating both pristine AB and PAT 1 units were synthesized during this work, namely N*spe*N*azb*N*2tz* and N*spe*N*2tz*N*azb*. For this study, only N*spe*N*azb*N*2tz* was investigated by LC-MS analysis, as the $t_{1/2}$ of the pristine AB unit at the central position is known to be less stable and slightly shorter than that of PAT derivatives.[114] Clear differences in peak intensities were observed between the two irradiation conditions, allowing unambiguous assignment of the various signals to their corresponding isomers. As expected, the most polar species, appearing at the left end of the chromatogram, correspond to the peptoid in which both AB and PAT units are in the *Z*-form, while the less polar species at the

right end correspond to the *E*,*E*-form. The two intermediate peaks at 3.3 min and 4.3 min were attributed to the mixed isomers. Specifically, the signal at 3.3 min corresponds to the species bearing *Z*-AB and *E*-PAT, whereas the signal at 4.3 min corresponds to *E*-AB and *Z*-PAT. This assignment is supported by the evolution of peak intensities under different irradiation sources: under visible light, the 4.3 min signal increases markedly while the 3.3 min peak decreases, consistently with the more efficient excitation of the PAT moiety under visible irradiation. Conversely, under UV light, the trend reverses, as the AB chromophore primarily absorbs in the UV region.

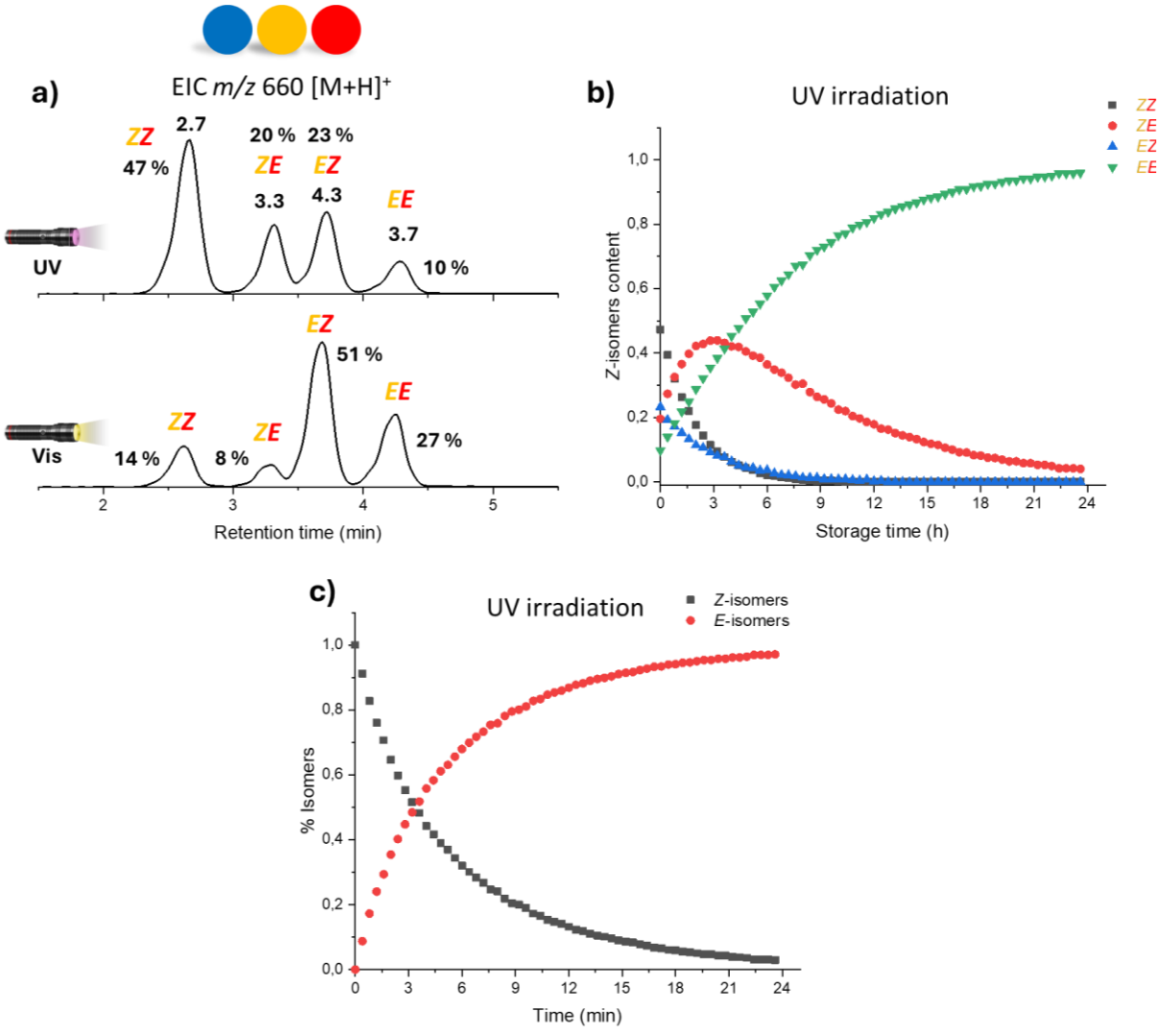

Figure 79. *a) LC-MS analysis (EIC chromatograms of the [M+H]⁺ ions at m/z 660) of NspeNazbN2tz under UV and visible irradiation in the LC-MS autosampler at 25 °C and in MeOH. b) Monitoring of the thermal Z → E back-isomerization kinetics by LC-MS analyses at 25 °C for NspeNazbN2tz. Normalized*

content of each isomer present on the chromatogram plotted against the storage time. c) Normalized Z-isomer content plotted against the time showing a first-order biexponential decay in MeOH.

By plotting the absorbance of each isomer as a function of storage time (**Figure 79b**), no first-order kinetic behavior is observed for the individual isomers. This deviation arises because several isomers interconvert during the thermal relaxation process, leading to biased product distributions, particularly noticeable for the *ZE*-isomer. However, when considering the total Z-isomer content (*i.e.*, the combined population of all Z-containing species) as a function of time, a clear exponential decay is obtained. Fitting this decay with a biexponential function yields two distinct kinetic constants, corresponding respectively to the thermal back-isomerization of the AB and PAT units. Applying the same approach to data collected under visible-light irradiation produces comparable kinetic constants and $t_{1/2}$ values, as expected, since the irradiation wavelength should not affect the intrinsic thermal stability of the *Z*-isomers.

25 °C	k_1 (10^{-5} s^{-1})	$t_{1/2}$ (h)	k_2 (10^{-5} s^{-1})	$t_{1/2}$ (h)
 (UV)	11.91 ± 0.13	1.62 ± 0.05	3.75 ± 0.12	5.13 ± 0.05
 (Vis)	11.59 ± 0.28	1.66 ± 0.04	3.66 ± 0.13	5.26 ± 0.19
	10.38 ± 0.28	1.85 ± 0.02	n.a	n.a
	n.a	n.a	4.28 ± 0.14	4.50 ± 0.14

Table 10. *Kinetic constants and $t_{1/2}$ values obtained at 25 °C in MeOH for different peptoids: NspeNazbN2tz (under UV and visible irradiation), NspeNspeN2tz and NspeNazbNspe.*

Table 10 summarizes the comparison between the peptoid containing both AB and PAT chromophores and the homologous peptoids bearing only AB or only PAT units. No significant difference in $t_{1/2}$ is observed for the PAT derivatives, whereas a difference of approximately 45 minutes is noted for the AB derivatives. This suggests that additional interactions may occur within the hybrid peptoid containing both AB and PAT, potentially influencing the back-isomerization of the AB unit compared to its single-chromophore analogue. These findings highlight the promising potential of such dual-chromophore systems. However, further investigations are required to determine the kinetic parameters and elucidate the mechanism of the thermal back-isomerization in order to fully understand the impact of these interactions.

2.2 GAS/LIQUID PHASE CONCORDANCE

Previously, a linear correlation between the kinetic constants and solvent polarity for Cter-PAT 1 in MeOH/H_2O mixtures as determined suggesting a potential continuity between liquid- and gas-phase behaviors, a hypothesis that requires further experimental confirmation. To validate this observation and assess its generality, an additional derivative was examined using the same methodological approach. The 4-unit peptoid was selected as an ideal candidate for this investigation, given its extended backbone and previously characterized kinetic behavior, which makes it particularly suitable for probing solvent-dependency.

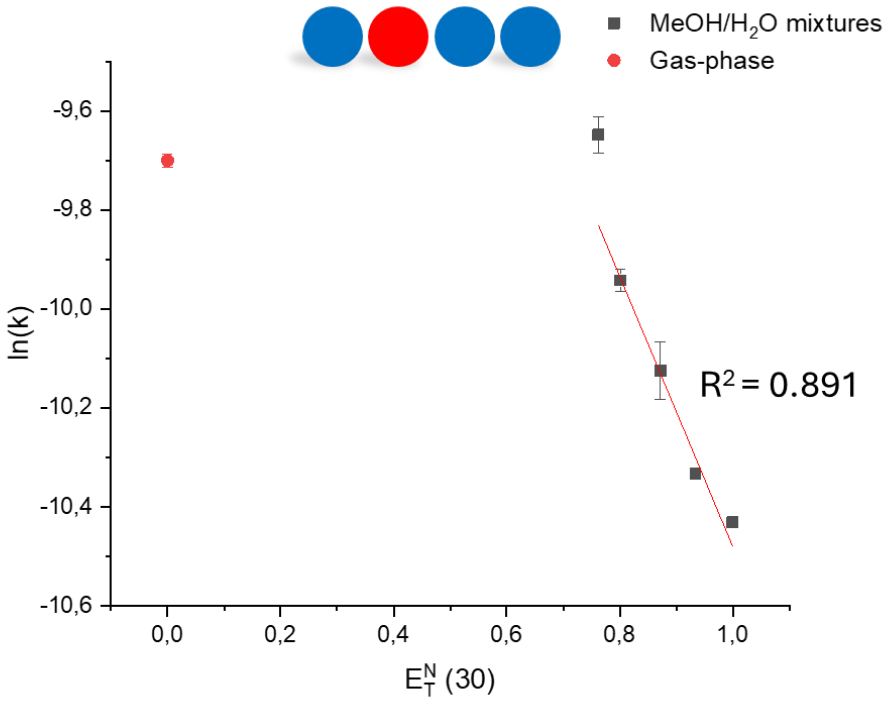

Figure 80. *Dimroth-Reichardt plot showing the kinetic constant of the 4-unit peptoid in H_2O/MeOH mixtures and in gas-phase plotted against E_T^N (30) parameter.*

Figure 80 presents the results obtained for the 4-unit peptoid, which, however, do not corroborate the observations made for Cter-PAT 1, as no clear linear correlation is observed in the MeOH/H_2O series. Interestingly, a partial linear trend appears when considering only H_2O and the mixed solvent systems, while MeOH deviates from this behavior. Notably, the gas-phase kinetic constants exhibit values comparable to those measured in MeOH,

suggesting that distinct back-isomerization mechanisms may be operative in these environments, thereby disrupting linearity between them. A key condition for observing a linear correlation could be that the mechanism of thermal back-isomerization remains identical in both the solvent and gas phase. Only under these conditions can a meaningful and consistent linear relationship between the two environments be expected. At this stage, however, confirmation of this hypothesis remains challenging due to the absence of complete kinetic parameter determination for the 4-unit peptoid. Nevertheless, the recent installation of a new cyclic ion mobility spectrometry instrument in the laboratory, offering significantly enhanced resolution, is expected to allow more effective separation of the E- and Z-isomers of the Center-PAT 1. This advancement will enable a more rigorous evaluation of the proposed correlation between gas- and liquid-phase kinetics in future work. Until such data is available, however, this hypothesis remains speculative.

2.3 CATALYTIC INVESTIGATION THROUGH TRIPLET STATE

Regarding the catalytic activation using formic acid evaluated in this thesis, alternative approaches for promoting the back-isomerization process are also possible. As demonstrated by Riemann *et al.*, the presence of external heavy atoms, such as iodide ions in solution, can enhance spin–orbit coupling, thereby increasing both the activation entropy and the rate of thermal back-isomerization of pristine AB, which proceeds via a type II rotational mechanism.[37] Building on this concept, Robert et al. employed LC–MS analysis to investigate the thermal back-isomerization kinetics of two peptoids, N*spe*N*azb*N*spe* and N*spe*N*spe*N2*tz*, in the presence of ammonium iodide (NH_4I).[273] The results revealed distinct mechanistic pathways for the two systems. For the pristine azobenzene-based peptoid, the back-isomerization rate increased by approximately fourfold in the presence of 100 equivalents of NH_4I at 30 °C, consistent with literature reports for AB in solution with tetra-*n*-butylammonium iodide, confirming a type II rotational mechanism. In contrast, for the PAT-based peptoid, no significant change in thermal back-isomerization kinetics is observed, suggesting that the reaction proceeds predominantly through an inversion pathway in MeOH. These findings highlight the

potential of heavy-atom-induced catalysis as a complementary strategy to probe the isomerization mechanisms of PAT-based systems. Applying this methodology to the derivatives synthesized in this work could provide valuable mechanistic insight and confirm whether a type II rotation pathway operates in these peptoid frameworks.

Part 6 – References

References

(1) Hannah Ritchie; Lucas Rodés-Guirao. Peak global population and other key findings from the 2024 UN World Population Prospects https://ourworldindata.org/un-population-2024-revision (accessed May 25, 2025).

(2) Euan Mearns. Fossil Fuels and Mankind https://euanmearns.com/fossil-fuels-and-mankind/ (accessed May 25, 2025).

(3) planetoscope croissance de la population mondiale https://www.planetoscope.com/natalite/5-croissance-de-la-population-mondiale-naissances---deces-.html (accessed May 13, 2025).

(4) Visual Capitalist. Charted: What Powered the World in 2023? https://www.visualcapitalist.com/visualizing-global-energy-production-in-2023/ (accessed Apr 25, 2025).

(5) International Energy Institute (IEI). Statistical Review of World Energy 2024 https://www.energyinst.org/statistical-review (accessed Apr 25, 2025).

(6) Robert Rapier. Global Energy Trends: Insights From The 2023 Statistical Review Of World Energy https://www.forbes.com/sites/rrapier/2023/08/06/global-energy-trends-insights-from-the-2023-statistical-review-of-world-energy/ (accessed May 13, 2025).

(7) BP. Bp Statistical Review of World Energy 2022. *2022 Stat. Rev. World Energy*.

(8) Ian Hore-Lacy. Energy Use. In *Nuclear Energy in the 21st Century*; 2007; pp 11–19.

(9) Perez, R.; Perez, M. A Fundamental Look At Energy Reserves For The Planet. *Int. Energy Agency SHC Program. Sol. Updat.* **2009**, *50* (April), 4–6.

(10) Yang, T.; Fang, S.; Du, A. M.; Du, Q. Navigating the Nexus: Geopolitical Risk, Fossil Energy Prices, and European Utility Stock Returns - Implications for Environmental Management and Energy Security in a Conflict-Ridden Global Landscape. *J. Environ. Manage.* **2024**, *352* (August 2023), 120086.

(11) Rice, K. C.; Herman, J. S. Acidification of Earth: An Assessment across Mechanisms and Scales. *Appl. Geochemistry* **2012**, *27* (1), 1–14.

(12) gaffney S. Jeffrey; Marley, N. A.; Frederick E. John. FORMATION AND EFFECTS OF SMOG. In *ENVIRONMENTAL AND ECOLOGICAL CHEMISTRY VOLUME II*; EOLSS Publications, Ed.; 2009; pp 25–51.

(13) Lelieveld, J.; Haines, A.; Burnett, R.; Tonne, C.; Klingmüller, K.; Münzel, T.; Pozzer, A. Air Pollution Deaths Attributable to Fossil Fuels: Observational and Modelling Study. *Bmj* **2023**, 1–10.

(14) Siddik, M. A.; Islam, M. T.; A. K. M. Mostafa Zaman et al. CURRENT STATUS AND CORRELATION OF FOSSIL FUELS CONSUMPTION AND GREENHOUSE GAS EMISSIONS. *Int. J. Energy, Environ. Econ.* **2021**, *28* (2).

(15) International Energy Agency. Global Energy Review 2025. *Glob. Energy Rev. 2025* **2025**.

(16) Shiogama, H.; Stone, D.; Emori, S.; Takahashi, K.; Mori, S.; Maeda, A.; Ishizaki, Y.; Allen, M. R. Predicting Future Uncertainty Constraints on Global Warming Projections. *Sci. Rep.* **2016**, *6* (November 2015), 1–7.

(17) Shah Fahad. *Environment, Climate Change and Biodiversity*; Springer Cham, 2020.

(18) United Nations. United Nations Secretariat Climate Action Plan. **2020**, No. September 2019.

(19) Saive, R. Entering the Solar Era : The Next 50 Years of Energy Generation. *Bridg.* **2021**, No. April.

(20) British Petroleum. Bp Energy Outlook 2023 Edition 2023 Explores the Key Trends and Uncertainties. *Stat. Rev. World Energy* **2023**, No. July, 1–53.

(21) S.R.C Roy. IRENA Reports Record-Breaking Annual Growth in Renewable Power Capacity https://solarquarter.com/2025/03/26/irena-reports-record-breaking-annual-growth-in-renewable-power-capacity/ (accessed May 14, 2025).

(22) Lewis, N. S.; Nocera, D. G. Powering the Planet: Chemical Challenges in Solar Energy Utilization. *Proc. Natl. Acad. Sci. U. S. A.* **2006**, *103* (43), 15729–15735.

(23) Dimitriev, O.; Yoshida, T.; Sun, H. Principles of Solar Energy Storage. *Energy Storage* **2020**, *2* (1), 1–13.

(24) Wright, M.; Uddin, A. Organic-Inorganic Hybrid Solar Cells: A Comparative Review. *Sol. Energy Mater. Sol. Cells* **2012**, *107*, 87–111.

(25) Habas, S. E.; Platt, H. A. S.; Van Hest, M. F. A. M.; Ginley, D. S. Low-Cost Inorganic Solar Cells: From Ink to Printed Device. *Chem. Rev.* **2010**, *110* (11), 6571–6594.

(26) Günes, S.; Neugebauer, H.; Sariciftci, N. S. Conjugated Polymer-Based Organic Solar Cells. *Chem. Rev.* **2007**, *107* (4), 1324–1338.

(27) Ma, Y.; Wang, X.; Jia, Y.; Chen, X.; Han, H.; Li, C. Titanium Dioxide-Based Nanomaterials for Photocatalytic Fuel Generations. *Chem. Rev.* **2014**, *114* (19), 9987–10043.

(28) Wang, H.; Liu, J.; Wang, Y.; Zhao, Y.; Zhang, G. A Review of the Performance and Application of Molten Salt-Based Phase Change Materials in Sustainable Thermal Energy Storage at Medium and High Temperatures. *Appl. Energy* **2025**, *389* (March), 125766.

(29) Sharma, A.; Tyagi, V. V.; Chen, C. R.; Buddhi, D. Review on Thermal Energy Storage with Phase Change Materials and Applications. *Renew. Sustain. Energy Rev.* **2009**, *13* (2), 318–345.

(30) Kucharski, T. J.; Tian, Y.; Akbulatov, S.; Boulatov, R. Environmental Science Chemical Solutions for the Closed-Cycle Storage of Solar Energy. **2011**, 4449–4472.

(31) Ürge-Vorsatz, D.; Cabeza, L. F.; Serrano, S.; Barreneche, C.; Petrichenko, K. Heating and Cooling Energy Trends and Drivers in Buildings. *Renew. Sustain. Energy Rev.* **2015**, *41*, 85–98.

(32) Wang, Z.; Erhart, P.; Li, T.; Zhang, Z. Y.; Sampedro, D.; Hu, Z.; Wegner, H. A.; Brummel, O.; Libuda, J.; Nielsen, M. B.; Moth-Poulsen, K. Storing Energy with Molecular Photoisomers. *Joule* **2021**, *5* (12), 3116–3136.

(33) Jago, D.; Gaschk, E. E.; Koutsantonis, G. A. History and Fundamentals of Molecular Photochromism. *Aust. J. Chem.* **2023**, *76* (10), 635–654.

(34) Bolton, J. R.; Hall, D. Photochemical Conversion and Storage of Solar Energy. *Anll. Rev. Energy.* **1979**, No. 204, 353–401.

(35) Börjesson, K.; Lennartson, A.; Moth-Poulsen, K. Efficiency Limit of Molecular Solar

Thermal Energy Collecting Devices. *ACS Sustain. Chem. Eng.* **2013**, *1* (6), 585–590.

(36) Jiang, Y.; Li, Y.; Tong, J.; Mao, L.; Zhou, Y.; Zhang, F. *Molecular Devices for Solar Energy Conversion and Storage*; 2018. https://doi.org/10.1007/978-981-10-5924-7_2.

(37) Reimann, M.; Teichmann, E.; Hecht, S.; Kaupp, M. Solving the Azobenzene Entropy Puzzle: Direct Evidence for Multi-State Reactivity. *J. Phys. Chem. Lett.* **2022**, *13* (46), 10882–10888.

(38) Singer, N. K.; Schlögl, K.; Zobel, J. P.; Mihovilovic, M. D.; González, L. Singlet and Triplet Pathways Determine the Thermal Z/E Isomerization of an Arylazopyrazole-Based Photoswitch. *J. Phys. Chem. Lett.* **2023**, *14* (40), 8956–8961.

(39) Strubbe, D. A.; Grossman, J. C. Thermodynamic Limits to Energy Conversion in Solar Thermal Fuels. *J. Phys. Condens. Matter* **2019**, *31* (3).

(40) Shangguan, Z.; Sun, W.; Zhang, Z. Y.; Fang, D.; Wang, Z.; Wu, S.; Deng, C.; Huang, X.; He, Y.; Wang, R.; Li, T.; Moth-Poulsen, K.; Li, T. A Rechargeable Molecular Solar Thermal System below 0 °C. *Chem. Sci.* **2022**, *13* (23), 6950–6958.

(41) Khodasevych, I. E.; Wang, L.; Mitchell, A.; Rosengarten, G. Micro- and Nanostructured Surfaces for Selective Solar Absorption. *Adv. Opt. Mater.* **2015**, *3* (7), 852–881.

(42) Qiu, Q.; Shi, Y.; Han, G. G. D. Solar Energy Conversion and Storage by Photoswitchable Organic Materials in Solution, Liquid, Solid, and Changing Phases. *J. Mater. Chem. C* **2021**, *9* (35), 11444–11463.

(43) Mony, J.; Climent, C.; Petersen, A. U.; Moth-Poulsen, K.; Feist, J.; Börjesson, K. Photoisomerization Efficiency of a Solar Thermal Fuel in the Strong Coupling Regime. *Adv. Funct. Mater.* **2021**, *31* (21), 1–8.

(44) Feng Wei. Introduction of Solar Thermal Fuel. In *Organic Solar Thermal Fuels*; 2024; pp 1–80.

(45) Philippopoulos, C.; Marangozls, J. Kinetics and Efficiency of Solar Energy Storage in the Photochemical Isomerization of Norbornadiene to Quadricyclane. *Ind. Eng. Chem. Prod. Res. Dev.* **1984**, *23* (3), 458–466.

(46) Dong, L.; Feng, Y.; Wang, L.; Feng, W. Azobenzene-Based Solar Thermal Fuels: Design, Properties, and Applications. *Chem. Soc. Rev.* **2018**, *47* (19), 7339–7368.

(47) Brummel, O.; Besold, D.; Döpper, T.; Wu, Y.; Bochmann, S.; Lazzari, F.; Waidhas, F.; Bauer, U.; Bachmann, P.; Papp, C.; Steinrück, H. P.; Görling, A.; Libuda, J.; Bachmann, J. Energy Storage in Strained Organic Molecules: (Spectro)Electrochemical Characterization of Norbornadiene and Quadricyclane. *ChemSusChem* **2016**, *9* (12), 1424–1432.

(48) Gimenez-Gomez, A.; Rollins, B.; Steele, A.; Hölzel, H.; Baggi, N.; Moth-Poulsen, K.; Funes-Ardoiz, I.; Sampedro, D. Unveiling the Potential of Heterogeneous Catalysts for Molecular Solar Thermal Systems. *Chem. - A Eur. J.* **2024**, *30* (1), 1–4.

(49) Mansø, M.; Petersen, A. U.; Wang, Z.; Erhart, P.; Nielsen, M. B.; Moth-Poulsen, K. Molecular Solar Thermal Energy Storage in Photoswitch Oligomers Increases Energy Densities and Storage Times. *Nat. Commun.* **2018**, *9* (1), 1–7.

(50) Wang, Z. Molecular Solar Thermal Energy Storage System: Evaluation of Different Candidates- Characterization, Modification and Integration of Different Candidates, 2019.

(51) Giménez-Gómez, A.; Magson, L.; Merino-Robledillo, C.; Hernáez-Troya, S.; Sanosa, N.; Sampedro, D.; Funes-Ardoiz, I. State-of-the-Art and Challenges towards a Molecular

Solar Thermal (MOST) Energy Storage Device. *React. Chem. Eng.* **2024**, *9* (7), 1629–1640.

(52) Molecular Solar Thermal Energy Storage Systems https://cordis.europa.eu/project/id/951801 (accessed May 22, 2025).

(53) The MOST systems https://mostsolarproject.eu/project (accessed May 22, 2025).

(54) The MOST Project https://mostsolarproject.eu/a-hybrid-collector-goes-on-a-journey (accessed May 22, 2025).

(55) NBC. Scientists are trying to bottle solar energy and turn it into liquid fuel https://www.nbcnews.com/mach/science/scientists-are-trying-bottle-solar-energy-turn-it-liquid-fuel-ncna930676 (accessed May 22, 2025).

(56) carl wilhelm Scheele. *Chemische Abhandlung von Der Luft Und Dem Feuer*; 1777.

(57) Grootthuss, theodor von. Auszug Aus Vier Abhandlungen Physikalisch-Chemischen Inhalts. *Ann. Phys* **1819**, *61*, 50–74.

(58) Data gathered on www.scopus.com using keywords “Molecular Solar Thermal Systmes” and “Solar Thermal Fuels.”

(59) Robert Luther; Weigert, F. Ueber Die Festen Kohlenwasserstoffe Des Steinkohlentheers. *J. für Prakt. Chemie* **1867**, *101* (1), 333–343.

(60) Weigert, F.; Krüger, O. Über Umkehrbare Photochemische Reaktionen Im Homogenen System. *Zeitschrift für Phys. Chemie* **1905**, *53*, 385–427.

(61) Weigert, F. Zur Thermodynamischen Behandlung Photochemischer Prozesse. *Zeitschrift für Phys. Chemie* **1908**, *63*, 458–466.

(62) Weigert, F. Über Chemische Lichtwirkungen. IV. Weitere Beiträge Zur Thermodynamischen Theorie Photochemischer Prozesse. *Berichte der Dtsch. Chem. Gesellschaft* **1909**, *42*, 850–862.

(63) Weigert, F. *Jahrbuch Für Photographie, Kinematographie Und Reproduktionsverfahren*; 1909.

(64) Lennartson, A.; Roffey, A.; Moth-poulsen, K. Designing Photoswitches for Molecular Solar Thermal Energy Storage. *Tetrahedron Lett.* **2015**, *56* (12), 1457–1465.

(65) Wang, Z.; Hölzel, H.; Moth-Poulsen, K. Status and Challenges for Molecular Solar Thermal Energy Storage System Based Devices. *Chem. Soc. Rev.* **2022**, *51* (17), 7313–7326.

(66) Donati, D.; Guarini, G.; Sarti-fantoni, P. Thermal Behaviour and Monomerization Kinetics of 9-CN Anthracene and 9-CN, 10-Acetoxy Anthracene Dimers in the Solid State. *Mol. Cryst. Liq. Cryst.* **1972**, *17* (3), 187–195.

(67) Li, X.; Cho, S.; Wan, J.; Han, G. G. D. Photoswitches and Photochemical Reactions for Optically Controlled Phase Transition and Energy Storage. *Chem* **2023**, *9* (9), 2378–2389.

(68) Baggi, N.; Muhammad, L. M.; Liasi, Z.; Elholm, J. L.; Baronas, P.; Molins, E.; Mikkelsen, K. V.; Moth-Poulsen, K. Exploring Ortho-Dianthrylbenzenes for Molecular Solar Thermal Energy Storage. *J. Mater. Chem. A* **2024**, *12* (39).

(69) V Caia, G Cum, R Gallo, V Mancini, E. P. Ahigh Enthalpy Value in Thermal Isomerisation of Photosynthesised Cis-9-Styrylacrinides. *Annu. Rev. Biochem.* **1983**, *24* (36), 3903–3904.

(70) Zhang, B.; Feng, Y.; Feng, W. *Azobenzene-Based Solar Thermal Fuels: A Review*; Springer Nature Singapore, 2022; Vol. 14.

(71) Waldeck, D. H. Photoisomerization Dynamics of Stilbenes. *Chem. Rev.* **1991**, *91* (3), 415–436.

(72) Bastianelli, C.; Caia, V.; Cum, G.; Gallo, R.; Mancini, V. Thermal Lsomerization of Photochemically Synthesized (Z)-9-Styrylacridines. *J. Chem. Soc. Perkin Trans. 2* **1991**, *35* (5), 679–683.

(73) Villarón, D.; Wezenberg, S. J. Stiff-Stilbene Photoswitches: From Fundamental Studies to Emergent Applications. *Angew. Chemie - Int. Ed.* **2020**, *59* (32), 13192–13202.

(74) Xu, F.; Sheng, J.; Stindt, C. N.; Crespi, S.; Danowski, W.; Hilbers, M. F.; Buma, W. J.; Feringa, B. L. All-Visible-Light-Driven Stiff-Stilbene Photoswitches. *Chem. Sci.* **2024**, *15* (18), 6763–6769.

(75) Vollhardt, K.; Peter, C.; Weidman, T. W. Efficient Syntheses of New Fulvalene-Bridged Carbonyl Complexes of Cobalt, Ruthenium, Chromium, Molybdenum, and Tungsten. *Am. Chem. Soc.* **1984**, *3*, 82–86.

(76) Weidman, T. W.; Peter, K.; Vollhardt, C. Synthesis, Structure, and Photochemistry of Tetracarbonyl(Fulvalene)Diruthenium. Thermally Reversible Photoisomerization Involving Carbon-Carbon Bond Activation at a Dimetal Center. *Am. Chem. Soc.* **1983**, *105*, 1676–1677.

(77) Börjesson, K.; Lennartson, A.; Moth-Poulsen, K. Fluorinated Fulvalene Ruthenium Compound for Molecular Solar Thermal Applications. *J. Fluor. Chem.* **2014**, *161*, 24–28.

(78) Kanai, Y.; Srinivasan, V.; Meier, S. K.; Vollhardt, K. P. C.; Grossman, J. C. Mechanism of Thermal Reversal of the (Fulvalene)Tetracarbonyldiruthenium Photoisomerization: Toward Molecular Solar-Thermal Energy Storage. *Angew. Chemie - Int. Ed.* **2010**, *49* (47), 8926–8929.

(79) Hou, Z.; Nguyen, S. C.; Lomont, J. P.; Harris, C. B.; Vinokurov, N.; Vollhardt, K. P. C. Switching from Ru to Fe: Picosecond IR Spectroscopic Investigation of the Potential of the (Fulvalene)Tetracarbonyldiiron Frame for Molecular Solar-Thermal Storage. *Phys. Chem. Chem. Phys.* **2013**, *15* (20), 7466–7469.

(80) Zhu, B.; Miljanic, O. S.; Peter, C.; Vollhardt, C.; West, M. C. Synthesis of 2,2',3,3'-Tetramethyl- and 2,2',3,3'-Tetra-Tert-Butylfulvalene: Attractive Platforms for Dinuclear Transition Metal Fragments, as Exempli- Fied by (H5:H5-2,2',3,3'-t-Bu4C10H4)M2(CO)n (M = Fe, Ru, Os, Mo) and First X-Ray Crystal Structures Of. *Synthesis (Stuttg).* **2005**, *19*, 3373–3379.

(81) Jutz, C. Carbonium-Ionen, V. Heptafulven-Derivate. *Chem. Ber.* **1964**, *97*, 2050–2065.

(82) Daub, J.; Knochel, T.; Mannschreck, A. Photosensitive Dihydroazulenes with Chromogenic. *Angew. Chem. Int. Ed. Engl.* **1984**, *94* (12), 960–961.

(83) Saritas, K.; Grossman, J. C. Accurate Isomerization Enthalpy and Investigation of the Errors in Density Functional Theory for Dihydroazulene/Vinylheptafulvene Photochromism Using Diffusion Monte Carlo. *J. Phys. Chem. C* **2017**, *121* (48), 26677–26685.

(84) Görner, H.; Fischer, C.; Gierisch, S.; Daub, J. Dihydroazulene/Vinylheptafulvene Photochromism: Effects of Substituents, Solvent, and Temperature in the Photorearrangement of Dihydroazulenes to Vinylheptafulvenes. *J. Phys. Chem.* **1993**, *97* (16), 4110–4117.

(85) Boggio-Pasqua, M.; Bearpark, M. J.; Hunt, P. A.; Robb, M. A. Dihydroazulene/Vinylheptafulvene Photochromism: A Model for One-Way Photochemistry via a Conical Intersection. *J. Am. Chem. Soc.* **2002**, *124* (7), 1456–1470.

(86) Broman, S. L.; Nielsen, M. B. Dihydroazulene: From Controlling Photochromism to Molecular Electronics Devices. *Phys. Chem. Chem. Phys.* **2014**, *16* (39), 21172–21182.

(87) Görner, H.; Fischer, C.; Daub, J. Photoreaction of Dihydroazulenes into Vinylheptafulvenes: Photochromism of Nitrophenyl-Substituted Derivatives. *J. Photochem. Photobiol. A Chem.* **1995**, *85* (3), 217–224.

(88) Broman, S. L.; Jevric, M.; Nielsen, M. B. Linear Free-Energy Correlations for the Vinylheptafulvene Ring Closure: A Probe for Hammett σ Values. *Chem. - A Eur. J.* **2013**, *19* (29), 9542–9548.

(89) Kilde, M. D.; Hansen, M. H.; Broman, S. L.; Mikkelsen, K. V.; Nielsen, M. B. Expanding the Hammett Correlations for the Vinylheptafulvene Ring-Closure Reaction. *European J. Org. Chem.* **2017**, *2017* (6), 1052–1062.

(90) Jevric, M.; Broman, S. L.; Nielsen, M. B. Palladium-Mediated Strategies for Functionalizing the Dihydroazulene Photoswitch: Paving the Way for Its Exploitation in Molecular Electronics. *J. Org. Chem.* **2013**, *78* (9), 4348–4356.

(91) Torres-Pierna, H.; Roscini, C.; Vlasceanu, A.; Broman, S. L.; Jevric, M.; Cacciarini, M.; Nielsen, M. B. Photochromism of Dihydroazulene-Based Polymeric Thin Films. *Dye. Pigment.* **2017**, *145*, 359–364.

(92) J. hyman. Bicycloheptadienes. *Belgian Pat.* **1951**, 498176.

(93) Dauben, W. G.; Cargill, R. L. Photochemical Transformations-VIII. The Isomerization of Δ2,5-Bicyclo[2.2.1]Heptadiene to Quadricyclo[2.2.1.02,6·03,5]Heptane (Quadricyclene). *Tetrahedron* **1961**, *15* (1–4), 197–201.

(94) Hemauer, F.; Steinrück, H. P.; Papp, C. The Norbornadiene/Quadricyclane Pair as Molecular Solar Thermal Energy Storage System: Surface Science Investigations. *ChemPhysChem* **2024**, *25* (9).

(95) *Molecular Photoswitches*; Pianowski, Z. L., Ed.; 2022.

(96) Luchs, T.; Lorenz, P.; Hirsch, A. Efficient Cyclization of the Norbornadiene-Quadricyclane Interconversion Mediated by a Magnetic [Fe3O4−CoSalphen] Nanoparticle Catalyst. *ChemPhotoChem* **2020**, *4* (1), 52–58.

(97) Bren', V. A.; Dubonosov, A. D.; Minkin, V. I.; Chernoivanov, V. A. Norbornadiene–Quadricyclane — an Effective Molecular System for the Storage of Solar Energy. *Russ. Chem. Rev.* **1991**, *60* (5), 451–469.

(98) Jorner, K.; Dreos, A.; Emanuelsson, R.; El Bakouri, O.; Galván, I. F.; Börjesson, K.; Feixas, F.; Lindh, R.; Zietz, B.; Moth-Poulsen, K.; Ottosson, H. Unraveling Factors Leading to Efficient Norbornadiene-Quadricyclane Molecular Solar-Thermal Energy Storage Systems. *J. Mater. Chem. A* **2017**, *5* (24), 12369–12378.

(99) Miki, S.; yoshinobu asako; Zen-ichi Yoshida. Photochromic Solid Films Prepared by Doping with Donor–Acceptor Norbornadienes. *Chem. Lett.* **1987**, *16* (1), 195–198.

(100) Aslam, A. S.; Muhammad, L. M.; Erbs Hillers-Bendtsen, A.; Mikkelsen, K. V.; Moth-Poulsen, K. Norbornadiene-Quadricyclane Photoswitches with Enhanced Solar Spectrum Match. *Chem. - A Eur. J.* **2024**, *30* (46), 1–9.

(101) Dwight, P.; Kutal, C.; Kutal, S. Transition Metal Photoassisted Valence Isomerization of

Norbornadiene. An Attractive Energy-Storage Reaction. *Inorg. Chem.* **1977**, *16* (3), 719–721.

(102) Kutal, C.; Schwendiman, D. P.; Grutsch, P. USE OF TRANSITION METAL COMPOUNDS TO SENSITIZE A PHOTOCHEMICAL ENERGY STORAGE REACTION. **1977**, *19*, 651–655.

(103) E. Mitscherlich. Ueber Die Zusammensetzung Des Nitrobenzids and Sulfobenzids. *Ann. Pharm.* **1934**, *12*, 311–314.

(104) Benkhaya, S.; Souad, M.; El, A. Classifications , Properties , Recent Synthesis and Applications of Azo Dyes. *Heliyon* **2020**, *6*.

(105) Berradi, M.; Hsissou, R.; Khudhair, M.; Assouag, M.; Cherkaoui, O.; El, A.; El, A. Textile Finishing Dyes and Their Impact on Aquatic Environs. *Heliyon* **2019**, *5*.

(106) Bafana, A.; Devi, S. S.; Chakrabarti, T. Azo Dyes: Past, Present and the Future. *Environ. Rev.* **2011**, *19* (1), 350–370.

(107) geerhard domagk. Ein Beitrag Zur Chemotherapie Der Bakteriellen Infektionen. *Dtsch. MEDIZINISCHE WOCHEÑSCHRIFT* **1935**, *61* (7), 250–253.

(108) Chung, K. T. Azo Dyes and Human Health: A Review. *J. Environ. Sci. Heal. - Part C Environ. Carcinog. Ecotoxicol. Rev.* **2016**, *34* (4), 233–261.

(109) Gerhard Domagk https://www.nobelprize.org/prizes/medicine/1939/domagk/facts/ (accessed Jul 2, 2025).

(110) Hartley, G. S. The Cis-Form of Azobenzene. *Nature* **1937**, 281.

(111) Ľubica Vetrákov; Vít Ladányi; Al Anshori, J.; Dvořák, P.; Wirz, J.; Heger, D. The Absorption Spectrum of Cis-Azobenzene. *Photochem. Photobiol. Sci.* **2017**, *16*, 1749–1756.

(112) Olmsted, J.; Lawrence, J.; Yee, G. G. Photochemical Storage Potential of Azobenzenes. *Sol. Energy* **1983**, *30* (3), 271–274.

(113) Toada, H.; Hayakawa, K.; Kawase, K.; Yamakita, H. Photochemical Conversion and Storage of Solar Energy by Azobenzene. *Chem. Eng. Japan* **1987**, *20*, 265–270.

(114) Tassignon, B.; Wang, Z.; Galanti, A.; De Winter, J.; Samorì, P.; Cornil, J.; Moth-Poulsen, K.; Gerbaux, P. Site Selectivity of Peptoids as Azobenzene Scaffold for Molecular Solar Thermal Energy Storage. *Chem. - A Eur. J.* **2023**, *29* (70).

(115) Gao, M.; Kwaria, D.; Norikane, Y.; Yue, Y. Visible-Light-Switchable Azobenzenes: Molecular Design, Supramolecular Systems, and Applications. *Nat. Sci.* **2023**, *3* (1), 1–45.

(116) Volarić, J.; Buter, J.; Schulte, A. M.; Van Den Berg, K. O.; Santamaría-Aranda, E.; Szymanski, W.; Feringa, B. L. Design and Synthesis of Visible-Light-Responsive Azobenzene Building Blocks for Chemical Biology. *J. Org. Chem.* **2022**, *87* (21), 14319–14333.

(117) Wang, Z.; Losantos, R.; Sampedro, D.; Morikawa, M. A.; Börjesson, K.; Kimizuka, N.; Moth-Poulsen, K. Demonstration of an Azobenzene Derivative Based Solar Thermal Energy Storage System. *J. Mater. Chem. A* **2019**, *7* (25), 15042–15047.

(118) Borisenko, V.; Burns, D. C.; Zhang, Z.; Woolley, G. A.; Ms, O. Optical Switching of Ion - Dipole Interactions in a Gramicidin Channel Analogue. *Am. Chem. Soc.* **2000**, *122* (27), 6364–6370.

(119) Cembran, A.; Bernardi, F.; Garavelli, M.; Gagliardi, L.; Orlandi, G. On the Mechanism of the Cis-Trans Isomerization in the Lowest Electronic States of Azobenzene : S0 , S1 , and T1. *Am. Chem. Soc.* **2004**, *126* (10), 3234–3243.

(120) Halpern, J.; Brady, G. W.; Winkler, C. A. THE CIS_TRANS ISOMERIZATION OF AZOBENZENE IN SOLUTION. *Can. J. Res.* **1950**, *28b* (4), 140–155.

(121) Ciccone, S.; Halpern, J. CATALYSIS OF THE CIS-TRANS ISOMERIZATION OF AZOBENZENE BY ACIDS AND CUPRIC SALTS. *Can. J. Chem.* **1959**, *37* (1903–1910).

(122) Arya, P.; Jelken, J.; Lomadze, N.; Santer, S.; Bekir, M. Kinetics of Photo-Isomerization of Azobenzene Containing Surfactants. *J. Chem. Phys.* **2020**, *152*.

(123) Schatz, D.; Wegner, H. A. Electrochemistry of Azobenzenes and Its Potential for Energy Storage. **2025**.

(124) Adamson, arthur W.; Vogler, A.; Kunkely, H.; Wachter, R. Photocalorimetry. Enthalpies of Photolysis of Trans- Azobenzene, Ferrioxalate and Cobaltioxalate Ions, Chromium Hexacarbonyl, and Dirhenium Decarbonyl. *J. Am. Chem. Soc.* **1978**, *100* (4), 1298–1300.

(125) Mahimwalla, Z.; Yager, K. G.; Barrett, C. J. Azobenzene Photomechanics : Prospects and Potential Applications. *Polym. Bull.* **2012**, *69*, 967–1006.

(126) Bortolus, P.; Monti, S. Cis-Trans Photoisomerization of Azobenzene. Solvent and Triplet Donor Effects. *Am. Chem. Soc.* **1979**, *83* (6), 648–652.

(127) Ladányi, V.; Dvořák, P.; Al Anshori, J.; Vetráková, Ľ.; Wirz, J.; Heger, D. Azobenzene Photoisomerization Quantum Yields in Methanol Redetermined. *Photochem. Photobiol. Sci.* **2017**, *16* (12), 1757–1761.

(128) Bandara, H. M. D.; Burdette, S. C. Photoisomerization in Different Classes of Azobenzene. *Chem. Soc. Rev.* **2012**, *41* (5), 1809–1825.

(129) Siampiringue, N.; Guyot, G.; Monti, S.; Bortolusb, P. The Cis -> Trans PHOTOISOMERIZATION AN EXPERIMENTAL RE-EXAMINATION. *J. Photochem.* **1987**, *37*, 185–188.

(130) Brown, C.; Rastogi, S. K.; Barrett, S. L.; Anderson, H. E.; Twichell, E.; Gralinski, S.; Mcdonald, A.; Brittain, W. J. Chemistry Differential Azobenzene Solubility Increases Equilibrium Cis / Trans Ratio in Water. *"Journal Photochem. Photobiol. A Chem.* **2017**, *336*, 140–145.

(131) Gimenez-gomez, A.; Magson, L.; Peñin, B.; Sanosa, N.; Soil, J.; Sampedro, D. A Photochemical Overview of Molecular Solar Thermal Energy Storage. *Photochem* **2022**, *2*, 694–716.

(132) Crecca, C. R.; Roitberg, A. E. Theoretical Study of the Isomerization Mechanism of Azobenzene and Disubstituted Azobenzene Derivatives. *J. Phys. Chem. A* **2006**, *110*, 8188–8203.

(133) Magee, J. L.; Shand, W.; Eyring, H. Non-Adiabatic Reactions. Rotation about the Double Bond. *J. Am. Chem. Soc.* **1941**, *63* (3), 677–688.

(134) Rau, H. Photoisomerization of Azobenzene. In *Photochemistry and Photophysics, Volume 2*; 1989; pp 120–137.

(135) Bandara, H. M. D.; Friss, T. R.; Enriquez, M. M.; Isley, W.; Incarvito, C.; Frank, H. A.; Gascon, J.; Burdette, S. C. Proof for the Concerted Inversion Mechanism in the Trans f Cis Isomerization of Azobenzene Using Hydrogen Bonding To Induce Isomer Locking. *J. Org. Chem.* **2010**, *75* (14), 4817–4827.

(136) Tan, E. M. M.; Amirjalayer, S.; Smolarek, S.; Vdovin, A.; Zerbetto, F.; Buma, wybren jan. Fast Photodynamics of Azobenzene Probed by Scanning Excited-State Potential Energy Surfaces Using Slow Spectroscopy. *Nat. Commun.* **2015**, *6* (5860).

(137) Asano, T.; Okada, T.; Si, S.; Shigemats, K. Temperature and Pressure Dependences of Thermal Cis-to-Trans Isomerization of Azobenzenes Which Evidence an Inversion Mechanism. *J. Am. Chem. Soc.* **1981**, *103*, 5161–5165.

(138) Jadranka Dokic; Gothe, M.; Wirth, J.; Peters, M. V; Schwarz, J.; Hecht, S.; Saalfrank, P. Quantum Chemical Investigation of Thermal Cis-to-Trans Isomerization of Azobenzene Derivatives : Substituent Effects , Solvent Effects , and Comparison to Experimental Data. *J. Phys. Chem. A* **2009**, *113*, 6763–6773.

(139) *CRC Handbook of Organic Photochemistry and Photobiology, Volumes 1 & 2*, 2nd Editio.; Horspool, W. M., Lenci, F., Eds.; CRC Press, 2003.

(140) Hamm, P.; Ohline, S. M.; Zinth, W. Vibrational Cooling after Ultrafast Photoisomerization of Azobenzene Measured by Femtosecond Infrared Spectroscopy. *J. Chem. Phys.* **1997**, *106* (2), 519–529.

(141) Lednev, I. K.; Ye, T.; Matousek, P.; Towrie, M.; Foggi, P.; Neuwahl, F. V. R. Femtosecond Time-Resolved UV-Visible Absorption Spectroscopy of Trans-Azobenzene : Dependence on Excitation Wavelength. *Chem. Phys. Lett.* **1998**, *290*, 68–74.

(142) Crespi, S.; Simeth, N. A.; König, B. Heteroaryl Azo Dyes as Molecular Photoswitches. *Nat. Rev. Chem.* **2019**, *3* (3), 133–146.

(143) Demchenko, A. P.; Tomin, V. I.; Chou, P. Breaking the Kasha Rule for More Efficient Photochemistry. *Chem. Rev.* **2017**, *117*, 13353–13381.

(144) Nenov, A.; Borrego-varillas, R.; Oriana, A.; Ganzer, L.; Conti, I.; Segarra-martí, J.; Omachi, J.; Dapor, M.; Manzoni, C.; Mukamel, S.; Cerullo, G.; Garavelli, M. UV-Light Induced Vibrational Coherences , the Key to Understand Kasha Rule Violation in Trans -Azobenzene. *J. Phys. Chem. Lett.* **2018**, *9* (7), 1534–1541.

(145) Griffiths, J. Photochemistry of Azobenzene and Its Derivatives. *Chem. Soc. Rev.* **1972**, *1*, 481–493.

(146) Monti, S.; Orlandi, G.; Palmeri, P. FEATURES OF THE PHOTOCHEMCALLY ACTIVE STATE SURFACES OF AZOBENZENE. *Chem. Phys.* **1982**, *71* (1), 87–99.

(147) H. H. JAFFE; YEH SI-JUNG; GADNER, R. W. The Electronic Spectra of Azobenzene and Their Conjugate Acids. *J. Mol. Spectrosc.* **1958**, *2*, 120–136.

(148) Sun, W.; Shangguan, Z.; Zhang, X.; Dang, T.; Zhang, Z. Solar Efficiency of Azo-Photoswitches for Energy Conversion : A Comprehensive Assessment. *ChemSusChem* **2023**, *16* (18).

(149) Li, S.; Wang, H.; Fang, J.; Liu, Q.; Wang, J.; Guo, S. Photo-Isomerization Energy Storage Using Azobenzene and Nanoscale Templates: A Topical Review. *J. Therm. Sci.* **2020**, *29* (2), 280–297.

(150) Beharry, A. A.; Sadovski, O.; Woolley, G. A. Azobenzene Photoswitching without Ultraviolet Light. *J. Am. Chem. Soc.* **2011**, *133*, 19684–19687.

(151) Hermann Rau. Azo Compounds. In *Photochromism molecules and systems*; Heinz Dürr, Henri bouas-laurent, Eds.; 2003; pp 165–192.

(152) Hermann Rau. Photoisomerization of Azobenzenes. In *Photoreactive Organic Thin Films*; Wolfgang, K., Zouheir Sekkat, Eds.; 2002; pp 3–47.

(153) Samanta, S.; Beharry, A. A.; Sadovski, O.; Mccormick, T. M.; Babalhavaeji, A.; Tropepe, V.; Woolley, G. A. Photoswitching Azo Compounds in Vivo with Red Light. *J. Am. Chem. Soc.* **2013**, *135* (26), 9777–9784.

(154) Knie, C.; Utecht, M.; Zhao, F.; Kulla, H.; Kovalenko, S. Ortho -Fluoroazobenzenes : Visible Light Switches with Very Long- Lived Z Isomers. *Chem. - A Eur. J.* **2014**, *20*, 16492–16501.

(155) Lützel, K.; Laqua, H.; Sathian, M. B.; Nißl, B.; Szántó, J. K.; Senser, C.; Savasci, G.; Allmendinger, L.; Kicin, B.; Ruf, V.; Kammerer, D.; Lohmüller, T.; Karaghiosoff, K.; Ali, A. M.; Storch, U.; Mederos, M.; Ochsenfeld, C.; Konrad, D. B. A Platform for the Development of Highly Red-Shifted Azobenzene-Based Optical Tools. *Angew. Chemie - Int. Ed.* **2025**, *e202501779*.

(156) jaume garcia-amoros; Antoni sanchez-ferrer; Massad, walter A.; Nonell, S.; Velasco, D. Kinetic Study of the Fast Thermal Cis -to- Trans Isomerisation of Para - , Ortho - and Polyhydroxyazobenzenes. *Phys. Chem. Chem. Phys.* **2010**, *12*, 13238–13242.

(157) Gajda, K.; Zarychta, B.; Daszkiewicz, Z.; Domanski, andrezj A.; Ejsmont, K. Substituent Effects in Trans-p,p-Disubstituted Azobenzenes: X-Ray Structures at 100 K and DFT-Calculated Structures. *Acta Crystallogr. C* **2014**, *70*, 575–579.

(158) Sun, Z.; Xu, Z.; Ding, M.; Wang, L.; Zhao, L.; Sui, P. Ultrathin Polymersomes with Controllable Light-Responsivity via Adjusting the Electronic Effect from Para - Substituents of Azobenzene. *Angew. Chem. Int. Ed.* **2025**, *202503104*.

(159) García-amorós, J.; Velasco, D. Recent Advances towards Azobenzene-Based Light-Driven Real-Time Information-Transmitting Materials. *beilstein J. Org. Chem.* **2012**, *8*, 1003–1017.

(160) Amrutha, A. S.; Kumar, S.; Kikukawa, T.; Tamaoki, N. Targeted Activation of Molecular Transportation by Visible Light. *ACS Nano* **2017**, *11*, 12292–12301.

(161) Mourot, A.; Kienzler, M. A.; Banghart, M. R.; Fehrentz, T.; Huber, F. M. E.; Stein, M.; Kramer, R. H.; Trauner, D. Tuning Photochromic Ion Channel Blockers. *ACS Chem. Neurosci.* **2011**, *2* (9), 536–543.

(162) Mustroph, H. Studies on UV / Vis Absorption Spectra of Azo Dyes. Electronic Absorption Spectra of 4 , 4 ' - Diaminoazobenzenes. *Dye Pigment.* **1991**, *16*, 223–230.

(163) Ahmed, Z.; Siiskonen, A.; Virkki, M.; Priimagi, A. Controlling Azobenzene Photoswitching through Combined Ortho -Fluorination and -Amination. *Chem. Commun.* **2017**, *53* (93), 12520–12523.

(164) Joshi, N. K.; Fuyuki, M.; Wada, A. Polarity Controlled Reaction Path and Kinetics of Thermal Cis-to- Trans Isomerization of 4 - Aminoazobenzene. *J. Phys. Chem. B* **2014**, *118* (7), 1891–1899.

(165) Aleotti, F.; Nenov, A.; Salvigni, L.; Bonfanti, M.; El-Tahawy, M. M.; Giunchi, A.; Gentile, M.; Spallacci, C.; Ventimiglia, A.; Cirillo, G.; Montali, L.; Scurti, S.; Garavelli, M.; Conti, I. Spectral Tuning and Photoisomerization Efficiency in Push-Pull Azobenzenes: Designing Principles. *J. Phys. Chem. A* **2020**, *124* (46), 9513–9523.

(166) Kienzler, M. A.; Reiner, A.; Trautman, E.; Yoo, S.; Trauner, D.; Isacoff, ehud Y. A Red-Shifted, Fast-Relaxing Azobenzene Photoswitch for Visible Light Control of an Ionotropic Glutamate Receptor. *J. Am. Chem. Soc.* **2013**, *135* (47), 17683–17686.

(167) Wang, L.; Wang, X. Ab Initio Study of Photoisomerization Mechanisms of Push – Pull p , p Disubstituted Azobenzene Derivatives on S1 Excited State. *J. Mol. Struct.* **2007**, *847*, 1–9.

(168) Liu, R.; Li, Y.; Chang, J.; Xiao, Q.; Zhu, H.; Sun, W. Photophysics and Nonlinear Absorption of 4 , 4 -Diethynylazobenzene Derivatives Terminally Capped with Substituted Aromatic Rings. *J. Photochem. Photobiol. A Chem.* **2012**, *239*, 47–54.

(169) Chen, P.; Finikova, O. S.; Ou, Z.; Vinogradov, S. A.; Kadish, K. M. Electrochemistry of Platinum(II) Porphyrins: Effect of Substituents and π -Extension on Redox Potentials and Site of Electron Transfer. *Inorg. Chem.* **2012**, *51*, 6200–6210.

(170) Dudek, M.; Trojnar, J.; Jasik, P.; Samoc, M.; Matczyszyn, K. Linear and Nonlinear Optical Properties of Azobenzene Derivatives Modified with an (Amino)Naphthalene Moiety. *J. Phys. Chem. B* **2022**, *126* (32), 6063–6073.

(171) Liu, H.; Tang, J.; Dong, L.; Wang, H.; Xu, T.; Gao, W.; Zhai, F. Optically Triggered Synchronous Heat Release of Phase-Change Enthalpy and Photo-Thermal Energy in Phase-Change Materials at Low Temperatures. *Adv. Funct. Mater.* **2021**, *31*, 2008496.

(172) Han, G. G. D.; Li, H.; Grossman, J. C. Optically-Controlled Long-Term Storage and Release of Thermal Energy in Phase-Change Materials. *Nat. Commun.* **2017**, *8*, 1446.

(173) Grace G. D. Han; Deru, J. H.; Cho, E. N.; Grossman, J. C. Optically-Regulated Thermal Energy Storage in Diverse Organic Phase-Change Materials. *ChemComm* **2018**, *54*, 10722–10725.

(174) Chen, Y.; Yu, H.; Quan, M.; Zhang, L.; Yang, H.; Lu, Y. Photothermal Effect of Azopyridine Compounds and Their Applications. *RSC Adv.* **2014**, *5*, 4675–4680.

(175) Kerckho, A.; Christensen, K. E.; Langton, M. J. Fast Relaxing Red and Near-IR Switchable Substituents : Periodic Trends , Tuneable Thermal. *Chem. Sci.* **2022**, *13*, 11551–11559.

(176) Hammerich, M.; Schütt, C.; Stähler, C.; Lentes, P.; Röhricht, F.; Höppner, R.; Herges, R. Heterodiazocines: Synthesis and Photochromic Properties, Trans to Cis Switching within the Bio-Optical Window. *J. Am. Chem. Soc.* **2016**, *138* (40), 13111–13114.

(177) Siewertsen, R.; Neumann, H.; Buchheim-Stehn, B.; Herges, R.; Näther, C.; Renth, F.; Temps, F. Highly Efficient Reversible Z-E Photoisomerization of a Bridged Azobenzene with Visible Light through Resolved S1(Nπ*) Absorption Bands. *J. Am. Chem. Soc.* **2009**, *131* (43), 15594–15595.

(178) Sell, H.; Näther, C.; Herges, R. Amino-Substituted Diazocines as Pincer-Type Photochromic Switches. *Beilstein J. Org. Chem.* **2013**, *9*, 1–7.

(179) Wang, D.; Wagner, M.; Butt, H. J.; Wu, S. Supramolecular Hydrogels Constructed by Red-Light-Responsive Host-Guest Interactions for Photo-Controlled Protein Release in Deep Tissue. *Soft Matter* **2015**, *11* (38), 7656–7662.

(180) Hansen, M. J.; Lerch, M. M.; Szymanski, W.; Feringa, B. L. Direct and Versatile Synthesis of Red-Shifted Azobenzenes. *Angew. Chemie - Int. Ed.* **2016**, *55* (43), 13514–13518.

(181) Ruiz-Soriano, A.; Lamelza, L.; Pizzamiglio, E.; Just-Baringo, X. Synthesis of Tetra-Ortho-Methoxylated Azobenzene Photoswitches via Sequential Catalytic C-H Activation and Methoxylation. *J. Org. Chem.* **2024**, *89* (23), 17141–17146.

(182) Kerckhoffs, A.; Christensen, K. E.; Langton, M. J. Fast Relaxing Red and Near-IR Switchable Azobenzenes with Chalcogen and Halogen Substituents: Periodic Trends, Tuneable Thermal Half-Lives and Chalcogen Bonding. *Chem. Sci.* **2022**, *13* (39), 11551–11559.

(183) Cardano, F.; Márquez García, R.; Szymanski, W. Manipulation of Chemistry and Biology

with Visible Light Using Tetra-Ortho-Substituted Azobenzenes and Azonium Ions. *Angew. Chemie - Int. Ed.* **2025**, *64* (24).

(184) Bleger, D.; Schwarz, J.; Brouwer, A. M.; Hecht, S. O-Fluoroazobenzenes as Readily Synthesized Photoswitches Offering.Pdf. *J. Am. Chem. Soc.* **2012**, *134* (51), 20597–20600.

(185) Konrad, D. B.; Savasci, G.; Allmendinger, L.; Trauner, D.; Ochsenfeld, C.; Ali, A. M. Computational Design and Synthesis of a Deeply Red-Shifted and Bistable Azobenzene. *J. Am. Chem. Soc.* **2020**, *142* (14), 6538–6547.

(186) Fischer, E. Temperature Dependence of Photoisomerization Equilibria. Part I. Azobenzene and the Azonaphthalenes. *J. Am. Chem. Soc.* **1960**, *82* (13), 3249–3252.

(187) Weston, C. E.; Richardson, R. D.; Haycock, P. R.; White, A. J. P.; Fuchter, M. J. Arylazopyrazoles: Azoheteroarene Photoswitches Offering Quantitative Isomerization and Long Thermal Half-Lives. *J. Am. Chem. Soc.* **2014**, *136* (34), 11878–11881.

(188) Calbo, J.; Weston, C. E.; White, A. J. P.; Rzepa, H. S.; Contreras-García, J.; Fuchter, M. J. Tuning Azoheteroarene Photoswitch Performance through Heteroaryl Design. *J. Am. Chem. Soc.* **2017**, *139* (3), 1261–1274.

(189) Heindl, A. H.; Wegner, H. A. Rational Design of Azothiophenes—Substitution Effects on the Switching Properties. *Chem. - A Eur. J.* **2020**, *26* (60), 13730–13737.

(190) Dolai, A.; Box, S. M.; Bhunia, S.; Bera, S.; Das, A.; Samanta, S. Photoisomerization of 2-Arylazoimidazoles under Visible Light: Identifying a Predictive Tool to Anticipate and Tune Likely Photoswitching Performance and Cis Half-Life. *J. Org. Chem.* **2023**, *88* (13), 8236–8247.

(191) Lin, R.; Hashim, P. K.; Sahu, S.; Amrutha, A. S.; Cheruthu, N. M.; Thazhathethil, S.; Takahashi, K.; Nakamura, T.; Kikukawa, T.; Tamaoki, N. Phenylazothiazoles as Visible-Light Photoswitches. *J. Am. Chem. Soc.* **2023**, *145* (16), 9072–9080.

(192) Simeth, N. A.; Crespi, S.; Fagnoni, M.; König, B. Tuning the Thermal Isomerization of Phenylazoindole Photoswitches from Days to Nanoseconds. *J. Am. Chem. Soc.* **2018**, *140* (8), 2940–2946.

(193) Steinmüller, S. A. M.; Odaybat, M.; Galli, G.; Prischich, D.; Fuchter, M. J.; Decker, M. Arylazobenzimidazoles: Versatile Visible-Light Photoswitches with Tuneable Z-Isomer Stability. *Chem. Sci.* **2024**, *15* (14), 5360–5367.

(194) Dang, T.; Zhang, Z. Y.; Li, T. Visible-Light-Activated Heteroaryl Azoswitches: Toward a More Colorful Future. *J. Am. Chem. Soc.* **2024**, *146* (29), 19609–19620.

(195) Tsuzuki, S.; Fujii, A. Nature and Physical Origin of CH/p Interaction: Significant Difference from Conventional Hydrogen Bonds. *Phys. Chem. Chem. Phys.* **2008**, *10* (19), 2581–2583.

(196) Kiessling, L. L.; Diehl, R. C. CH- π Interactions in Glycan Recognition. *ACS Chem. Biol.* **2022**, *16* (10), 1884–1893.

(197) Sun, Y.; Sun, J.; Yin, Z. Synthesis, Crystal Structures and Solvent Dependent Cis-Trans Conversion of 2-(4-Hydroxylphenyl)-Azopyrrole. *J. Mol. Struct.* **2023**, *1294* (P2), 136415.

(198) Huang, X.; Shangguan, Z.; Zhang, Z.; Yu, C.; He, Y.; Fang, D.; Sun, W.; Li, Y.; Yuan, C.; Wu, S.; Li, T. Visible-Light-Induced Reversible Photochemical Crystal − Liquid Transitions of Azo-Switches for Smart and Robust Adhesives. *Chem. Mater.* **2022**, *34* (6), 2636–2644.

(199) Gerkman, M. A.; Gibson, R. S. L.; Calbo, J.; Shi, Y.; Fuchter, M. J.; Han, G. G. D. Arylazopyrazoles for Long-Term Thermal Energy Storage and Optically Triggered Heat Release below 0 °c. *J. Am. Chem. Soc.* **2020**, *142* (19), 8688–8695.

(200) Fernández, I.; Frenking, G. Correlation between Hammett Substituent Constants and Directly Calculated π-Conjugation Strength. *J. Org. Chem.* **2006**, *71* (6), 2251–2256.

(201) Zhang, Z. Y.; He, Y.; Zhou, Y.; Yu, C.; Han, L.; Li, T. Pyrazolylazophenyl Ether-Based Photoswitches: Facile Synthesis, (Near-)Quantitative Photoconversion, Long Thermal Half-Life, Easy Functionalization, and Versatile Applications in Light-Responsive Systems. *Chem. - A Eur. J.* **2019**, *25* (58), 13402–13410.

(202) Gupta, D.; Gaur, K.; Kumar, H.; Singh, S. Light-Switchable Metal Complexes : Introducing Photoresponsive Behaviour Through Azoheteroarenes. *ChemPhotoChem* **2023**, *7*, e202300068.

(203) Chung, H. T.; Choe, Y.; Sagirli, F. Z. E.; Kayali, E. S.; Dow, W. Synthesis of New Azo Imidazole Ligand and Fabricating It ' s Chelate Complexes with Some Metallic Ions Synthesis of New Azo Imidazole Ligand and Fabricating It ' s Chelate Complexes with Some Metallic Ions. *J. Phys. Conf. Ser.* **2020**, *1660* (012031).

(204) Otsuki, J.; Suwa, K.; Narutaki, K.; Sinha, C.; Yoshikawa, I. Photochromism of 2- (Phenylazo) Imidazoles. *J. Phys. Chem. A* **2005**, *109* (35), 8064–8069.

(205) Wendler, T.; Schutt, C.; Nather, C.; Herges, R. Photoswitchable Azoheterocycles via Coupling of Lithiated Imidazoles with Benzenediazonium Salts. *J. Org. Chem.* **2012**, *77*, 3284–3287.

(206) Kumar, P.; Srivastava, A.; Sah, C.; Devi, S. Arylazo-3 , 5-Dimethylisoxazoles : Azoheteroarene Photoswitches Exhibiting High Z -Isomer Stability , Solid-State Photochromism , and Reversible Light-Induced Phase Transition. *Chem. - A Eur. J.* **2019**, *25*, 11924–11932.

(207) Anwer, K. E.; El-hddad, S. S. A.; El-sattar, N. E. A. A.; El-morsy, A.; Khedr, F.; Mohamady, S.; Keshek, D. E.; Salama, S. A.; Adl, K. El; Hanafy, N. S. Five and Six Membered Heterocyclic Rings Endowed with Azobenzene as Dual EGFR T790M and VEGFR-2 Inhibitors : Design , Synthesis , in Silico ADMET pro Fi Le ,. *RSC Adv.* **2023**, *13*, 35321–35338.

(208) Hamama, W. S.; Ibrahim, M. E.; Zoorob, H. H. Synthesis and Biological Evaluation of Some Novel Isoxazole Derivatives. *J. Heterocycl. Chem.* **2016**, *54* (1), 11–16.

(209) Egli, M.; Sarkhel, S. Lone Pair-Aromatic Interactions: To Stabilize or Not to Stabilize. *Acc. Chem. Res.* **2007**, *40* (3), 197–205.

(210) Slavov, C.; Yang, C.; Heindl, A. H.; Wegner, H. A.; Dreuw, A.; Wachtveitl, J. Thiophenylazobenzene: An Alternative Photoisomerization Controlled by Lone-Pair···π Interaction. *Angew. Chemie - Int. Ed.* **2020**, *59* (1), 380–387.

(211) Cheruthu, N. M.; Hashim, P. K.; Sahu, S.; Takahashi, K.; Nakamura, T.; Mitomo, H.; Ijiro, K.; Tamaoki, N. Azophotoswitches Containing Thiazole, Isothiazole, Thiadiazole, and Isothiadiazole. *Org. Biomol. Chem.* **2025**, *23* (1), 207–212.

(212) Garcia-Amorós, J.; Maerz, B.; Reig, M.; Cuadrado, A.; Blancafort, L.; Samoylova, E.; Velasco, D. Picosecond Switchable Azo Dyes. *Chem. - A Eur. J.* **2019**, *25* (32), 7726–7732.

(213) Yaman, M.; Renklitepe, C.; Kaplan, G.; Sakalli, Y.; Seferoğlu, N.; Şahin, E.; Seferoğlu, Z. D- π-A Azo Dyes Bearing Thiazole-Diphenylamine Units: Synthesis, Photophysical and Molecular Structure Properties, and Use for Dyeing of Polyester Fabrics. *Dye.*

Pigment. **2024**, *222*.

(214) Kolpak, A. M.; Grossman, J. C. Hybrid Chromophore/Template Nanostructures: A Customizable Platform Material for Solar Energy Storage and Conversion. *J. Chem. Phys.* **2013**, *138* (3).

(215) Kolpak, A. M.; Grossman, J. C. Azobenzene-Functionalized Carbon Nanotubes As High-Energy Density Solar Thermal Fuels. *Nano Lett.* **2011**, *11* (8), 3156–3162.

(216) Kucharski, T. J.; Ferralis, N.; Kolpak, A. M.; Zheng, J. O.; Nocera, D. G.; Grossman, J. C. Templated Assembly of Photoswitches Significantly Increases the Energy-Storage Capacity of Solar Thermal Fuels. *Nat. Chem.* **2014**, *6* (5), 441–447.

(217) Huang, J.; Jiang, Y.; Wang, J.; Li, C.; Luo, W. A High Energy, Reusable and Daily-Utilization Molecular Solar Thermal Conversion and Storage Material Based on Azobenzene/Multi-Walled Carbon Nanotubes Hybrid. *Thermochim. Acta* **2017**, *657* (September), 163–169.

(218) Pang, W.; Xue, J.; Pang, H. A High Energy Density Azobenzene/Graphene Oxide Hybrid with Weak Nonbonding Interactions for Solar Thermal Storage. *Sci. Rep.* **2019**, *9* (1), 1–12.

(219) Feng, Y.; Liu, H.; Luo, W.; Liu, E.; Zhao, N.; Yoshino, K.; Feng, W. Covalent Functionalization of Graphene by Azobenzene with Molecular Hydrogen Bonds for Long-Term Solar Thermal Storage. *Sci. Rep.* **2013**, *3*, 1–8.

(220) Luo, W.; Feng, Y.; Cao, C.; Li, M.; Liu, E.; Li, S.; Qin, C.; Hu, W.; Feng, W. A High Energy Density Azobenzene/Graphene Hybrid: A Nano-Templated Platform for Solar Thermal Storage. *J. Mater. Chem. A* **2015**, *3* (22), 11787–11795.

(221) Zhao, X.; Feng, Y.; Qin, C.; Yang, W.; Si, Q.; Feng, W. Controlling Heat Release from a Close-Packed Bisazobenzene–Reduced-Graphene-Oxide Assembly Film for High-Energy Solid-State Photothermal Fuels. *ChemSusChem* **2017**, *10* (7), 1395–1404.

(222) Luo, W.; Feng, Y.; Qin, C.; Li, M.; Li, S.; Cao, C.; Long, P.; Liu, E.; Hu, W.; Yoshino, K.; Feng, W. High-Energy, Stable and Recycled Molecular Solar Thermal Storage Materials Using AZO/Graphene Hybrids by Optimizing Hydrogen Bonds. *Nanoscale* **2015**, *7* (39), 16214–16221.

(223) Eugene, N. C. Understanding and Engineering Azobenzene for Thermal Energy Storage, Massachusetts Institute Of Technology, 2017.

(224) Zhitomirsky, D.; Cho, E.; Grossman, J. C. Solid-State Solar Thermal Fuels for Heat Release Applications. *Adv. Energy Mater.* **2016**, *6*, 1502006.

(225) Xu, X.; Feng, J.; Li, W. Y.; Wang, G.; Feng, W.; Yu, H. Azobenzene-Containing Polymer for Solar Thermal Energy Storage and Release: Advances, Challenges, and Opportunities. *Prog. Polym. Sci.* **2024**, *149*.

(226) Jeong, S. P.; Renna, L. A.; Boyle, C. J.; Kwak, H. S.; Harder, E.; Damm, W.; Venkataraman, D. High Energy Density in Azobenzene-Based Materials for Photo-Thermal Batteries via Controlled Polymer Architecture and Polymer-Solvent Interactions. *Sci. Rep.* **2017**, *7* (1), 1–12.

(227) Zhitomirsky, D.; Grossman, J. C. Conformal Electroplating of Azobenzene-Based Solar Thermal Fuels onto Large-Area and Fiber Geometries. *ACS Appl. Mater. Interfaces* **2016**, *8* (39), 26319–26325.

(228) Shin, S. B. Y.; Kirshenbaum, K. Conformational Rearrangements by Water-Soluble Peptoid Foldamers. *Org. Lett.* **2007**, *9* (24), 5003–5006.

(229) Hill, D. J.; Mio, M. J.; Prince, R. B.; Hughes, T. S.; Moore, J. S. A Field Guide to Foldamers. *Chem. Rev.* **2001**, *101* (12), 3893–4011.

(230) Xuan, S.; Zuckermann, R. N. Engineering the Atomic Structure of Sequence-Defined Peptoid Polymers and Their Assemblies. *Polymer (Guildf).* **2020**, *202*, 122691.

(231) Sui, Q.; Borchardt, D.; Rabenstein, D. L. Kinetics and Equilibria of Cis/Trans Isomerization of Backbone Amide Bonds in Peptoids. *J. Am. Chem. Soc.* **2007**, *129* (39), 12042–12048.

(232) Luxenhofer, R.; Fetsch, C.; Grossmann, A. Polypeptoids: A Perfect Match for Molecular Definition and Macromolecular Engineering? *J. Polym. Sci. Part A Polym. Chem.* **2013**, *51* (13), 2731–2752.

(233) Leuchs, H.; Manasse, W. Über Die Isomerie Der Carbäthoxyl-glycyl Glycinester. *Berichte der Dtsch. Chem. Gesellschaft* **1907**, *40* (3), 3235–3249.

(234) Leiske, M. N.; Kempe, K. A Guideline for the Synthesis of Amino-Acid-Functionalized Monomers and Their Polymerizations. *Macromol. Rapid Commun.* **2022**, *43* (2), 1–24.

(235) Bauer, T. A.; Simić, L.; Van Guyse, J. F. R.; Duro-Castaño, A.; Nebot, V. J.; Barz, M. Polypept(o)Ides – Origins, Synthesis, Applications and Future Directions. *Prog. Polym. Sci.* **2024**, *158*.

(236) Saha, U. K.; Roy, R. First Synthesis of N-Linked-Glycopeptoid as New Glycopeptidomimetics. *Tetrahedron Lett.* **1995**, *36* (21), 3635–3638.

(237) Seo, J.; Lee, B. C.; Zuckermann, R. N. Peptoids: Synthesis, Characterization, and Nanostructures. In *Comprehensive Biomaterials II*; 2011; Vol. 2, pp 41–66.

(238) Zuckermann, R.; Kerr, J.; Kent, S.; Moos, W. Efficient Method for the Preparation of Peptoids [Oligo(N-Substituted Glycines)]. *J. Am. Chem. Soc.* **1992**, *114* (6), 10646–10647.

(239) Knight, A. S.; Zhou, E. Y.; Francis, M. B.; Zuckermann, R. N. Sequence Programmable Peptoid Polymers for Diverse Materials Applications. *Adv. Mater.* **2015**, *27*, 5665–5691.

(240) Roy, O.; Caumes, C.; Esvan, Y.; Didierjean, C.; Faure, S.; Taillefumier, C. The Tert-Butyl Side Chain: A Powerful Means to Lock Peptoid Amide Bonds in the Cis Conformation. *Org. Lett.* **2013**, *15* (9), 2246–2249.

(241) Shah, N. H.; Kirshenbaum, K. Photoresponsive Peptoid Oligomers Bearing Azobenzene Side Chains. *Org. Biomol. Chem.* **2008**, *6*, 2516–2521.

(242) Laursen, J. S.; Engel-Andreasen, J.; Fristrup, P.; Harris, P.; Olsen, C. A. Cis -Trans Amide Bond Rotamers in β-Peptoids and Peptoids: Evaluation of Stereoelectronic Effects in Backbone and Side Chains. *J. Am. Chem. Soc.* **2013**, *135* (7), 2835–2844.

(243) Benjamin C. Gorske; Stringer, J. R.; Brent L. Bastian; Fowler, S. A.; Blackwell, H. E. New Strategies for the Design of Folded Peptoids Revealed by a Survey of Noncovalent Interactions in Model Systems. *J. Am. Chem. Soc.* **2009**, *131* (45), 16555–16567.

(244) Wu, C. W.; Kirshenbaum, K.; Sanborn, T. J.; Patch, J. A.; Huang, K.; Dill, K. A.; Zuckermann, R. N.; Barron, A. E. Structural and Spectroscopic Studies of Peptoid Oligomers with R-Chiral Aliphatic Side Chains. *J. Am. Chem. Soc.* **2003**, *125* (44), 13525–13530.

(245) Laursen, J. S.; Engel-Andreasen, J.; Olsen, C. A. β-Peptoid Foldamers at Last. *Acc. Chem. Res.* **2015**, *48* (10), 2696–2704.

(246) Hoyas, S.; Halin, E.; Lemaur, V.; De Winter, J.; Gerbaux, P.; Cornil, J. Helicity of Peptoid

Ions in the Gas Phase. *Biomacromolecules* **2020**, *21* (2), 903–909.

(247) Weber, P.; Hoyas, S.; Halin, É.; Coulembier, O.; De Winter, J.; Cornil, J.; Gerbaux, P. On the Conformation of Anionic Peptoids in the Gas Phase. *Biomacromolecules* **2022**, *23* (3), 1138–1147.

(248) Hoyas, S.; Lemaur, V.; Duez, Q.; Saintmont, F.; Halin, E.; De Winter, J.; Gerbaux, P.; Cornil, J. PEPDROID: Development of a Generic DREIDING-Based Force Field for the Assessment of Peptoid Secondary Structures. *Adv. Theory Simulations* **2018**, *1* (12), 1–14.

(249) Sanborn, T. J.; Wu, C. W.; Zuckermann, R. N.; Barron, A. E. Extreme Stability of Helices Formed by Water-Soluble Poly-N-Substituted Glycines (Polypeptoids) with α-Chiral Side Chains. *Biopolymers* **2002**, *63* (1), 12–20.

(250) Wu, C. W.; Sanborn, T. J.; Zuckermann, R. N.; Barron, A. E. Peptoid Oligomers with α-Chiral, Aromatic Side Chains: Effects of Chain Length on Secondary Structure. *J. Am. Chem. Soc.* **2001**, *123* (13), 2958–2963.

(251) Swanson, H. W. A.; Lau, K. H. A.; Tuttle, T. Minimal Peptoid Dynamics Inform Self-Assembly Propensity. *J. Phys. Chem. B* **2023**, *127* (49), 10601–10614.

(252) Grewal, S.; Roy, S.; Kumar, H.; Saraswat, M.; Bari, N. K.; Sinha, S.; Venkataramani, S. Temporal Control in Tritylation Reactions through Light-Driven Variation in Chloride Ion Binding Catalysis-a Proof of Concept. *Catal. Sci. Technol.* **2020**, *10* (20), 7027–7033.

(253) Tran, H.; Gael, S. L.; Connolly, M. D.; Zuckermann, R. N. Solid-Phase Submonomer Synthesis of Peptoid Polymers and Their Self-Assembly into Highly-Ordered Nanosheets. *J. Vis. Exp.* **2011**, No. 57, e3373.

(254) Hammamatsu LC8 9588-03 https://www.hamamatsu.com/eu/en/product/light-and-radiation-sources/lamp-module_unit/spot-light-source/L9588.html.

(255) Hammamatsu LC8 9588-02A https://www.hamamatsu.com/eu/en/product/light-and-radiation-sources/lamp-module_unit/spot-light-source/L9588.html.

(256) OptoSigma UV transmitting filter https://www.optosigma.com/eu_en/optics/filters/colored-glass-filters/uv-transmitting-filter-50mm-wavelength-350nm.html.

(257) Solar irradiance https://sunclimate.gsfc.nasa.gov/article/solar-irradiance.

(258) Pandian, R.; Burda, H.; Alfurayj, I.; Reichardt, C.; Burda, C. 60 Years of Betaine 30 – From Solvatochromic Discovery to Future Frontiers. *J. Phys. Chem. B* **2024**, *128* (29), 6990–7001.

(259) Jaunet-lahary, T.; Laurent, D.; Laurence, C. Exploring the Solvatochromism of Betaine 30 with Ab Initio Tools : From Accurate Gas-Phase Calculations to Implicit and Explicit Solvation Models. *Chem. - A Eur. J.* **2017**, *23* (17), 4108–4119.

(260) Dimroth and Reichardt ET(30) https://www.stenutz.eu/chem/dimroth.php?sort=3.

(261) Shakerizadeh-shirazi, F. Analytical Methods Determination of the Empirical Solvent Polarity. *Anal. Methods* **2013**, *5*, 891–896..

(262) Rickhoff, J.; Arndt, N. B.; Marcus, B.; Doltsinis, N. L.; Ravoo, B. J. Reversible, Red-Shifted Photoisomerization in Protonated Azobenzenes. *J. Org. Chem.* **2022**, *87* (16), 10605–10612.

(263) Hashim, P. K.; Sahu, S.; Takahashi, K.; Thazhathethil, S. Geometry-Induced Oligomerization of Fluorine-Substituted Phenylazothiazole Photoswitches. *Chem. - A*

Eur. J. **2024**, *30*, e202400047.

(264) Halin, E.; Hoyas, S.; Lemaur, V.; Winter, J. De; Laurent, S.; Connolly, M. D.; Zuckermann, R. N.; Cornil, J.; Gerbaux, P. Backbone Cleavages of Protonated Peptoids upon Collision-Induced Dissociation: Competitive and Consecutive B-Y and A1-Yx Reactions. *J. Am. Soc. Mass Spectrom.* **2019**, *30* (12), 2726–2740.

(265) Steen, H.; Mann, M. The ABC's (and XYZ's) of Peptide Sequencing. *Nat. Rev. Mol. Cell Biol.* **2004**, *5* (9), 699–711.

(266) Morishetti, K. K.; Russell, S. C.; Zhao, X.; Robinson, D. B.; Ren, J. Tandem Mass Spectrometry Studies of Protonated and Alkali Metalated Peptoids: Enhanced Sequence Coverage by Metal Cation Addition. *Int. J. Mass Spectrom.* **2011**, *308* (1), 98–108.

(267) Boyd, R.; Somogyi, Á. The Mobile Proton Hypothesis in Fragmentation of Protonated Peptides: A Perspective. *J. Am. Soc. Mass Spectrom.* **2010**, *21* (8), 1275–1278.

(268) Dongré, A. R.; Jones, J. L.; Somogyi, Á.; Wysocki, V. H. Influence of Peptide Composition, Gas-Phase Basicity, and Chemical Modification on Fragmentation Efficiency: Evidence for the Mobile Proton Model. *J. Am. Chem. Soc.* **1996**, *118* (35), 8365–8374.

(269) Paizs, B.; Suhal, S. Fragmentation Pathways of Protonated Peptides. *Mass Spectrom. Rev.* **2005**, *24* (4), 508–548.

(270) Halin, E.; Hoyas, S.; Lemaur, V.; De Winter, J.; Laurent, S.; Cornil, J.; Roithová, J.; Gerbaux, P. Side-Chain Loss Reactions of Collisionally Activated Protonated Peptoids: A Mechanistic Insight. *Int. J. Mass Spectrom.* **2019**, *435*, 217–226.

(271) Reichardt, C.; Erwin Harbusch-Gornert. Erweiterung, Korrektur Und Neudefinition Der E,-Losungs- Mittelpolaritatsskala Mit Hilfe Eines Lipophilen Penta-Tert-Butyl-Substituierten Pyridinium-N-Phenolat-Betainfarbstoffe. *Liebigs Ann. Chem* **1983**, *5*, 721–743.

(272) Spange, S. Polarity of Organic Solvent/Water Mixtures Measured with Reichardt's B30 and Related Solvatochromic Probes—A Critical Review. *Liquids* **2024**, *4* (1), 191–230.

(273) Robert, T.; Henrard, G.; Tassignon, B.; Serez, A.; De Winter, J.; Dugourd, P.; Cornil, J.; Chirot, F.; Gerbaux, P. Back Isomerization Kinetics of Molecular Photoswitches: Complementary Insights from Liquid Chromatography and Ion Mobility Measurements. *Anal. Chem.* **2025**, *97* (17), 9405–9413.

(274) Wettermark, G.; Langmuir, M. E.; Anderson, D. G. Catalysis of the Cis - Trans Isomerization of 2-Hydroxy-5-Methylazobenze. *J. Am. Chem. Soc.* **1965**, *87* (3), 476–481.

(275) Gupta, M.; Da Silva, E. F.; Svendsen, H. F. Explicit Solvation Shell Model and Continuum Solvation Models for Solvation Energy and PKa Determination of Amino Acids. *J. Chem. Theory Comput.* **2013**, *9* (11), 5021–5037.

(276) Metzger, J. V.; Vincent, E. J.; Chouteau, J.; Mille, G. Properties and Reactions of Thiazole. *Chem. Heterocycl. Compd.* **1979**, *34*, 5–164.

(277) Hoefnagel, M. A.; van Veen, A.; Wepster, B. M. Protonation of Azo-compounds. Part II: The Structure of the Conjugate Acid of Trans-azobenzene. *Recl. des Trav. Chim. des Pays-Bas* **1969**, *88* (5), 562–572.

Part 7 - Accomplishments

Accomplishments

1. PUBLICATIONS

- T. Robert, G. Henrard, B. Tassignon, A. Serez, J. De Winter, P. Dugourd, J. Cornil, F. Chirot, and P. Gerbaux. Back Isomerization Kinetics of Molecular Photoswitches: Complementary Insights from Liquid Chromatography and Ion Mobility Measurements, *Analytical Chemistry* **2025** *97* (17), 9405-9413.

2. ORAL COMMUNICATIONS

- *Mass Spectrometry and Photochemical Study of Photoisomerization and Thermal Back-isomerization of Substituted Azobenzenes anchored on Peptoids for the Chemical Storage of Solar Energy*
  Flash presentation at the one-day meeting of Young Chemists
  Liège (Belgium), 01/04/2022

- *Mass Spectrometry and Photochemical Study of Photoisomerization and Thermal Back-isomerization of Substituted Azobenzenes anchored on Peptoids for the Chemical Storage of Solar Energy*
  Flash presentation at the annual meeting of the Belgian Society for Mass Spectrometry
  UCB Pharma (Belgium), 07/10/2022

- *Original Heteroaryl Azobenzene derivatives As Solar Thermal Fuel Candidates : a Mass Spectrometry and UV-vis Spectrophotometry Investigation*
  One-day meeting of Young Chemists
  Mons (Belgium), 22/05/2023

- *Original Heteroaryl Azobenzenes Anchored on Peptoids As Solar Thermal Fuel*
  One-day meeting of Young Chemists
  Namur (Belgium), 17/05/2024

- *Phenylazothiazole photoswitches on macromolecules for solar energy storage : photoisomerization and thermal back-isomerization kinetics by MS*
  Annual meeting of the Belgian Society for Mass Spectrometry
  Mons (Belgium), 12/09/2025

3. POSTERS

- G. Henrard, B. Tassignon, J. De Winter, J. Cornil, P. Gerbaux. *Mass Spectrometry and Photochemical Study of Photoisomerization and Thermal Back-isomerization of Substituted Azobenzenes anchored on Peptoids for the Chemical Storage of Solar Energy*
  One-day meeting of Young Chemists
  Liège (Belgium), 01/04/2022

- G. Henrard, B. Tassignon, J. De Winter, J. Cornil, P. Gerbaux. *Mass Spectrometry and Photochemical Study of Photoisomerization and Thermal Back-isomerization of Substituted Azobenzenes anchored on Peptoids for the Chemical Storage of Solar Energy*
  The 24th International Mass Spectrometry Conference
  Maastricht (Netherlands), 30/08/2022

- G. Henrard, T. Robert, B. Tassignon, J. De Winter, J. Cornil, P. Gerbaux. Mass Spectrometry and Photochemical Study of Photoisomerization and Thermal Back-isomerization of Substituted Azobenzenes anchored on Peptoids for the Chemical Storage of Solar Energy
  Annual meeting of the Belgian Society for Mass Spectrometry
  UCB Pharma (Belgium), 07/10/2022

- G. Henrard, T. Robert, B. Tassignon, J. De Winter, J. Cornil, P. Gerbaux. *Mass Spectrometry and Photochemical Study of Photoisomerization and Thermal Back-isomerization of Substituted Azobenzenes anchored on Peptoids for the Chemical Storage of Solar Energy*
  SRC 2022 Scientific Day
  Liège (Belgium), 18/10/2022

- G. Henrard, T. Robert, B. Tassignon, J. De Winter, J. Cornil, P. Gerbaux. *Original Heteroaryl Azobenzene derivatives As Solar Thermal Fuel Candidates : a Mass Spectrometry and UV-vis Spectrophotometry Investigation*
  39th Informal Meeting on Mass Spectrometry
  Paris (France), 14/05/2023

- G. Henrard, T. Robert, B. Tassignon, J. De Winter, J. Cornil, P. Gerbaux. *Mass Spectrometry and Photochemical Study of Photoisomerization and Thermal Back-isomerization of Heteroaryl Azobenzenes anchored on Peptoids for the Chemical Storage of Solar Energy*
  6th International Mass Spectrometry School
  Cagliari (Italy), 17/09/2023

- G. Henrard, T. Robert, B. Tassignon, J. De Winter, J. Cornil, P. Gerbaux. *Mass Spectrometry and Photochemical Study of Photoisomerization and Thermal Back-isomerization of Heteroaryl Azobenzenes anchored on Peptoids for the Chemical Storage of Solar Energy*
  SRC 2023 Scientific Day
  Louvain-La-Neuve (Belgium), 19/10/2023

- G. Henrard, T. Robert, B. Tassignon, J. De Winter, J. Cornil, P. Gerbaux. *Original Heteroaryl Azobenzenes anchored on Peptoids as Solar Thermal Fuel*
  Functional Molecular Photoswitches for Energy Storage and Beyond
  Barcelona (Spain), 24/04/2024

- G. Henrard, T. Robert, B. Tassignon, J. De Winter, J. Cornil, P. Gerbaux. *Original Heteroaryl Azobenzenes anchored on Peptoids as Solar Thermal Fuel*
  SRC 2024 Scientific Day
  Mons (Belgium), 17/10/2024

- G. Henrard, T. Robert, B. Tassignon, J. De Winter, J. Cornil, P. Gerbaux. *Phenylazothiazole photoswitches on macromolecules for solar energy storage : photoisomerization and thermal back isomerization kinetics by MS*
  ASMS 2025, 73rd Conference on mass spectrometry and allied topics
  Baltimore (United States), 04/06/2025

4. AWARDS AND GRANTS

Best Poster prize at the annual meeting of the Belgian Society for Mass Spectrometry

UCB Pharma (Belgium), 07/10/2022

Best MS solver award at the 6th International Mass Spectrometry School

Cagliari (Italy), 17/09/2023